The Catalytic Mechanism of the Iron-Dependent Sulfoxide Synthase EgtB

Inauguraldissertation

zur

Erlangung der Würde eines Doktors der Philosophie

vorgelegt der

Philosophisch-Naturwissenschaftlichen Fakultät

der Universität Basel

von

Kristina Vadimovna Goncharenko

aus Sewastopol, Russland

Basel, 2019

Genehmigt von der Philosophisch-Naturwissenschaftlichen Fakultät

auf Antrag von

Prof. Dr. Florian P. Seebeck

Prof. Dr. Thomas R. Ward

Basel, 18.04.2017

Prof. Dr. M. Spiess

Dekan der Philosophisch-

Naturwissenschaftlichen Fakultät

"Ever tried. Ever failed. No matter. Try Again. Fail again. Fail better."

Samuel Beckett

Abbreviations

MMH	N^{α}-monomethyl-L-histidine
DMH	N^{α},N^{α}-dimethyl-L-histidine
TMH	N^{α},N^{α},N^{α}-trimethyl-L-histidine
γGluCys	γ-glutamyl-L-cysteine
Cys	L-cysteine
γGluSeCys	γ-glutamyl-L-selenocysteine
SeCys	L-selenocysteine
HEPES	4-(2-hydroxyethyl)-1-piperazineethanesulfonic acid
$EgtB_1$	EgtB from *Mycobacterium thermoresistibile*
$EgtB_2$	EgtB from *Candidatus chloracidobacterium thermophilum B*
$EgtB_{cur}$	EgtB from *Thermomonospora curvata*
CDO	Cysteine dioxygenase
TCEP	Tris(2-carboxyethyl)phosphine
CD	Circular dichroism
ET	L-ergothioneine
DSBH	Double-stranded β-helix
DFT	Density functional theory
NHI	Non-haem iron-dependent
HRMS	High-resolution mass spectrometry
ESI	Electrospray ionization
NMR	Nuclear magnetic resonance
ROS	Reactive oxygen species
LMCT	Ligand-to-metal charge transfer
KIE	Kinetic isotope effect
KSIE	Kinetic solvent isotope effect
PCET	Proton coupled electron transfer
HAT	Hydrogen atom transfer
EDTA	Ethylenediaminetetraacetic acid
QM/MM	Quantum mechanics / molecular mechanics

Table of Contents

Abstract

Sulfoxide synthases EgtB form a class of non-haem iron enzymes, which catalyze the oxygen-dependent sulfur-carbon bond formation between low molecular weight thiols and N^{α},N^{α},N^{α}-trimethyl-L-histidine as a central step in ergothioneine biosynthesis.[1] The crystal structure of EgtB from *Mycobacterium thermoresistibile*, in complex with γ-glutamylcysteine and N^{α},N^{α}-dimethyl-L-histidine, implicate both substrates and three histidine residues as ligands in an octahedral iron binding site.[2] In the secondary coordination sphere we identified a tyrosine residue which serves as a proton donor to an iron(III)-superoxo species. Mutation of this residue to phenylalanine produced a variant with 500-fold reduced sulfoxide synthase activity. Moreover, this protein catalyzes thiol dioxygenation with an efficacy that rivals naturally evolved cysteine dioxygenases.[3] We also demonstrated that a catalytic tyrosine residue is present among different sulfoxide synthases.

Furthermore, the replacement of cysteine with selenocysteine in EgtB from *Candidatus chloracidobacterium thermophilum B* might catalyze the formation of the selenoxide, which is further reduced to hercynylselenocysteine. We suggest that the enzymes involved in the biosynthetic pathway of ergothioneine are able to synthesize selenoneine, where first the selenoxide is formed by the sulfoxide synthase EgtB, which is then reduced by the intracellular reductants, and then the β-lyase EgtE catalyzes selenoneine formation. However, the enzymatic formation of the C-Se bond has a moderate rate in comparison to C-S bond formation. Additionally, selenocysteine is an excellent mechanistic probe; it acts as a competitive inhibitor towards cysteine and uncompetitive towards TMH, suggesting a sequential binding order in the mechanism of EgtB.

Protein design based on the crystal structure of EgtB from *Mycobacterium thermoresistibile* allowed the remodeling of the active site and the tuning of the reactivity of the sulfoxide synthase by introducing an additional hydrogen bond to the thiolate coordinated to the iron center of the enzyme. It was found that the resulting hydrogen bond between the thiolate of the substrate and S82 in the active site disturbs the formation of the proposed thiyl radical. This intermediate is required in the catalytic mechanism to further proceed to attack of this thiyl radical on the imidazole ring of the second substrate.

Overall we have used crystallographic data and kinetic analysis to probe the mechanistic details of EgtB-catalyzed C-S bond formation. This data would allow us to probe the activity of related enzymes as well as designing antibacterial inhibitors.

1. Introduction

1.1. Oxygen activation

Dioxygen is an essential molecule for life in many organisms. Dioxygen is an attractive substrate for use in biological systems because its potentially high reactivity is kept under control by its molecular structure. The presence of two unpaired electrons in degenerate molecular orbitals results in the triplet ground state of dioxygen. Therefore, the direct reaction with singlet molecules, the spin-paired state of most potential reaction partners, is a forbidden process.[4] But until the 1950's, it was believed that oxygen played a role as a terminal electron acceptor for the energy-generating pathways of the oxidative phosphorylation pathway. It was thought that the source of oxygen was water in most natural transformations. In 1955, Hayaishi *et al.* demonstrated that molecular oxygen could be the direct source of the oxygen atom incorporated into organic substrates during biological oxidations.[5] Labeled dioxygen ($^{18}O_2$) and isotopically labeled water (H_2O^{18}) were used to identify the source of oxygen. This discovery provided an opportunity for researchers to discover how Nature developed the way to overcome the spin-forbidden and the one-electron reduction potential of O_2.

Controlled oxidation is required in many chemical reactions crucial for life, such as DNA and RNA repair, hypoxia sensing in mammalian cells, desaturation of fatty acids in plants, and the hydroxylation of methane in methanotrophs.[6,7,8,9] The catalytic four-electron reduction of O_2 to water has also gained increased attention because of its relevance to fuel cell technology.[10] For the controlled oxidation, oxygen needs to be excited or activated to the singlet state in order to overcome the spin restriction. Nature has solved this problem of specific activation of molecular oxygen by activation using transition metal complexes containing iron, copper, and manganese, often with organic cofactor such as pterin, flavin or both, as in case of haem.[11] In many biological systems, the oxygen is reductively activated, because inversion of an oxygen electron to yield the singlet state directly is highly endothermic.

In recent years, the mechanism of oxygen activation in the biological systems has been investigated through the coordinated use of chemical, structural, spectroscopic, and computational approaches. An overview of oxygen activation by iron in Fe-containing enzymes will be discussed.

1.2. Oxygen activation by iron

A wide range of metalloenzymes and artificial organic catalysts mimicking the active site of enzymes have been widely studied over the past decades, in particular, oxygen activation by iron-dependent enzymes, such as haem- and non-haem monooxygenases containing mononuclear, homo- and heterodinuclear active sites. The active intermediates of these enzymes include high-valent metal−oxo and metal−dioxygen (superoxo, peroxo, and hydroperoxo) cores (Figure 1).

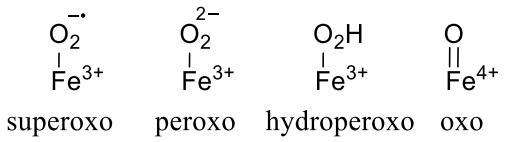

Figure 1. Iron-oxygen intermediates present in active complexes of non-haem iron-dependent enzymes.

Many of these intermediates were discovered in haem enzymes. Haem is a cofactor consisting of an ion coordinated at the center of a porphyrin ring, a ligand which is built from four pyrrolic groups joined together by methine bridges. Hemoproteins is a large biologically important group of proteins such as myoglobin, cytochrome, catalase and haem peroxidase.

One of the most well-known classes of haem-containing enzymes are the cytochrome P450 monooxygenases. These monooxygenases catalyze a diverse range of oxidative reactions, including hydroxylation of C−H bonds, O- and N-dealkylation, N-hydroxylation, S-oxidation, and epoxidation reactions. There have been many studies regarding the mechanism of this enzyme, the most recent of which is shown on Scheme 1.[12] Cytochrome P450 monooxygenases use iron-protoporphyrin IX as a cofactor, where the haem iron is axially coordinated by the thiolate of cysteine (1). The catalytic cycle of cytochrome P450 monooxygenases starts by the displacement of a water molecule from the metal center by the substrate (1-2), followed by a one-electron reduction of the haem by a redox partner (3). The oxygen molecule then binds to complex (3) resulting in ferrous-dioxygen or a ferric-superoxide complex (4), which further forms a haem-peroxo intermediate by the transfer of a second electron (5). Next, proton transfer allows for the formation of a hydroperoxo adduct (6), which breaks down to give a high-valent iron-oxo species (7). The iron-oxo species is thought to abstract a hydrogen atom from the substrate, forming a radical on the substrate and the intermediate (8), which can be represented as a protonated oxidoiron(IV) or a protonated oxidoiron(III)-protoporphyrin radical. The substrate radical undergoes hydroxylation (9) by intermediate (8), followed by product release and completion of the catalytic cycle.[13]

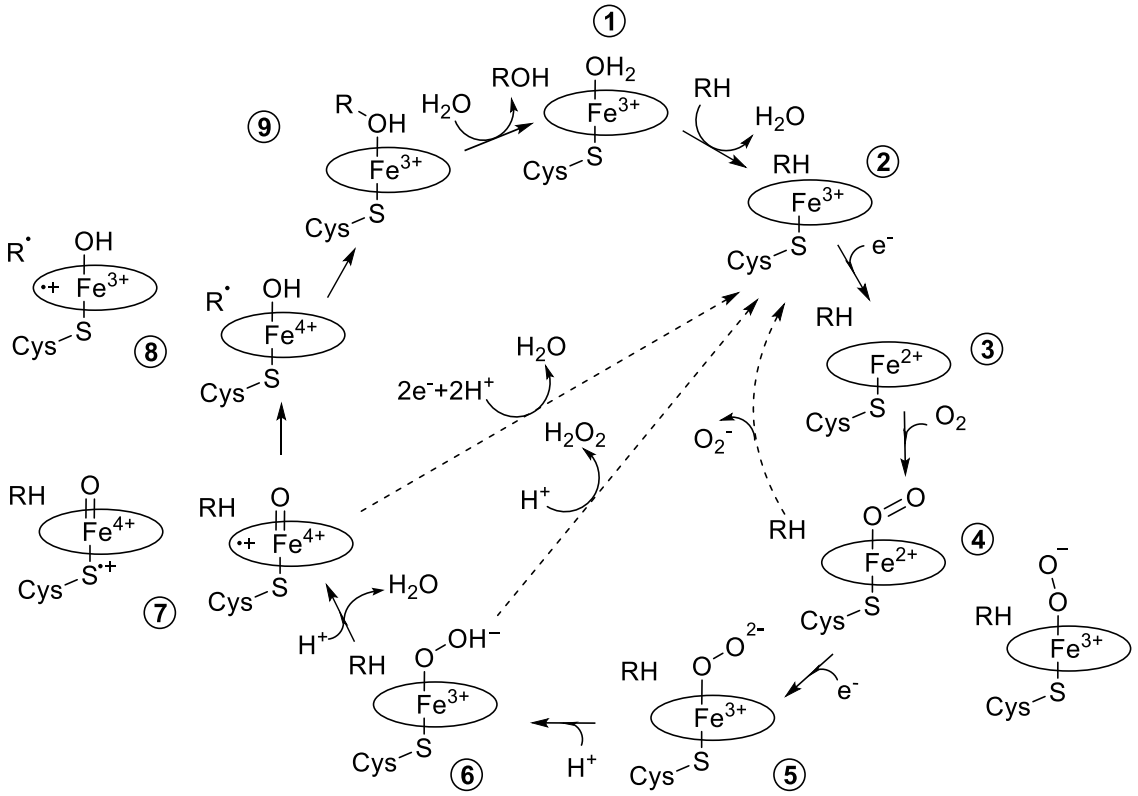

Scheme 1. Proposed catalytic cycle of P450 enzymes. Dashed arrows show possible uncoupling processes.[12-14]

The knowledge of the mechanism of hemoproteins and detection of the intermediates gives us a deeper understanding of the mechanisms of oxygen activation in haem enzymes. Some of the detected intermediates might be similar for non-haem dependent enzymes which lack the P450 cofactor. Since the active site architecture differs within non-haem iron-dependent enzymes, the difference in the coordination sphere of iron centers and overall folds of non-haem iron enzymes will be discussed.

1.3. Structural insides of non-haem enzymes

Mononuclear, non-haem iron-dependent (NHI) enzymes catalyze a broad range of reactions including hydroxylation, chlorination, epimerization, cyclization and ring cleavage of various organic substrates.[11b] The absence of haem in non-haem iron-dependent enzymes makes the binding of the metal not as direct as in the case of a bulky stable haem molecule. Nevertheless, various ways evolved to keep iron sequestered within an enzyme and proceed with a reaction in absence of haem. It has been shown that there are four main coordination ligands in non-haem iron enzymes, also known as facial triads: 2-His-1-carboxylate, 3-His, 3-His-1-carboxylate and 4-His facial triads.[15] The facial triad binds a metal, leaving the opposite site of the octahedron available to coordinate ligands. The substrate binding activates the metal center for oxygen attack. Metal binding residues are highly conserved among different protein structures and span different fold families.[16] The diverse activity of non-haem

iron-dependent enzymes raises the question of the role of the protein environment around the active site metal on the type and selectivity of the reaction.

Coordination of iron in the active site of mononuclear NHI enzymes

A crystal structure analysis of available NHI enzymes reveals that iron is preferably coordinated in an octahedral manner with a facial arrangement of the metal ligands. Therefore, three *cis*-sites are left open on the iron cofactor for binding of the substrate, co-substrate and oxygen. The most common iron binding motif consists of a 2-His-1-Asp/Glu triad. This triad is present in a wide range of enzymes: α-ketoglutarate dependent enzymes, pterin-dependent hydroxylases, Rieske dioxygenases, extradiol-cleaving catechol dioxygenases and other oxidases, such as isopenicillin N synthase or 1-aminocyclopropane-1-carboxylic acid oxidase.[17]

The example of a 2-His-1-Asp/Glu triad is discussed for an α-ketoglutarate (α-KG) dioxygenase.[18] In most reported structures, α-KG binds to the iron center in a bidentate fashion by replacing two water molecules, and the 1-carboxylate of α-KG coordinates *trans* to the proximal histidine of the facial triad motif. It has been proposed that the carboxylate residue in the facial triad serves to stabilize the water ligand.[19] For example, in the crystal structure of TauD the remaining open site for O_2 binding points directly towards the substrate (Figure 2, left).[20] However, this binding mode is not conserved amongst all α-KG dioxygenases. The example of the 2-keto group of α-KG coordinating to the iron center *trans* to aspartate has been found in the FtmOx1-Fe(II)–α-KG complex, (Figure 2, right).[21] There is a water ligand in close proximity to Y224 at the place where oxygen binds. This close coordination of oxygen ligated to Y224 explains the formation of 3,4-dihydroxyphenylalanine (DOPA) in the FtmOx1 self-hydroxylation reaction.

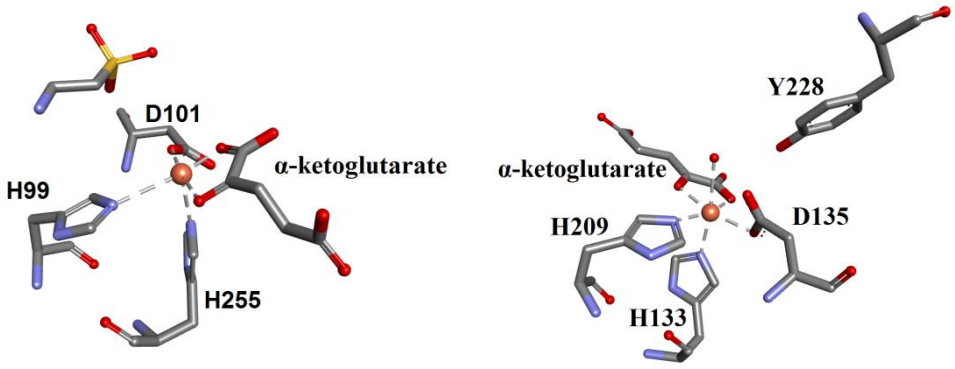

Figure 2. Structure of the active site of α-ketoglutarate dioxygenases TauD (left; pdb: 1OS7, 2.5 Å) and FtmOx1 (right; pdb: 4Y5S, 2.54 Å).

Less common motifs for iron binding in non-haem iron-dependent enzymes consist of a 3-His facial triad (Figure 3, left). This facial triad coordinates iron in thiol dioxygenases (CDO), diketone dioxygenase (Dke1) and aromatic ring-cleaving reactions.[22] 3-His and 2-His-1-carboxylate facial

triads of NHI enzymes have a remarkably high degree of structural similarity despite the non-conservative exchange of the uncharged side chain of the histidine residue by the negatively charged side chain of the aspartate residue. A structural comparison between 3-His and 2-His-1-carboxylate facial triads reveals a difference in the coordination distance of the ligands bound to the iron center. For example, in TauD, the metal-ligand distances are: H99-2.48 Å, H255-2.31 Å, D101-2.05 Å; as for CDO active site the distance of three histidine residues are shorter: 2.07-2.08 Å.[15]

Another type of a facial triad is utilized by the halogenase SyrB2.[23] Analyses of the SyrB2 sequence shows that the common conserved metal binding residue Glu/Asp is replaced by an alanine residue.[24] Crystallographic data revealed that the active site of this enzyme differs from other α-KG-dependent iron enzymes by placing a halide ligand in place of the carboxylate of the canonical 2-His-1-carboxylate facial triad.[25] The metal binding center of SyrB2 in the presence of chloride and α-KG shows a six-coordinate geometry (Figure 3, right). The magnetic circular dichroism spectroscopy revealed a weaker affinity of iron(II) in the 2-His binding site compared to that in the 2-His-1-carboxylate facial triad and the metal will bind only in the presence of α-KG.[26]

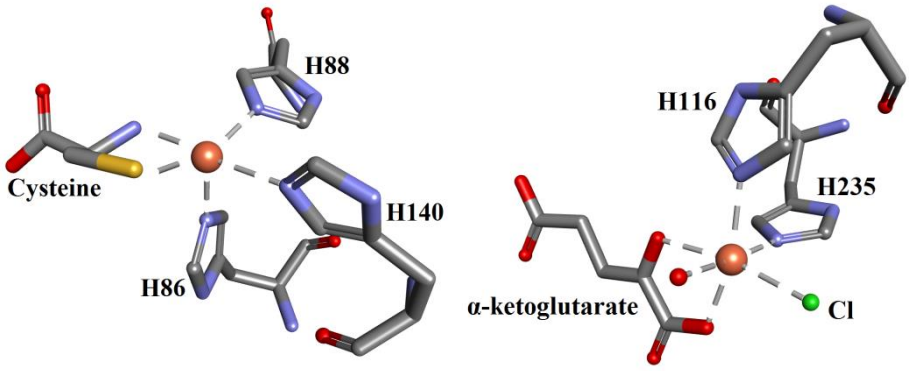

Figure 3. Metal center of CDO with cysteine bound to the active site (left, pdb: 4Z82, 1.7 Å). Active site of halogenase SyrB2 (right, pdb: 2FCT, 1.6 Å).

Fold types of non-haem iron-dependent enzymes

The different families of non-haem iron-dependent enzymes differ not only in the coordination pattern of the metal, but also in the architecture of the secondary coordination sphere. In general all iron-dependent superfamilies are found in six large fold groups, including the Rossmann fold, the jelly roll, the TIM barrel, the immunoglobulin-like, the alpha-beta plait and the four-helix bundle.[16b]

X-ray structures of various non-haem iron-dependent oxygenases feature one of the most common folds - the DSBH (double-stranded β-helix) fold also known as “cupin” or “the jelly roll”, which adopts a barrel-like structure. Even when the sequence motifs differ throughout different families, the structural motif favors a convergent evolutionary pattern. The iron-binding motif differs among families of enzymes by a conserved $HX_nD/E/HX_nH$ motif, where the number of residues X

varies between n = 1 - 193.[15,17] This fold is characterized by a pair of four-stranded antiparallel β-sheets constituting up to eight β-strands. Overall, this fold forms the typical β-sandwich structure. The metal center is located on the inside of the rigid core of the overall protein structure. The example of the DSBH fold is represented by the structure of the diketone dioxygenase Dke1, which displays a typical cupin fold with the cupin metal-binding motif (Figure 4, left).[22]

Another example of a fold in non-haem iron-dependent enzymes is represented by phenylalanine hydroxylase.[27] The iron ligands, most commonly histidine residues, are located in helices while the other ligands are found in a variety of structural contexts. In structurally similar enzymes, such as peptide deformylase (pdb code 1LM4) and sulfur oxygenase reductase (pdb code 2CB2, 1.7 Å), there is a $HX_{3\text{-}4}H$ iron coordination motif embedded in a helix. The two ligands closely spaced in a helix is a common pose adopted by various proteins to support the structure of iron sites.[16b]

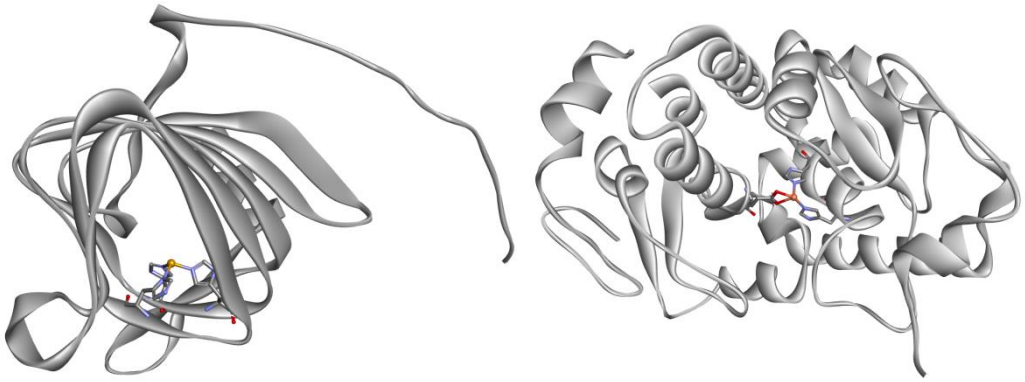

Figure 4. Examples of a structural template representing the mononuclear iron site in the DSBH fold of Dke1 (left, pdb: 3BAL, 1.95 Å) and the different fold of phenylalanine hydroxylase (right, pdb: 1LTZ, 1.4 Å).

Within a large number of non-haem iron-dependent enzymes having quite different functions, it is hard to predict the function based on the first-sphere ligand of the iron center or by the architecture of the secondary fold. Therefore, the investigation of reactions catalyzed by non-haem iron-dependent enzymes requires analysis of the secondary coordination sphere of the iron center. The reactivity can be then finely tuned by the residues which interact directly or through a hydrogen-bond network with the first sphere ligands.

1.4. Mechanisms of reactions catalyzed by NHI enzymes

Non-haem iron-dependent enzymes can be differentiated into two classes: those that incorporate atoms derived from O_2 into their enzymatic products (oxygenases) and those that transfer electrons to O_2 without incorporating atoms derived from O_2 into their enzymatic products (oxidases). Mechanisms of the major non-haem iron-dependent enzymes are well-known and intermediates of active iron species are well characterized. The knowledge of catalytic intermediates can give a great overview on the mechanistic similarities of NHI enzymes. Four examples are discussed below,

representing a general overview on the catalytic cycle of families of NHI enzymes. The first example is based on a class of well-characterized enzymes – the α-ketoglutarate-dependent enzymes, which are among the most common of NHI enzymes. The second interesting member of this group is isopenicillin N synthase, which catalyzes oxidative ring closure of the linear tripeptide substrate δ-(L-α-aminoadipoyl)-L-cysteinyl-D-valine and is particularly interesting due to the formation of C-N and C-S bonds. The third are the thiol dioxygenases, which directly modify the thiolate to sulfinic acid by the incorporation of both oxygen atoms to the product. Cysteine dioxygenase from this class shows *cis*-labilizing thiolate sulfur to the oxygen bound to the iron center. The fourth example is superoxide reductase, which has a similar iron-coordination as cysteine dioxygenase, but the active enzyme shows *trans*-labilizing thiolate sulfur, meaning that the thiolate is located opposite from the superoxide binding site in the iron octahedral complex, which was suggested to make the iron-complex more reactive. The mechanisms of these enzymes are well studied and provide the information on the catalytic intermediates and steps that promote oxygen activation in non-haem iron-dependent enzymes.

α-Ketoglutarate-dependent oxidases and oxygenases

Iron-dependent α-ketoglutarate (α-KG)-dependent enzymes catalyze a diverse range of reactions that result in protein side-chain modifications, reparation of alkylated DNA/RNA, antibiotic biosynthesis, biodegradation of certain compounds and even halogenation reactions.[28,29] Other family members catalyze desaturation, ring expansion, ring formation and other types of oxidative reactions. These enzymes possess a β-strand "jellyroll" structural fold. In most α-KG-dependent enzymes iron is coordinated by a 2-His-1-carboxylate facial triad; however, halogenase SyrB2 displays a 2-His binding mode.

The general mechanism of action for a majority of α-KG-dependent enzymes is represented in Scheme 2. Iron(II) is ligated by two histidines and one carboxylate or a halide (1). The binding of α-KG and a substrate induces the conversion of the six-coordination complex to a five-coordinated complex (2). This then provides an open site for oxygen binding (3). Further, an Fe(IV)–peroxo species forms and nucleophilically attacks α-KG, resulting in a peroxo-bridged Fe(IV) species (4). Oxidative decarboxylation of α-KG yields succinate and carbon dioxide and leads to the generation of a highly reactive iron-oxo Fe(IV)=O intermediate (5). This intermediate is thought to be similar for all α-KG-dependent enzymes and, in related enzymes, catalyzes desaturations, ring expansions, or ring closures. It was first detected in taurine/alpha-ketoglutarate dioxygenase from *Escherichia coli*.[30] The iron-oxo species abstracts a hydrogen atom from the substrate to form an Fe(III)–OH species (6) and a substrate radical. In hydroxylases, the hydroxyl radical is rebound to form a hydroxylated product; in halogenases, the substrate is chlorinated instead.[31,32,25]

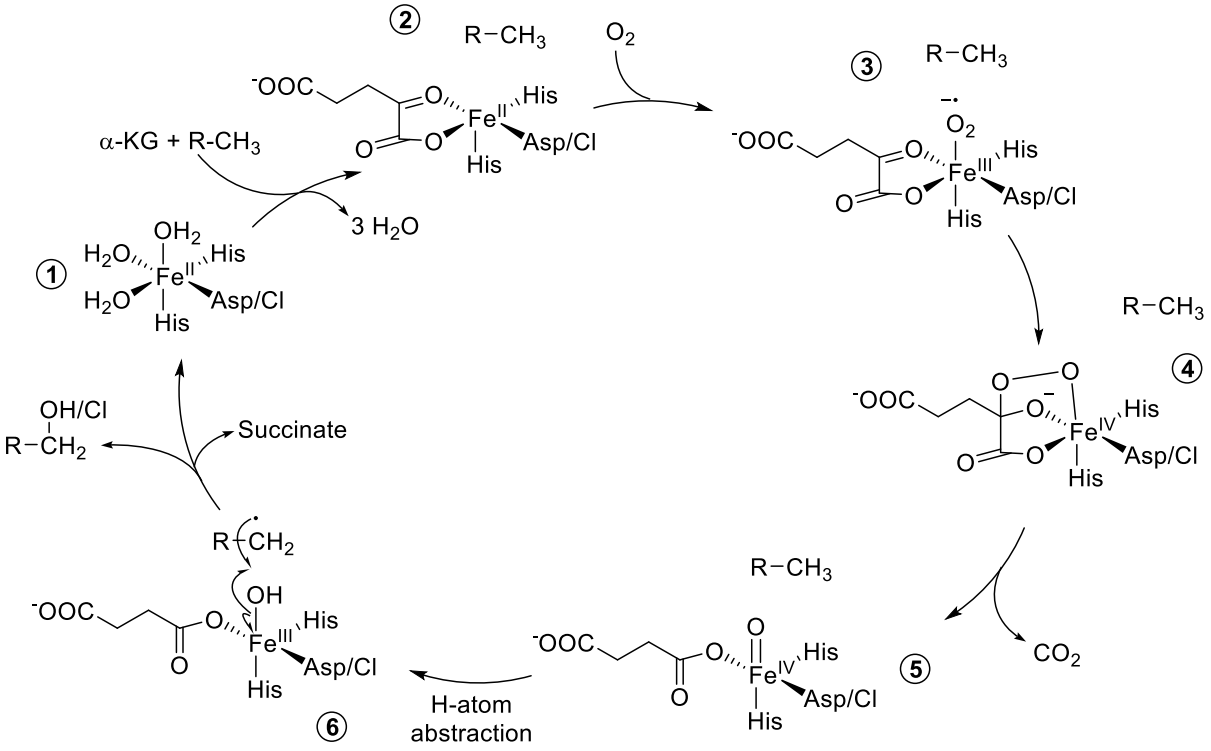

Scheme 2. Catalytic cycle of α-KG-dependent non-haem iron-dependent enzymes.

Isopenicillin N synthase

A well-studied example of enzymatic C-S bond formation is the reaction catalyzed by isopenicillin N synthase (IPNS), a non-haem iron-dependent oxidase. IPNS catalyzes the cyclization reaction of the linear tripeptide substrate δ-(L-α-aminoadipoyl)-L-cysteinyl-D-valine (ACV) to isopenicillin N (Scheme 3), using molecular oxygen. The formation of isopenicillin N is a crucial step in the synthesis of penicillins and cephalosporins.[33]

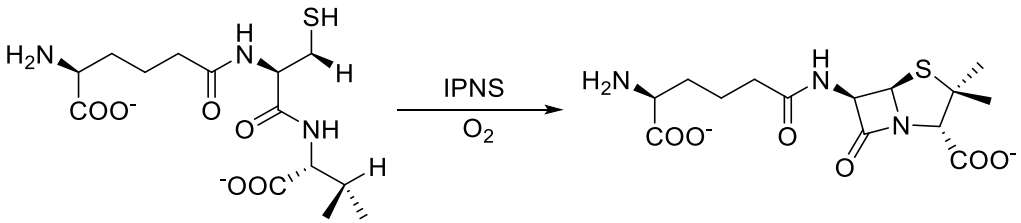

Scheme 3. Reaction catalyzed by IPNS.

IPNS has been widely studied in the past decades. Crystallographic studies revealed a 2-His-1-Asp iron binding triad in the active site of IPNS.[34] The mechanistic proposal of IPNS is based on data from crystallographic, computational, and spectroscopic studies (Scheme 4).[35,36] In the crystal structure of IPNS there is a glutamine or a water molecule bound to iron (1) which then is replaced by the substrate through thiolate (2). After oxygen binding, the iron-bound dioxygen species first

activates the β-C-H bond (3) resulting in a ferrous peroxide species (4). Then, abstraction of the valine N-H proton (5) triggers the cyclization to the β-lactam ring – the first irreversible step in isopenicillin N formation (6). This step was experimentally confirmed by generating a ^{2}H-labeled substrate, and determining the KIE.[37] After the first cyclization step, a high-valent ferryl-oxo species (7) abstracts a hydrogen atom from C3 of valine. A carbon centered radical on valine side-chain in the intermediate (8) reacts with sulfur on a ferric-hydroxy species and result in the formation of the C-S bond in the five-membered thiazolidine ring (9). A combination of Mössbauer spectroscopy, stopped-flow UV-vis experiments, together with computational studies identified both C−H-cleaving intermediates (3) and (7).[38] The key intermediates (3) and (7) are high-spin Fe(III)-superoxo and high-spin Fe(IV)-oxo complexes. The reactive Fe(III)-peroxo species can carry out crucial hydrogen atom abstraction from a C−H bond to initiate the four-electron oxidation of substrates proposed for some non-haem iron-dependent enzymes.[39]

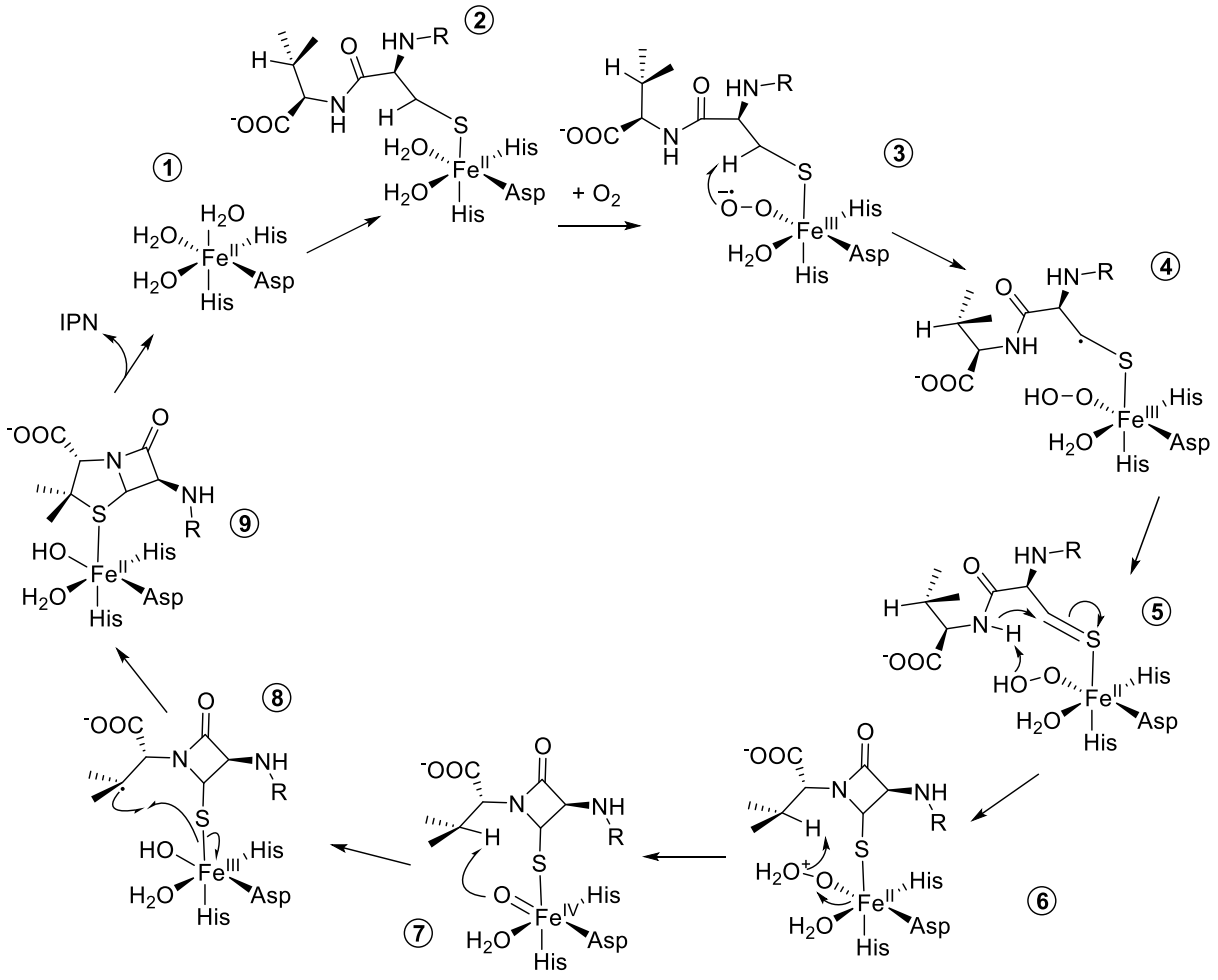

Scheme 4. Proposed mechanism of IPNS.

Cysteine dioxygenase

Another class of non-haem iron-dependent oxygenases are the thiol dioxygenases. This class of oxygenases oxidize the thiol group of various substrates, generating sulfinic acids. Thiol dioxygenases include cysteine dioxygenase (CDO), which catalyzes the oxidation of L-cysteine to L-cysteine sulfinic acid; 2-aminoethanethiol dioxygenase (ADO), which catalyzes the oxidation of cysteamine to hypotaurine in mammalian livers[40] and conversion of 3-mercaptopropionate to 3-sulfinopropionate by 3-mercap-topropionate dioxygenase (MDO) (Scheme 5).[41]

Over the past decade, thiol dioxygenases were recognized as potential targets for the therapy of cancers, antimicrobials and anti-inflammatory substances.[42] CDO regulates the cellular concentration of L-cysteine by catalyzing the first step in the catabolism that leads to the formation of taurine, pyruvate or sulfate as the final product.[43] Recently, it was shown that an insufficient level of CDO causes exogenous cysteine accumulation to harmful levels. A dysfunction in the sulfur metabolism has been shown to be associated with some human neurodegenerative disease states, including Parkinson's and Alzheimer's, which are conditions of significant medical interest.[44, 45]

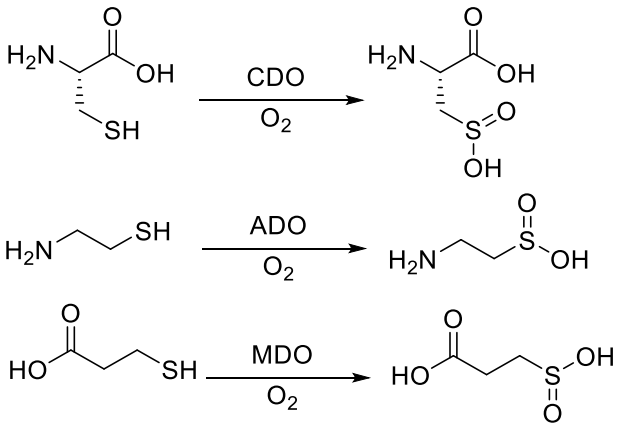

Scheme 5. Reactions catalyzed by thiol dioxygenases CDO, ADO and MDO.

Cysteine dioxygenase has been well characterized with the first crystal structure being solved in 2006.[46] The crystal structure of mouse CDO reveals the coordination of Fe(II) by a facial triad of histidine side chains ligating the metal center with their ε-N atoms. The metal center has a distorted octahedral geometry, where the cysteine substrate is coordinated to iron with the amine and thiolate, leaving an open coordination space for oxygen to bind. Interestingly, in mammalian CDO's, there is an unusual structural feature of a cross-link between Cys and Tyr in the active site, similar to the one observed in galactose oxidase.[47] It has been shown that the Cys93–Tyr157 cross-link increases the catalytic efficiency of the enzyme by over 10-fold.[48, 49] The Tyr157–OH of the Cys93–Tyr157 cross-link is located near the iron and is proposed to be a catalytic acid/base that is activated *via* a Ser153-His155-Tyr157 catalytic triad. Interestingly, this cross-link is absent in prokaryotic CDO's and other thiol dioxygenases, and it is not present in newly transcribed CDO but builds up as the result of a

reaction that occurs during turnovers.[50] The proposed mechanism of cross-link formation suggests that it is strictly dependent on the presence of the substrate cysteine bound in the active site, the physiological substrate of the enzyme (Scheme 6). In practice, recombinantly expressed CDO exists as a mixture of protein partly containing the cross-link. Cysteine-dependent cross-link formation appears to be a physiologically important mechanism for the regulation of CDO activity and *in vivo* regulation of intracellular cysteine levels.[50]

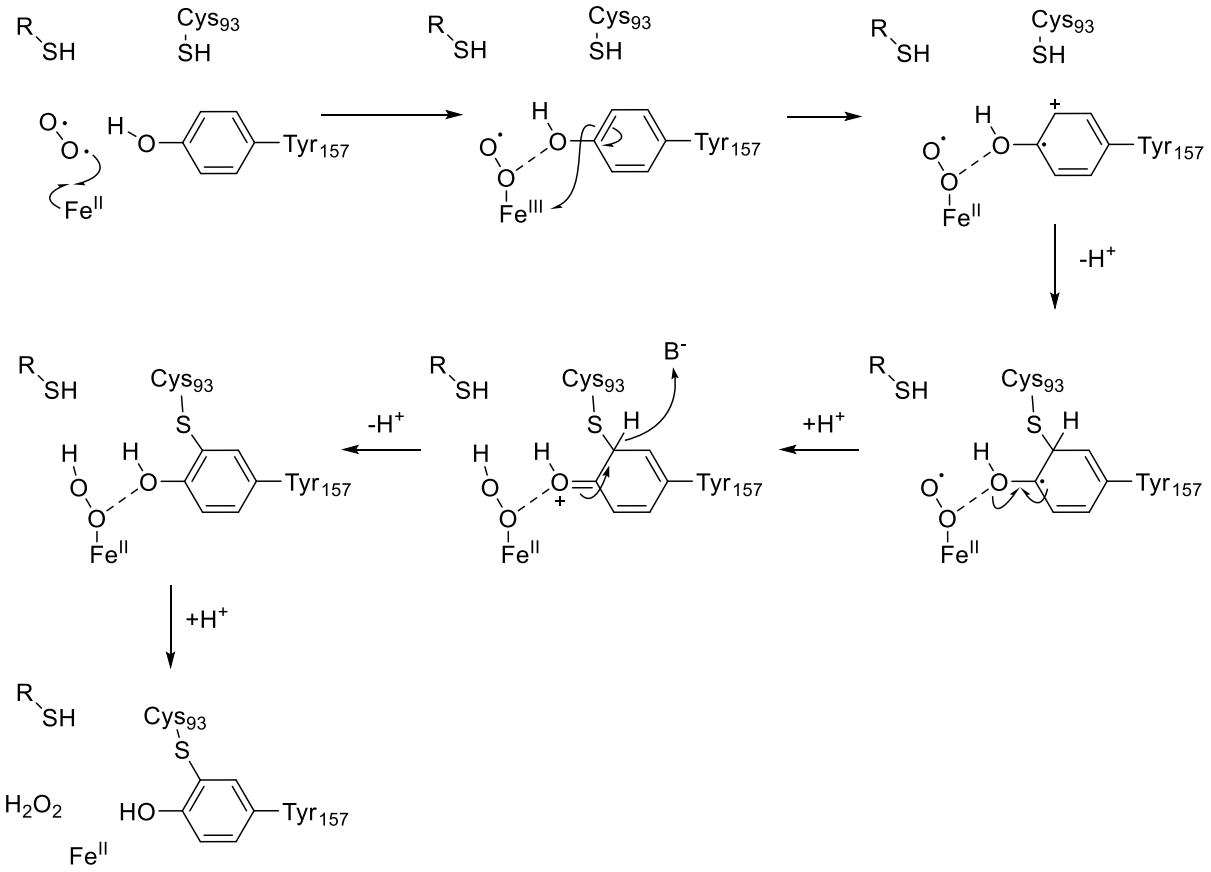

Scheme 6. Proposed mechanism of cross-link formation.

The mechanism of CDO was proposed based on a combination of spectroscopic, structural and computational studies (Scheme 7).[51] After cysteine is bound to the iron, CDO binds dioxygen to form an iron(III)–superoxo species (B). The distal oxygen of superoxide then attacks the sulfur of cysteine by formation of a four-membered ring (C). The cleavage of the O-O bond results in the formation of an iron(IV)-oxo intermediate (D). Then after rotation of the sulfenate or dissociation and recoordination to (D'), the insertion of the second oxygen onto sulfur occurs (E) and product release.[52]

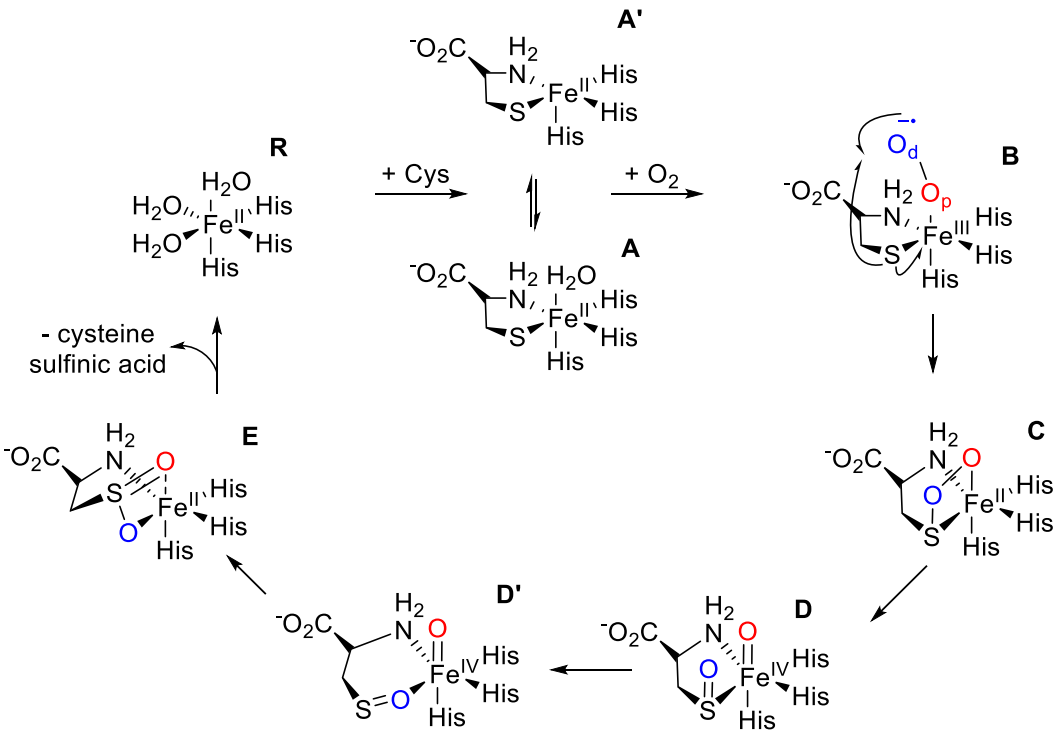

Scheme 7. Catalytic cycle of cysteine dioxygenase.

Superoxide reductase

Oxygen can be activated upon reaction with transition metals or radicals forming a superoxide anion radical, which then further reacts, leading to the formation of harmful reactive oxygen species. High concentrations of reactive oxygen species, including superoxide, are harmful because they may significantly damage the cell structure, DNA and RNA.[53] Many living organisms have protective mechanisms against superoxide, including enzymes such as superoxide dismutases (SOD) or super oxide reductases (SOR).[54] Superoxide reductase is another important example of a non-haem iron-dependent enzyme, which might contain one or two iron centers in its active site.

The active site of SOR consists of iron bound to four equatorial histidine residues and one axial cysteine in a square pyramidal geometry.[54,55] In the oxidized enzyme the sixth position of the octahedral iron complex is occupied by a water molecule or glutamate. Most of the enzymes of this family have a conserved –EKHVP– motif, which is located in close proximity to the active site. The lysine residue of this motif provides the positive surface patch which attracts the superoxide anion.[55]

The mechanism of SOR was investigated by using pulse radiolysis and stopped flow spectroscopy. The reaction was initiated by the formation of superoxide anion by pulse radiolysis in defined amounts. The reduced enzyme was pulsed with an electron beam in presence of oxygen, which made sub-stoichiometric amounts of superoxide generating the first observed intermediate T_1 (Scheme 8). The T_1 intermediate was proposed from theoretical calculations to be either Fe(III)-hydroperoxo or

short-lived Fe(II)-superoxo species.[56] However, this process occurs with a second-order rate constant of ~10^9 M^{-1} s^{-1}. The next detectable species is the resting form of the enzyme - T_2. The Fe(III)−hydroperoxo species decays in a pseudo first-order process to the intermediate T_2. This intermediate has an computed electronic absorption spectrum strikingly identical to that of the Fe(III)-hydroxo form. This means that at this stage, the product H_2O_2, was already released to the bulk solvent mixture. This intermediate T_2, depending on the pH, is either a water molecule or hydroxide anion bound to Fe(III), with an absorbance maximum at 580 nm. The rate of the decay (k_2) of T_1 to T_2 is a rate-limiting, pH-dependent protonation step which shows a solvent isotope effect.[57] The iron center is then substituted by a glutamate ligand, before finally being reduced by cellular reductants, completing the catalytic cycle.

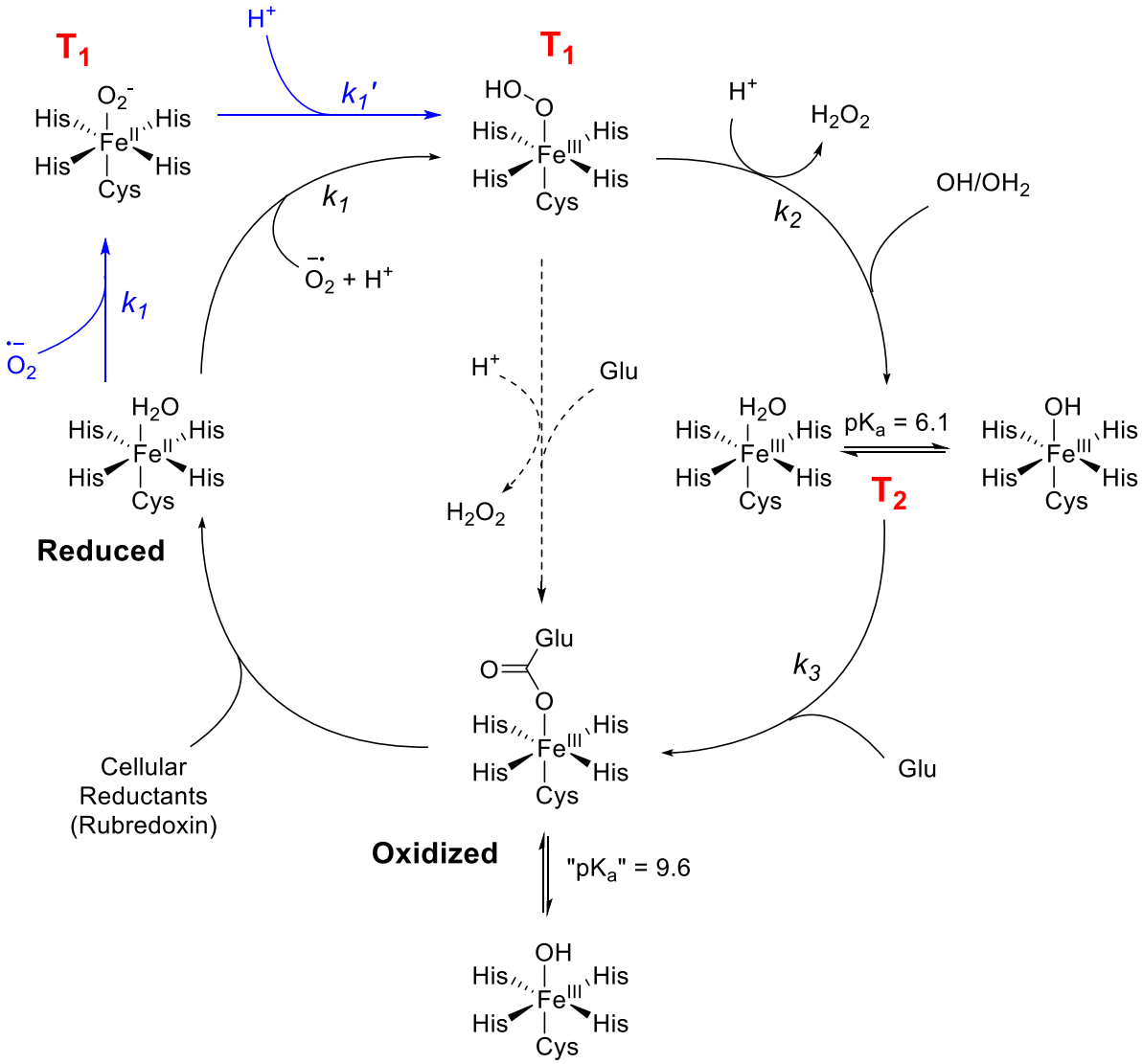

Scheme 8. Catalytic cycle of superoxide reductase. There are the two possible structures for T_1 and two mechanisms involving one or two macroscopically observed intermediates.

The coordination sphere of the active enzyme shows a *trans*-labilizing thiolate sulfur, where the thiolate is located opposite from the superoxide binding in the iron octahedral complex. Generally,

trans-labilizing complexes are more reactive. However, studies on organic complexes showed that the model complex catalyzed the reaction *via* an inner sphere reduction of superoxide.[58] Moreover, the rates of hydrogen peroxide displacement are comparable between that of the enzyme and the synthetic model (Scheme 9). Thus, both systems show superoxide reductase reactivity with no signs of dismutase activity for both *cis*- and *trans*-coordinated thiolate to the open-binging site.

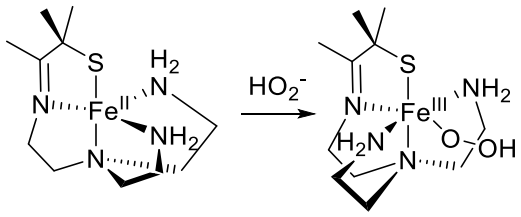

Scheme 9. The model compound with *cis*-labilizing thiolate sulfur has SOR activity as the naturally evolved SOR with *trans*-labilizing thiolate sulfur.

These four examples of NHI enzymes have been discussed to give a general overview on their catalytic cycle and intermediates. The investigation of the mechanism of NHI enzymes gives us a perspective for the rational design of tuning the oxygen reactivity towards different substrates and interconverting the activities of similar enzymes.

1.5. Sulfoxide synthases

Another class of non-haem iron-dependent enzymes, which combines C-S bond formation with oxygenation, are the sulfoxide synthases. Recent mechanistic studies revealed unique features which distinguishes this class of enzymes from other known non-haem iron-dependent enzymes.

Biological role of the sulfoxide synthases in the biosynthesis of thiohistidines

Sulfur-containing metabolites were found to act as messenger, pathogenicity factors, antibacterial compounds or redox buffers.[59] Thiol-containing compounds, such as glutathione, were found to be present in the human body in up to millimolar concentrations. In different microorganisms similar thiol-containing molecules, such as mycothiol, bacillithiol or trypoanothione can be found.[60] The high cellular concentration of such thiols present keeps protein based cysteine residues in a reduced form, to trap electrophilic toxins, and to assist in the trafficking of transition metals across the cell.[59]

In addition to main intracellular thiols, a thiol-containing derivative of histidine - L-ergothioneine (ET) was isolated from ergot in 1909 (Figure 5).[61] ET is produced only by certain bacteria, cyanobacteria and non-yeast fungi, however high concentrations of ET are found in some

human and animal tissues, such as the liver.[61] ET is absorbed through the specific transporter OCTN1, delivering ET to injured tissues or tissues with high oxidative damage.[62] Unfortunately, the precise physiological role of ET has not been established yet, but its *in vitro* antioxidant properties have been demonstrated.[63] This thiol-containing amino acid reveals properties of an antioxidant at physiological pH against hydroxyl radicals, hypochlorous acid, peroxynitrite or singlet oxygen.[64] Interestingly ET exhibits a high redox potential (-0.06 V), therefore it is classified as a powerful antioxidant. Furthermore, ET is present in aqueous solutions predominantly as the thione form rather than as the tautomeric thiol. This property of ET prevents it from autoxidizing and thus differentiates it from other thiol-containing compounds (Figure 5).

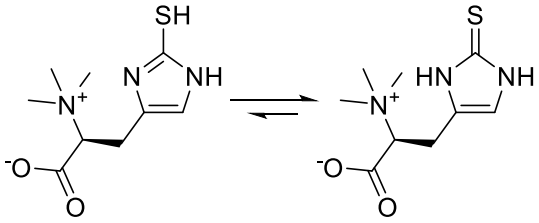

Figure 5. Structure of ergothioneine in the thiol (left) and thione (right) forms.

The first biosynthetic pathway of ET was identified for *Mycobacterium smegmatis* (Scheme 10).[1] The biosynthesis of ET first starts with the trimethylation of the α-amino group of L-histidine by a SAM-dependent methyltransferase EgtD forming **2**.[65] Then, the C-S bond on the C2 carbon of the imidazole ring is formed by the sulfoxide synthase EgtB. The mycobacterial biosynthetic pathway proceeds *via* an intermediate **3** which is generated by $EgtB_{smeg}$. The substrate of $EgtB_{smeg}$ is γ-glutamylcysteine (which in turn is formed from L-Cys and glutamate by EgtA). Further hydrolysis of the amide bond of γ-glutamylcysteine is catalyzed by EgtC, resulting intermediate **4**.[66] The formation of the final product from sulfoxide **4** is suggested to be catalyzed by EgtE. EgtE was proposed to be a β-lyase, but unfortunately the production of the soluble recombinant protein is yet to be accomplished. However, replacement of EgtE with another unrelated β-lyase from *Erwinia tasmaniensis* led to the formation of the final product, ET.[1]

A shorter biosynthetic pathway for ET was identified in the fungus, *Neurospora crassa*.[67] The main difference with the mycobacterial pathway lies in the activity of the sulfoxide synthase. $EgtB_{crassa}$-type sulfoxide synthase is able to accept L-cysteine as a substrate (**2** → **4**), eliminating the need for EgtA- and EgtC-catalyzed reactions.

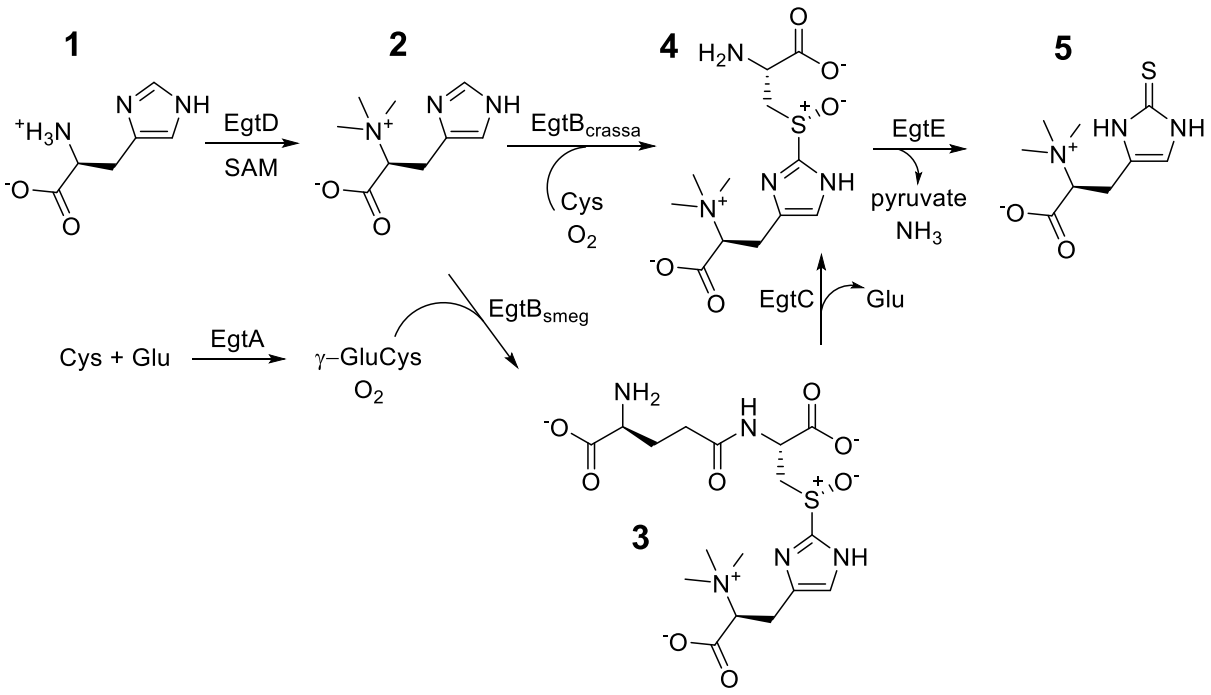

Scheme 10. The ergothioneine biosynthetic pathway found in *Mycobacterium smegmatis* and *Neurospora crassa*.

An isomer of thiohistidine which has been discovered in sea urchin eggs and called ovothiol A.[68] The redox potential of ovothiol A is (-0.09 V vs SHE) and the low thiolate pK_a of 1.4 allows ovothiols to function as protective radical scavengers. It has been proposed that ovothiol protects the DNA of the sea urchin eggs from oxidative stress, however the precise role of ovothiol is not yet established.[69]

Similar to ergothioneine, the biosynthesis of ovothiol A starts from L-histidine and L-cysteine.[70] In *Erwinia tasmaniensis*, two enzymes have been identified that are involved in the biosynthesis of ovothiol A (Scheme 11). The first key step of this reaction is catalyzed by an enzyme functionally similar to EgtB called OvoA. This sulfoxide synthase catalyzes the oxidative insertion of sulfur into the C5 carbon of the imidazole ring of histidine, resulting in sulfoxide **2**. Further elimination of the carbon scaffold of cysteine is performed by the β-lyase OvoB leading to the formation of **3**. Interestingly OvoA does not only contain sulfoxide synthase activity, but the presence of a methyltransferase domain allows for methyltransferase activity. Thus, the last step of ovothiol A biosynthesis is a methyl group transfer onto the imidazole ring of **3**, also catalyzed by OvoA.

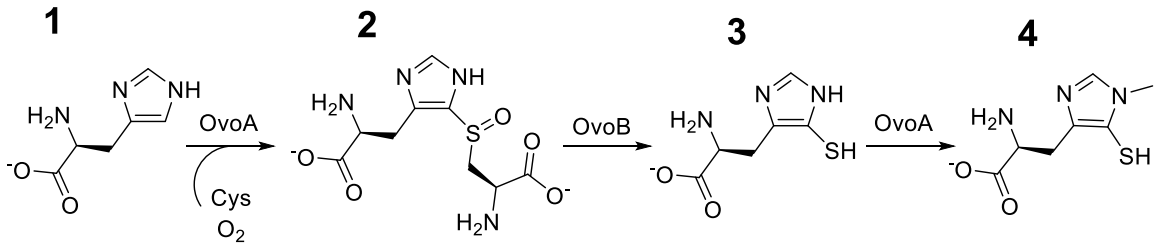

Scheme 11. The biosynthetic pathway of ovothiol A in *Erwinia tasmaniensis*.

Proposed mechanisms of sulfoxide synthases EgtB and OvoA

Two key enzymes in the ergothioneine and ovothiol biosynthetic pathway are the sulfoxide synthases, EgtB and OvoA. Both enzymes bind iron(II) and, before the crystal structure was obtained for EgtB, the metal binding mode of both EgtB and OvoA were first identified as 2-His-1-carboxylate binding motif (HX_3HXE).[16a,1, 70] Mutation of each residue of this binding motif of OvoA led to a more than 100-fold loss in the activity, implying that these residues are involved in iron binding. Both sulfoxide synthases require oxygen as a four electron acceptor to mediate C-S bond formation together with sulfoxidation. The chemically interesting reaction of C-S bond formation brings an opportunity to design low molecular thiols for biotechnological applications, such as production of conopeptides.[71] Interestingly the reaction is highly specific for the imidazole ring as the sulfur acceptor. Furthermore, ergothioneine plays a role as an antioxidant in pathologic bacteria such as *Mycobacterium tuberculosis*, and ovothiol protects several plant pathogens. This addresses a question of designing inhibitors for the central enzymes in both pathways, and raises the question of the mechanism of these novel types of enzymes.[63, 72]

One of the first studies on the sulfoxide synthase mechanism was done by density functional theory (DFT) calculations.[73] The gas-phase thermodynamic free energies of possible reactive intermediates were calculated. The calculations revealed that neither a Fe(II)-superoxo nor a Fe(IV)-oxo intermediate were competent enough to oxidize the imidazole substrate directly. However, a four-membered Fe(II)-peroxysulfur species was suggested to oxidize the imidazole of histidine, as in the case of CDO. This suggests that the oxidation of histidine was thermodynamically most favorable by the formation of a $HisN_{\delta}(-H)^{\bullet}$ radical *via* a PCET process (Scheme 12). However, these DFT calculations were performed before the first crystal structure was published.

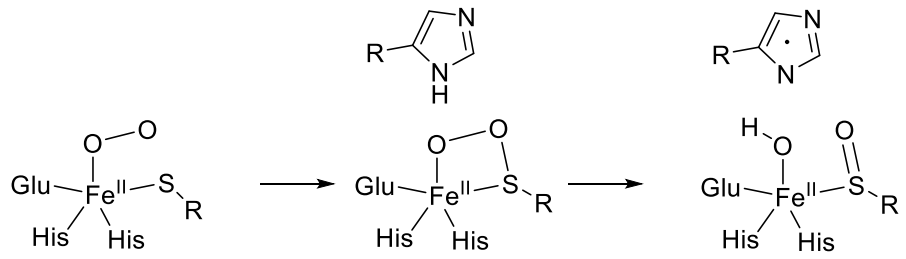

Scheme 12. Proposed intermediates for the formation of histidyl sulfoxide based on thermodynamic stability.[73]

Further mechanistic investigations were performed based on the substrate promiscuity of OvoA in 2013 by Mashabela *et al.* and Song *et al.*[74] The OvoA-catalyzed reaction was performed with cysteine and N^{α} mono-, di-, or trimethylated histidine. The modification efficiency on the C5 imidazole carbon ranged from 100% to 0%, with a corresponding increase in functionalization at the C2 position (Scheme 13).[74b] When OvoA is incubated with D-histidine, it produces a mixture of C2 and C5 modified products (2:3, respectively).[74a] This substrate promiscuity suggests that the product distribution is a function of substrate positioning in the active site.

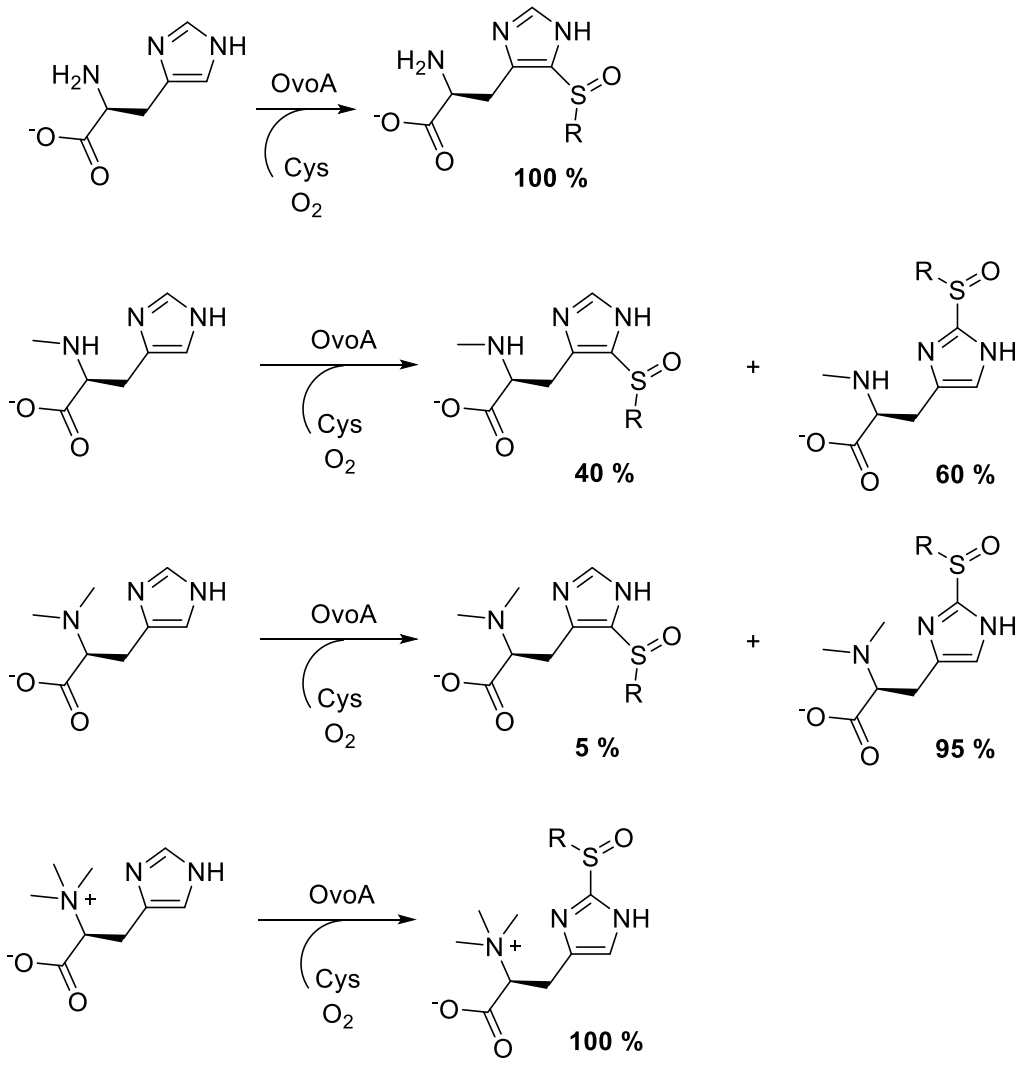

Scheme 13. The selectivity in the OvoA-catalyzed reaction is dependent on the number of methyl groups on N^{α} of L-histidine.[74b]

Mashabela *et al.* also considered a number of mechanisms for OvoA.[74a] The first mechanism suggests the formation of an enzyme bound iron-oxo species (**a**) when all substrates are bound (Scheme 14). This species then mediates C-S bond formation (**b, c, d**). If the second step (**b**) is a hemolytic cleavage of the C5-H bond of the imidazole, the resulting product would be an unstable sp^2 radical, and this step would become the rate limiting. However, no kinetic isotope effect (KIE) was detected by comparing the reaction rates between L-histidine and L-histidine with a deuterium at C5. This result indicates that hydrogen abstraction does not occur in a rate-determining step. However, KIE could have been suppressed by saturated oxygen concentration.

The second mechanism (**c**) proposed a one-electron oxidation of the imidazole ring coupled with deprotonation of the resulting imidazyl radical cation. In order to determine whether this step is rate-limiting, the kinetic solvent isotope effect was measured (KSIE). The kinetic data suggested that there was no significant solvent isotope effect (KSIE = 1.2 ± 0.1). Moreover, it was shown that OvoA catalyzes an efficient reaction with the electron poor 2-fluoro-L-histidine to form 2-fluoro-5-L-histidyl-

L-cysteine sulfoxide. These results suggest that mechanism (**c**) and the mechanism which implicates the imidazole ring as a nucleophile **(d**) are not rate-liming or do not occur.

The fourth mechanism is more consistent with the observed kinetic data. First, the iron-superoxide complex forms a thiyl radical which attacks the imidazole ring (**e**), followed by rearomatization (**f**). The formed thioester is then sulfoxidized and restores the ferrous iron state to complete the catalytic cycle. The formation of 2-fluoro-5-L-histidyl-L-cysteine sulfoxide can therefore be explained by the imidazole ring being an electrophilic target for the nucleophilic thiyl radical.

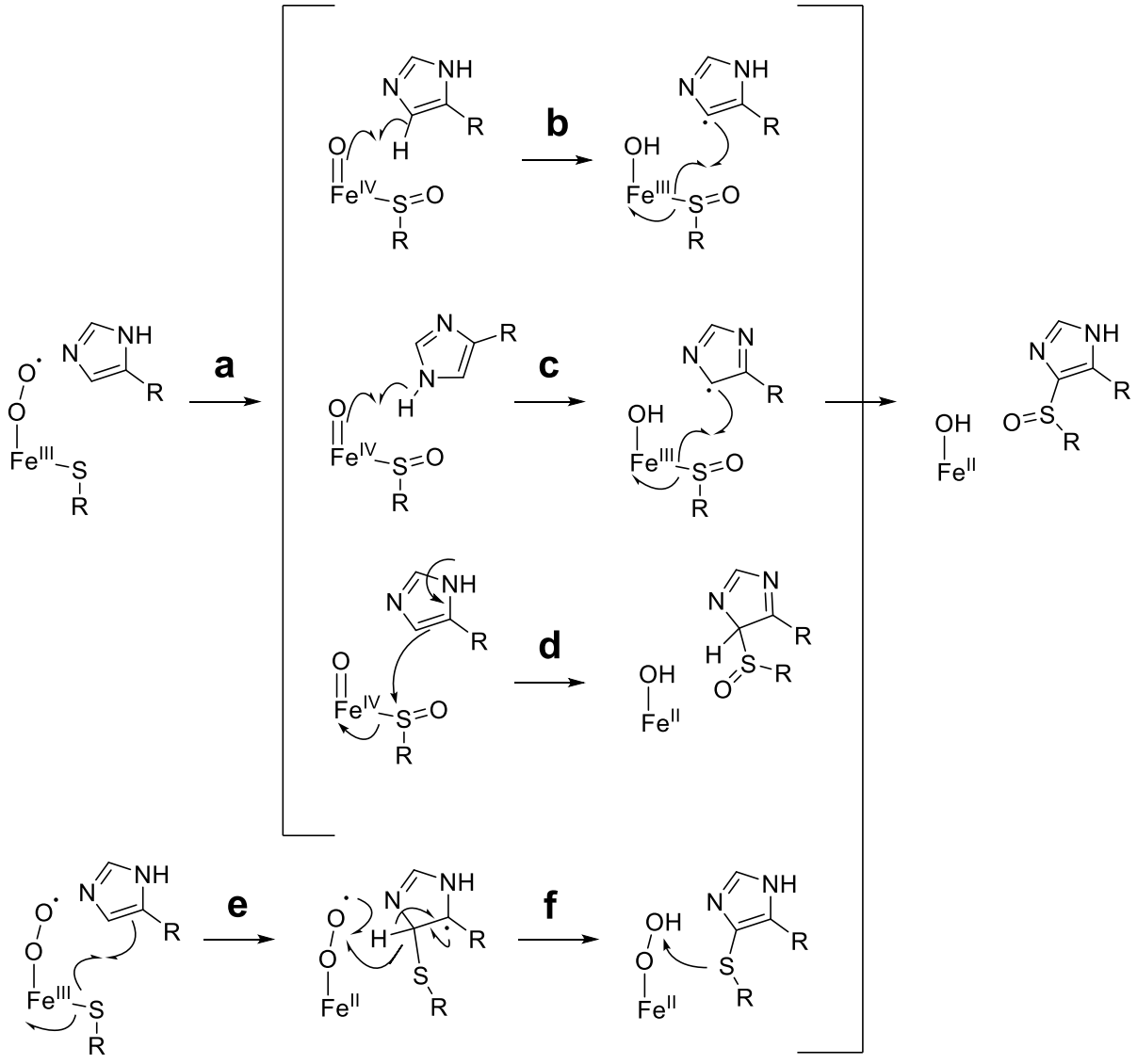

Scheme 14. Proposed mechanism for OvoA-catalyzed sulfoxide formation.[74a]

Song *et al.* proposed two intermediate models for both EgtB and OvoA (reaction with TMH) (Scheme 15).[74b] Those models compare whether the sulfenic acid formation (model A) or the C-S bond formation (model B) is the first step in OvoA and EgtB catalysis. However, no direct evidence of either model has been shown.

Wei *et al.* followed up with a theoretical study of the mechanism of EgtB based on the proposed models by Song *et al.*[75] The calculations suggest that the S–O bond formation occurs first between the thiolate and the ferric superoxide, followed by homolytic O–O bond cleavage, very similar to the case of cysteine dioxygenase.

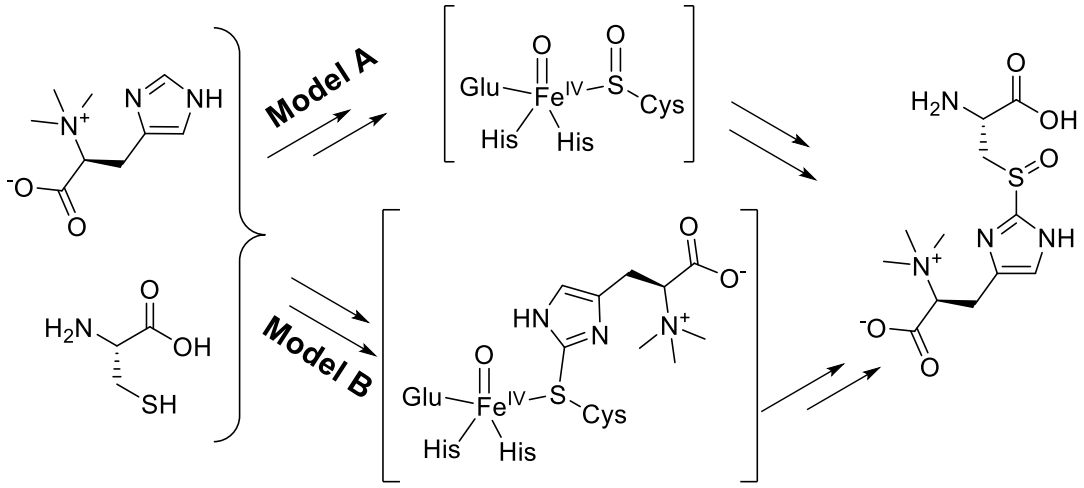

Scheme 15. Proposed model intermediates for OvoA reaction with hercynine suggest that either sulfenic acid formation (model A) or C-S bond formation (model B) are the first step of catalysis.[74b]

Catalytic oxidative C-S bond formation by sulfoxide synthases EgtB and OvoA are distinct from other known C-S bond forming reactions. Both enzymes are involved in the key steps of ergothioneine and ovothiol biosynthetic pathways. Thus, in this thesis, different approaches, such as crystallographic, kinetic and rational design were applied to elucidate the mechanism of novel sulfoxide synthases and will be discussed.

2. Structure of the sulfoxide synthase EgtB from the ergothioneine biosynthetic pathway

The sulfoxide synthases, EgtB and OvoA catalyze a key step in the biosynthesis of ergothioneine and ovothiol A (Scheme 16).[1, 70] Both sulfoxide synthases are non-haem iron-dependent enzymes that catalyze oxidative C-S bond formation. Both enzymes belong to a new class of C-S bond forming enzymes that do not appear to have a relationship with other known sulfur oxidizing enzymes, such as cysteine dioxygenase.[34, 46, 76] In order to understand the mechanism of sulfoxide synthases, the crystal structure and kinetics of EgtB were analyzed. The following chapter suggests a correlation between structure and enzyme activity based on the rational design of EgtB. Furthermore, a possible mechanism of EgtB is discussed based on the results obtained.

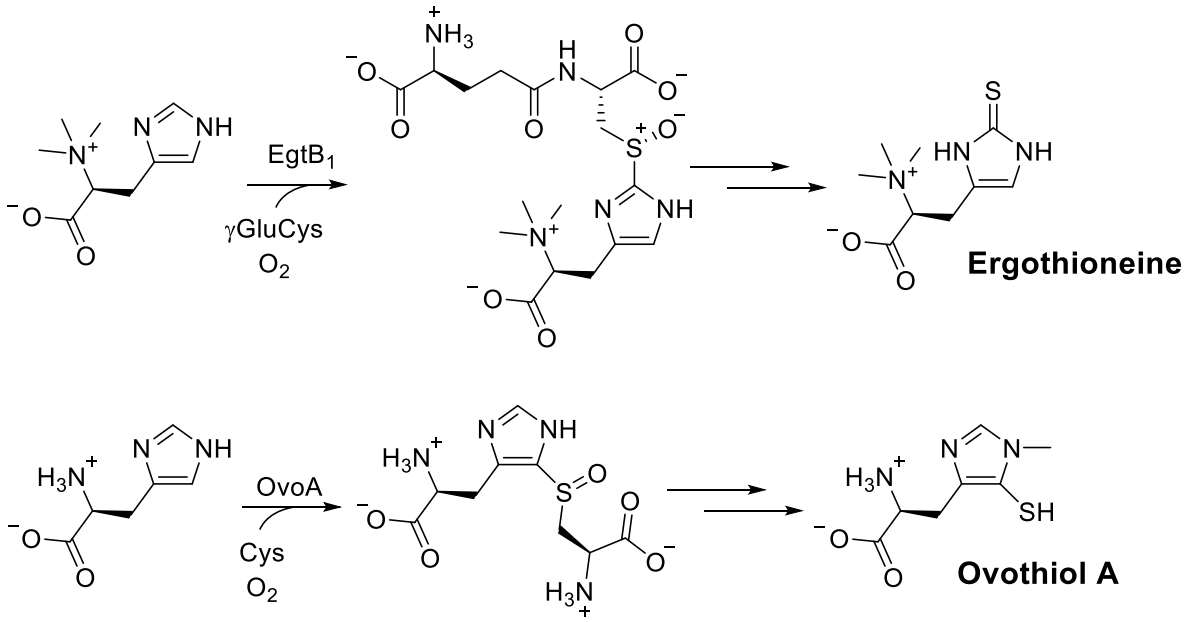

Scheme 16. $EgtB_1$- and OvoA-catalyzed C-S bond formation between γGluCys and TMH or between cysteine and histidine with subsequent sulfoxidation as the central steps in the syntheses of ergothioneine and ovothiol, respectively.

2.1. Kinetic parameters of sulfoxide synthase EgtB

A previously identified sulfoxide synthase EgtB from *Mycobacterium smegmatis* ($EgtB_{smeg}$) catalyzes the reaction of sulfoxide formation between N^{α},N^{α},N^{α}-trimethyl-L-histidine (TMH) and γ-glutamylcysteine (γGC) with oxygen as the oxidant.[1] Another mycobacterial EgtB was identified from the thermostable organism *Mycobacterium thermoresistibile* ($EgtB_1$). $EgtB_1$ shares 81 % sequence homology with $EgtB_{smeg}$. The advantage of working with proteins from thermostable organisms is associated with higher protein yields and better structural stabilities during general use and for crystallization. Both enzymes were produced in *Escherichia coli* and purified, yielding 7-10 mg/L of

culture of the purified enzyme. The quaternary structure was analyzed by size-exclusion chromatography showing that $EgtB_{smeg}$ and $EgtB_1$ were both present in a monomer-dimer equilibrium (Figure 6, left). However, the addition of TCEP led to monomer formation, suggesting that a surface-exposed cysteine residue is involved in disulfide bond formation between the two protein molecules. A cysteine residue in position 100 in $EgtB_{smeg}$ was identified as a candidate for this surface exposed cysteine. This residue was then mutated to serine using site-directed mutagenesis. The resulting mutant $EgtB_{smeg\_C100S}$ had no loss in activity and was confirmed to be a monomer using analytical gel-filtration (Figure 6).

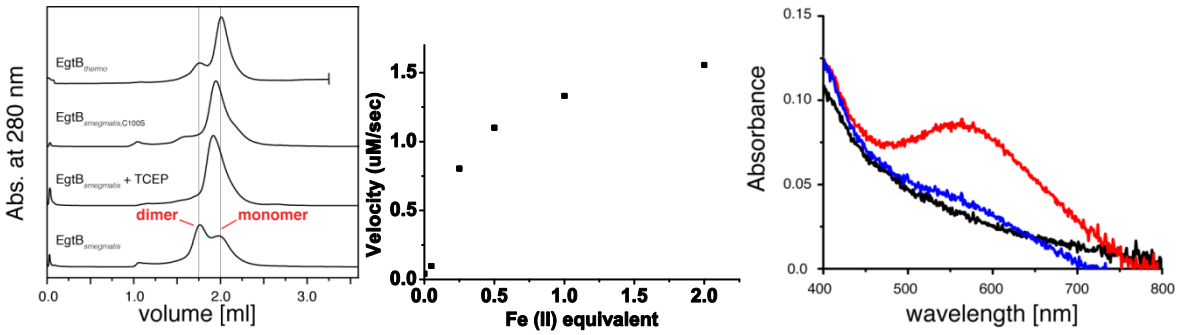

Figure 6. Left: Analytical size-exclusion chromatography of $EgtB_{smeg}$ and $EgtBsmeg_{,C100S}$ and $EgtB_1$. Purified $EgtB_{smeg}$ elutes as a monomer-dimer mixture. Treatment with TCEP leads to monomeric homogenity, suggesting that the dimer-interaction is mediated by an intramolecular disulfide bond. Consistently, the $EgtB_{smeg,C100S}$ variant does not dimerize during protein purification. **Middle:** EgtB activity depends on the presence of more than 1 equivalent iron. EDTA-dialyzed $EgtB_{smeg}$ showed no measurable activity when assayed in a reaction containing 100 mM HEPES pH 8.0, 100 mM NaCl, 2 mM TCEP, 2 mM ascorbate, 0.4 mM TMH, 1.2 mM γGC and 1.6 µM $EgtB_{smeg}$ but no $FeSO_4$. Titration of this reaction with $FeSO_4$ induced 80 % activity in the presence of 1 equivalent of iron(II) and full activity (V_{max}) in the presence of >2 equivalents of iron(II). Consequently, all EgtB activities were determined in presence of 4 equivalents of $FeSO_4$. **Right:** Absorption spectra of a) 100 µM $EgtB_1$ in 50 mM Tris pH 8.0, 50 mM NaCl (black); b) sample a) plus 500 µM γGC (red); c) sample b) plus 1 mM ascorbate (blue). In the presence of γGC, $EgtB_1$ is characterized by a strong absorbance band at 565 nm consistent with a charge transfer from γGC to the iron(III) center (LMCT – band).[77]

Purified $EgtB_1$ and $EgtB_{smeg}$ already contained iron in the active site, as inferred by a ferrozine-based colorimetric assay ($EgtB_1$ > 95 %, $EgtB_{smeg}$ > 50 % of iron in the protein).[78] EgtB activity is highly depending on the presence of iron, which was confirmed by the fact that EDTA-dialyzed $EgtB_{smeg}$ did not catalyze sulfoxide formation (Figure 6, middle). However, titration of this protein sample with $FeSO_4$ revealed that the enzyme gains full activity in presence of more than 2 equivalents of iron. Furthermore, the *in vitro* activity was assayed under optimized conditions in 100 mM HEPES-buffered solutions at pH 8.0 in the presence of 1 mM TMH, 1 mM γGC, 4 eq. with respect to the enzyme concentration of $FeSO_4$, 2 mM sodium ascorbate, 100 mM NaCl, and 2 mM TCEP at 26 °C. Sulfoxide formation was determined by cation-exchange HPLC at 265 nm, due to the specific absorbance for the modification at the 2' position of imidazole ring. Kinetic analyses show that both $EgtB_{smeg}$ and $EgtB_1$ catalyze up to one turnover per second and remained active for hundreds of turnovers (Table 1 and Figure 7).

Table 1. Catalytic parameters of sulfoxide synthase activity for $EgtB_{smeg}$ or $EgtB_1$. The sulfoxide formation was measured in reactions containing 100 mM HEPES pH 8.0, 100 mM NaCl, 2 mM TCEP, 0.8 µM $FeSO_4$, 2 mM ascorbate, (20 – 1000) µM TMH, (20 – 1200) µM γGC and 0.2 µM $EgtB_{smeg}$ or $EgtB_1$.

	Substrate	k_{cat}, s^{-1}	K_M, $x10^{-6}$ M	k_{cat}/K_M, s^{-1} M^{-1}
$EgtB_{smeg}$	TMH	1.2 ± 0.1	43 ± 10	28000 ± 11000
	γGluCys	1.1 ± 0.1	80 ± 10	13500 ± 3500
$EgtB_1$	TMH	0.87 ± 0.03	39 ± 3	22000 ± 2000
	γGluCys	0.86 ± 0.01	44 ± 2	20000 ± 1000

Interestingly, in the absence of ascorbate, $EgtB_1$ catalyzes 120 ± 20 turnovers (Figure 7, left) after which the enzyme become inactive. However, supplementation of ascorbate led to a burst of product formation at the time point when ascorbate was added (Figure 7, left). This observation suggests that ascorbic acid is required for the reduction of a reversibly oxidized inactive state, which is formed during a side reaction of the ferrous enzyme with oxygen. Unproductive oxygen activation is known for αKG-dependent enzymes that lead to the formation of ferrous iron, and which could then be reduced with ascorbate.[28, 79] Thus, ascorbate is always present in the reaction mixture to prevent accumulation of the inactive enzyme. In order to reveal which substrate was involved in oxygen binding and further inactivation in this side reaction, $EgtB_1$ was incubated either with buffer, TMH or γGluCys (Figure 7, middle). After one hour of incubation, the enzyme was assayed for its activity at standard conditions. The kinetic analyses demonstrated that, in the presence of γGluCys, $EgtB_1$ loses activity by more than 20 fold. Thus suggesting that γGluCys is required for oxygen binding to the active site of $EgtB_1$.

This hypothesis was further supported by UV-vis spectroscopy. Incubation of inactivated Fe(III)-containing $EgtB_1$ with γGluCys induced an absorption band at 565 nm (ε = 450 M^{-1} cm^{-1}, Figure 6, right). The addition of ascorbate led to the disappearance of this absorption band, which suggests that this band might be the result of a ligand-to-metal change transfer (LMCT) corresponding to the sulfur-to-iron(III) charge-transfer transition. These types of LMCT features have been observed in other non-haem iron-dependent enzymes, such as cysteine dioxygenase and superoxide reductase.[80,77] The spectroscopic absorption provides the first indication that the sulfur atom of γGluCys may directly interact with the catalytic iron center.

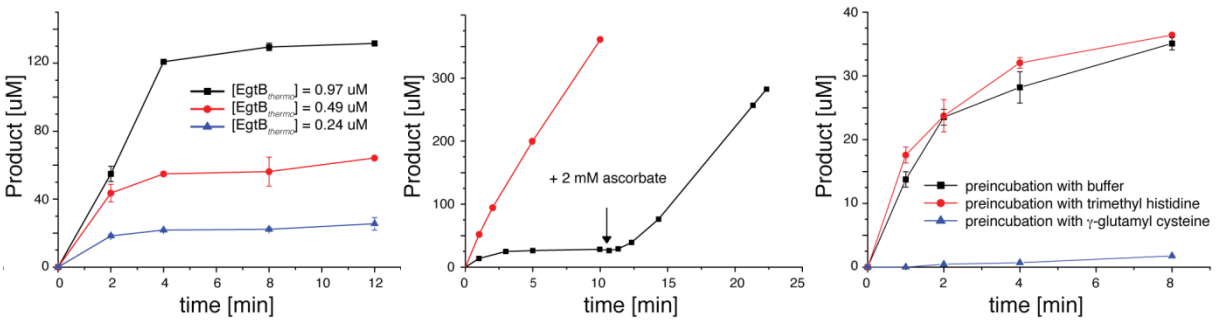

Figure 7. Left: Number of catalyzed turnovers by $EgtB_1$ in the absence of ascorbate. Reaction mixtures containing 100 mM HEPES pH 8.0, 100 mM NaCl, 2 mM ascorbate, 0.4 mM TMH, 1.2 mM γGC, 2 mM TCEP were initiated by addition of 0.24, 0.49 or 0.97 µM $EgtB_1$. Product formation was monitored by HPLC. Product formation ceases after 120 ± 20 turnovers. **Middle:** γGC dependent inactivation is reversible by addition of ascorbate: Product formation by $EgtB_1$ in a 100 mM HEPES pH 8.0, containing 100 mM NaCl, 0.8 mM TMH, 1.2 mM γGC and 0.9 µM $EgtB_1$ at 26 °C, was monitored by HPLC. On reaction contained 2 mM ascorbate (red line). In absence of ascorbate $EgtB_1$ activity ceased (black line). The enzyme reaction resumed after the addition of 2 mM ascorbate. **Right:** $EgtB_1$ is inactivated by preincubation with γGC: $EgtB_1$ was incubated at 4 °C for 1 h with either 0.5 mM γGC or 0.5 mM TMH or buffer as a control. The remaining activities of these proteins (1.4 uM) were assayed in reactions containing 100 mM HEPES pH 8.0, 100 mM NaCl, 2 mM TCEP, 0.8 mM TMH and 1.2 mM γGC. Product formation was monitored by iron-exchange HPLC. The initial rates of the three reaction indicate that incubation with γGC reduces $EgtB_1$ activity by at least 80-fold. Incubation with TMH leaves $EgtB_1$ activity unchanged.

2.2. The first crystal structure of EgtB

In order to elucidate the mechanism of sulfoxide synthase, a crystallographic approach was used to identify the crucial catalytic residues in the active site. The crystal structure of EgtB from *Mycobacterium thermoresistibile* ($EgtB_1$) was solved in the *apo* form (pdb: 4X8B, 1.7 Å), in complex with iron and TMH (pdb: 4X8E, 1.6 Å), and as a quaternary complex with manganese, DMH and γGC (pdb: 4X8D, 1.98 Å). $EgtB_1$ was crystallized and solved by Allegra Vit at the Helmholtz Center for Infection Research in Braunschweig, Germany.

The analysis of the electron densities of three $EgtB_1$ structures revealed a continuous polypeptide chain from Pro7 to Asp434 (Figure 8). The N-terminal part of the protein represented in grey (residues 7–150) is folded in a DinB-like four-α-helix bundle with long linkers between helices 1 and 2 (18 residues), 2 and 3 (34 residues), and 3 and 4 (7 residues). The fourth helix is followed by an extended two-stranded β-sheet (residues 151–210, green) wrapped around the C-terminal domain, which adopts a C-type lectin fold (CLec, blue and orange).[81] This fold contains few secondary structure elements and is stabilized by a dense array of buried ionic interactions, such as the salt bridges observed between Arg and Glu residues (Arg409:Glu196, Arg413:Glu296, Arg397:Glu300, and Arg428:Glu360). Furthermore, a calcium ion in the center of the C-terminal domain immobilizes six oxygen ligands from side chains and backbone amides (Met354 2.8 Å; Gly399 2.9 Å; Val358 2.6 Å; Gly356 2.7 Å; Gln353 3.6 Å; and Glu360 3.3 Å). This part of the protein represents an unusual loop-rich fold, which is likewise found in two other single-domain proteins with completely different

functions. One of these enzymes with less than 30 % sequence homology is a copper-dependent formylglycine-generating enzyme (FGE), which catalyzes the O_2-dependent post-translational maturation of sulfatases.[82] The second homologue is a diversity-generating retroelement variable protein TvpA from *Treponema denticola*.[81a] This structural similarity suggests that iron-dependent sulfoxide synthases, such as EgtB and OvoA, may have emerged from these FGE-like proteins through fusion with an N-terminal DinB domain. Thus, the active site of EgtB maps to the interface between the two domains.

As mentioned previously, $EgtB_1$ exists in a monomer and a disulfide induced dimer in solution (Figure 6, left). However, in the crystal structure the dimer interface in $EgtB_1$ does not form a disulfide bond and the equivalent C105 of C100 in $EgtB_{smeg}$ is buried in the protein structure. Instead, C243 was identified as a potential surface exposed cysteine which could form an intermolecular disulfide bond between the C243 residues of two separate polypeptide chains. Because the protein was treated with a reducing agent prior to crystallization, the crystal structure of $EgtB_1$ revealed a different dimer structure - an interface formed between two monomers by non-covalent interactions (Figure 8). This indicates that the disulfide dimer of EgtB is not physiological.

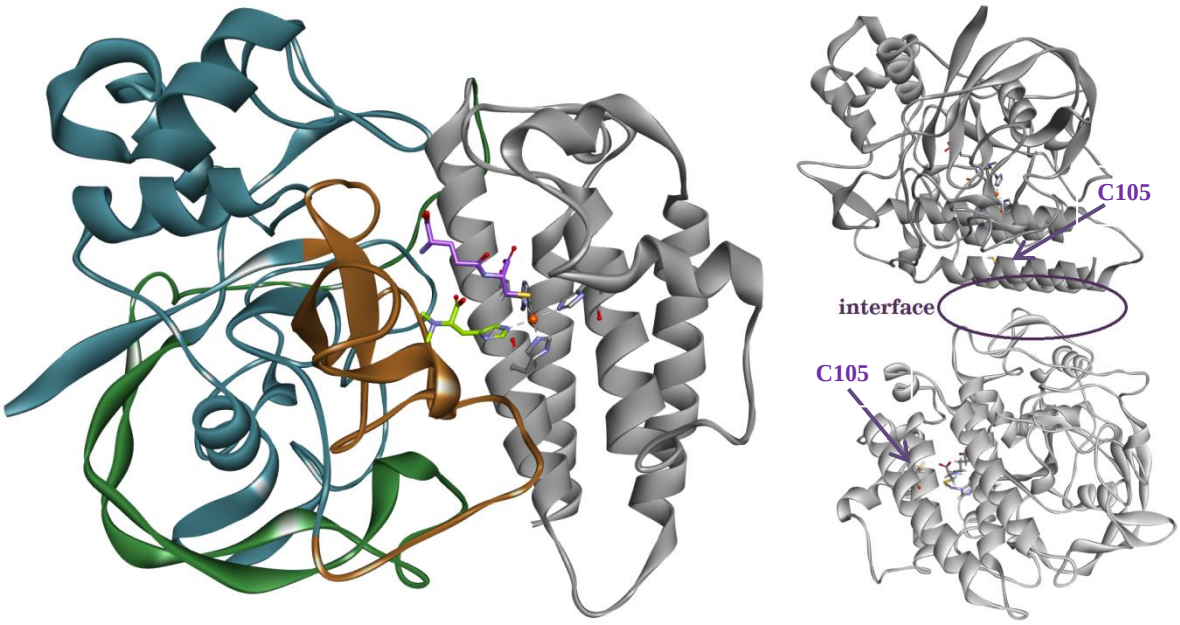

Figure 8. Left: Crystal structure of $EgtB_1$ represented as a cartoon diagram in complex with manganese (red), DMT (light green) and γGluCys (violet). The protein consists of an N-terminal DinB domain (grey, residues 1–150), a two-stranded β-sheet region (green, residues 151–210), and a C-terminal C-type lectin domain (blue/orange, residues 211–434). The active site, which contains a three-histidine facial triad (H51, H134, and H138) is formed between the DinB domain and residues 370–425 (orange). **Right:** Cartoon diagram of the asymmetric unit of $EgtB_1$ with C105 and the crystallographic interface indicated.

The active site of $EgtB_1$ is located in a 15 Å deep and 10 Å wide tunnel lined by residues 375 - 425 from the CLec domain and residues from helices 2 and 4 and the loops between helices 1, 2, and 3. At the bottom of this tunnel, three histidine residues from the DinB domain (residues 51, 134, and

138) coordinate the catalytic iron cation (Fe–N: 2.1 Å, 2.1 Å, and 2.3 Å). Earlier predictions of the facial triad were based on sequence alignments of different sulfoxide synthase homologues. Homologs of EgtB and OvoA contain three strongly conserved nucleophilic residues HX_3HXE and it has been proposed that these form a possible iron binding motif 2-His-1-Glu.[1, 70] Mutation of each residue in the HX_3HXE motif in OvoA resulted in a >100-fold difference in activity, implying that these residues are catalytically important and indeed involved in iron binding based on the sequence.[16a] The structure of $EgtB_1$ showed that H51 is the metal binding ligand, and not E140 as was proposed before. To analyze the role of the highly conserved E140 residue, it was mutated to glutamine ($EgtB_{1\_E140Q}$). Surprisingly, the mutant was active (Table 2). The binding of TMH remained the same (no change in K_M value for TMH) with a decrease of k_{cat} by ~3 fold. The K_M of γGluCys increased slightly by 2.5 fold which led to an overall 10-fold decrease in the catalytic efficiency. However, the $OvoA_{E176A}$ or $OvoA_{E176H}$ mutants revealed a dramatic decrease in activity.[83] It is possible that the $OvoA_{E176A}$ mutant was inactive due to the treatment in the non-optimized conditions. Therefore, the activity of OvoA variants had to be re-measured by using optimized conditions.

Table 2. Catalytic parameters of the sulfoxide activity of $EgtB_{1\_E140Q}$.

$EgtB_{1\_E140Q}$	k_{cat}, s^{-1}	K_M, 10^{-6} M	k_{cat}/K_M, s^{-1} M^{-1}
TMH	0.32 ± 0.02	30 ± 5	11000 ± 200
γGluCys	0.28 ± 0.02	120 ± 20	2300 ± 500

The reason why the glutamate residue is conserved among sulfoxide synthases might be due to a stabilizing effect on the secondary structure of enzyme. In the crystal structure of $EgtB_1$, E140 is placed in a DinB domain and hydrogen bonds to S400 and W359 from the FGE-like domain (Figure 9). This residue is one of the bridging residues between two domains. In order to demonstrate the role of this residue in stabilization of the secondary structure, CD measurements as a function of temperature were performed for $EgtB_1$ and $EgtB_{1\_E140Q}$.

The crystal structure of $EgtB_1$ largely consists of λ-helixes from the DinB domain and the FGE-like domain, which is mainly unstructured. Structures rich in λ-helixes display a minimum of ellipticity for CD spectra at 220 nm, as was observed for $EgtB_1$ (Figure 10).[84] Furthermore, the temperature dependence of the CD signal was measured for both proteins at 220 nm (Figure 10). Interestingly, this data did not follow classic melting curve features. First, they show stabilization of the structure and then denaturation. Denaturation of $EgtB_1$ began at 53 °C, whereas for $EgtB_{1\_E140Q}$ at 47 °C. The structure of the protein somehow became more organized after heating at 45-50 °C. This might be due the formation of a more stable secondary structure during the rearrangement of unorganized loops or due to aggregation. However, a clear difference between the melting curves of

$EgtB_1$ and $EgtB_{1\_E140Q}$ mutant were observed suggesting that the E140Q mutation destabilized the secondary structure.

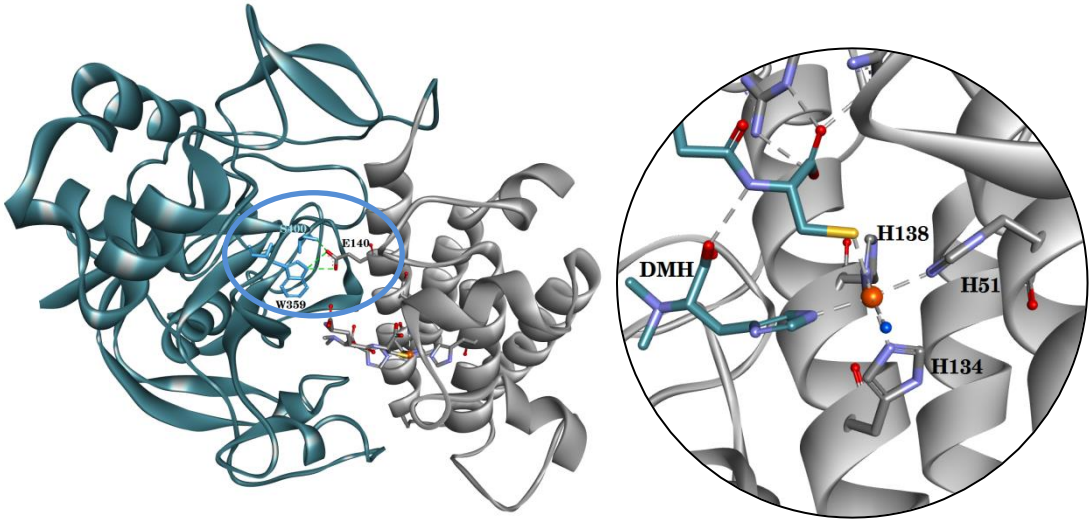

Figure 9. Left: Structure of $EgtB_1$ shows that E140 residue connects two domains: DinB (grey) and FGE-like (blue). **Right:** In the active site of $EgtB_1$, the Fe(II) iron is coordinated by a 3-His facial triad (H51, H134 and H138).

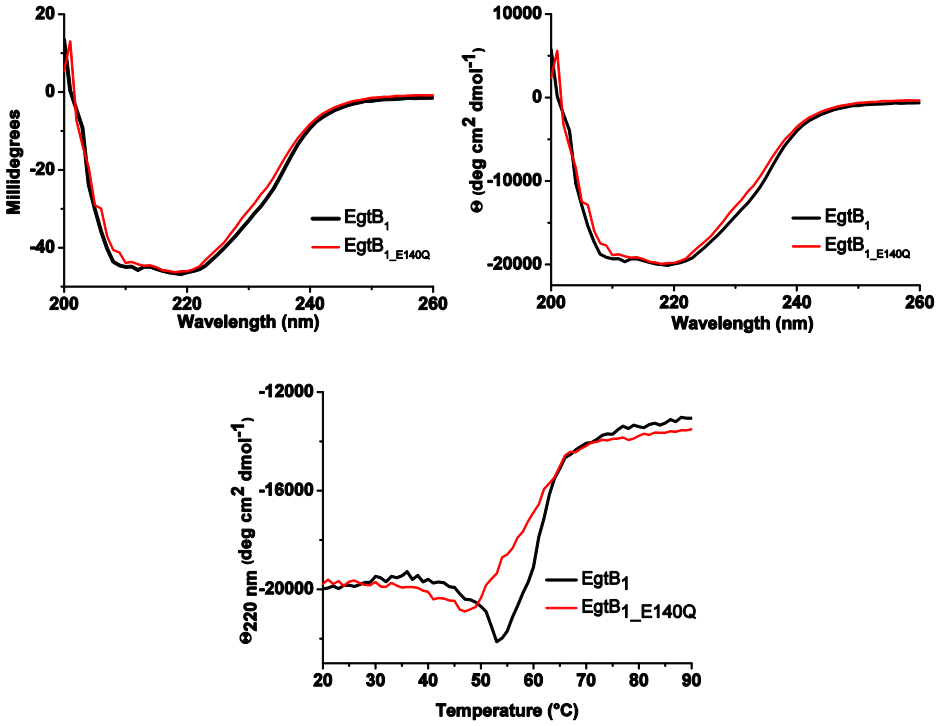

Figure 10. CD spectra of $EgtB_1$ and $EgtB_{1\_E140Q}$ mutant: (left) raw data, (right) mean residue ellipticity. Curves of ellipticity are represented as a function of temperature (bottom).

The active site of $EgtB_1$ contains a 3-His facial triad for iron binding. This facial triad is also found in other non-haem iron-dependent enzymes, such as thiol dioxygenases, diketone dioxygenase and enzymes catalyzing aromatic ring-cleaving reactions.[22] This facial triad is fairly conserved among

proteins from the DinB protein superfamily.[85] Some single-domain DinB proteins were described to catalyze zinc-dependent C-S bond formation. Metal-dependent C-S bond formation might be one of the activity features for DinB-like proteins, even though the mechanisms differ for sulfoxide synthases.[86] Nevertheless, the active site of EgtB is located between the DinB domain and FGE-like domain, thus to understand the mechanism of EgtB, the substrate binding mode was studied.

2.3. Substrate binding modes of the sulfoxide synthase $EgtB_1$

TMH as a substrate for sulfoxide formation

In order to catalyze sulfoxide formation, EgtB requires three substrates: TMH, γGluCys and oxygen. The sulfur donor availability for EgtB in the ergothioneine biosynthetic pathway is regulated by methyl transferase EgtD, which catalyzes formation of TMH from histidine.[65] It has been shown that EgtD mainly produces TMH (88 ± 4%) together with 13 ± 9 % of DMH and less than 1 % of MMH, showing a remarkable apparent processivity of EgtD. We were interested in the specificity of EgtB towards the various methylation states of histidine. Therefore, $EgtB_{smeg}$ was reacted with different histidine derivatives. EgtB catalyzed reactions with N^{α}-monomethyl-L-histidine (MMH), N^{α},N^{α}-dimethyl-L-histidine (DMH) and $N^{\alpha},N^{\alpha},N^{\alpha}$-trimethyl-L-histidine (TMH) forming the corresponding sulfoxides. The catalytic efficiencies do not change between DMH and TMH (Table 1), however, it drops 36-fold when MMH is used as the substrate. These results suggest that the binding of the histidine is depended on the N^{α} substitution pattern and increases among the tested histidine derivatives in the order: MMH < DMH < TMH (Figure 11).

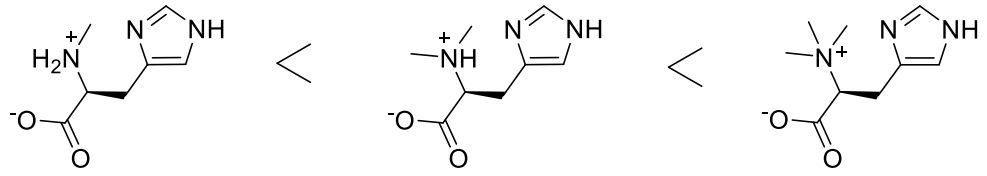

Figure 11. Structures of N^{α}-monomethyl-L-histidine (MMH), N^{α},N^{α}-dimethyl-L-histidine (DMH) and $N^{\alpha},N^{\alpha},N^{\alpha}$-trimethyl-L-histidine (TMH). The binding of histidine derivatives increases with N^{α} methylation.

Table 3. Michaelis-Menten parameters of $EgtB_{smeg}$ catalyzed reaction with different sulfur acceptors.

Substrate	k_{cat}, s^{-1}	K_M, 10^{-6} M	k_{cat}/K_M, s^{-1} M^{-1}
MMH	0.23 ± 0.01	300 ± 40	780 ± 250
DMH	2.3 ± 0.1	100 ± 10	22000 ± 2000
TMH	1.2 ± 0.1	43 ± 10	28000 ± 11000

Furthermore, the crystal structure of $EgtB_1$ was examined for the TMH binding pocket (Figure 12). In the structure of $EgtB_1$ with TMH and iron, the substrate imidazole ring (Fe–Nτ: 2.2 Å; Figure 2) and two water molecules (Fe–O: 2.1 and 2.2 Å) join the 3-His facial triad in an octahedral

coordination sphere around the iron center. The substrate imidazole ring also interacts with Y380 through a water-mediated hydrogen bond (Y380-Nπ: 5.4 Å), and the substrate 1-carboxylate group is loosely connected to R87 (4.9 Å), again *via* a bridging water molecule. Two N^{α}-methyl groups of TMH pack against the indole side chain of W415. The third N^{α}-methyl group appears to make dipolar contacts to the amide side chains of Q137 (3.2 Å) and N414 (3.5 Å).

Underneath the TMH binding pocket, there is an aspartate residue at position 194 which, through a water molecule, provides a negative charge to the surface of the substrate binding pocket. This residue was mutated to the uncharged asparagine to determine whether this would decrease the overall negative charge in the TMH binding pocket. The resulting mutant, $EgtB_{1\_D194N}$, had a two-fold decrease in k_{cat} and five-fold increase in K_M. The binding affinity for $EgtB_{1\_D194N}$ did not change significantly, suggesting that the TMH binding pocket has an overall negative charge, which could be distributed among aromatic residues at the bottom of the active site (Y380, W415, F412).

Table 4. Catalytic parameters of the sulfoxide activity for $EgtB_{1\_D194N}$ mutant

$EgtB_{1\_D194N}$	**k_{cat}, s^{-1}**	**K_M, 10^{-6} M**	**k_{cat}/K_M, s^{-1} M^{-1}**
TMH	0.49 ± 0.10	190 ± 50	2500 ± 1100
γGluCys	0.19 ± 0.01	85 ± 5	2200 ± 200

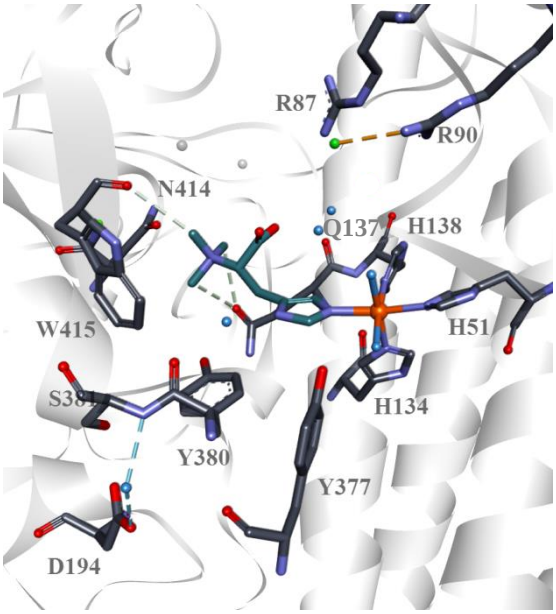

Figure 12. The active site of $EgtB_1$ in the ternary complex with TMH (dark cyan) and iron (orange) (pdb: 4X8E, 1.6 Å). Localized water molecules are shown in blue. A chloride ion (green) in the ternary complex occupies the cationic docking site of γGC.

γGluCys binding

The binding mode for the second substrate (γGC) was investigated by analysis of the crystal structure of $EgtB_1$ with DMH, γGC, and manganese(II). Initial efforts to co-crystalize $EgtB_1$ with γGC, by soaking iron-containing crystals with γGC, resulted in the disintegration of the crystals. Therefore iron was exchanged to manganese. The corresponding crystals were tolerant to soaking with DMH and γGC and diffracted to a resolution of 1.98 Å.

The superimposition of the EgtB structures with and without γGC adopts similar positions of the active site residues (r.m.s.d. = 0.041). In the resulting structure, the thiolate of γGC coordinates as the fifth ligand to the metal center (Figure 13, Mn–S: 2.6 Å). The direct metal-thiolate contact is in agreement with the assigned LMCT absorption band from sulfur to the ferric iron species (Figure 6, p. 24).

Four residues were identified for the γGC binding (Figure 13). The α-amino group and the two carboxylates of γGC form salt bridges to D416 (2.8 Å), R420 (2.7 Å), R87 (3.0 Å), and R90 (2.6 Å). Furthermore, the amide functionality of γGC hydrogen bonds with the 1-carboxylate of DMH (2.8 Å).

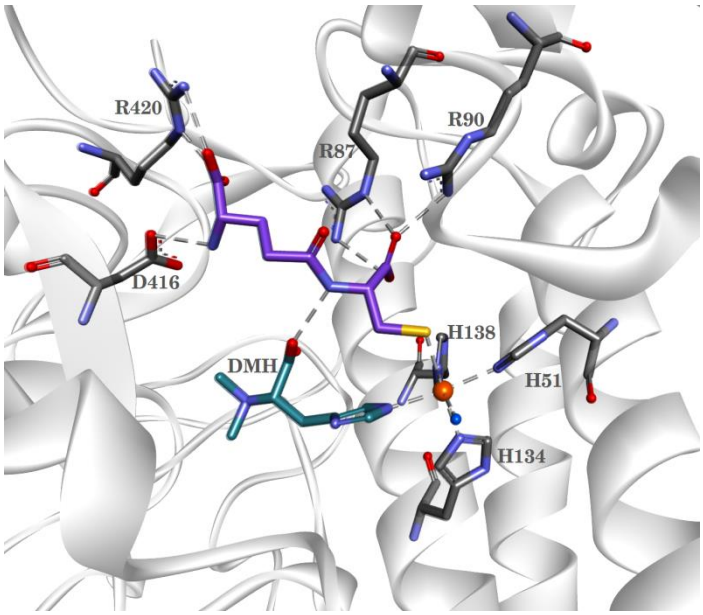

Figure 13. The active site of $EgtB_1$ in the ternary complex with DMH (dark cyan), γGC (violet), and manganese (orange) (pdb: 4X8D, 1.98 Å).

Since the structure of $EgtB_1$ in complex with γGC was solved with manganese instead of iron, one cannot exclude that the γGC binding mode might be different in the manganese complex rather than in the iron complex. To probe the γGC binding in the active form of $EgtB_1$, site-directed mutagenesis was used. As the crystal structure revealed, there are four residues to which γGC salt bridges. One of these residues, D416, was mutated to the non-charged asparagine or the hydrophobic non-polar leucine. In comparison to the wild-type, $EgtB_{1\_D416N}$ had an increased K_M for γGC (45-fold)

without a significant change in K_M of TMH. Furthermore, k_{cat} of this mutant decreased by just 3-fold, resulting in the drop of the catalytic efficiency by 150-fold (Table 5). The D416L mutation caused an even more significant effect on γGC binding, resulting in a ~700-fold decrease in the catalytic efficiency. Those mutations mainly affected the K_M of γGC, suggesting that D416 residue is only responsible for substrate binding. The loss of the negative charge at position 416 led to a lowered efficiency in the binding of γGC by the mutants.

To probe the significance of the interaction between D416 and γGC, a derivative of γGC which lacks the α-amino group, was synthesized (N-glutarylcysteine, NGC, Figure 14). $EgtB_1$ was assayed with NGC showing a 90-fold decrease in catalytic efficiency, suggesting that NGC is a worse substrate than γGC, because NGC lacks additional hydrogen bond to the enzyme. Nevertheless, for the mutants $EgtB_{1\_D416N}$ and $EgtB_{1\_D416L}$, a comparison of the k_{cat}/K_M values showed that NGC was a better substrate than γGC by 10- and 50-fold, respectively. The binding of NGC to the mutants had a similar K_M value as the wild-type for γGC. Thus, the design of the mutant EgtB and the mutant substrate NGC allowed us to create a new and efficient sulfoxide synthase. Furthermore, these results suggest that the salt bridge between the α-amino group of γGC and D416 found in the manganese-containing quaternary complex of $EgtB_1$ is important for substrate recognition during catalysis.

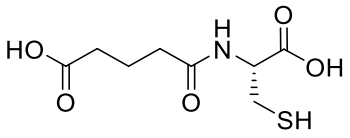

Figure 14. The chemical structure of N-glutarylcysteine, NGC.

Overall, the sulfur donor (γGC) binding in $EgtB_1$ is caused by hydrogen bonding with R90, R87, R420, D416 and TMH. Furthermore, the thiolate of γGC is the first sphere ligand to the catalytic metal center. The crystal structure of $EgtB_1$ allowed us to change the substrate specificity from γGC to NGC by designing $EgtB_{1\_D416N}$ and $EgtB_{1\_D416L}$ mutants and open up new possibilities for the sulfur-donor design.

Table 5. Kinetic parameters for the $EgtB_1$ variants.

	Substrate	k_{cat}, s^{-1}	K_M, $x10^{-6}$ M	k_{cat}/K_M, s^{-1} M^{-1}
$EgtB_1$	NGC	0.25 ± 0.06	1100 ± 400	230 ± 130
$EgtB_{1\_D416N}$	$TMH_{\gamma GluCys}$	0.11 ± 0.01	6 ± 2	19000 ± 7500
	γGluCys	0.27 ± 0.06	2000 ± 600	130 ± 70
	NGC	0.10 ± 0.01	95 ± 17	1100 ± 300
$EgtB_{1\_D416L}$	$TMH_{\gamma GluCys}$	0.19 ± 0.02	47 ± 10	4100 ± 1300
	γGluCys	0.12 ± 0.02	4300 ± 1000	30 ± 10
	TMH_{NGC}	0.20 ± 0.02	59 ± 13	3500 ± 1100
	NGC	0.16 ± 0.01	95 ± 10	1600 ± 300

Oxygen binding

The third substrate crucial for EgtB catalysis is oxygen. There is no direct crystallographic evidence of oxygen binding available yet. One possibility to test for O_2-binding modes would be to co-crystalize the enzyme with oxygen inhibitors, such as cyanide or azide. Nevertheless, having a closer look at the active site of the $EgtB_1$, the sixth metal ligand in the quaternary complex was identified as a water molecule or hydroxide (Mn–O: 2.5 Å). This water molecule or hydroxide is hydrogen bonded to the phenolic side chain of Y377 (2.8 Å). This residue might be involved in oxygen binding and the catalytic role of Y377 in the catalysis of EgtB1 is discussed in the next chapter.

The crystal structure of $EgtB_1$ shows a second entrance to the active site. This entrance appears to be a narrow tunnel, which directly leads to the water molecule ligated to the metal center (Figure 15). The narrow tunnel may serve as a binding pathway for oxygen to the active site of $EgtB_1$. Similar structural organization for oxygen binding has already been described in cholesterol oxidase.[87]

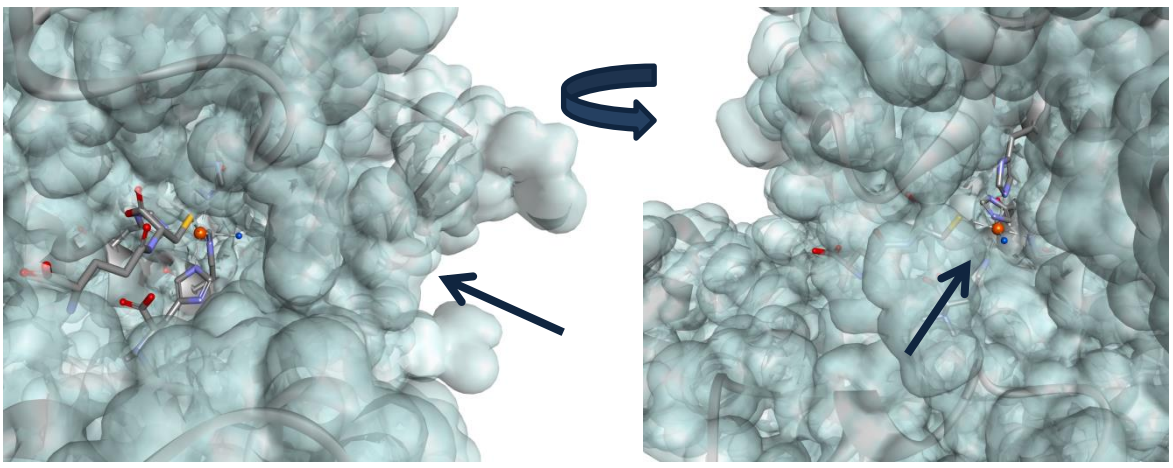

Figure 15. The view on the narrow tunnel which leads to the water molecule ligated to the metal center (the arrow points to the narrow tunnel). It seems possible that this tunnel allows oxygen to reach the iron center to initiate the oxidation reaction.

2.4. Conclusions

Three crystal structures of EgtB from *Mycobacterium thermoresistibile* ($EgtB_1$) were solved: the *apo* form, in complex with iron and TMH and as a complex with manganese, DMH and γGC. The crystal structure shows an unexpected iron-binding facial triad – a 3-His instead of 2-His-1-Glu triad as was previously proposed.[1] Based on the crystal structure and UV-vis spectroscopic data, we propose that all three substrates (TMH, γGC and oxygen) are directly coordinated to the metal center of EgtB.

Furthermore, the binding of γGC was probed by site-directed mutagenesis. Kinetic analyses of two mutants revealed that the crystal structure containing manganese at the active site most likely represents the actual binding of γGC as with iron. Both mutants were also designed in a way that NGC became a better substrate than γGC, thus changing the scope of substrate specificity by rational design.

The enzyme requires ascorbate due to unproductive oxidation of the metal center, resulting in an inactive ferric iron in the active site, which takes place after ~120 turnovers in absence of ascorbate. Under the optimized conditions, EgtB is able to catalyze the sulfoxidation reaction at a rate of ~1 s^{-1} for more than 1000 turnovers.

Kinetic analyses of $EgtB_1$, together with the crystal structure, allowed us to propose a mechanism of sulfoxide formation (Scheme 17). First, after binding of all substrates, an iron(III)-superoxo species (2) is formed. This species may have partial iron(III) character and forms a complex with a peroxide anion (O_2^{2-}) and a thiyl radical (3). The protonation of oxygen by Y377 stabilizes the peroxide anion (4), allowing the thiyl radical attack on the imidazole ring to form an iminyl radical (5). Further deprotonation (6) leads to the re-aromatization of the imidazole moiety and product release, returning $EgtB_1$ to its resting state (7).

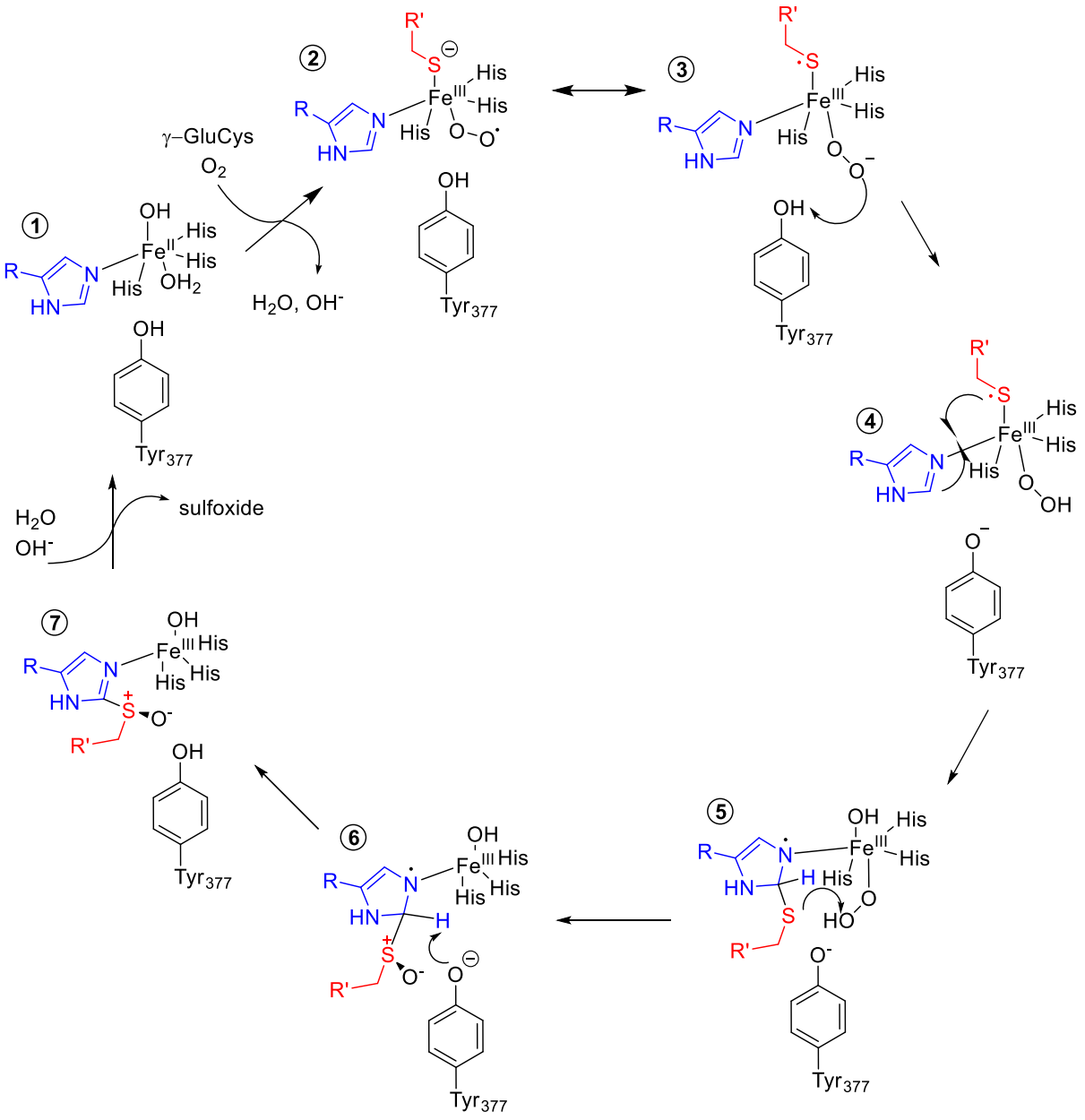

Scheme 17. Proposed mechanism for EgtB-catalyzed C-S bond formation and sulfoxidation.

2.5. Experimental

Recombinant EgtB constructs. Cloning and production of $EgtB_{smeg}$ was done as described previously.[1] The gene for EgtB from *Mycobacterium thermoresistible* ($EgtB_1$, WP_003925249) was codon-optimized for protein production in *Escherichia coli* and purchased from Genscript. The gene was ligated as a NdeI-XhoI fragment into a pET28b cloning vector.

Sequence of $EgtB_{smeg}$:

GSSHHHHHHSSGLVPRGSHMIARETLADELARARERTLRLVEFDDAELHRQYNPLMS
PLVWDLAHIGQQEELWLLRDGNPDRPGMLAPEVDRLYDAFEHSRASRVNLPLLPPSDARAYC
ATVRAKALDTLDTLPEDDPGFRFALVISHENQHDETMLQALNLREGPPLLDTGTPLPTGRPGV
AGTSVLVPGGPFVLGVDALTEPHSLDNERPAHVVDIPSFRIGRVPVTNAEWREFIDDGGYDEP
RWWSPRGWAHRQEAGLVAPQFWNPDGTRTRFGHIEEIPGDEPVQHVTFFEAEAYAAWAGA
RLPTEIEWEKACAWDPVAGARRRFPWGSAQPSAALANLGGDARRPAPVGAYPAGASAYGAE
QMLGDVWEWTSSPLRPWPGFTPMIYERYSTPFFEGTTSGDYRVLRGGSWAVAPGILRPSFRN
WDHPIRRQIFSGVRLAWDV

Sequence of $EgtB_1$:

GSSHHHHHHSSGLVPRGSHMGVAVPHRAELARQLIDARNRTLRLVDFDDAELRRQY
DPLMSPLVWDLAHIGQQEELWLLRGGDPRRPGLLEPAVEQLYDAFVHPRASRVHLPLLSPAQ
ARRFCATVRSAVLDALDRLPEDADTFAFGMVVSHEHQHDETMLQALNLRSGEPLLGSGTALP
PGRPGVAGTSVLVPGGPFVLGVDLADEPYALDNERPAHVVDVPAFRIGRVPVTNAEWRAFID
DGGYRQRRWWSDAGWAYRCEAGLTAPQFWNPDGTRTRFGHVEDIPPDEPVQHVTYFEAEA
YAAWAGARLPTEIEWEKACAWDPATGRRRRYPWGDAAPTAALANLGGDALRPAPVGAYPA
GASACGAEQMLGDVWEWTSSPLRPWPGFTPMIYQRYSQPFFEGAGSGDYRVLRGGSWAVA
ADILRPSFRNWDHPIRRQIFAGVRLAWDVDRQTARPGPVGGC

EgtB variants. $EgtB_{smeg\_C100S}$, $EgtB_{1\_D194N}$, $EgtB_{1\_D416N}$, $EgtB_{1\_E140Q}$ and $EgtB_{1\_D416L}$ were constructed by primer extension using the following primers. The resulting fragments were cloned into pET28 vectors. For protein crystallization, we cloned the $EgtB_1$ gene into a modified vector pET19m to encode an EgtB fusion construct with an N-terminal His_6-tag followed by a TEV (tobacco etch virus) protease cleavage site.

Table 6. Primer sequences used for the mutation of the EgtB variants.

Primer	Sequence 5' – 3'
$EgtB_1$	
$EgtB_1$_for	TATACATATGGGTGTCGCCGTGC
$EgtB_1$_rev	ATATCTCCGAGCTAACAACCACCCACCGG
D416N_for	TATATCGCAATTGGAACCACCCGATTC
D416N_rev	TATAGAATCGGGTGGTTCCAATTGCGA
D416L_for	TCGCAATTGGCTGCACCCGATTCGT
D416L_rev	ACGAATCGGGTGCAGCCAATTGCGA
D194N_for	TATAGTATGCCCTGAACAACGAACGTC
D194N_rev	TATAGACGTTCGTTGTTCAGGGCATAC
E140Q_for	TATAACCAGCATGATCAGACCATGCTGCA
E140Q_rev	TATATGCAGCATGGTCTGATCATGCTGGT
$EgtB_{smeg}$	
$EgtB_{smeg}$_for	ATATCATATGATCGCACGCGAGACACT
$EgtB_{smeg}$_rev	ATATCTCGAGTTAGACGTCCCAGGCCAG
C100S_for	ATGCGCGCGCCTACTCTGCGACGGTGCGGGCCAA
C100S_rev	CCGCACCGTCGCAGAGTAGGCGCGCGCATCCGAA

Recombinant protein production. *E. coli* BL21(DE3) transformed with the EgtB expression vectors were cultured in LB medium supplemented with 50 µg mL^{-1} kanamycin (pET28b) or 100 µg mL^{-1} ampicillin (pET19m) and 34 µg mL^{-1} chloramphenicol. At an optical density of OD_{600} of 0.6 - 0.8 protein production was induced with 0.5 mM IPTG for 16 hours at 19 C°. Cells were harvested by centrifugation, resuspended in buffer A (300 mM NaCl, 50 mM Na_2HPO_4 pH 8.0) and lysed by sonication. After centrifugation for 1 h at 48000 rpm, the protein was purified using Ni^{2+} NTA agarose beads (Qiagen) by washing the beads with buffer A containing 10 mM imidazole and then by elution in buffer A supplemented with 250 mM imidazole. The proteins were dialyzed into 50 mM Tris/HCl, 50 mM NaCl buffer, pH 8.0 and stored at -80°C. Protein homogeneity was assessed by SDS PAGE (Figure 18), protein concentration was determined by UV-vis using calculated extinction coefficients. Removal of the N-terminal histidine-tag from EgtB with recombinant TEV protease proceeded after Ni^{2+} NTA agarose purification during dialysis against 50 mM Tris/HCl, 50 mM NaCl pH 7.5 overnight at 18°C. Unprocessed EgtB and TEV were separated by filtration through Ni^{2+} NTA Agarose. The protein was further purified by size exclusion chromatography and concentrated to 15 mg mL^{-1} and stored at -80°C.

Table 7. Calculated and observed molecular weights of proteins.

Protein	m/z, calc., Da	m/z, obs., Da	Delta, Da
$EgtB_{smeg}$	49997	49998	1
$EgtB_{smeg\_C100S}$	49844	49843	1
$EgtB_1$	51343	51374	31*
$EgtB_1$ without his tag	49505	49536	31*
$EgtB_{1\_D416N}$	51342	51373	31*
$EgtB_{1\_D416L}$	51341	51372	31*
$EgtB_{1\_D194N}$	51342	51373	31*
$EgtB_{1\_E140Q}$	51342	51372	31*

* The calculated mass is 31 Da smaller that the measured mass. This may be due to two oxidation events (irreversible by addition of DTT), for example on methionine and cysteine residues. The exposed C-terminal Cys residue (C446) is a possible recipient of this oxidation. However, this residue is invisible in the X-ray structures.

FPLC analysis. Quaternary structures were analyzed by SEC (Äkta FPLC, GE Healthcare) using a Superdex 200 5/150 GL column. 0.1 mg of protein were injected and eluted in an isocratic flow of 0.2 mL/min in a degassed buffer containing 50 mM Tris/HCl pH 8.0 and 200 mM NaCl at room temperature.

HPLC assay. Reaction mixtures were analyzed by cation-exchange HPLC (20 mM phosphoric acid pH 2 as the mobile phase) on a Luna 5u SCX column (100 Å, 150 x 4 mm, Phenomenex). The compounds were eluted in NaCl gradient using the following method (Table 8). Sulfoxide formation was monitored at 265 nm.

Table 8. Standard method for HPLC analysis of EgtB reactions.

Time (min)	Solvent A*(%)	Solvent B*(%)
0.01	85	15
2	80	20
8	1	99
9	1	99
11	85	15

*Solvent A: 20 mM phosphate pH 2.0; Solvent B: 20 mM phosphate pH 2.0 containing 1 M NaCl

Ferrozine assay. For the determination of the iron content in a protein sample a colorimetric assay with ferrozine reagent was used. Ferrozine forms a stable oxidation-resistant magenta colored complex with ferrous iron which has absorbance maximum at 565 nm (Figure 16). A 10 µL aliquot of the protein sample was incubated with 5 µL of 8 M urea for 10 min at 95 °C. The sample was spun down and to ensure that all iron was in the ferrous form, ascorbate was added to a final concentration

of 2 mM prior to the addition of 5 mM ferrozine. Absorbance at 565 nm was then measured using the NanoDrop2000 spectrophotometer.

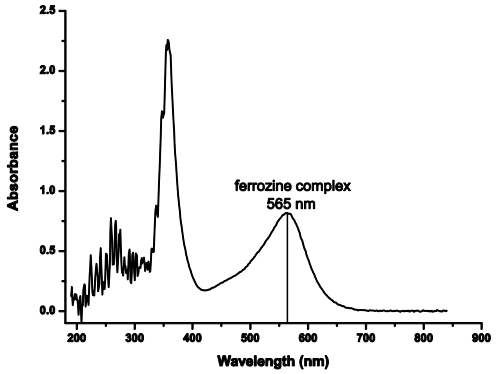

Figure 16. Absorption spectrum of ferrozine complex.

Activity assay for the iron content determination. The iron content was estimated by the enzymatic method under standard assay conditions. In presence of ascorbate the rates of reactions with and without additional iron were compared. In Table 9 a comparison of the values for the iron content determined by the Ferrozine and activity assays is shown. The data displayed in Table 9 are averages from three independent measurements.

Table 9. Iron content in recombinant EgtB proteins

Protein	Ferrozine assay [equivalent x 100]	Activity assay [% residual activity]
$EgtB_1$	98 ± 2	95 ± 2
$EgtB_{1\_D416N}$	55 ± 6	61 ± 3
$EgtB_{1\_D194N}$	31 ± 2	48 ± 4
$EgtB_{smeg}$	61 ± 6	54 ± 4

Synthesis of N-glutaryl-L-cysteine. To a solution of L-cysteine (1.21 g, 0.2 mol, 1 eq) in degassed H_2O (50 mL) at RT, pH 9.0, was added glutaric anhydride (1.14 g, 0.2 mmol, 1 eq) and the mixture was stirred under N_2. After addition of glutaric anhydride pH was adjusted to 9.0 with ammonia. The reaction was stirred overnight at room temperature. HPLC analysis showed no remaining starting material (Figure 17). The reaction was lyophilized to give N-glutaryl-L-cysteine (2.213 g, 0.188 mol, 94 %) as colorless oil. The crude product was analyzed by HPLC, ESI and NMR providing the evidence of the pure compound, presented as a mixture of thiol and disulfide. **^{1}H NMR (400 MHz, DMSO-d6)** δ ppm 7.43 (d, J = 6.9 Hz, 1H), 4.01 (dt, J = 6.8, 5.1 Hz, 1H), 2.82 (dd, J = 13.0, 4.7 Hz, 1H), 2.73 (dd, J = 13.0, 5.6 Hz, 1H), 2.13 (t, J = 7.4 Hz, 2H), 2.04 (t, J = 7.4 Hz, 2H), 1.67 (p, J = 7.4 Hz, 2H). **ESI-MS** *m/z* calcd. for $C_8H_{13}NO_5S$ $[M+H^+]$: 236.1, found: 236.1

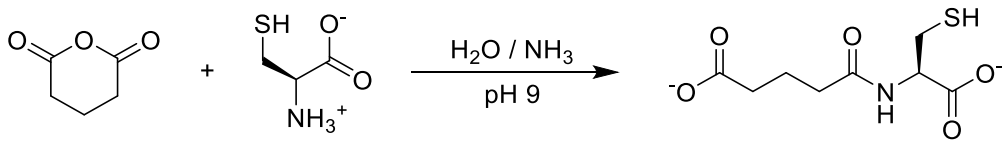

Scheme 18. Synthesis of N-glutaryl-L-cysteine.

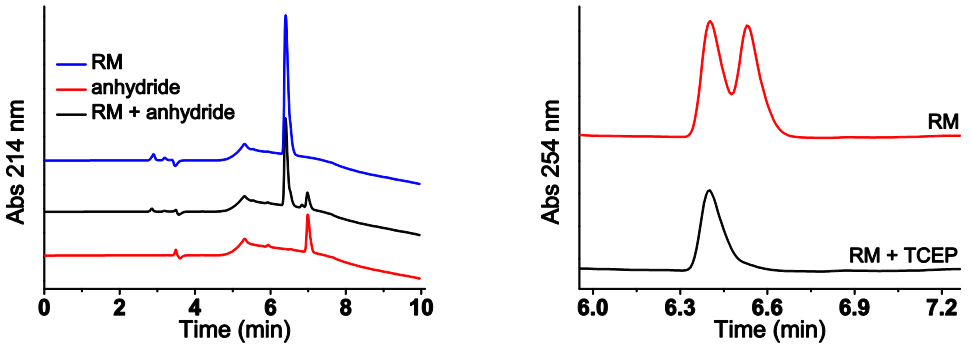

Figure 17. RP-HPLC analysis of the reaction mixture of NGC. The reaction mixture (represented in blue) shows full consumption of anhydride (left). The crude product contains N-gluraryl-L-cysteine disulfide (right).

Michaelis-Menten plots/Enzyme assay. All enzymes were analyzed under the following standard conditions. Reactions contained 100 mM HEPES, 100 mM NaCl, 2 mM TCEP, 2 mM ascorbate, sulfur acceptor TMH (or alternative sulfur acceptors) and EgtB. Reactions were started by addition of γGC and incubated at 26°C. 40 µL aliquots of the reactions were quenched by addition of 20 uL 1 M phosphoric acid and analyzed by cation exchange HPLC using 20 mM phosphoric acid at pH 2 as a mobile phase.[70] Compounds were eluted in a NaCl gradient. All HPLC chromatograms were recorded at 265 nm. The data were fitted to the function $v = V_{max}[s]/(K_M + [s])$. All reported data represent averages of at least two independent measurements. Michaelis-Menten plots are shown below. k_{cat} and k_{cat}/K_M were determined in the presence of co-substrate at a concentration at least 3-fold higher than the corresponding $K_{M,cosubstrate}$ and in air saturated buffers.

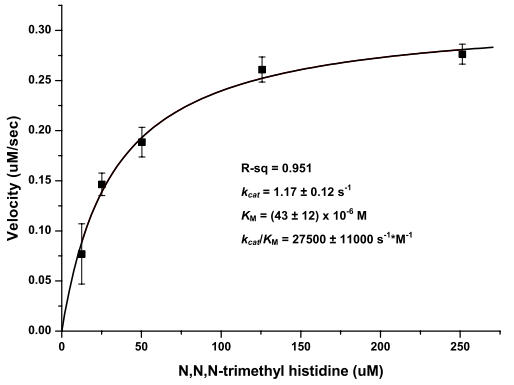

$EgtB_{smeg}$, [γGC] = 1200 µM

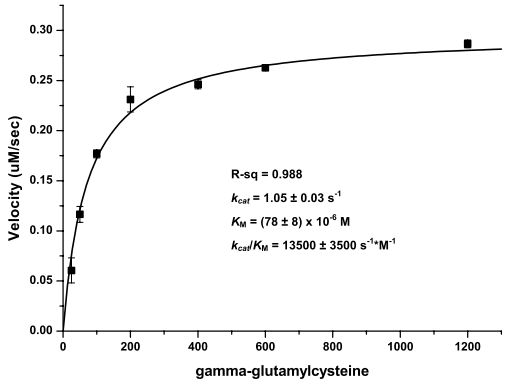

$EgtB_{smeg}$, [TMH] = 500 µM

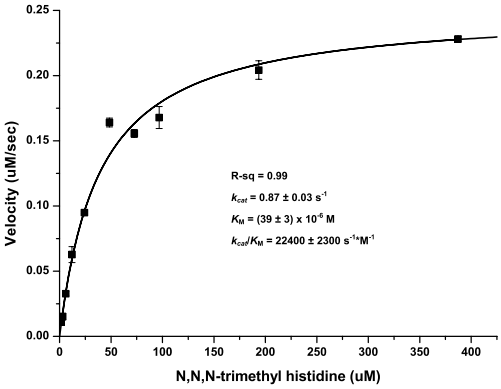

EgtB$_1$, [γGC] = 1200 µM

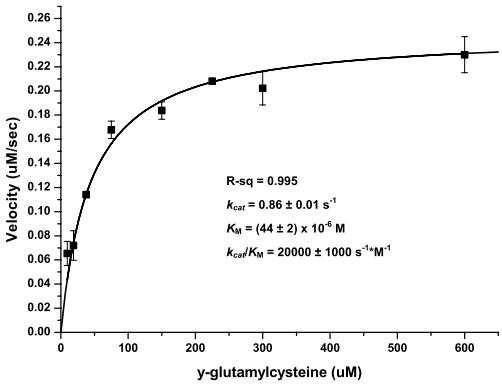

EgtB$_1$, [TMH] = 290 µM

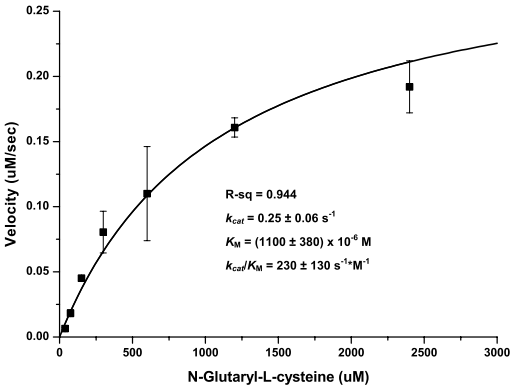

EgtB$_1$, [TMH] = 200 µM

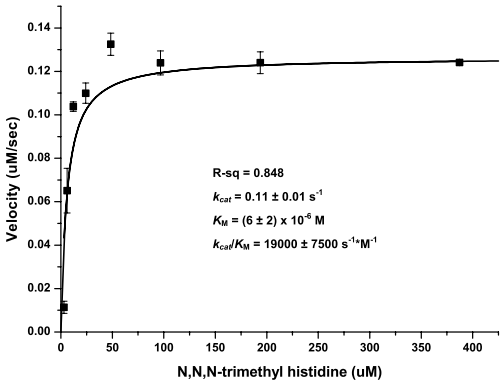

EgtB$_{1_D416N}$, [γGC] = 1200 µM

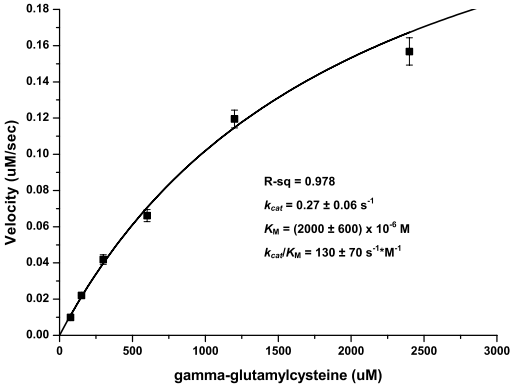

EgtB$_{1_D416N}$, [TMH] = 200 µM

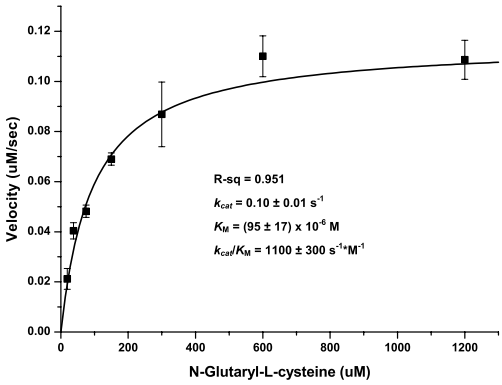

EgtB$_{1_D416N}$, [TMH] = 200 µM

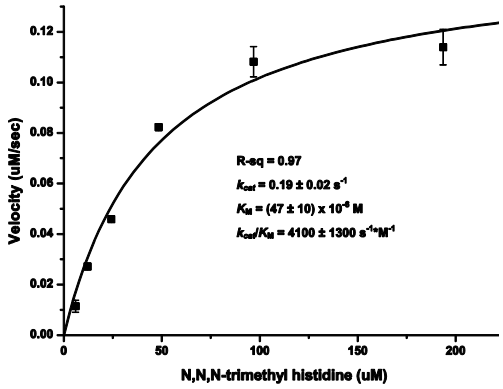

$EgtB_{1\_D416L}$, [γGC] = 3000 µM

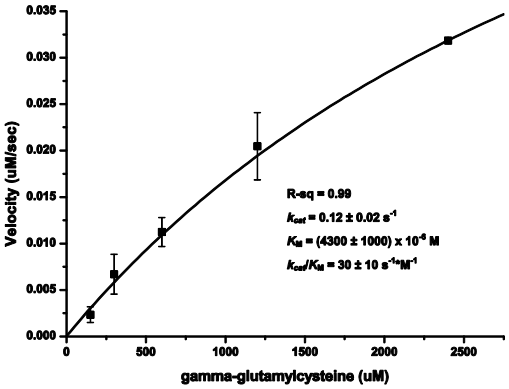

$EgtB_{1\_D416L}$, [TMH] = 200 µM

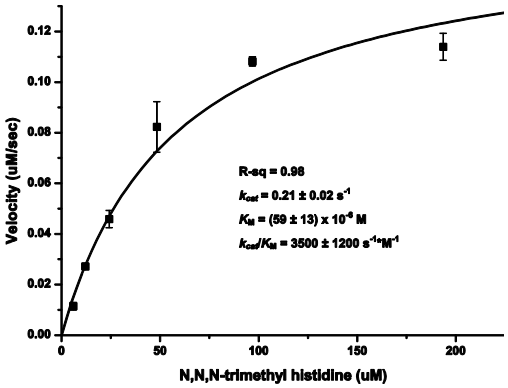

$EgtB_{1\_D416L}$, [NGC] = 1200 µM

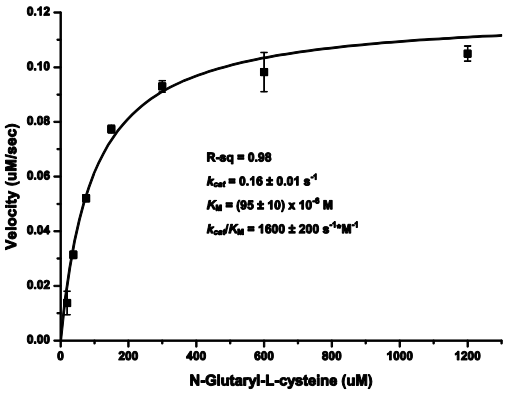

$EgtB_{1\_D416L}$, [TMH] = 200 µM

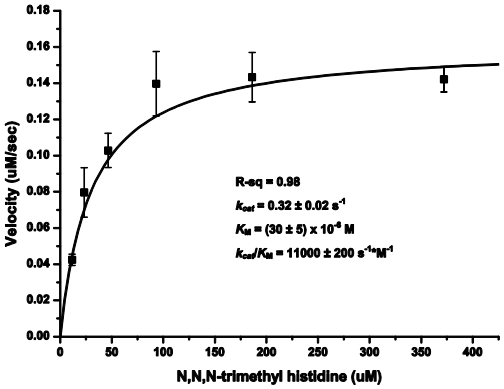

$EgtB_{1\_E140Q}$, [γGC] = 1200 µM

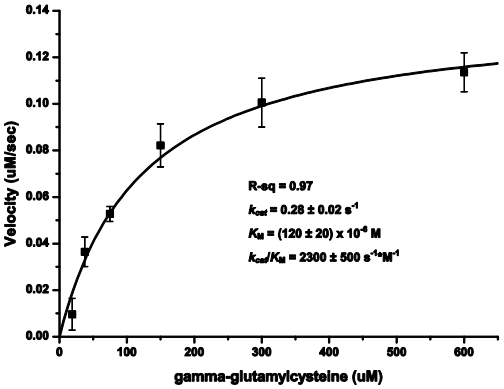

$EgtB_{1\_E140Q}$, [TMH] = 400 µM

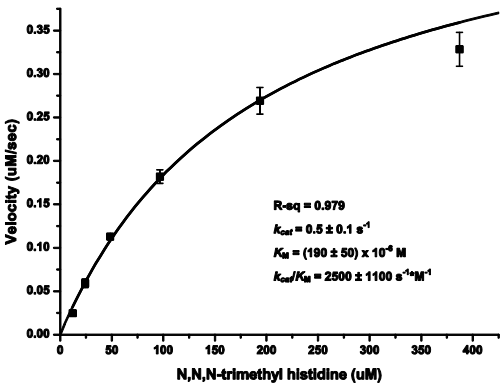

$EgtB_{1\_D194N}$, [γGC] = 1200 µM

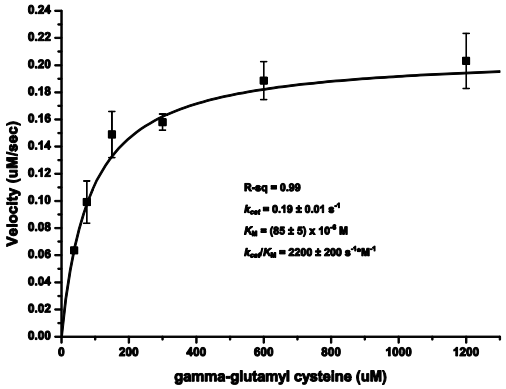

$EgtB_{1\_D194N}$, [TMH] = 500 µM

2.6. Appendix

General. All standard reagents were purchased from Aldrich/Sigma if not otherwise stated. Synthetic oligonucleotides were purchased from Microsynth, Switzerland. ESI-MS measurements were performed on a Bruker Esquire 3000plus, measuring in the positive ion mode. Absorbance was measured on a Nanodrop 2000 Spectrophotometer from Thermo Scientific. NMR spectra were acquired on a Bruker 400 MHz or a Bruker 500 MHz instrument. Chemical shifts (δ values) are reported in ppm, ^{1}H chemical shifts are quoted relative to solvent signals.[88] Multiplicity is reported as follows: s – singlet, d – doublet, dd – doublet of doublet, t – triplet, q – quartet, quin – quintet and coupling constant J in Hz.

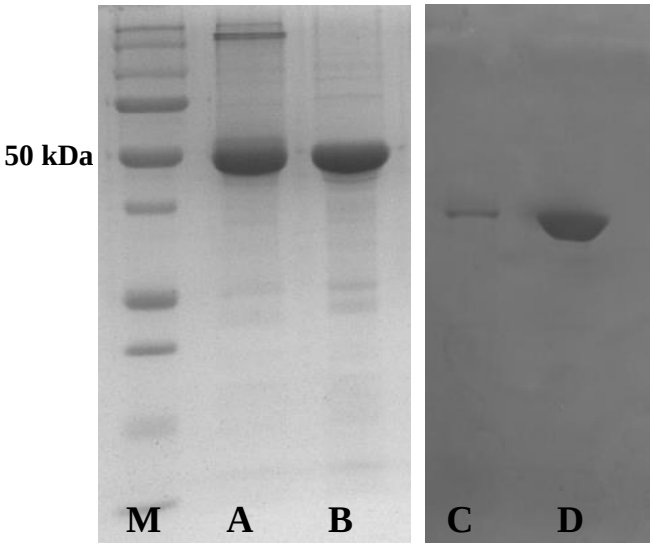

Figure 18. SDS-PAGE pictures of $EgtB_1$ after Ni-NTA affinity chromatography. M – Molecular weight marker; A – $EgtB_1$ without addition of a reducing agent; B - $EgtB_1$ with addition of DTT; C – $EgtB_1$ with the his-tag used for crystallization; D- $EgtB_1$ without the his-tag used for crystallization .

3. Conversion of a sulfoxide synthase into a thiol dioxygenase by a single point mutation

The sulfoxide synthase EgtB catalyzes a key step in ergothioneine biosynthesis.[1-2] EgtB catalyzes the C-S bond formation between γ-glutamylcysteine (γGluCys) and the C2 carbon of the imidazole ring of N^{α},N^{α},N^{α}-trimethyl-L-histidine (TMH) together with the subsequent oxidation to yield a sulfoxide product. EgtB is classified as a monooxygenase due to the overall four-electron oxidation reaction. Another enzyme which also catalyzes four-electron oxidation reaction and has a similar active site as EgtB is cysteine dioxygenase (CDO). Cysteine sulfinic acid (CSA) is the product of CDO-catalyzed oxidation of cysteine (Scheme 19).[52]

Mechanistic similarities between the sulfoxide synthases EgtB and OvoA to CDO were proposed after the observation that OvoA catalyzes the formation of CSA as a side reaction (10 %).[83] Therefore, in this chapter, the common intermediate shared between sulfoxide synthases and dioxygenases was proposed. Furthermore, identification of catalytic site residues within sulfoxide synthases that would be important to tune the reaction pathway towards dioxygenation instead sulfoxidation is discussed (Scheme 19).

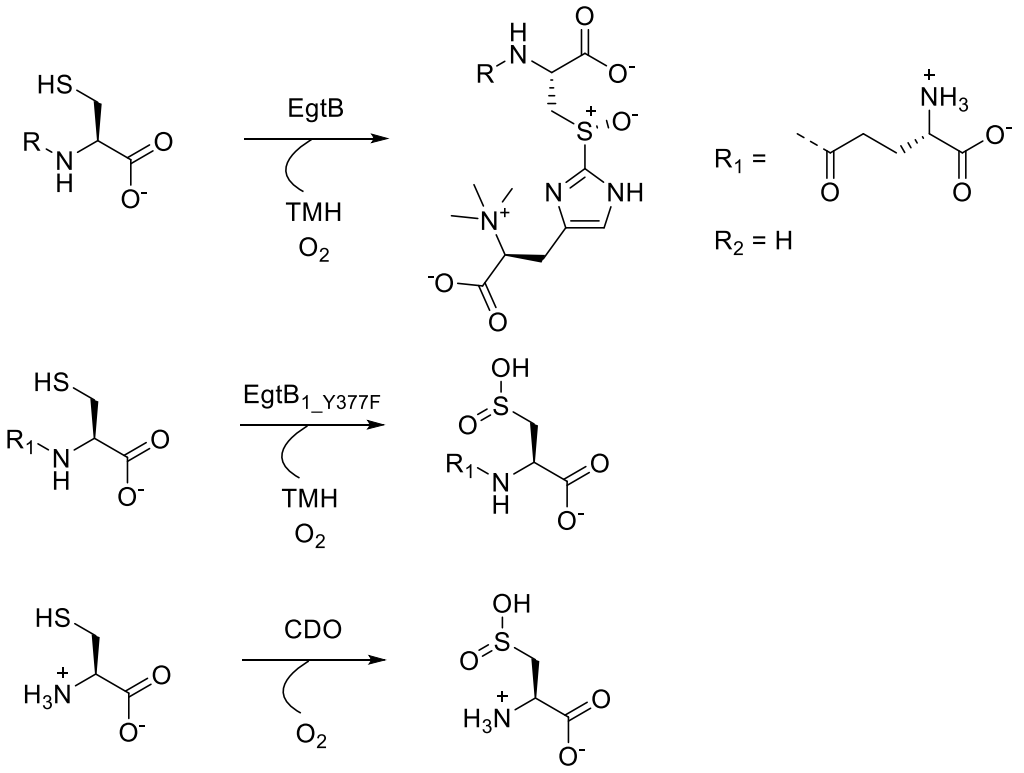

Scheme 19. Top: EgtB catalyzes oxidative C–S bond formation between cysteine derivative and TMH to form a corresponding sulfoxide. **Middle:** $EgtB_{1\_Y377F}$ mutant catalyze the oxidation of γGluCys into γGluCys sulfinic acid **Bottom:** Cysteine dioxygenases (CDO) catalyze the oxidation of cysteine into cysteine sulfinic acid.

3.1. The role of tyrosine 377 in the catalytic cycle of $EgtB_1$

In the Chapter 2, the structural information obtained from the crystal structure of $EgtB_1$ from *Mycobacterium thermoresistibile* was used to assess the importance of active site residues. The $EgtB_1$ active site architecture showed that the iron center is coordinated by a 3-His facial triad, the Nτ of TMH and the thiolate of γGluCys in an octahedral complex. The sixth position of the first sphere ligands is occupied by a water molecule or hydroxide, which is hydrogen bonded to the phenolic side chain of Y377 (2.8 Å) (Figure 19).

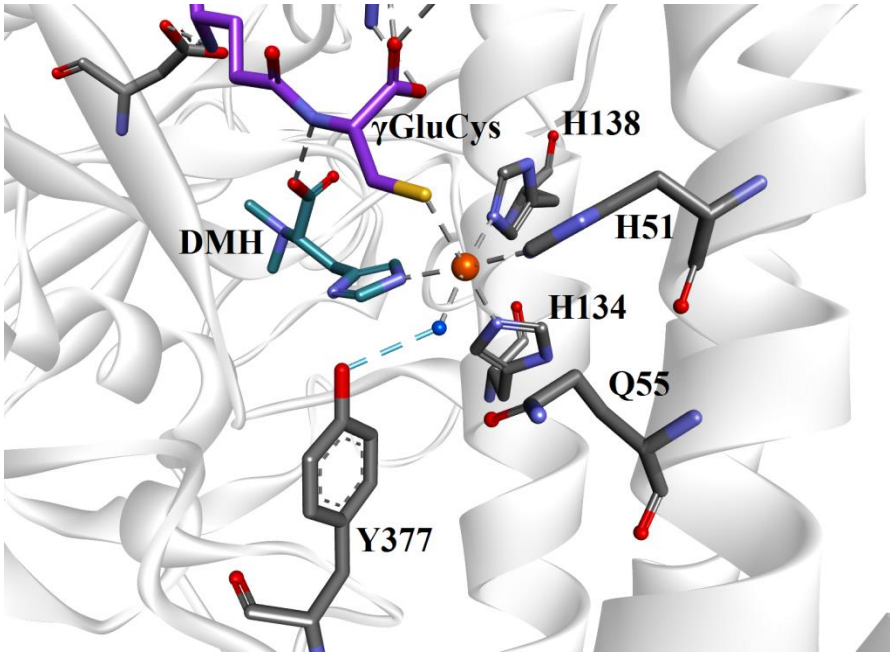

Figure 19. The active site of $EgtB_1$ in the ternary complex with DMH (dark cyan), γGC (violet), and manganese (orange) (pdb: 4X8D, 1.98 Å). Y377 forms a hydrogen bond to the iron-coordinated water/hydroxide molecule (2.8 Å).

To examine the catalytic role of Y377, the $EgtB_{1\_Y377F}$ mutant was generated using site-directed mutagenesis. The mutant protein was produced and purified in *E. coli* following the same protocol as for the wild-type variant (Chapter 2). The sulfoxide synthase activity of the $EgtB_{1\_Y377F}$ mutant was analyzed by HPLC. Michaelis–Menten analysis of the data revealed a 10^3-fold decrease in sulfoxide synthase activity for $EgtB_{1\_Y377F}$ compared to $EgtB_1$ (Table 10). The reduction in this activity is mainly due to a change in k_{cat}, as the K_M for TMH remained unchanged. The dramatic decrease in k_{cat} suggests that Y377 might have a crucial role in the catalysis of sulfoxide formation. The role of Y377 in the catalytic cycle of $EgtB_1$ might be in the deprotonation of TMH or in protonation of iron(III)-superoxo species.

Table 10. Kinetic parameters of $EgtB_1$ and $EgtB_{1\_Y377F}$ on the sulfoxide synthase activity.

	Substrate	k_{cat}, s^{-1}	K_M, x10^{-6} M	k_{cat}/K_M, s^{-1} M^{-1}
$EgtB_1$	TMH	0.85 ± 0.01	12 ± 1	74000 ± 5200
	γGluCys	0.75 ± 0.01	27 ± 1	28000 ± 1000
$EgtB_{1\_Y377F}$	TMH	0.0009 ± 0.0001	10 ± 4	85 ± 44

To determine whether Y377 might be involved in the deprotonation of C2 of TMH during catalysis, the substrate kinetic isotope effect (KIE) was determined using C2-^{2}H-N$^\alpha$,N$^\alpha$,N$^\alpha$-trimethyl-L-histidine (D-TMH). The rates of the sulfoxide formation were compared at the saturating concentration of the substrates, using either TMH or D-TMH (Figure 20). Both $EgtB_1$ and $EgtB_{1\_Y377F}$ showed a substrate KIE near unity. Therefore, it was concluded that the cleavage of C2-H is not the rate limiting step in both $EgtB_1$ and $EgtB_{1\_Y377F}$. Moreover, this kinetic data suggests that the essential function of Y377 is not in hydrogen or proton removal from TMH.

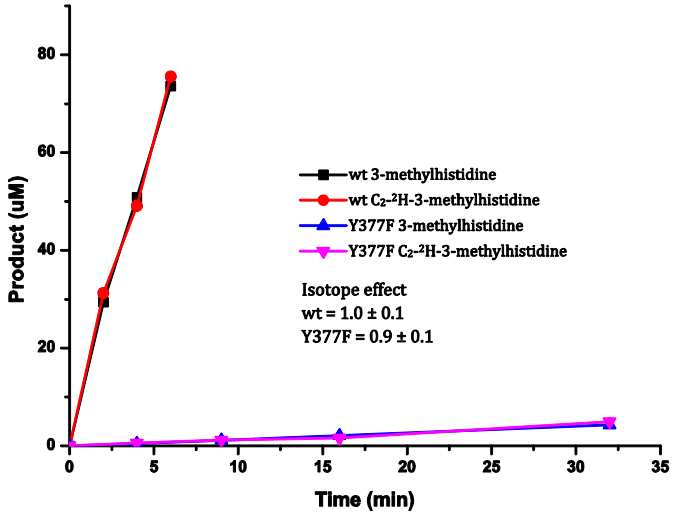

Figure 20. Determination of the substrate KIE for $EgtB_1$ and $EgtB_{1\_Y377F}$. Catalytic activity assayed in 250 µL reactions containing 100 mM HEPES pH 8.0, 100 mM NaCl, 2 mM TCEP, 2 mM ascorbate, 4 µM $FeSO_4$, 400 µM TMH or C2-deuterated TMH, 1.2 mM γGC and 1.2 µM $EgtB_1$ or $EgtB_{1\_Y377F}$. The reactions were incubated at 26 °C; product formation was monitored by HPLC.

Previously, the kinetic analyses of the reaction mixtures were based on the detection of the sulfoxide reaction product. To further analyze the $EgtB_{1\_Y377F}$ mutant, the rate of γGluCys consumption was measured by a derivatization method (see experimental). The rates of γGluCys consumption and the sulfoxide formation were compared for both $EgtB_1$ and $EgtB_{1\_Y377F}$ mutant and a noticeable difference between both variants was observed (Figure 21). $EgtB_1$ catalyzes reactions where the substrate consumption ($k_{\gamma GC,wt}$ = 0.4 ± 0.02 s^{-1}) and sulfoxide formation ($k_{sulfoxide,wt}$ = 0.3 ± 0.06 s^{-1}) are coupled. In contrast, $EgtB_{1\_Y377F}$-catalyzed γGC consumption was much faster ($k_{\gamma GC,Y377F}$ = 0.6 ± 0.1 s^{-1}) than sulfoxide production ($k_{sulfoxide,Y377F}$ = 0.001 s^{-1}). One possible explanation for the large difference in the rates of the substrate consumption and the product formation for the $EgtB_{1\_Y377F}$ mutant might be a side reaction which consumes γGC.

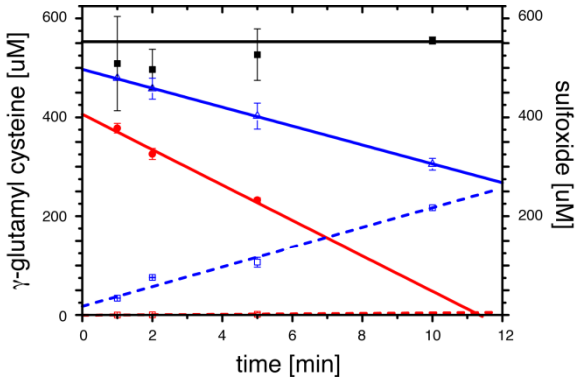

Figure 21. $EgtB_1$ and $EgtB_{1\_Y377F}$ catalyzed consumption of γGC and sulfoxide production in presence of 0.5 mM TMH, 0.55 mM γGC, 2 mM ascorbate, 100 mM HEPES pH 8.0, and 0.9 µM of the respective enzyme. γGC consumption by $EgtB_1$: 0.4 ± 0.02 s^{-1} (blue line); by $EgtB_{1\_Y377F}$: 0.6 ± 0.1 s^{-1} (red line). Sulfoxide production by $EgtB_1$: 0.3 ± 0.06 s^{-1} (blue dash); by $EgtB_{1\_Y377F}$: < 0.002 s^{-1} (red dash). In the absence of enzyme, γGC was not consumed (black line).

In order to identify the product formed by the $EgtB_{1\_Y377F}$ mutant, the reaction mixtures were analyzed by ^1H NMR. This analysis shows characteristic signals for protons of the imidazole ring of the histidine derivatives or the sulfoxide, as well as α- and β- protons of γGluCys (Scheme 20). Under saturated substrate conditions, both $EgtB_1$ and $EgtB_{1\_Y377F}$ reactions were analyzed by ^1H NMR and comparised to a control reaction carried out in the absence of either enzyme. In the $EgtB_1$-catalyzed reaction, γGluCys is consumed to form its corresponding sulfoxide. In the same time, $EgtB_{1\_Y377F}$-catalyzed reaction, less than 1 % of γGluCys converted to the sulfoxide. The region near the β-protons of γGluCys showed the formation of a new product – γGluCys sulfinic acid.[89] Furthermore, ^1H NMR revealed that $EgtB_{1\_Y377F}$ oxidizes a large proportion of γGluCys to γGluCys sulfinic acid (Figure 22, p. 49).

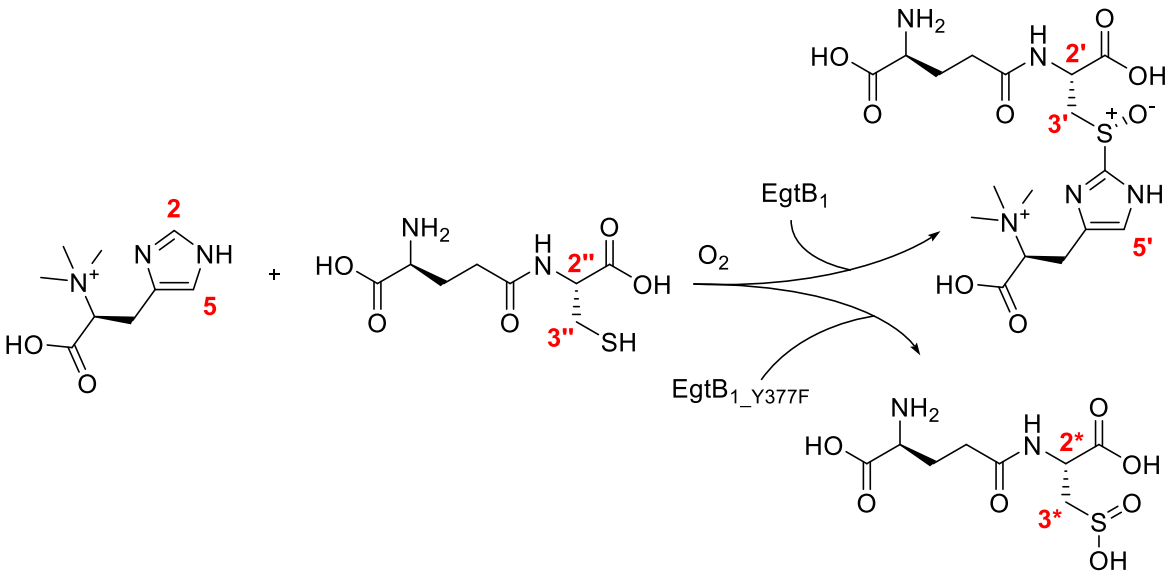

Scheme 20. $EgtB_1$ substrates (TMH and γGluCys) and products (sulfoxide and γGluCys sulfinic acid) were quantified by ^1H NMR. Protons in the positions highlighted in red were compared to distinguish between the starting materials and products.

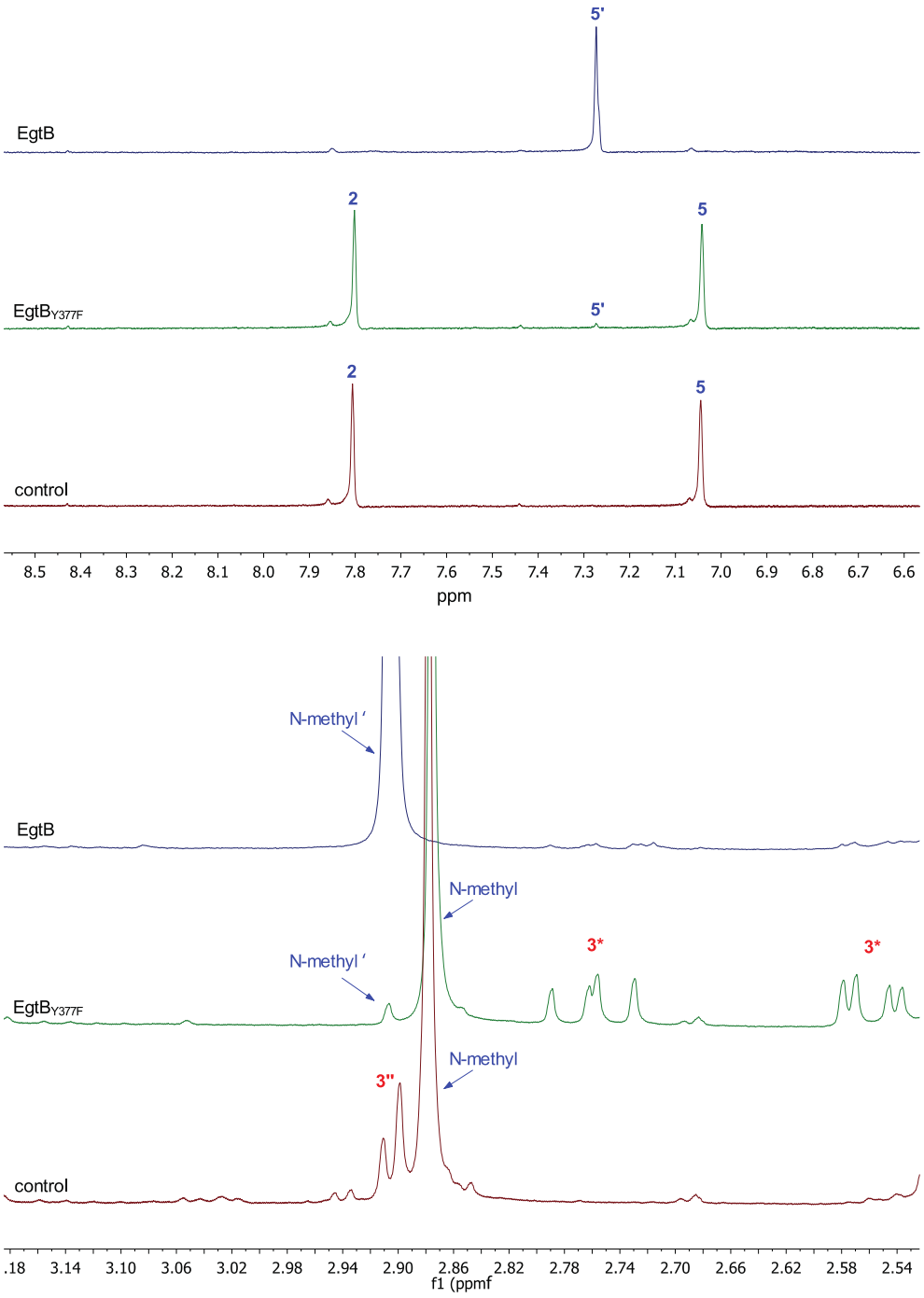

Figure 22. The product of $EgtB_{1\_Y377F}$ catalyzed γGC conversion was identified as γGC dioxide by ^{1}H NMR. Reactions containing 100 mM sodium phosphate buffer pH 8.0, 100 mM NaCl, 2 mM ascorbate, 4 µM $FeSO_4$, 2 mM TCEP, 0.5 mM DMH, 0.5 mM γGC and 1 µM $EgtB_1$ or $EgtB_{1\_Y377F}$ were incubated for 12 h at 26 °C. A reaction containing no enzyme was used as control experiment. The reactions were lyophilized, the residue was dissolved in D_2O. Top: aromatic region: ^{1}H NMR (400 MHz, D_2O): $EgtB_1$ reaction: δ 7.27 (s, 1H, H-5'); $EgtB_{1\_Y377F}$ reaction: δ 7.80 (s, 1H, H-2), 7.27 (s, 1H, H-5'), 7.04 (s, 1H, H-5); Control reaction: δ 7.81 (s, 1H, H-2), 7.04 (s, 1H, H-5). Bottom: aliphatic region: $EgtB_1$ reaction: δ 2.91 (s, 6H, N-methyl'); $EgtB_{1\_Y377F}$ reaction: δ 2.91 (s, 6H, N-methyl'), 2.88 (s, 6H, N-methyl), 2.76 (dd, J = 13.1, 10.7 Hz, 1H, H-3*), 2.56 (dd, J = 13.3, 3.7 Hz, 1H, H-3*); control reaction: δ 2.95 – 2.83 (m, 8H, N-methyl, H-3'', H-3'').

The dioxygenase activity found in $EgtB_{1\_Y377F}$ is TMH-dependent, which indicates that dioxygenation proceeds via the same substrate complex as the sulfoxide production. In the absence of TMH both $EgtB_1$ and $EgtB_{1\_Y377F}$ catalyzed γGC dioxygenation at a similarly rate ($k_{\gamma GC}$ = 0.008 s^{-1},

Figure 23). This result suggests that γGluCys binds to the active site of $EgtB_1$ in the absence of TMH. The single substrate complex is significantly less reactive than in the complex with TMH. However, the reactivity of the single substrate complex is not affected by the Y377F mutation.

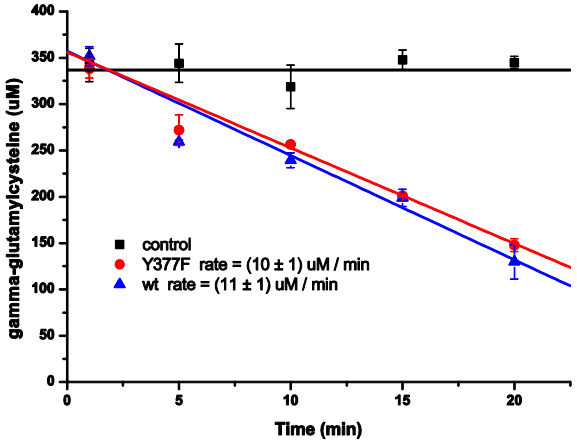

Figure 23. γGC consumption in absence of TMH. Reactions containing 100 mM HEPES pH 8.0, 100 mM NaCl, 4 µM $FeSO_4$, 2 mM ascorbate, 0.35 mM γGC and 21 µM of either $EgtB_1$ or $EgtB_{1\_Y377F}$ were incubated at 26 °C. Residual γGC was quantified by the formation of a coumarin adduct by HPLC.

In order to fully characterize the new activity of $EgtB_{1\_Y377F}$ mutant, the Michaelis-Menten parameters for dioxygenase activity were determined (Table 11). The kinetic parameters for $EgtB_{1\_Y377F}$-catalyzed dioxygenation were very similar those of $EgtB_1$-catalyzed sulfoxide synthesis (Table 10, p. 47). This similarity suggests that the k_{cat} was not affected by the mutation, even though the mutant catalyzes a completely different reaction. The binding of TMH and γGC were not affected by the mutation, due to the absence of the significant change in the apparent K_M. Both variants oxidize γGC at similar rates, therefore the efficiency of oxygen binding and activation did not change.

The catalytic efficiency of $EgtB_{1\_Y377F}$ dioxygenase activity closely matches the naturally evolved cysteine dioxygenases (Table 11), even sulfoxide synthases may never have developed the ability to catalyze the dioxygenation.[90]

Table 11. Kinetic parameters at pH 6.0 and 8.0 for dioxygenase activity of $EgtB_{1\_Y3777F}$ and of CDO at pH 7.5.

	pH	**Substrate**	k_{cat}, s^{-1}	K_M, $x10^{-6}$ M	k_{cat}/K_M, s^{-1} M^{-1}
$EgtB_{1\_Y377F}$	8.0	γGluCys	1.2 ± 0.1	110 ± 20	11000 ± 3000
$EgtB_{1\_Y377F}$	6.0	γGluCys	0.85 ± 0.26	320 ± 140	2650 ± 2000
CDO_{murine}[90]	7.5	L-Cys	1.8 ± 0.02	700 ± 200	2600

Taking into account that oxygen binding and activation have not changed for $EgtB_{1\_Y377F}$, the rate of autoxidation reaction of oxygen to superoxide anion was compared between $EgtB_{1\_Y377F}$ and $EgtB_{1\_Y377F}$. In the presence of ascorbate, $EgtB_1$ and $EgtB_{1\_Y377F}$ catalyzes hundreds of turnovers, without any sign of inactivation. However, in absence of ascorbate, $EgtB_1$ oxidizes to the inactive

iron(III) form after approximately 100 turnovers (Chapter 2.1), possibly caused by unproductive decay of the iron(III)–superoxo species to superoxide and ferric $EgtB_1$. Reduction is much slower and limits the ascorbate-independent turnover in the steady state to (2 ± 0.4) min^{-1} with a corresponding $k_{autoxidation}$ of 0.01 s^{-1} (Figure 24). This inactivation is reversible when ascorbate added. A similar behavior was observed for $EgtB_{1\_Y377F}$, however the mutant inactivated 10-fold faster ($k_{autoxidation}$ = 0.1 s^{-1}, Figure 25) and calculated rate of the sulfoxide formation in the steady state is (0.9 ± 0.1) min^{-1}, which is two times smaller than that for the wild-type. This observation indicates that the initial iron-coordinated oxygen species may be destabilized, when Y377 is substituted by phenylalanine.

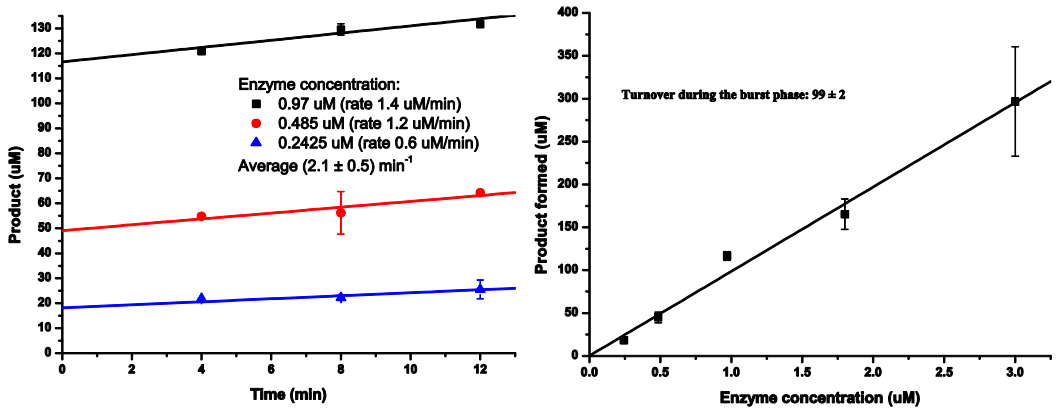

Figure 24. Autoxidation of $EgtB_1$. In the absence of ascorbate, $EgtB_1$ loses activity within the first 1 - 2 min of catalysis owing to reversible autoxidation of EgtB to the inactive iron(III) form. In the presence of ascorbate this inactive species does not accumulate because reduction to the active iron(II) form is faster than oxidation to the inactive iron(III) form. Reduction by γGC is much slower which limits ascorbate-independent turnover in the steady state (starting after 4 min) to 2 min^{-1}. Linear regression of this slow phase to t = 0 gives an estimate of how many turnovers were completed before EgtB oxidizes the first time (left). These estimates from experiments with different enzyme concentrations plotted against enzyme concentrations reveal that each EgtB molecule catalyzes on average 100 turnovers before autoxiation occurs. In other words, k_{cat} is 100-fold faster than $k_{autoxidation}$ i.e. $k_{autoxidation}$ = k_{cat}/100 (right). Catalytic rates were determined in reactions containing 100 mM HEPES pH 8.0, 100 mM NaCl, 4 eq. of $FeSO_4$, 2 mM TCEP, 0.4 mM TMH, 1.2 mM γGC, and 0.25-3 µM EgtB.

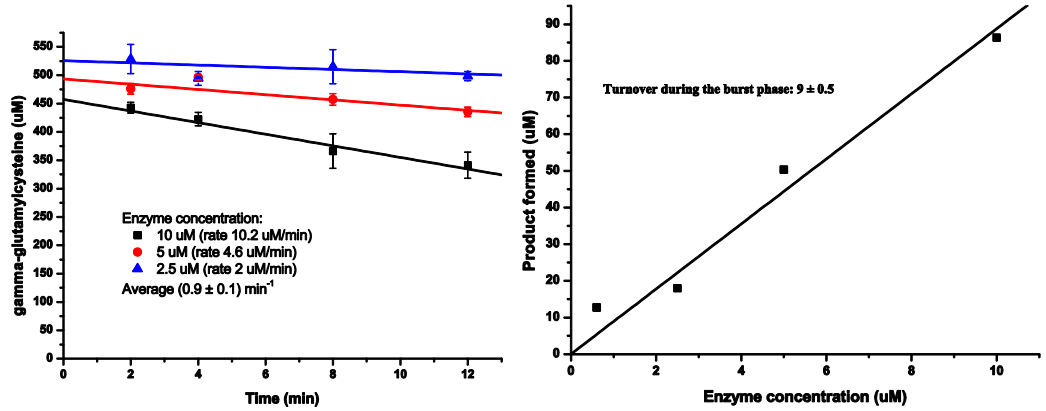

Figure 25. Autoxidation of $EgtB_{1\_Y377F}$. In the absence of ascorbate, $EgtB_{1\_Y377F}$ also loses activity within the first 1 - 2 min due to reversible autoxidation. Determination of $k_{autoxidation}$ = k_{cat}/9 was achieved using the same methodology as described above. Catalytic rates were determined in reactions containing 100 mM sodium phosphate buffer pH 8.0, 100 mM NaCl, 4 eq. of $FeSO_4$, 2 mM TCEP, 0.4 mM TMH, 0.55 mM γGC, 2.5-10 µM $EgtB_{1\_Y377F}$.

To better establish the role of Y377 in the catalytic cycle of $EgtB_1$, the kinetic solvent isotope effect (KSIE) was determined on the sulfoxide synthase and dioxygenase reactions. The exchange of the solvent from H_2O to D_2O did not affect the sulfoxide synthase activity of $EgtB_1$, resulting in a KSIE near unity 1.2 ± 0.2 (Figure 26, left). Likewise the γGluCys dioxygenase activity of $EgtB_{1\_Y377F}$ has a KSIE of 0.9 ± 0.1 (Figure 27). In contrast, the sulfoxide synthase activity of $EgtB_{1\_Y377F}$ exhibited a solvent KIE of 1.9 ± 0.1 (Figure 26, right), indicating that one or multiple protons or hydrogen atoms are being transferred in the rate limiting step of the reaction.

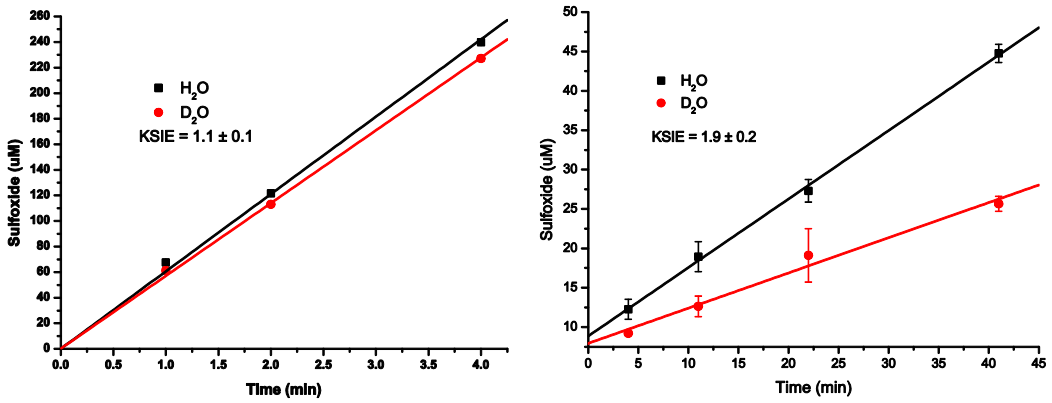

Figure 26. Solvent KIEs on $EgtB_1$ (left) and $EgtB_{1\_Y377F}$ (right) catalyzed sulfoxide production were determined at 26 °C in reactions containing 100 mM HEPES pH 8, 100 mM NaCl, 2 mM TCEP, 2 mM ascorbate, 4 or 40 µM $FeSO_4$, 1 mM TMH and 1.2 mM γGC, 1.4 µM $EgtB_1$ or 10 µM $EgtB_{1\_Y377F}$.

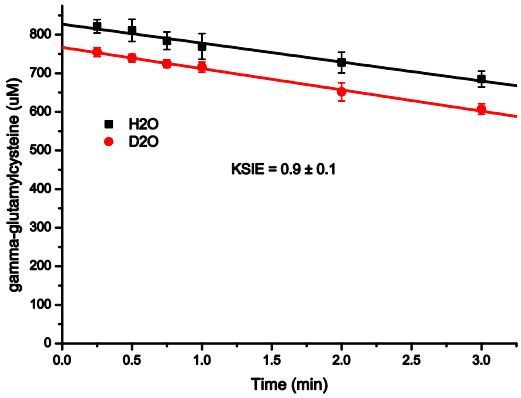

Figure 27. The solvent KIE on $EgtB_{1\_Y377F}$ catalyzed γGC dioxygenation was determined at 26°C in reactions containing 100 mM HEPES pH 8, 100 mM NaCl, 2 mM TCEP, 4 µM $FeSO_4$, 2 mM ascorbate, 1 mM DMH, 0.8 mM γGC, and 0.5 µM $EgtB_{1\_Y377F}$. Consumption of γGC was monitored as described above.

Since dioxygenase activity of $EgtB_{1\_Y377F}$ was not affected by exchanging the solvent from H_2O to D_2O, suggests that the proton transfer occurs entirely on sulfoxide synthase pathway. Considering that the wild-type did not show any KSIE on sulfoxide synthase activity, we proposed that the role of Y377 might lie in protonation of the iron(III)-superoxo species. Mutation of this residue to phenylalanine led to the loss of the sulfoxide synthase activity by 10^3-fold. These observations suggest that either a water molecule or hydronium ion might replace the role of Y377 in the mutant. The observed KSIE for the mutant would support this, hence the difference between pK_a

of tyrosine or a water molecule (Figure 28). Therefore, to probe whether the protonation of iron(III)-superoxo species could be replaced by solvent, the product distribution and the kinetic analysis were performed at different pHs.

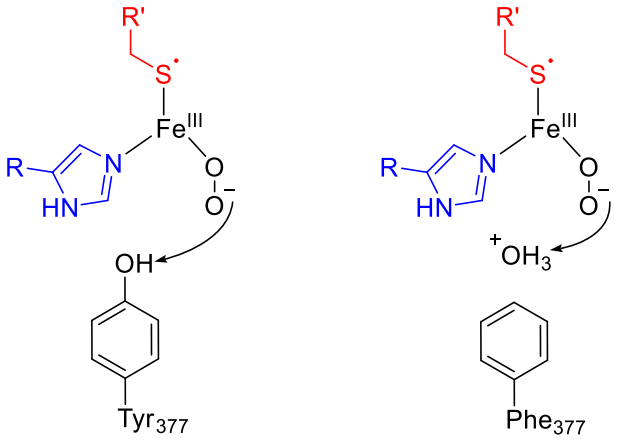

Figure 28. Iron(III)-superoxo species can be protonated by Y377 in the $EgtB_1$ or hydronium ion in the $EgtB_{1\_Y377F}$ mutant.

The sulfoxide synthase activity depends on the availability of an acidic proton in the active site. Thus, lowering the reaction pH from 8.0 to 6.0 led to a 3.5-fold increase in the k_{cat} for the $EgtB_{1\_Y377F}$-catalyzed sulfoxide synthesis, whereas k_{cat} for $EgtB_1$ did not changed significantly (Table 12). The kinetic data was supported by ^{1}H NMR for the $EgtB_{1\_Y377F}$ catalyzed reactions at different pH (Figure 29, top, p. 54). This analysis revealed that the KSIE remains the same in the examined pH range. Furthermore, by increasing the proton concentration, sulfoxide synthase activity of $EgtB_{1\_Y377F}$ increases as well. The observed sulfoxide synthase activity is a hyperbolic function of proton concentration with a half-saturation point ($K_{M,proton}$) near pH 7 (Figure 29, bottom, p. 54). This dependence is consistent with a general acid mechanism in which the phosphate buffer ($pK_{a,monoanion}$ = 7.2), or an alternative protein residue with a similar pK_a can replace Y377 as an indirect proton source. The pH change in the same range did not affect the k_{cat} of γGC for the dioxygenase activity of $EgtB_{1\_Y377F}$ (Table 12). These results suggest that acid catalysis is less important in the first irreversible step of thiol dioxygenation rather than in the catalytic cycle of the sulfoxide synthase.

Table 12. Kinetic parameters of EgtB variants at pH 8.0 and 6.0 for sulfoxide synthase and dioxygenase activities.

	Substrate	**k_{cat}, s^{-1}**	**K_M, x10^{-6} M**	**k_{cat}/K_M, s^{-1} M^{-1}**
Sulfoxide synthase				
$EgtB_1$	TMH, pH 8.0	0.85 ± 0.01	12 ± 1	74000 ± 5200
	TMH, pH 6.0	1.2 ± 0.1	22 ± 1	57000 ± 5500
$EgtB_{1\_Y377F}$	TMH, pH 8.0	0.0009 ± 0.0001	10 ± 4	85 ± 44
	TMH, pH 6.0	0.0032 ± 0.0005	40 ± 15	80 ± 40
γGluCys dioxygenation				
$EgtB_{1\_Y377F}$	γGluCys, pH 8.0	1.2 ± 0.1	110 ± 20	11000 ± 3000
	γGluCys, pH 6.0	0.85 ± 0.26	320 ± 140	2650 ± 2000

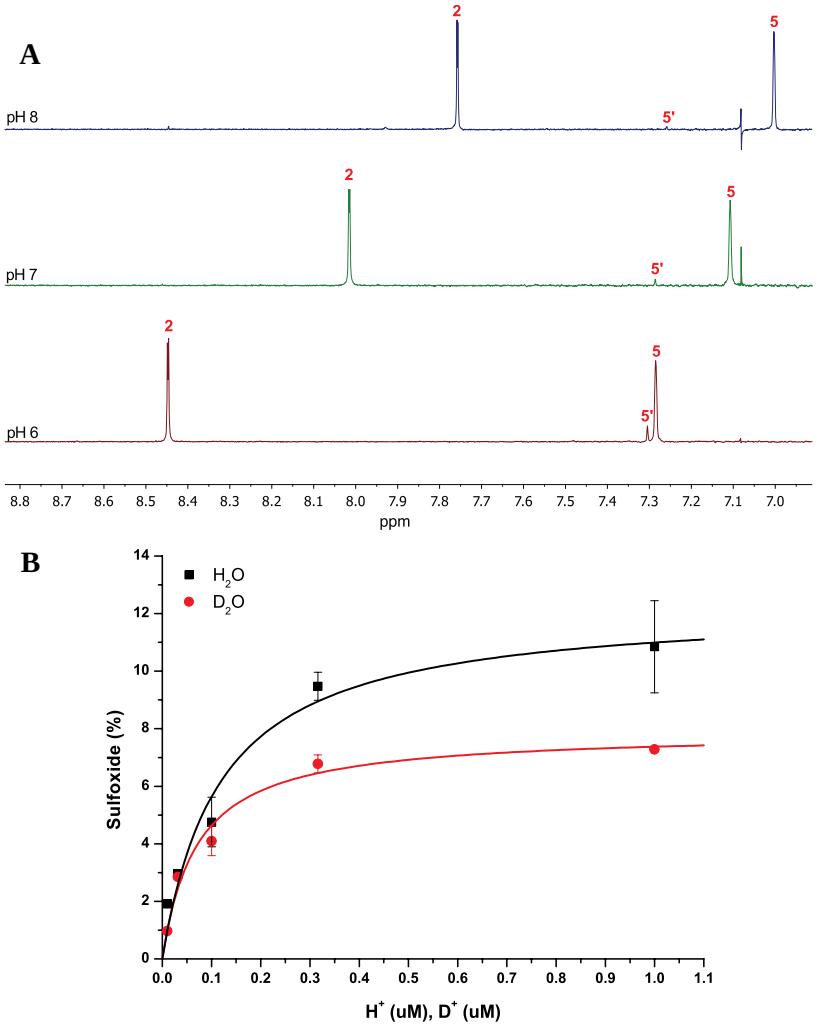

Figure 29. The dependence of $EgtB_{Y377F}$ catalyzed sulfoxide production on buffer pH was determined by the ratio between substrate TMH and product sulfoxide in completed reactions by ^1H NMR. The same analysis was repeated in D_2O, to probe the pH dependence of the solvent KIE. The reactions (in H_2O or D_2O) contained 100 mM sodium phosphate buffer at pH (or pD) 8.0, 7.0 or 6.0, 100 mM NaCl, 2 mM ascorbate, 4 µM $FeSO_4$, 2 mM TCEP, 0.5 mM TMH, 0.75 mM gGC and 1 µM $EgtB_{Y377F}$. The reactions were incubated at 26 °C. After 12 h the solutions were lyophilized and dissolved D_2O for NMR analysis (**A**). The aromatic signals of TMH (C2-H and C5-H) and of sulfoxide (C5'-H) were used to compute the percentage of consumed TMH, i.e. produced sulfoxide. (**B**)These values (obtained at pH 6.0, 6.5, 7.0, 7.5 and 8.0) were plotted against proton concentration and fitted with a hyperbolic function of the form: [sulfoxide] = $[\text{sulfoxide}]_{max}[H^+]/(K_{M,proton} + [H^+])$. This analysis revealed that a) the solvent KIE remains > 1.5 in the examined pH range; b) increased proton concentration stimulates sulfoxide production by $EgtB_{Y377F}$; c) pH dependent acceleration saturates with a pH below 7.

We concluded that the proton transfer from Y377 is crucial for the sulfoxide synthase pathway. Introduction of mutation Y377F perturbs the catalytic pathway of the reaction catalyzed by EgtB, by opening a new dioxygenation pathway. Considering that the dioxygenase activity was not affected by solvent deuteration, we propose that proton transfer is important for the sulfoxide synthase activity. Therefore, within the proposed mechanism the candidate for the solvent isotope sensitive step would be the protonation of the initially formed iron(III)–superoxo intermediate (A) (Scheme 21, p. 56). Proton transfer in the wild-type enzyme from Y377 generates a peroxo species (B), which may be important to increase the thiyl radical character of the γGC ligand. Then the thiyl radical could attack the imidazole ring of TMH, resulting in the formation of a C-S bond (C). Deprotonation, by the

tyrosinate at position 377, and sulfur oxidation via either the peroxo species or via a ferryl would generate the product.

However, in the $EgtB_{1\_Y377F}$ mutant there is no proton readily available to stabilize the iron(III)-superoxo species. Considering that the mutant primarily catalyzes sulfinic acid formation, suggests that the mechanism of dioxygenation in the mutant is similar to the one proposed in cysteine dioxygenase (CDO) (Scheme 22).[46, 51-52, 91] In this enzyme, the first irreversible step is the S–O bond forming step (a to b) and in a similar manner to CDO, the iron(III)-superoxo species of the mutant may attack the electron-deficient sulfur atom on γGC (A to B'). Therefore we proposed that species (A) can either react *via* irreversible proton transfer to intermediate B, or *via* irreversible S–O bond formation leading to intermediate B', depending on the availability of an acidic proton in the active site.

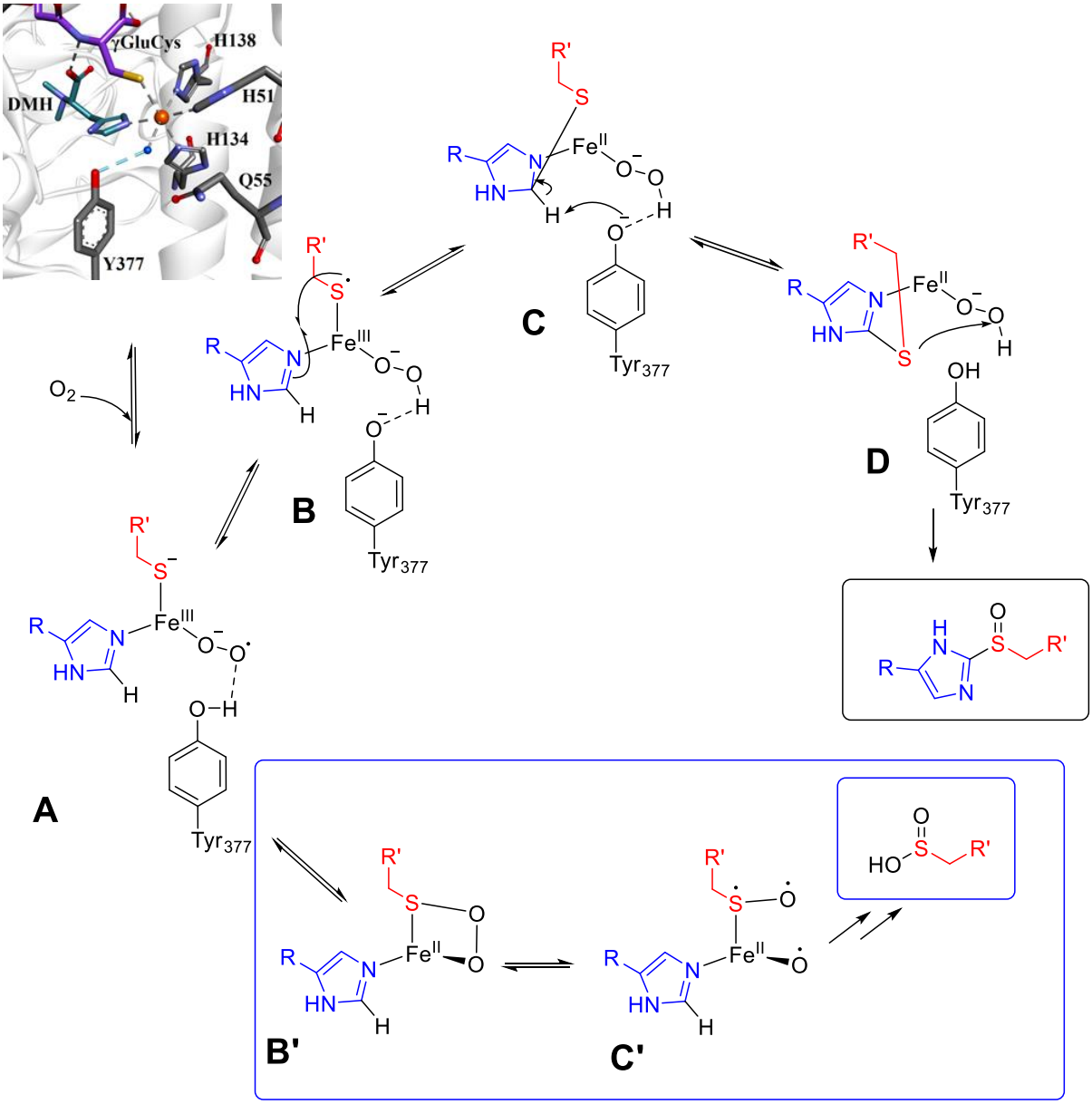

Scheme 21. Active site of $EgtB_1$ from *M. thermoresistibile* in complex with Mn(II), TMH and γGC (pdb: 4X8D). One plausible catalytic mechanism has been proposed for $EgtB_1$: the substrate bound complex reacts with O_2 to form an iron(III)–superoxo species (A). Protonation by Y377 and reduction by one-electron transfer from γGluCys leads to the iron(III)–hydroperoxo species (B). C–S bond formation between the γGC radical and TMH (C), deprotonation by Y377 and stereospecific sulfoxidation of D to the sulfoxide concludes the catalytic cycle. In the frame: in the absence of an acidic residue at position 377 species A predominantly reacts to B' which reacts further to γGC dioxide potentially through a CDO-like mechanism.

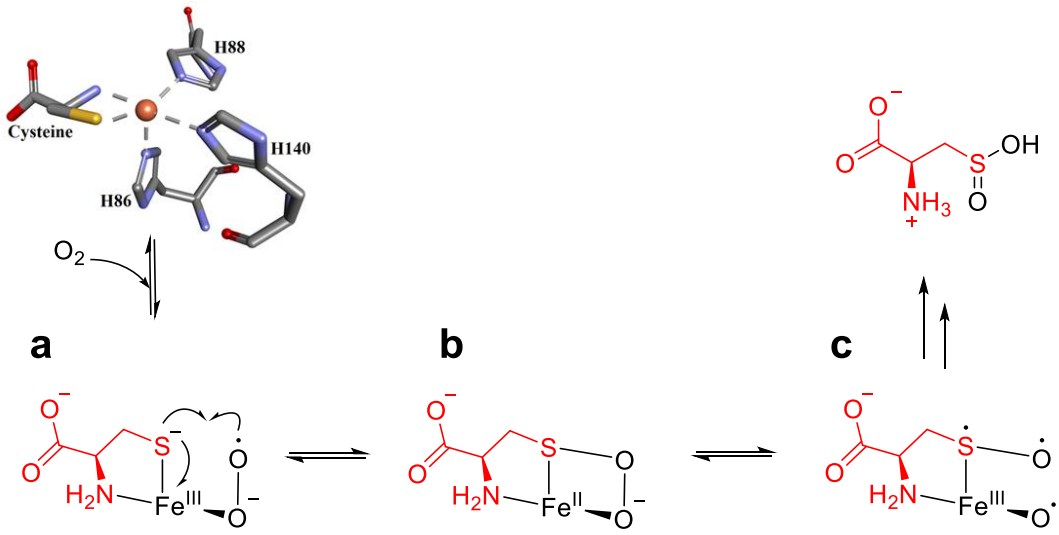

Scheme 22. Active site of murine CDO in complex with cysteine (pdb: 4IEW, 1.45 Å).[92] The consensus mechanism of CDO proceeds *via* a cysteine bond iron(III)–superoxo species (a), followed by irreversible S–O bond formation (b), homolytic O–O bond scission (c), and radical rebound to form cysteine sulfinic acid (3).[46, 51-52, 91]

The presented data identifies a crucial catalytic residue Y377 in $EgtB_1$. A single point mutation of this residue almost completely uncouples substrate consumption from sulfoxide synthase activity by oxidizing γGluCys into sulfinic acid. Furthermore, this mutation did not affect substrate binding or O_2 activation. The kinetic parameters of the newly generated dioxygenase are similar to the naturally evolved dioxygenases, such as murine CDO. However, by comparing k_{cat} values, the mutant still has sulfoxide synthase activity which is 1000-fold slower than in the wild-type and characterized by an increased KSIE and significant dependence on buffer pH. Within the mechanistic models suggested for sulfoxide synthases and dioxygenases, current data suggest that both pathways share a common intermediate – an iron(III)-superoxo species. Protonation of an iron(III)-superoxo species by Y377 triggers this reaction towards the sulfoxide formation, if this species is not protonated, dioxygenation takes place.

3.2. Identification of the catalytic tyrosine residue in EgtB homologues

The catalytic residue Y377 is conserved only among $EgtB_1$-like sulfoxide synthases. To test the importance of Y377 among other sulfoxide synthases, we analyzed a homologue of $EgtB_1$. An ergothioneine biosynthetic pathway similar to the one identified from *N. crassa* was found in bacteria *Candidatus chloracidobacterium thermophilum B* (Scheme 23).[67a] The main difference to the mycobacterial biosynthetic pathway lies in the sulfoxide synthase EgtB. The mycobacterial EgtB accepts γGluCys as a substrate ($EgtB_{smeg}$ and $EgtB_1$), whereas EgtB from *Candidatus chloracidobacterium thermophilum B* ($EgtB_2$) and $EgtB_{crassa}$ converts L-cysteine (Cys) to the corresponding sulfoxide. The sequence alignment between $EgtB_1$ and $EgtB_2$ shows a 32 % identity and a similar protein fold consistent of two domains: FGE-like and DinB-like. Furthermore, the iron-

binding motif remains the same consisting of a 3-His facial triad (Figure 30). Interestingly, Y377 is not conserved and an alanine residue is placed instead. The key catalytic residues usually have to be strictly conserved. Given that Y377 is crucial for the catalysis of $EgtB_1$ we proposed that this residue has to be present in $EgtB_2$, but evolutionally might have changed its position within the active site. Unfortunately the crystal structure of $EgtB_2$ was not available at the time. Therefore due to the lack of a crystal structure of $ErgtB_2$, a homology model was build.

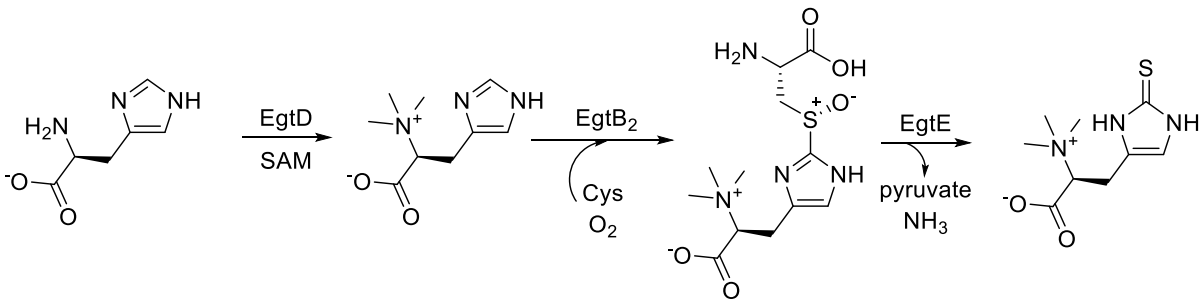

Scheme 23. The biosynthetic pathway of ergothioneine in bacteria *Candidatus chloracidobacterium thermophilum B*.

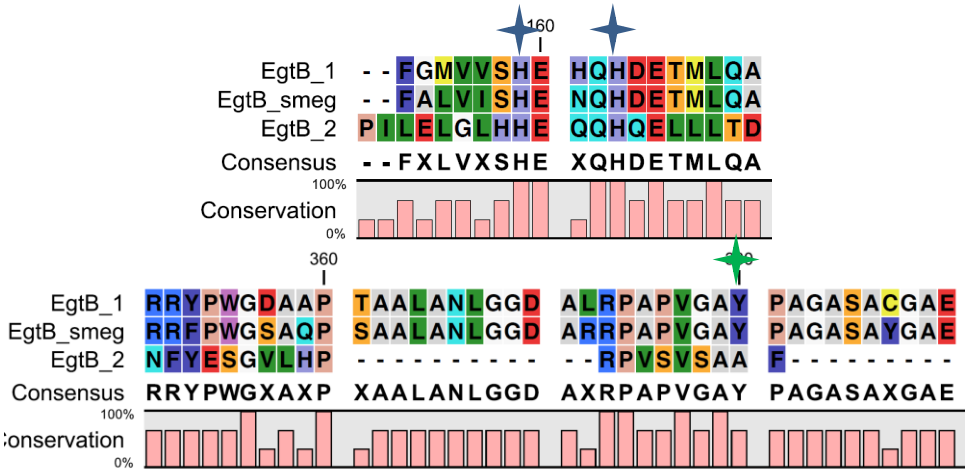

Figure 30. Sequence alignment of $EgtB_1$, $EgtB_{smeg}$ and $EgtB_2$ reveals the similar iron-binding motif (H134, H137). However, the loop with Y377 (marked with a green star) is absent in $EgtB_2$.

In order to identify the analogue of Y377 in $EgtB_2$, the model of $EgtB_2$ based on the structure of $EgtB_1$ was calculated *in silico* by using Accelrys Discovery Studio Client 2.5. The superimposition of the model (blue) with the $EgtB_1$ structure (red) together with sequence alignment shows that the overall model of $EgtB_2$ has a similar secondary structure and location of the active site to $EgtB_1$: between the DinB domain and the FGE-like domain (Figure 31). On the place of Y377 there is no other residue which might replace the role of Y377. However, in the model of $EgtB_2$ in close proximity to the metal center there is Y93, which could be a candidate for Y377 analogue. Interestingly, the Y93 residue is located within the unstructured region of the DinB domain. Next to this residue the serine residue S92 and the second tyrosine Y94 are placed. The model cannot predict the precise position of all residues, especially located in unstructured regions. Therefore, to test

whether identified tyrosine residues are involved in the catalysis, they were mutated to phenylalanine resulting in $EgtB_{2\_Y93F}$, $EgtB_{2\_Y94F}$ mutants. The total effect of both tyrosine residues located next to the active site was probed by generating the double mutant $EgtB_{2\_Y93F\_Y94F}$.

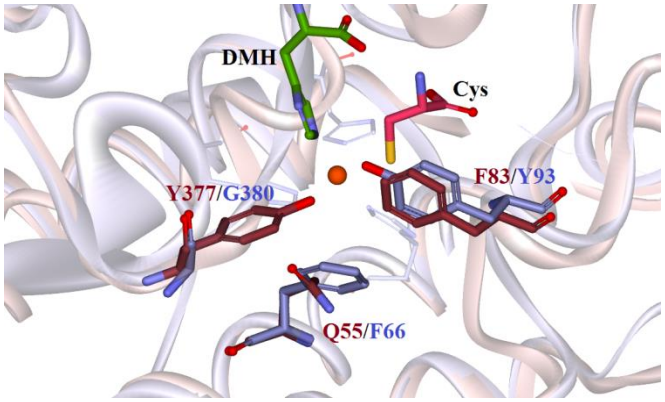

Figure 31. Calculated model of $EgtB_2$ (blue) superimposed with the structure of $EgtB_1$ (red). Y377 is replaced by G380. The tyrosine residue Y93 is placed in the close proximity to the iron center which might play the same role as Y377 of $EgtB_1$.

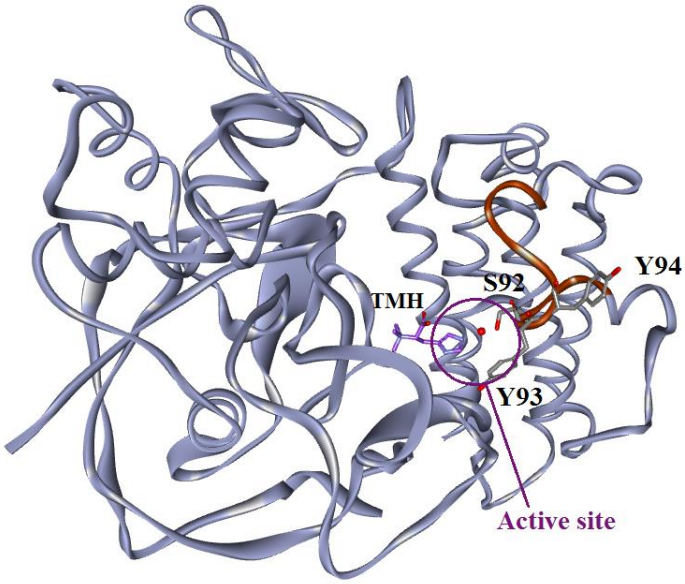

Figure 32. The model of $EgtB_2$, calculated based on the structure of $EgtB_1$. In the close proximity to the active site, there is an unstructured fragment (orange) containing two tyrosine residues Y93, Y94 and one serine residue S92.

Firstly, to check whether one of the identified tyrosine residues (Y93 and Y94) has a similar role in the catalytic pathway of sulfoxide synthase as Y377 in $EgtB_1$, we analyzed the product distribution of the generated mutants in comparison to the wild-type. Completed reactions catalyzed by $EgtB_2$ variants in excess of TMH were analyzed by ^1H NMR and assigned to the corresponding compounds (Scheme 24, Figure 33, p. 60-61).

The analysis of the complete reactions shows that $EgtB_2$ as efficient as $EgtB_1$. $EgtB_2$-catalyzed reaction forms not only its corresponding sulfoxide, in addition approximately 20 ±5 % of cysteine sulfinic acid (CSA). Similarly, dioxygenase side-activity was reported for OvoA-catalyzed reaction.[83] OvoA incubated with TMH and cysteine primarily produces cysteine sulfinic acid, identical to the product of the reaction catalyzed by cysteine dioxygenase. Thus, it seems that the reactive oxygen species is positioned to effect dioxygenation of sulfur in OvoA if sulfur is not precisely oriented for addition to the imidazole ring. Moreover, the native OvoA reaction revealed that, when OvoA was incubated with its native substrates (L-Cys and L-His), approximately 10% of the cysteine is converted to CSA. These data suggest that not all sulfoxide synthases catalyze specifically only sulfoxidation reaction, but as well dioxygenation, as in case of OvoA and $EgtB_2$.

Interestingly, mutation of tyrosine residues Y93 or Y94 in $EgtB_2$ uncouple the reaction towards sulfinic acid formation. Mutants $EgtB_{2\_Y93F}$ and $EgtB_{2\_Y94F}$ show mainly dioxygenase activity (99 %) with just 1 % of the sulfoxide being formed. Whereas in the double mutant $EgtB_{2\_Y93F\_Y94F}$ only CSA was observed, suggesting that the double mutant was completely converted into a cysteine dioxygenase. These results indicate that both Y93 and Y94 are catalytically important residues in the $EgtB_2$ catalyzed sulfoxide formation. However, in $EgtB_1$, only one tyrosine residue was identified as a catalytic acid. Therefore, in order to distinguish which tyrosine of $EgtB_2$ is the analogue of Y377 of $EgtB_1$, kinetic analysis on both sulfoxide synthase and dioxygenase activities were performed.

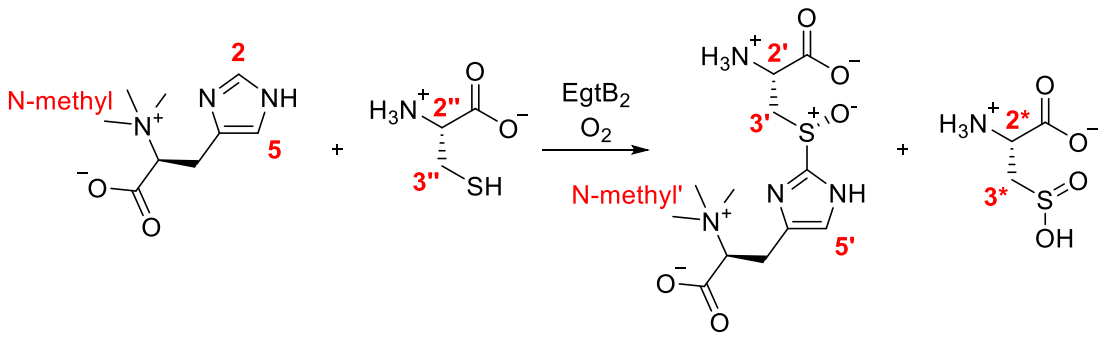

Scheme 24. $EgtB_2$ substrates (TMH and cysteine) and products (sulfoxide and cysteine sulfinic acid) were quantified by ^1H NMR based on α- and β-protons of cysteine and the aromatic protons of TMH.

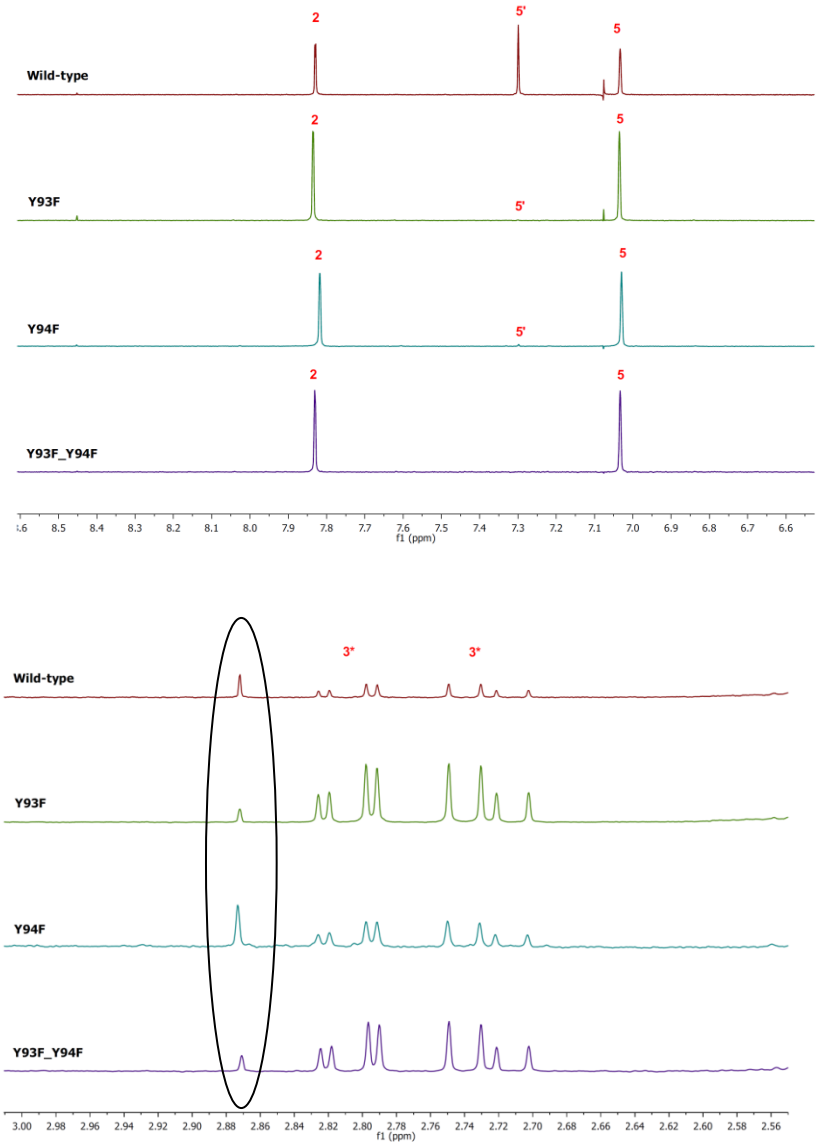

Figure 33. The product of $EgtB_2$ variants catalyzed Cys consumption was identified as cysteine sulfinic acid by ^1H NMR. Reactions containing 100 mM sodium phosphate buffer pH 8.0, 100 mM NaCl, 2 mM ascorbate, 4 µM $FeSO_4$, 2 mM TCEP, 1 mM TMH, 0.5 mM Cys and 1 µM $EgtB_2$ variant were incubated for 12 h at 26 °C. A reaction containing no enzyme was used as control experiment. The reactions were lyophilized, the residue was dissolved in D_2O. Top: aromatic region, bottom: aliphatic region. Highlighted peak was present in the starting material.

Firstly, the sulfoxide synthase activity of $EgtB_2$ variants were analyzed (Table 13). The wild-type catalyzed reaction shows comparable kinetic parameters to $EgtB_1$. Interestingly, the $EgtB_{2\_Y93F}$ mutant showed a dramatic drop in the sulfoxide synthase activity of 500-fold. For the second tyrosine mutant $EgtB_{2\_Y94F}$ the sulfoxide synthase activity decreased only by 65-fold. No sulfoxide formation was observed using HPLC-based analysis for the double mutant $EgtB_{2\_Y93F\_Y94F}$, confirming the previous NMR data.

Table 13. Catalytic parameters of $EgtB_2$ variants on the sulfoxide synthase activity. TMH is varied.

Enzyme	k_{cat}, s^{-1}	K_M, 10^{-6} M	k_{cat}/K_M, s^{-1} M^{-1}
$EgtB_2$	0.20 ± 0.01	65 ± 2	3200 ± 200
$EgtB_{2\_Y93F}$	0.0004 ± 0.0001	5 ± 1	90 ± 10
$EgtB_{2\_Y94F}$	0.003 ± 0.001	35 ± 10	80 ± 40
$EgtB_{2\_Y93F\_Y94F}$	N.D.	N.D.	N.D.

These kinetic data provides clear evidence that Y93 of $EgtB_2$ most likely has the same role as Y377 of $EgtB_1$. Mutation of the second tyrosine residue Y94 led to a smaller drop in the catalytic efficiency, suggesting that Y94 might not be involved in protonation of iron(III)-superoxo species and may have a different role in the catalysis. However, the fact that mutation of both Y93 and Y94 to phenylalanine completely decouples the sulfoxide synthase activity to dioxygenase activity, suggest that both residues are important to drive the reaction toward sulfoxidation. Additionally, it points out that in $EgtB_{2\_Y93F}$ mutant, Y94 can still protonate the iron(III)-superoxo species, however not as efficient as Y93. Moreover, it implies that there are no other residues in the active site, which could protonate iron(III)-superoxo species and replace the role of Y93 and Y94 residues.

To further identify the role of the two tyrosine residues in the active site of $EgtB_2$, consumption of cysteine was measured for all variants in order to estimate the dioxygenase activity (Table 14). The rate of the cysteine consumption for $EgtB_2$ remained unchanged upon introducing the Y93F mutation, showing that the $EgtB_{2\_Y93F}$ mutant mainly has cysteine dioxygenase activity with a minor sulfoxide synthase activity. Furthermore, it indicates that the oxygen binding was not affected by the $EgtB_{2\_Y93F}$ mutant, confirming that Y93 is indeed the analogue of Y377 in $EgtB_1$. However, the cysteine consumption by the $EgtB_{2\_Y94F}$ mutant shows that the cysteine consumption decreased in addition to sulfoxide synthase activity. Taking into account that thiol dioxygenation and sulfoxide synthesis share a common intermediate iron(III)-superoxo species, suggest that the $EgtB_{2\_Y94F}$ mutant might have affected the binding of one of the substrates. Given that the K_M for TMH and cysteine for the $EgtB_{2\_Y94F}$ mutant remained unchanged in comparison to the wild-type, therefore we conclude that the oxygen binding was affected by Y94F mutation.

Table 14. Catalytic parameters of $EgtB_2$ variants on the consumption of cysteine. Cysteine is varied.

Enzyme	k_{cat}, s^{-1}	K_M, 10^{-6} M	k_{cat}/K_M, s^{-1} M^{-1}
$EgtB_2$	0.14 ± 0.01	27 ± 3	5200 ± 800
$EgtB_{2\_Y93F}$	0.16 ± 0.02	120 ± 30	1400 ± 500
$EgtB_{2\_Y94F}$	0.021 ± 0.003	34 ± 12	600 ± 200
$EgtB_{2\_Y93F\_Y94F}$	0.049 ± 0.002	90 ± 15	550 ± 100

Interestingly, the kinetic analysis of the double mutant $EgtB_{2\_Y93F\_Y94F}$ shows that the dioxygenase activity is just 3-fold slower that the sulfoxide synthase activity for the wild-type, even

Y94 has been proposed to be involved in the oxygen binding. However, Y93 and Y94 are located within unstructured fragment which also contains S92 residue. The serine residue S92 might be involved in the dioxygenase activity of the double mutant. Further studies are required to test whether S92 is an important residue for dioxygenation, such as mutation of S92 to alanine in $EgtB_2$ and $EgtB_{2\_Y93F\_Y94F}$.

Therefore, by the mutation of two residues in the active site of $EgtB_2$ we were able to completely convert sulfoxide synthase into a cysteine dioxygenase without major loss in overall activity. As a result of kinetic analysis of $EgtB_2$ variants, we propose that within the catalytic cycle of the sulfoxide synthase $EgtB_2$ there are two catalytic acids involved: one which protonates the iron(III)-superoxo species (Y93) and the other one implicated in the oxygen binding (Y94).

3.3. Catalytic acid motifs in the active site of EgtB

In the active site of $EgtB_2$, two tyrosine residues were identified as catalytic acids. Y93 protonates the distal oxygen of iron(III)-superoxo species and Y94 coordinates the proximal oxygen through a hydrogen bond and might be responsible for oxygen positioning and binding. Kinetic analysis of $EgtB_2$ variants revealed that Y93 has a similar role in the catalysis as Y377 in $EgtB_1$. However, in the active site of $EgtB_1$ no candidates for Y94 analogue were identified, aside from Q55, which in the crystal structure also hydrogen bonds the water molecule, coordinated the iron center (2.8 Å, Scheme 25, p. 64). Q55 in the conformation represented in the crystal structure cannot form a hydrogen bond to the proximal oxygen of iron(III)-superoxo species. One possibility to form a hydrogen bond is to rotate side chain of Q55. However, in the crystal structure, the amino group of the side chain of Q55 is hydrogen bonding to Q54, making this rotation more difficult. Another possibility would be a different resonance structure of Q55 side chain with protonated hydroxyl group. For further investigations of the role of Q55 in the catalysis by $EgtB_1$ has to be probed by mutating this residue to glutamate or methionine.

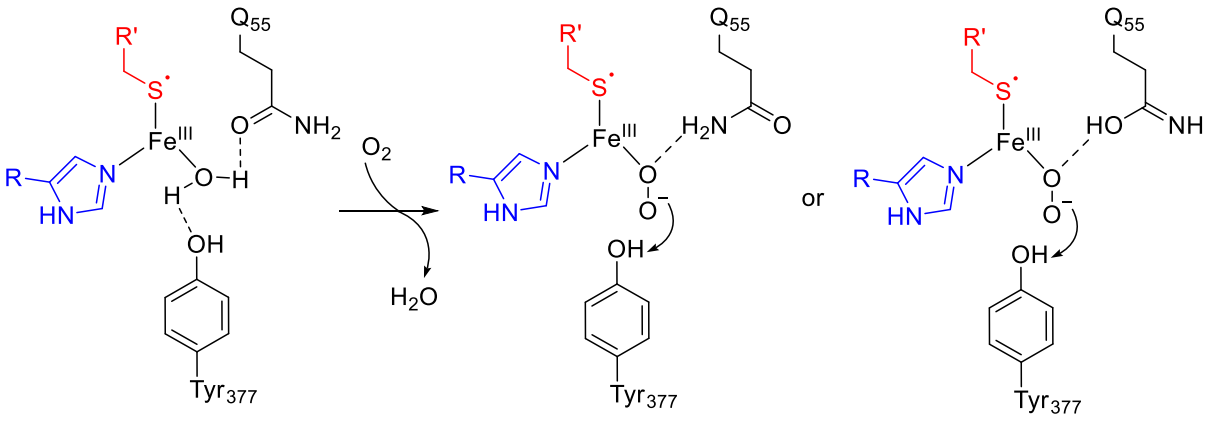

Scheme 25. The schematic representation of the $EgtB_1$ active site with hydrogen-bond network was identified in the crystal structure. Q55 and Y377 are hydrogen bond to the iron-coordinated water molecule (2.8 Å). Upon oxygen binding, two different structures were proposed to suggest hydrogen bonding to the proximal oxygen.

The discovery of the role of two different residues in the catalytic cycle is more complex, rather than comparison of two identical ones, as in case of $EgtB_2$. Therefore, we identified another EgtB from *Thermomonospora curvata* ($EgtB_{cur}$), with a sequence identity to the $EgtB_1$ of 53 % and with identical substrate specificity. In order to identify the position of catalytic residues, the model of $EgtB_{cur}$ was generated *in silico* based on the crystal structure of $EgtB_1$ (Figure 34). The tyrosine residue Y388 in the model is placed at the same position as Y377 in $EgtB_1$. The main difference between the active sites of those proteins lies in the second acid: there is a tyrosine residue placed instead of Q55. Thus, the $EgtB_{cur}$ provides us with a perfect system to analyze the system with two catalytic tyrosine residues in the active site by mutating each of them to phenylalanine.

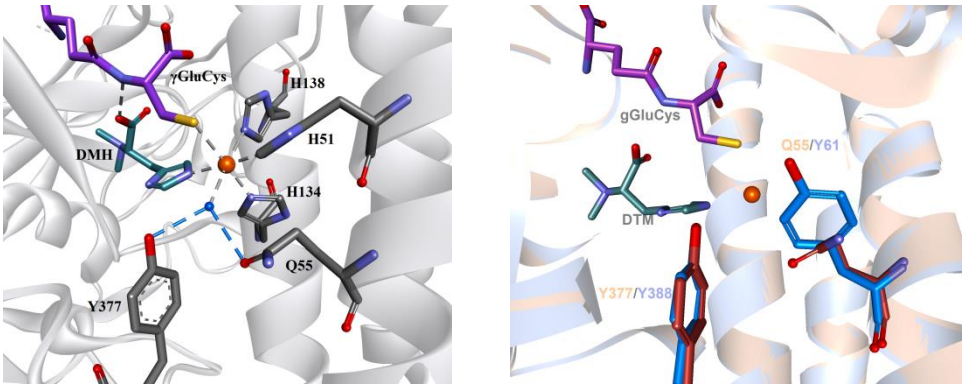

Figure 34. Left: The active site of $EgtB_1$ shows a water molecule bound to the iron center. The water molecule is hydrogen-bonded to Y377 and Q55 (2.78 Å). **Right:** Superimposition of the $EgtB_1$ (red) crystal structure and the model of $EgtB_{cur}$ (blue).

In order to analyze the role of tyrosine residues in the active site, the following mutants were generated: $EgtB_{cur\_Y61F}$, $EgtB_{cur\_Y388F}$ and $EgtB_{cur\_Y61F\_Y388F}$. The ^1H NMR analysis was performed on reactions catalyzed by $EgtB_{cur}$ variants in excess of TMH (Figure 36, p. 67). Protons were assigned accordingly (Scheme 20, p. 48). This analysis shows that the $EgtB_{cur}$ together with the $EgtB_{cur\_Y61F}$

mutant mainly produces the sulfoxide 97 % and 94 % respectively. Interestingly, the $EgtB_{cur\_Y388F}$ mutant forms a similar amount of the sulfoxide as of the γGluCys sulfinic acid (52:48 %), in contrast to the $EgtB_{1\_Y377F}$ mutant which mainly has dioxygenase activity. Moreover, the double mutant $EgtB_{cur\_Y61F\_Y388F}$ mostly forms γGluCys sulfinic acid, yet still exhibits the sulfoxide synthase activity (18 %) in contrary to the double mutant of $EgtB_{2\_Y93F\_Y94F}$, which exhibits only dioxygenase activity.

Kinetic analysis of sulfoxide synthase activity in the $EgtB_{cur}$ variants shows that the $EgtB_{cur\_Y61F}$ mutant is as active as the wild-type, suggesting that Y61 is not important for catalysis or oxygen binding (Table 15). It is possible that the Y61 side chain might be placed not towards the metal center, but somewhere else. As the crystal structure of $EgtB_{cur}$ is not solved yet, we cannot make a precise conclusion. The $EgtB_{cur\_Y388F}$ mutant has a loss in the activity of 7-fold and 27-fold decrease in catalytic efficiency, which is not surprising because the product distribution changed in the mutant and the sulfoxide concentration dropped to 52 %. However, the $EgtB_{cur\_Y388F}$ mutant did not have such a dramatic effect on the catalytic parameters and product distribution as the mutation of the corresponding residue in $EgtB_1$ and $EgtB_2$. One possibility could be that Y61 in the $EgtB_{cur\_Y388F}$ mutant can replace the role of Y388, thus protonating the iron(III)-superoxo species. To test this, the sulfoxide synthase activity of the double mutant $EgtB_{cur\_Y61F\_Y388F}$ was measured. Surprisingly, the double mutant was almost as active as the $EgtB_{cur\_Y388F}$ mutant, suggesting that Y61 cannot replace the role of Y388.

Table 15. Catalytic parameters of $EgtB_{cur}$ variants on the sulfoxide synthase activity. γGluCys is varied.

Enzyme	k_{cat}, s^{-1}	K_M, 10^{-6} M	k_{cat}/K_M, s^{-1} M^{-1}
$EgtB_{cur}$	0.2 ± 0.01	88 ± 3	2300 ± 100
$EgtB_{cur\_Y61F}$	0.22 ± 0.01	73 ± 3	3100 ± 200
$EgtB_{cur\_Y388F}$	0.028 ± 0.005	340 ± 80	85 ± 35
$EgtB_{cur\_Y61F\_Y388F}$	0.018 ± 0.001	190 ± 20	100 ± 10

Three different EgtB enzymes were identified containing different catalytic acids in the active site: $EgtB_1$ – Y377 and Q55, $EgtB_2$ – Y93 and Y94, $EgtB_{cur}$ – Y388 and Y61 (Figure 35, Table 16). Y61 and Y388 residues control the substrate specificity of the $EgtB_{cur}$, but not as strictly as their analogues in $EgtB_1$ or $EgtB_2$. The reason for this might be in a more acidic active site of the $EgtB_{cur}$ than $EgtB_1$. We have shown that the sulfoxide synthase activity of the $EgtB_{1\_Y377F}$ mutant is sensitive toward the pH, thus the acidity of the active site might influence the product distribution of EgtB-catalyzed reaction. Furthermore, the Y61 residue might not be a catalytic acid and $EgtB_1$ analogues require only one catalytic acid in the active site, due to the efficient oxygen binding through the tunnel. We observed that $EgtB_2$ requires Y94 for oxygen binding. Later, confirmed by the crystal structure of $EgtB_2$, solved by Anja Stampfli (unpublished data), no oxygen tunnel was identified in this protein, instead there is a flexible loop with might change the conformation upon oxygen binging. Therefore, one possibility could be that sulfoxide synthases with an oxygen tunnel require only one

catalytic acid for the protonation of iron(III)-superoxo species, whereas enzymes without the oxygen tunnel demand a second catalytic acid to favor with oxygen binding.

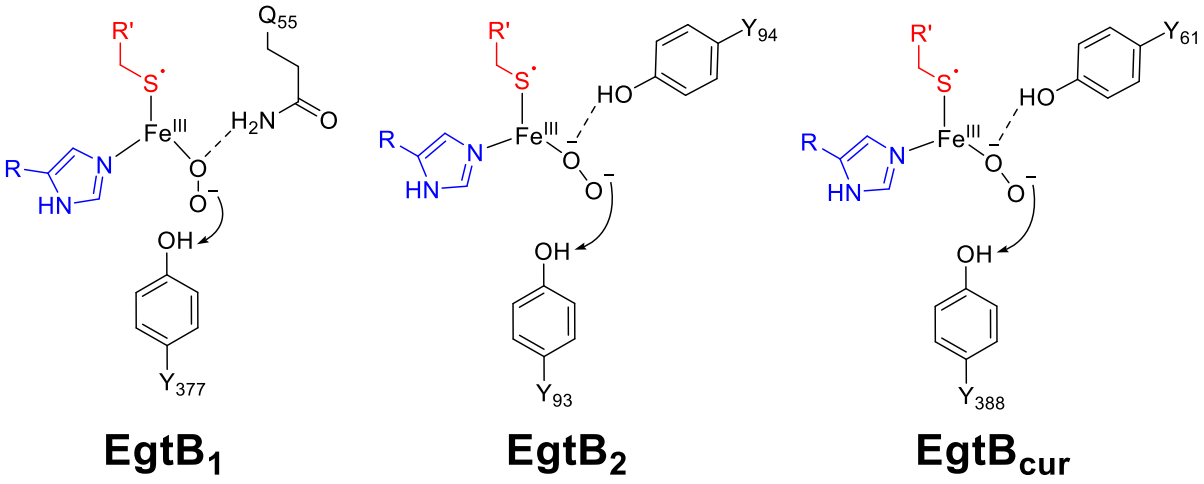

Figure 35. Proposed catalytic acids of the described sulfoxide synthases. $EgtB_1$ shows Y377 and Q55, $EgtB_2$ – Y93 and Y94, $EgtB_{cur}$ – Y388 and Y61.

Table 16. Comparative table combines kinetic and NMR analyses of EgtB variants.

Enzyme	Sulfoxide formation		%Sulfoxide/ Sulfinic acid	Cysteine consumption	
	k_{cat}, s^{-1}	k_{cat}/K_M, M^{-1} s^{-1}		k_{cat}, s^{-1}	k_{cat}/K_M, M^{-1} s^{-1}
$EgtB_1$	0.9	20000	99:1	-	-
$EgtB_{1\_Y377F}$	0.0012	65	1:99	1	7700
$EgtB_2$	0.2	3200	80:20	0.14	5200
$EgtB_{2\_Y93F}$	0.0004	90	1:99	0.16	1400
$EgtB_{2\_Y94F}$	0.003	80	1:99	0.021	600
$EgtB_{2\_Y93F\_Y94F}$	N.D.	N.D.	0:<99.9	0.049	550
$EgtB_{cur}$	0.2	2300	97:3	-	-
$EgtB_{cur\_Y61F}$	0.22	3100	94:6	-	-
$EgtB_{cur\_Y388F}$	0.028	85	52:48	-	-
$EgtB_{cur\_Y61F\_Y388F}$	0.018	100	18:82	-	-

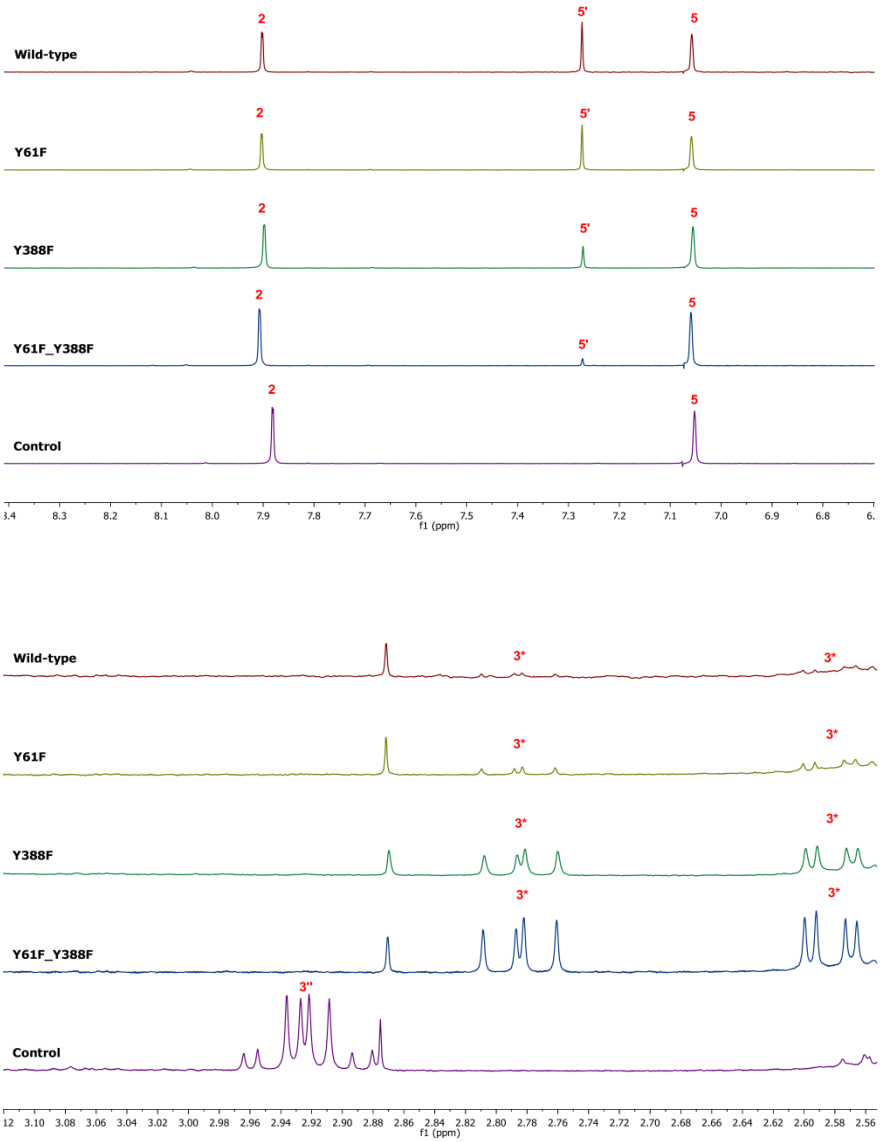

Figure 36. The product of $EgtB_{cur}$ variants catalyzed γGluCys consumption was identified as cysteine sulfinic acid by ^{1}H NMR. Reactions containing 100 mM sodium phosphate buffer pH 8.0, 100 mM NaCl, 2 mM ascorbate, 4 µM $FeSO_4$, 2 mM TCEP, 1 mM TMH, 0.5 mM γGluCys and 1 µM $EgtB_{cur}$ variant were incubated for 12 h at 26 °C. A reaction containing no enzyme was used as control experiment. The reactions were lyophilized, the residue was dissolved in D_2O. Top: aromatic region, bottom: aliphatic region. Highlighted peak was present in the starting materials.

3.4. Conclusions

This Chapter provides examples of how rational design can be applied to engineer an enzyme with a completely different reaction type than the parent enzyme and use of this strategy to probe the enzyme mechanism. The presented data identifies catalytic residues in the sulfoxide synthase, EgtB. In $EgtB_1$ from *Mycobacterium thermoresistibile* Y377 was identified as a crucial catalytic residue. Mutation of this residue to phenylalanine did not affect oxygen binding or activation, however changed the main activity of the $EgtB_{1\_Y377F}$ mutant to dioxygenation. The remaining sulfoxide

synthase activity of the $EgtB_{1\_Y377F}$ mutant is characterized by an increased KSIE and significant dependence on buffer pH.

In $EgtB_2$, two tyrosine residues Y93 and Y94 were identified. Y93 has a similar role as Y377 of $EgtB_1$ and Y94 is responsible for oxygen binding. Furthermore, protonation by a tyrosine residues of the iron(III)-superoxo species in $EgtB_1$ (Y377) and $EgtB_2$ (Y93) is essential to drive the reaction towards sulfoxide synthesis. Mutation of the following tyrosine to phenylalanine makes this protonation step more difficult and instead dioxygenation takes place. In addition, the $EgtB_1$ analogue containing two tyrosine residues in the active site ($EgtB_{cur}$) was characterized.

Overall, all described EgtB's have not only sulfoxide synthase activity, but also dioxygenase activity, which can be triggered by the mutation of a single tyrosine residue in the active site. Considering that there are structural and functional similarities between the active sites of CDO and EgtB, we propose that both reaction pathways proceed through at least one common catalytic intermediate – an iron(III)-superoxo species.

3.5. Experimental

Sequence of $EgtB_2$:

GSSHHHHHHSSGLVPRGSHMGVAVPHRAELARQLIDARNRTLRLVDFDDAELRRQY
DPLMSPLVWDLAHIGQQEELWLLRGGDPRRPGLLEPAVEQLYDAFVHPRASRVHLPLLSPAQ
ARRFCATVRSAVLDALDRLPEDADTFAFGMVVSHEHQHDETMLQALNLRSGEPLLGSGTALP
PGRPGVAGTSVLVPGGPFVLGVDLADEPYALDNERPAHVVDVPAFRIGRVPVTNAEWRAFID
DGGYRQRRWWSDAGWAYRCEAGLTAPQFWNPDGTRTRFGHVEDIPPDEPVQHVTYFEAEA
YAAWAGARLPTEIEWEKACAWDPATGRRRRYPWGDAAPTAALANLGGDALRPAPVGAYPA
GASACGAEQMLGDVWEWTSSPLRPWPGFTPMIYQRYSQPFFEGAGSGDYRVLRGGSWAVA
ADILRPSFRNWDHPIRRQIFAGVRLAWDVDRQTARPGPVGGC

Sequence of $EgtB_{cur}$:

GSSHHHHHHSSGLVPRGSHMAALTTVDEDDLKELIAAELEAVRRRSLGLTTEALPPGE
LTAQVSPLMSPLVWDLAHVGNYEELWLLRAAAGAEPMRPEIDHLYNAFEHPRAERPSLPLLP
PDEARAYIATVRAKVLDSLAKVPLREDDPLTAGGFVYGMVVQHEHQHDETMLATHQLRKG
APALLDAGEPPPAPGGAAAEPEVLIEAGPFEMGTSDEPWAYDNERPAHIVDLPAYYIDTYPVT
NRAYLAFMEAGGYEDPRWWHPEGWRWRSRHNRTAPGFWRREGGQWLRRRFGRIEPVPMD
EPVQHVSWYEADAYARWAGKRLPSEAEWEKAARWDPAAQRSRRFPWGDVYEEGRANLGQ
RRLRPAPVGSYPQGASAYGVQQMLGDVWEWTSSDFTGYPGFRAFPYKEYSQVFFGPEYKVL
RGGSWATHPLAVRGTFRNWDFPIRRQIFTGFRCARDAAR

EgtB variants. All mutants were constructed by primer extension using the following primers. The resulting fragments were cloned into pET28 vectors. For protein crystallization we cloned the $EgtB_1$ gene into a modified vector pET19m to encode an EgtB fusion construct with an N-terminal His_6-tag followed by a TEV (tobacco etch virus) protease cleavage site.

Table 17. Primer sequences used for the mutation of the EgtB variants.

Primer	Sequence 5' – 3'
$EgtB_1$	
$EgtB_1$_for	TATACATATGGGTGTCGCCGTGC
$EgtB_1$_rev	ATATCTCCGAGCTAACAACCACCCACCGG
Y377F_for	TATAGCCGATGATTTTTCAGCGCTACA
Y377F_rev	TATATGTAGCGCTGAAAAATCATCGGC
$EgtB_2$	
Y93F_for	ACATCTTCAACTCTTTTTACGAAGCGGTTGGT
Y93F_rev	ACCAACCGCTTCGTAAAAAGAGTTGAAGATGT
Y94F_for	ACATCTTCAACTCTTATTTTGAAGCGGTTGGT
Y94F_rev	ACCAACCGCTTCAAAATAAGAGTTGAAGATGT
Y93F_Y94F_for	ACATCTTCAACTCTTTTTTTGAAGCGGTTGGT
Y93F_Y94F_rev	ACCAACCGCTTCAAAAAAAGAGTTGAAGATGT
$EgtB_{cur}$	
Y61F_for	GCCCACGTTGGTAACTTTGAAGAACTGTGG
Y61F_rev	CCACAGTTCTTCAAAGTTACCAACGTGGGC
Y388F_for	TTTCGCGCGTTCCCGTTTAAAGAATACAGC
Y388F_rev	GCTGTATTCTTTAAACGGGAACGCGCGAAA

Recombinant enzyme production. All EgtB variants were produced and purified following previously described protocols (2.5).

Table 18. Calculated and observed molecular weights of proteins.

Protein	m/z, calc., Da	m/z, obs., Da	Delta, Da
$EgtB_1$	51343	51374 51550	31 (oxidation) 207 (gluconoylation, oxidation)[93]
$EgtB_{1\_Y377F}$	51327	51358	32 (oxidation)
$EgtB_2$	51131	51130 51307	1 176 (gluconoylation)
$EgtB_{2\_Y93F}$	51115	51291	176 (gluconoylation of His Tag)
$EgtB_{2\_Y94F}$	51115	51291	176 (gluconoylation of His Tag)
$EgtB_{2\_Y93F\_Y94F}$	51099	51100 51275	1 176 (gluconoylation of His Tag)
$EgtB_{cur}$	52234	52235	1
$EgtB_{cur\_Y61F}$	52218	52217	1
$EgtB_{cur\_Y388F}$	52218	52217	1
$EgtB_{cur\_Y61F\_Y388F}$	52202	52201	1

Solvent KIE. To measure the KSIE standard reaction mixture containing 100 mM HEPES, 100 mM NaCl, 2 mM TCEP, 4 µM $FeSO_4$, 2 mM ascorbate, 1 mM DMH was adjusted to pH 8.0 or 7.6 (final pD = 8.0).[94] Premixtures were lyophilized and then dissolved in H_2O or D_2O. The reactions were initiated by addition of enzyme. The final deuterium to hydrogen ratio was estimated to be at least 8.5:1.

Michaelis-Menten analysis/Enzyme assay. Enzyme activities were assayed in 100 mM sodium phosphate buffer containing 100 mM NaCl, 2 mM TCEP, 2 mM ascorbate, 4 eq. of $FeSO_4$, TMH and enzyme. Reactions were started by addition of γGC or Cys and incubated at 26°C. Aliquots of the reactions were quenched by addition of 20 µL 1 M phosphoric acid and analyzed by cation exchange HPLC using 20 mM phosphoric acid at pH 2 as a mobile phase.[70] Compounds were eluted in a NaCl gradient. All HPLC chromatograms were recorded at 265 nm. The data were fitted to the function $v = V_{max}[s]/(K_M + [s])$. Michaelis-Menten plots are shown below. k_{cat} and k_{cat}/K_M were determined in the presence of the second substrate at a concentration at least 3-fold higher than K_M of the second substrate. The data displayed corresponds to averages from two to three independent enzyme reactions.

γGC dioxygenase activity (marked as *), was quantified by monitoring consumption of γGC or Cys. For HPLC based quantification of γGC the 40 µL reaction aliquots were quenched by addition of 40 µL acetonitrile and 10 µL of 20 mM 4-bromomethyl-7-methoxycoumarin (BMC) in DMSO.

After incubation for 30 min the mixture was diluted with one volume equivalent of 0.1% TFA solution. Coumarin–adducts (Scheme 26) were quantified by RP-HPLC by absorbance at 330 nm.

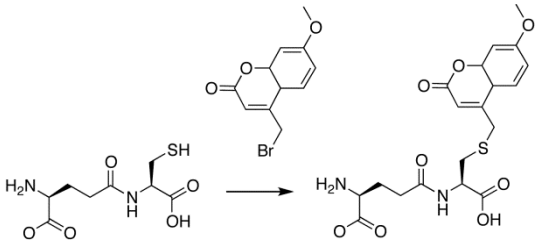

Scheme 26. Formation of methyl-7-methoxycoumarin adduct of γGC.

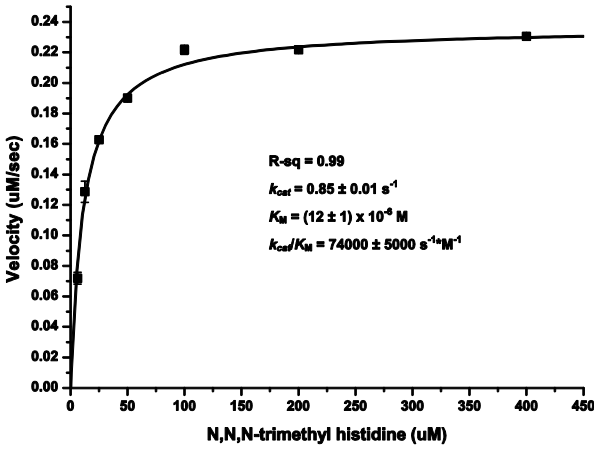

phosphate buffer, pH 8.0 $EgtB_1$, [γGC] = 1200 µM

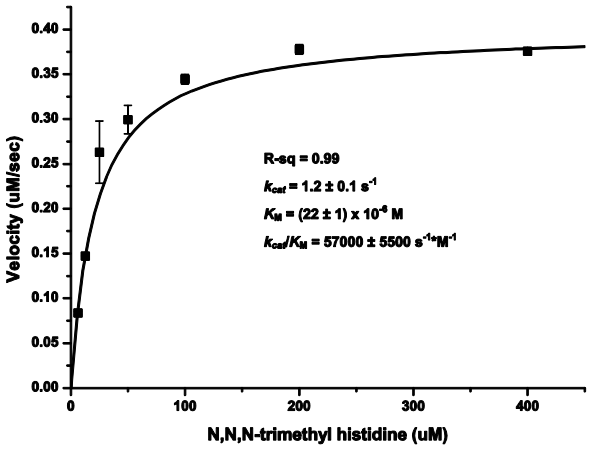

phosphate buffer, pH 6.0 $EgtB_1$, [γGC] = 1200 µM

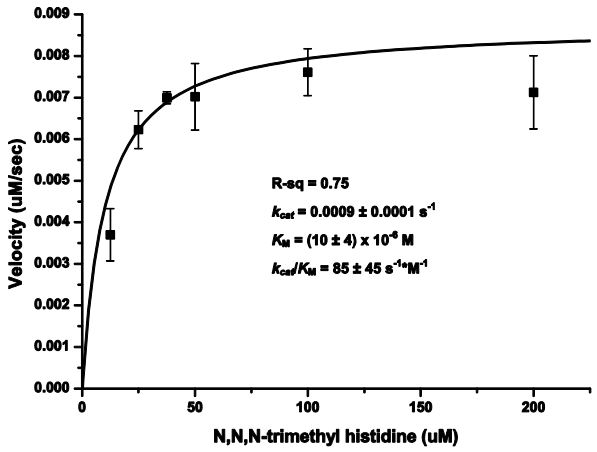

phosphate buffer, pH 8.0 $EgtB_{1\_Y377F}$, [γGC] = 1200 µM

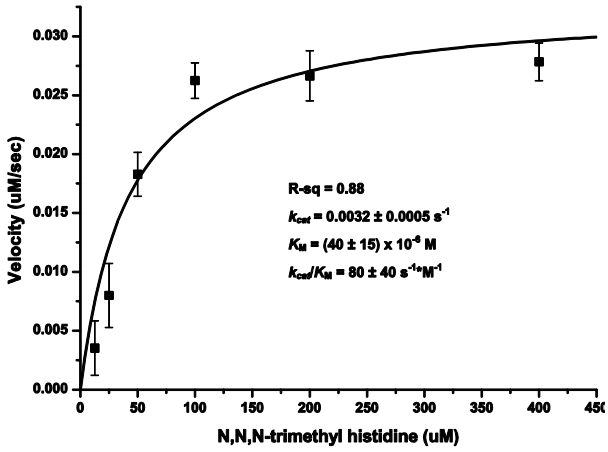

phosphate buffer, pH 6.0 $EgtB_{1\_Y377F}$, [γGC] = 1200 µM

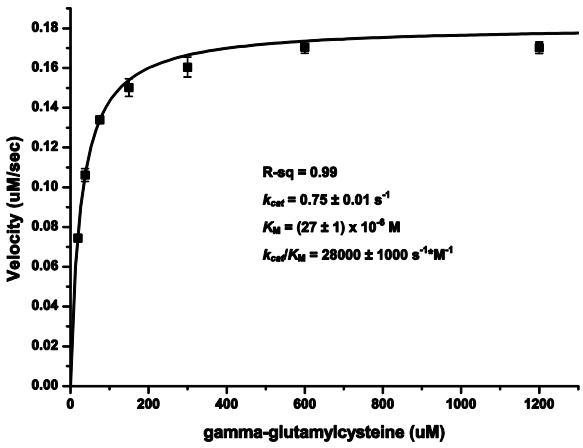

phosphate buffer, pH 8.0 $EgtB_1$,
[TMH] = 400 µM

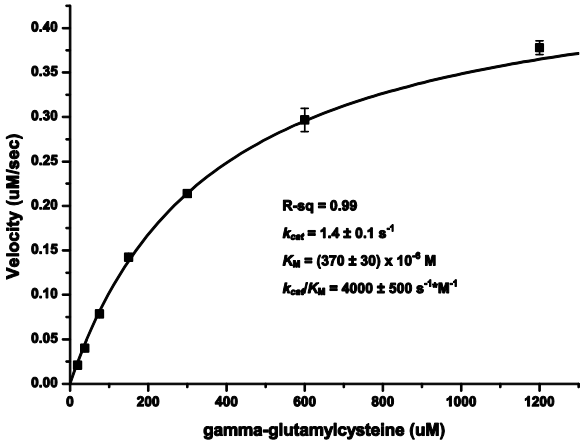

phosphate buffer, pH 6.0 $EgtB_1$,
[TMH] = 400 µM

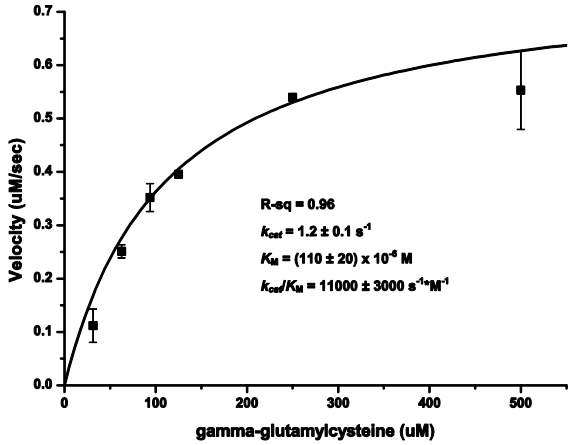

*phosphate buffer, pH 8.0 $EgtB_{1\_Y377F}$,
[TMH] = 400 µM

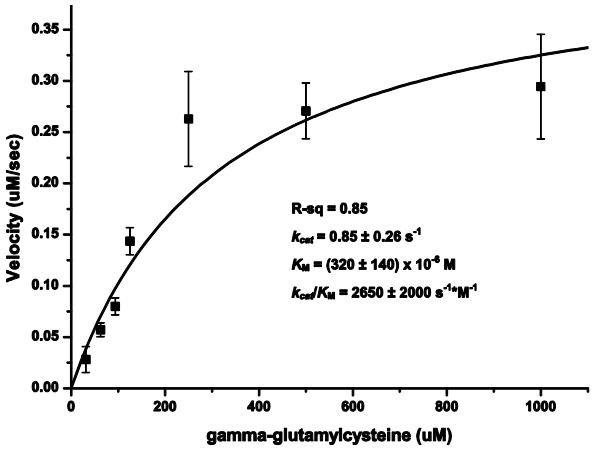

*phosphate buffer, pH 6.0 $EgtB_{1\_Y377F}$,
[TMH] = 400 µM

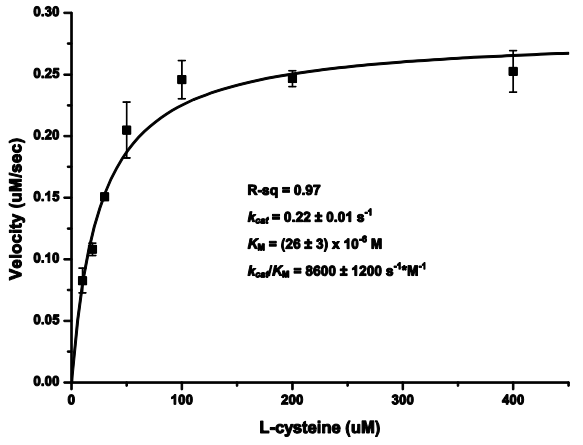

phosphate buffer, pH 8.0 $EgtB_2$,
[TMH] =200 µM

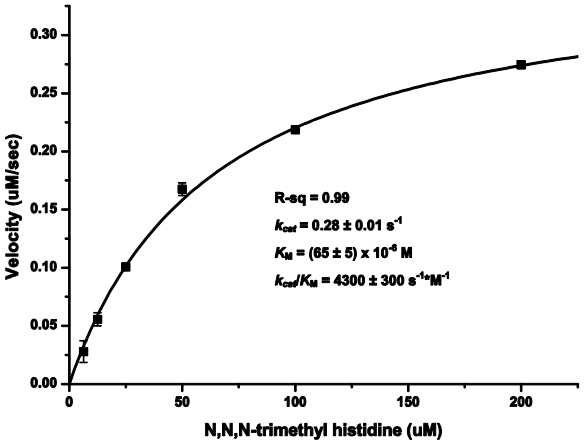

phosphate buffer, pH 8.0 $EgtB_2$,
[Cys] = 500 µM

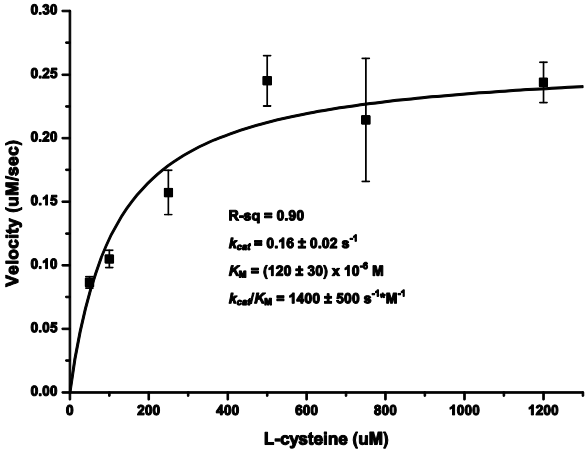

*phosphate buffer, pH 8.0 $EgtB_{2\_Y93F}$,

[TMH] = 500 µM

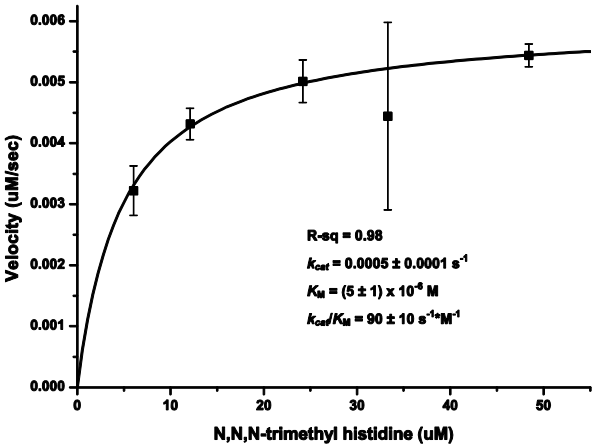

phosphate buffer, pH 8.0 $EgtB_{2\_Y93F}$,

[Cys] = 2 mM

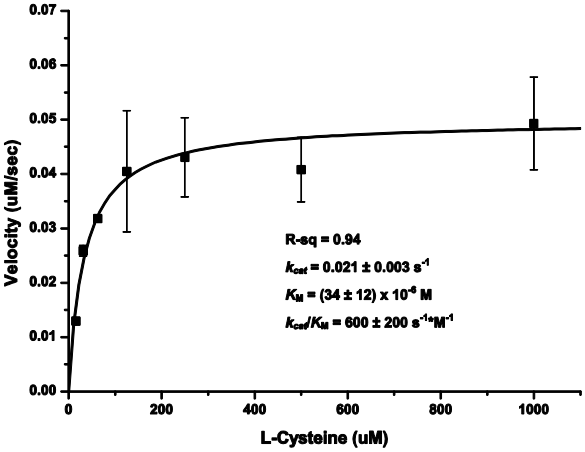

*phosphate buffer, pH 8.0 $EgtB_{2\_Y94F}$,

[TMH] = 500 µM

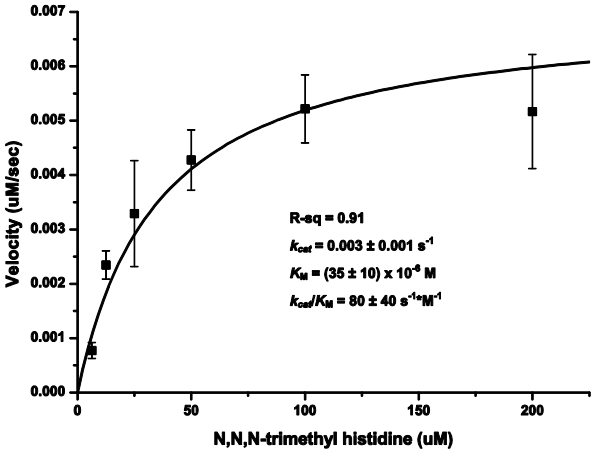

phosphate buffer, pH 8.0 $EgtB_{2\_Y94F}$,

[Cys] = 1 mM

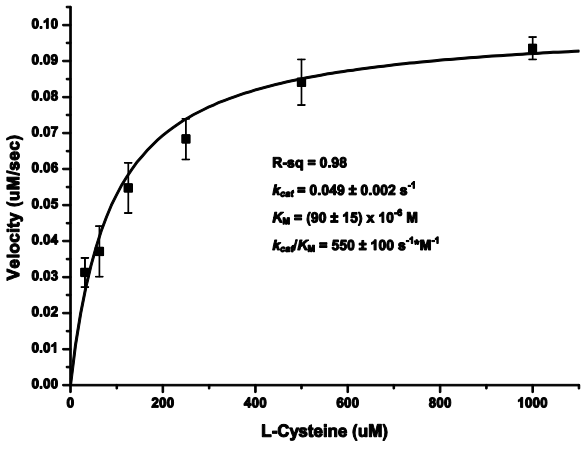

*phosphate buffer, pH 8.0 $EgtB_{2\_Y93F\_Y94F}$,

[TMH] = 500 µM

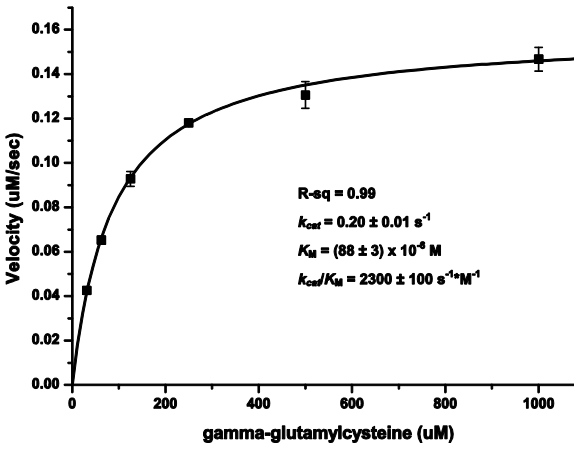

phosphate buffer, pH 8.0 $EgtB_{cur}$,

[TMH] = 1 mM

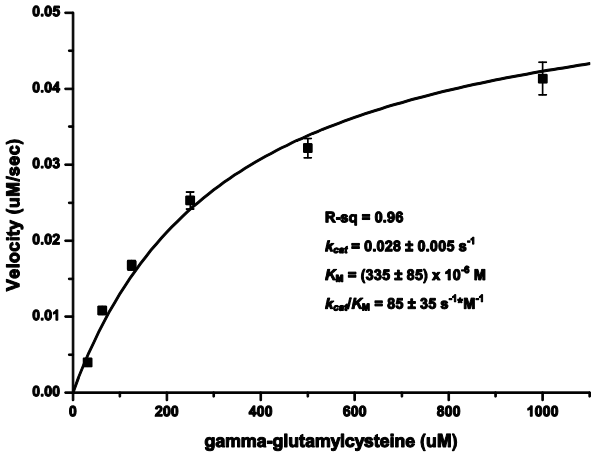

phosphate buffer, pH 8.0 $EgtB_{cur\_Y388F}$,

[TMH] = 1 mM

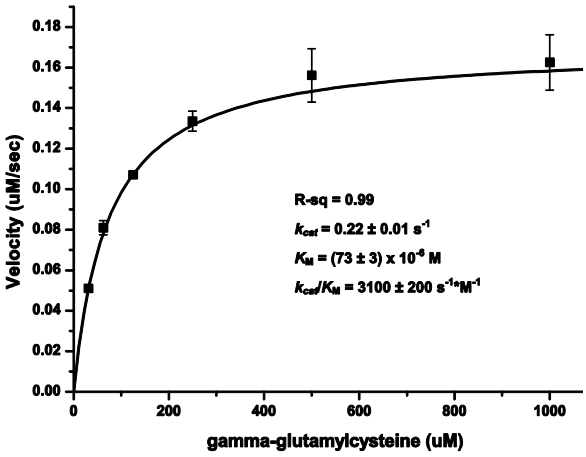

phosphate buffer, pH 8.0 $EgtB_{cur\_Y61F}$,

[TMH] = 1 mM

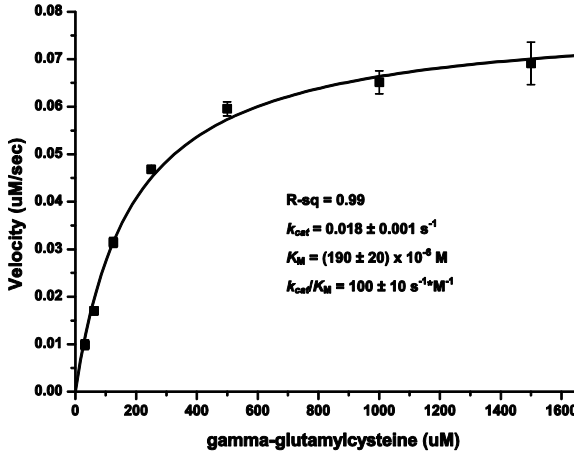

phosphate buffer, pH 8.0 $EgtB_{cur\_Y61F\_Y388F}$,

[TMH] = 1 mM

3.6. Appendix

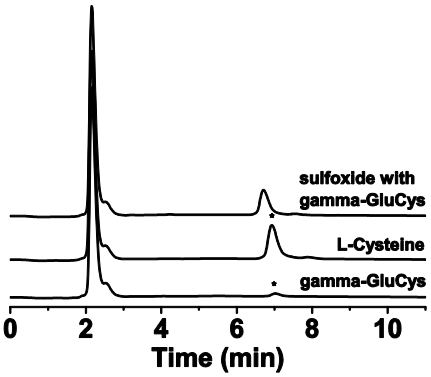

Figure 37. $EgtB_2$ catalyzes the sulfoxide formation with cysteine as a sulfur donor. HPLC traces were recorded at 265 nm. The sulfoxide product has a retention time of 7 minutes. Peak marked (*) is the sulfoxide with cysteine used as a substrate, in case of γ-glutamylcysteine small amount of the sulfoxide was formed due to presence of cysteine in the stock solution of γ-glutamylcysteine. A reaction mixture containing 100 mM phosphate buffer pH 8.0, 100 mM NaCl, 2 mM TCEP, 2 mM ascorbate, 4 μM $FeSO_4$, 1 mM N^{α},N^{α},N^{α}-trimethyl-L-histidine, 1 mM L-cysteine or γ-glutamylcysteine and 1 μM $EgtB_2$ was incubated for 30 minutes at 26°C.

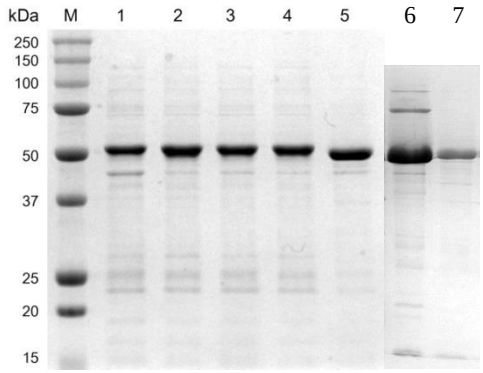

Figure 38. SDS-page picture of EgtB variants after Ni-NTA affinity chromatography. M – Molecular weight marker; 1 – $EgtB_2$; 2 – $EgtB_{2\_Y93F}$; 3 – $EgtB_{2\_Y94F}$; 4 – $EgtB_{2\_Y93F\_Y94F}$; 5 – $EgtB_{1\_Y377F}$; 6 – $EgtB_{cur}$; 7 – $EgtB_{cur}$.

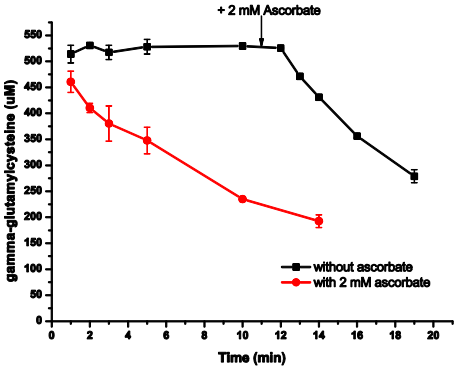

Figure 39. Effect of supplemental ascorbic acid on progress curves for $EgtB_{1\_Y377F}$. A reaction mixture contains 100 mM sodium phosphate buffer pH 8.0, 100 mM NaCl, 0/2 mM ascorbate, 2 µM $FeSO_4$, 2 mM TCEP, 0.4 mM N^{α},N^{α},N^{α}-trimethyl-L-histidine, 0.55 mM γ-glutamyl cysteine, 0.6 µM $EgtB_{1\_Y377F}$ from *Mycobacterium thermoresistible.*

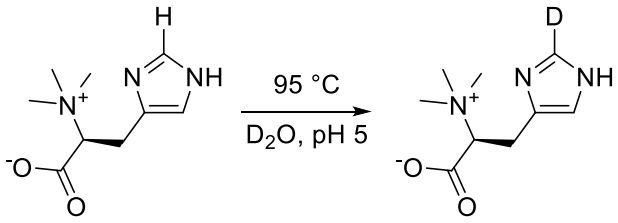

Figure 40. C2-deuterated TMH was prepared as follows: a 5 mM solution of TMH in D_2O was acidified to pD 5.0 with 20 % DCl. This solution was incubated at 90 °C for 72 h in a sealed glass vial. Specific and complete deuteration of the imidazole C2 position was confirmed by ESI-MS (m/z calc.: 199.13; meas.: 199.1) and ^1H NMR (400 MHz, D_2O) δ ppm 7.26 (s, 1H), 3.88 (dd, J = 12.0, 3.9 Hz, 1H), 3.44 – 3.24 (m, 2H), 3.23 (s, 9H).

4. Selenocysteine is an excellent mechanistic probe, but a poor substrate for the sulfoxide synthase EgtB

Ergothioneine (ET), a 2-mercapto-L-histidine betaine, is a dietary component capable of acting as antioxidant and cytoprotectant.[62a, 64, 95] The exact physiological role of ET is not clear yet, however, recent studies *in vitro* have demonstrated that ET is a powerful scavenger of reactive oxygen species (ROS), such as hydroxyl radicals and superoxide anion. Moreover, ET is able to bind transition metal ions in forms unable to catalyze redox reactions.[96] Currently, there are a plethora of studies on ET identifing new perspectives in targeted therapies to prevent endothelial dysfunction or defense against ROS in diabetes.[97] In fact, ET has been known for its antioxidant properties for over many years.[64]

Recently, the selenium analogue of ET, so-called selenoneine, was identified by Yamashita *et al.* in the blood of the bluefin tuna, *Thunnus orientalis*.[98] Selenoneine appeared to be the major selenium-containing compound in tissues of several species of fish and there was a strong correlation between physiological concentrations of selenoneine and environmental mercury levels, suggesting that selenium is involved in reduction of methylmercury toxicity.[99] Furthermore, selenoneine has a strong antioxidant capacity and binds to haem proteins, such as hemoglobin and myoglobin, to protect them from iron auto-oxidation [100] A methylated form of selenoneine, Se-methylselenoneine, has also been isolated from human blood and urine where it was thought to result from the ingestion of selenoneine derived from fish sources, and then further methylated in the kidneys or liver by a methyltransferase.[101]

Since the discovery of selenoneine, its biosynthetic pathway has remained unclear. *In vivo* studies by Pluskal *et al.* revealed that in the fission yeast, *S. pombe*, selenoneine could be produced by the enzymes from ergothioneine biosynthetic pathway, when selenium was supplemented in the culture medium.[102] In the ET biosynthetic pathway, the key enzyme EgtB catalyzes oxidative C-S bond formation, resulting in the sulfoxide intermediate.[1] However, in the mutant strain of *S. pombe*, which lacks β-lyase, accumulation of not oxidized compound – hercynylselenocysteine was detected (Scheme 27).[102] Any signal of the presumed intermediate, hercynyl-selenocysteine sulfoxide was observed. Therefore, Pluskal *et al.* proposed that the ergothioneine pathway can also synthesize selenoneine and that selenoneine biosynthesis involves a novel intermediate compound, hercynylselenocysteine.

To determine whether selenoneine is synthetized by the ergothioneine biosynthetic pathway, we investigated the ability of the sulfoxide synthase EgtB to catalyze an *in vitro* reaction with a selenium-substituted substrate.

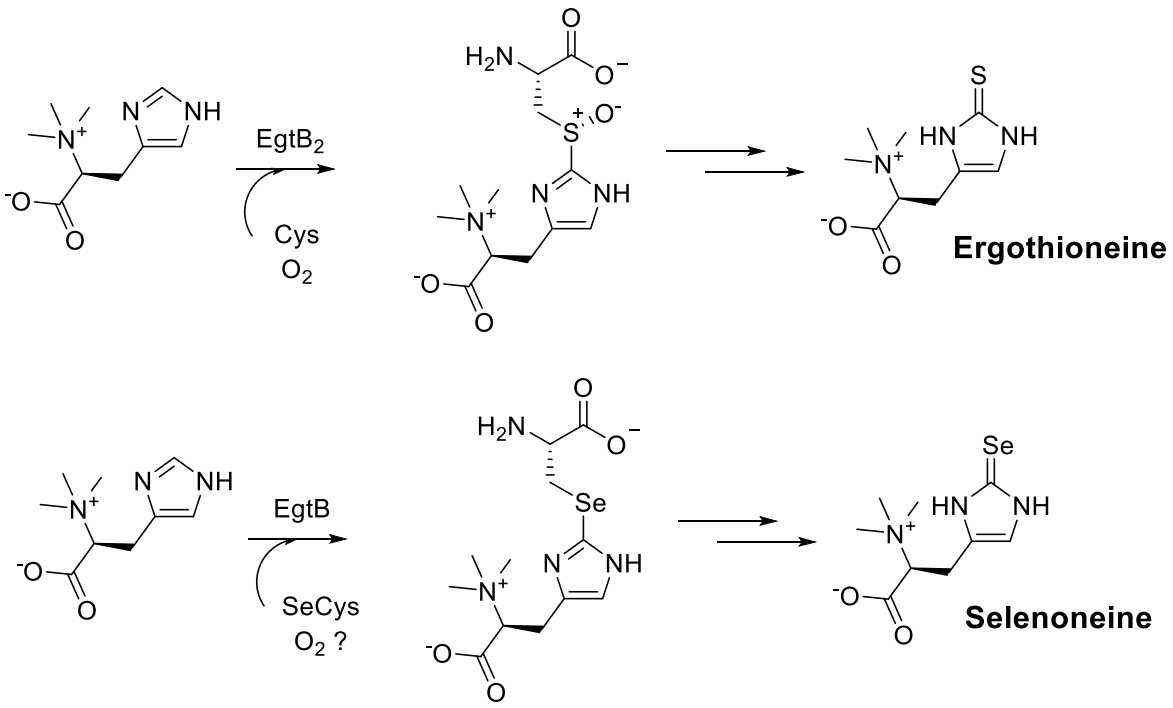

Scheme 27. $EgtB_2$-catalyzed sulfoxide formation, which is an intermediate in the ergothioneine biosynthetic pathway. In the fission yeast *S. pombe* grown in selenium-supplemented culture medium, hercynylselenocysteine was detected which could be further oxidized to selenoneine by β-lyase.[102]

4.1. Selenocysteine as a substrate for EgtB from *Candidatus chloracidobacterium thermophilum B*

The sulfoxide synthase $EgtB_2$ catalyzes sulfoxide formation using cysteine and TMH as substrates. Considering the findings by Pluskal *et al.*, that selenocysteine is made in the fission yeast *S. pombe* by the enzymes from ergothioneine biosynthetic pathway, we tested the *in vitro* activity of $EgtB_2$ when the substrate cysteine was exchanged with selenocysteine (SeCys).[102] If selenoneine is produced naturally by the enzymes from the ergothioneine biosynthetic pathway, selenium-substituted substrates should have a comparable activity to the natural occurring sulfur analogues. Overall, selenium and sulfur share many features, including size, electronegativity and major oxidation states. However, there is a difference in their nucleophilic character: selenium is more nucleophilic than sulfur and is more polarizable, making it a softer nucleophile. Further differences lie in selenols and thiols; selenols are more acidic (pKa ~ 5.2) than thiols (pKa ~ 8.3), which makes selenocysteine more reactive than cysteine at physiological pH. Additionally, the reduction potential for selenocysteine is lower than that of cysteine due to the greater electron donating capacity of selenium compared to sulfur.[103]

First, the standard reaction mixture for $EgtB_2$ containing selenocysteine instead of cysteine, was probed for the selenoxide synthase activity. However, HPLC analysis did not reveal any detectable amounts of selenoxide being formed (detection limit = 0.1 µM). Reasons for the absence of

detectable amounts of selenoxide might be product inhibition or the fast side reaction of selenocysteine sulfinic acid, peroxide or superoxide formation.[13] If the enzyme has an off-path reaction, the consumption of the substrate or one of the reducing agents would be increased. Therefore, at different enzyme concentrations the consumption of SeCys, TCEP and ascorbate were monitored (Figure 41).

The rates at which $EgtB_2$ was consuming SeCys were measured. The concentration of SeCys was monitored at standard reaction conditions, and showed that SeCys undergoes auto-oxidation at an initial rate of 3.7 ± 0.3 µM/min. An addition of up to 10 µM of $EgtB_2$ did not increase this rate. This result suggests that if $EgtB_2$ catalyzes irreversible SeCys consumption, it should be slower than 10^{-3} s^{-1}. The alternative electron donors present in the reaction mixtures, TCEP and ascorbate, were also not consumed at a measurable rate (k_{obs} < 0.01 s^{-1}). The substitution of Cys with SeCys as an $EgtB_2$ substrate suppresses oxygen activation by at least 20-fold. One possibility could be that SeCys cannot bind to $EgtB_2$ or SeCys-bound $EgtB_2$ cannot react with O_2.

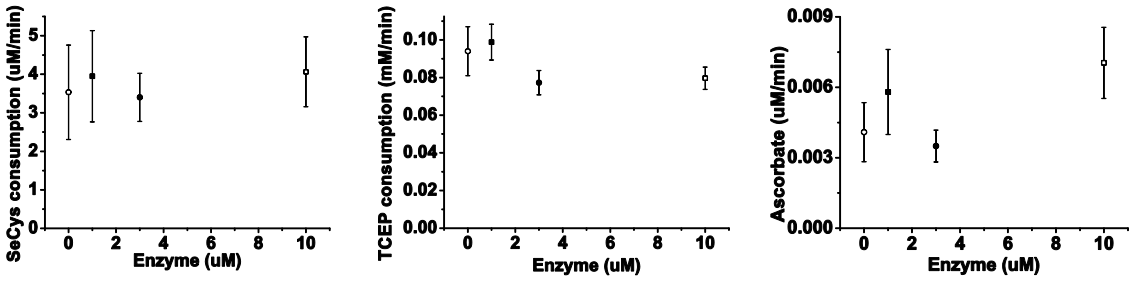

Figure 41. Selenocysteine, TCEP and ascorbate consumption at the different concentrations of $EgtB_2$ detected by derivatization with BMC at 330 nm. There was no significant selenocysteine consumption at the high enzyme concentrations. A reaction mixture containing 100 mM phosphate buffer pH 8.0, 100 mM NaCl, 2 mM ascorbate, 2 mM TCEP, 20 µM $FeSO_4$, 500 µM Nα,Nα,Nα-trimethyl-L-histidine, 500 µM L-cysteine and (0 – 10) µM $EgtB_2$ added last to a final volume of 250 µL. The reaction mixtures were incubated at 26 °C. At 3, 6, 10 15 and 20 min 40 µL aliquots of the reaction mxiture were quenched by addition of 40 µL acetonitrile. 10 µL of 20 mM 4-bromomethyl-7-methoxycoumarin (BMC) in DMSO was added and allowed to react for 30 minutes at room temperature in the dark. 60 µL of the reaction mixture was diluted two-fold by addition of 60 µL 0.1% trifluoroacetic acid and analyzed by HPLC.

In order to determine whether SeCys binds to the active site of $EgtB_2$, inhibition kinetics assays were performed with respect to Cys and TMH. The binding order of $EgtB_2$ was determined by performed a standard set of experiments for a bi-substrate system, where the K_M was determined for one substrate while varying the concentration of the second substrate (TMH or Cys) (Figure 42, p. 79). Plotting this data in form of Lineweaver-Burk plots showed that SeCys behaves as a reversible competitive inhibitor with respect to Cys and characterized by a K_i of 22 µM. With respect to TMH, SeCys is a reversible uncompetitive inhibitor with a K_{ii} of 40 µM. The observed inhibition pattern suggests that $EgtB_2$ has an ordered substrate binding sequence, where TMH binds first and Cys binds to the $EgtB_2$:TMH complex (Figure 43, left). These data suggest that SeCys binds to $EgtB_2$:TMH complex as efficient as natural substrate, Cys. This binding order is in agreement with the model of

$EgtB_2$, based on $EgtB_1$ co-crystalized with TMH and γGluCys, where the binding site of cysteine is on top of TMH (Figure 43, right).

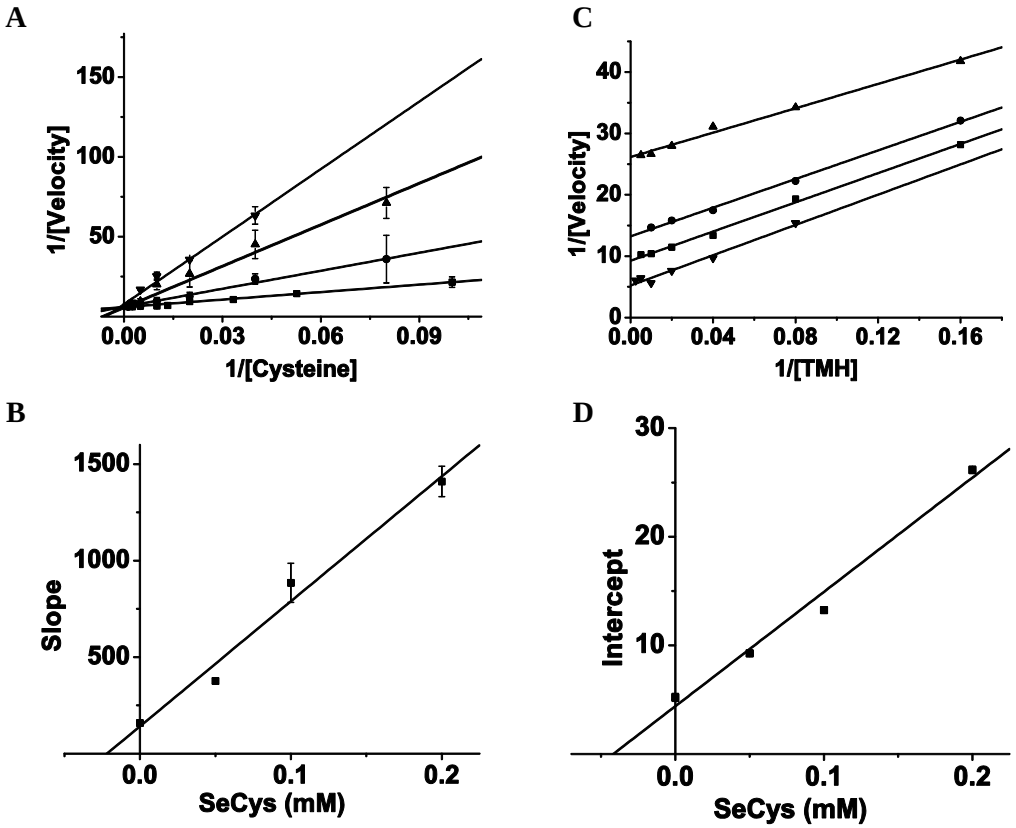

Figure 42. A) Double reciprocal plot for the competitive inhibition of $EgtB_2$-catalyzed sulfoxide formation by SeCys with Cys as variable substrate; **B)** A plot of the slopes in **A** versus SeCys concentration reveals the affinity of SeCys to the TMH bound $EgtB_2$ with a K_i of 22 µM; **C)** A double reciprocal plot for the uncompetitive inhibition of $EgtB_2$-catalyzed sulfoxide formation by SeCys with TMH as variable substrate; **D)** The plot of the intercepts in **C** versus SeCys concentration reveals K_{ii} of 40 µM The model for uncompetitive inhibition relates K_{ii} and K_i by the equation $K_{ii}=K_i$ (1+[B]/K_b), where K_b is approximated by apparent K_M for Cys (65 µM)

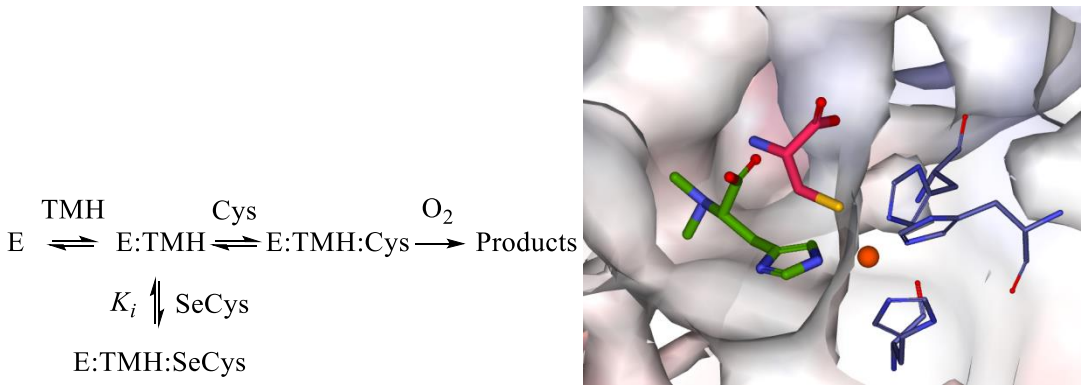

Figure 43. Left: SeCys is a competitive inhibitor with respect to Cys and uncompetitive to TMH, resulting in sequential binding order mechanism for $EgtB_2$. **Right:** The model of $EgtB_2$ shows that cysteine (pink) is bound on the top of DMH (green), which is buried at the bottom of the active site.

With the understanding that selenocysteine binds well to the active site of $EgtB_2$, but that neither selenoxide was formed, nor selenocysteine being consumed at a significant rate, the reaction mixture containing selenocysteine was examined for other products. Under the standard reaction conditions, a new product from the reaction mixture corresponding to hercynylselenocysteine which was identified by HRMS (*m/z* obs. 409.0360, calc. 409.0360), identical to the compound identified *in vivo* (Scheme 28, see Appendix, Figure 50, p. 91).[102] Furthermore, reacting this compound with β-lyase OvoB led to the formation of selenoneine, similar to the reaction of thioether with OvoB to form ergothioneine (Figure 44, left). To determine the rate of hercynylselenocysteine formation, the reaction was monitored at saturating concentrations of SeCys and TMH (Figure 45). The rate of selenoether formation of $(1.2 \pm 0.2)\ 10^{-3}\ s^{-1}$ is 170-fold slower than for $EgtB_2$ catalyzed sulfoxide formation with Cys (chapter 3.2). Interestingly, hercynylselenocysteine is an unstable compound and after one hour of incubation in the reaction mixture undergoes elimination to selenoneine, presumably by selenoxide elimination (Figure 44, right). Furthermore, during the oxidation of hercynylselenocysteine to selenoneine, no selenoxide was detected. From there observations we can conclude that $EgtB_2$ catalyzes the formation of hercynylselenocysteine in the presence of SeCys and the product further spontaneously oxidizes to selenoneine (Scheme 28).

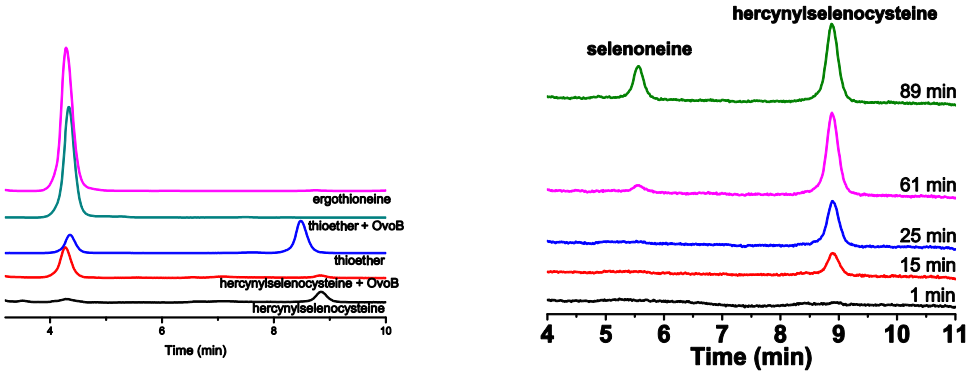

Figure 44. Left: The reaction of β-lyase OvoB with hercynylcysteine (thioether) or hercynylselenocysteine leads to the formation of ergothioneine or selenoneine, respectively. **Right:** Selenoneine is formed after one hour due to spontaneous degradation of the selenoether (absorbance measured at 265 nm).

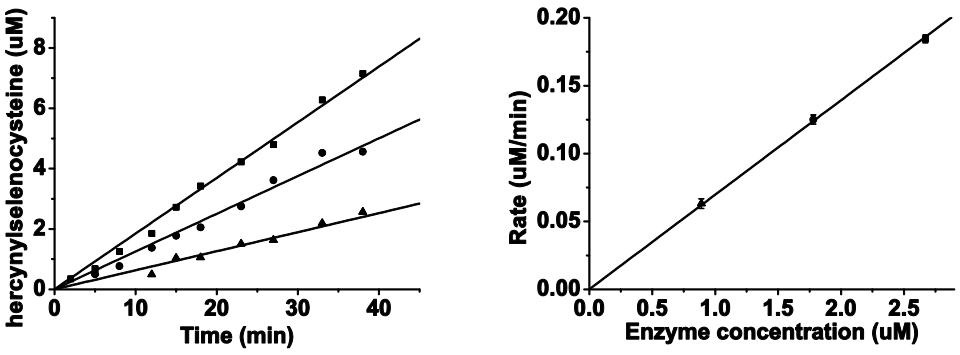

Figure 45. Left: Rate of hercynylselenocysteine formation using three different enzyme concentrations. Standard conditions for this assay were as follows: a reaction mixture containing 100 mM phosphate buffer pH

8.0, 100 mM NaCl, 2 mM ascorbate, 2 mM TCEP, 4 µM $FeSO_4$, 500 µM N^{α},N^{α},N^{α}-trimethyl-L-histidine, 500 µM L-selenocysteine and 0.9 µM (▲), 1.8 µM (●), 2.67 (■) µM $EgtB_2$ added in final volume of 250 µL. The reaction mixtures were incubated at 26°C. Aliquots of the reactions were quenched by addition of 20 µL 1 M phosphoric acid and analyzed by HPLC using the standard method. **Right:** A secondary plot of the rate of the reaction is plot against the $EgtB_2$ concentration allows determining the k_{cat} value.

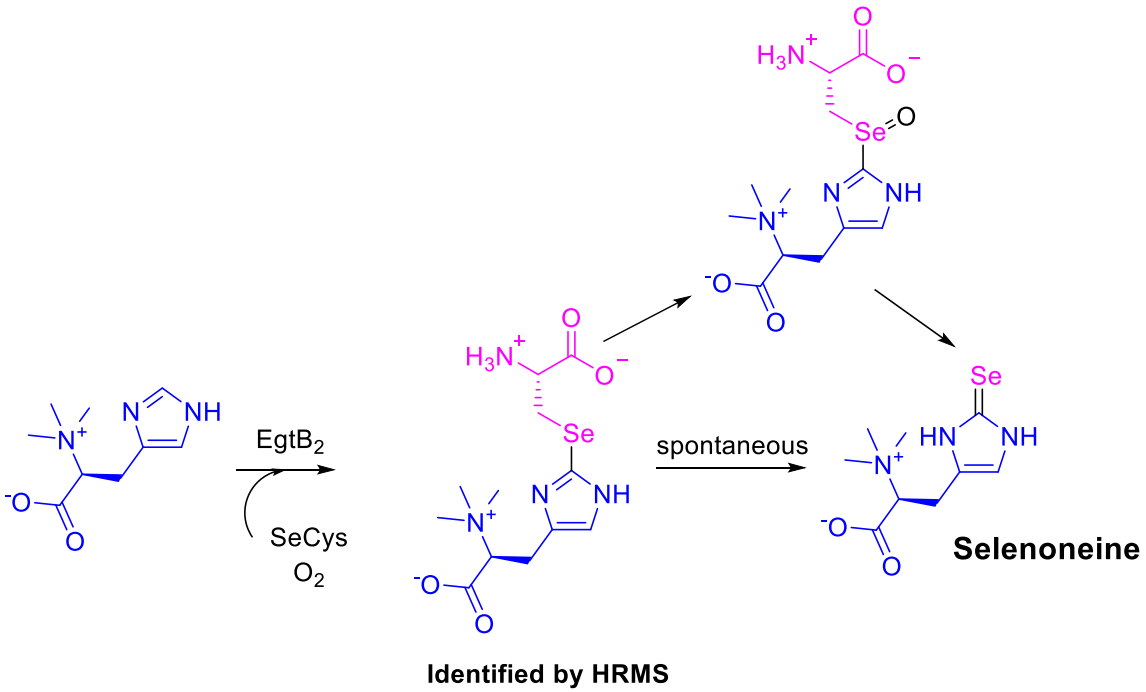

Scheme 28. $EgtB_2$ catalyzes the formation of hercynylselenocysteine in the presence of SeCys. After one hour, the compound spontaneously oxidizes to selenoneine, presumably by selenoxide elimination.

Hercynylselenocysteine instead of selenoxide was identified as a product of $EgtB_2$ reaction and identified as intermediate compound *in vivo* studies.[102] Therefore, we examined whether sulfoxide synthases, in general, do not catalyze selenoxide formation with selenium substrate congeners, or whether our observation is specific to $EgtB_2$. Rates for C-S and C-Se bond formation were compared for $EgtB_1$, $EgtB_{cur}$, $EgtB_{Chae.thermophilum}$, $OvoA_{E.tasmaniensis}$ and $OvoA_{C.reinhardii}$ (Table 19). All enzymes catalyzed the formation of hercynylselenocysteine at rates significantly slower than C-S bond formation. However, the difference between the rates of the reaction varies significantly among the sulfoxide synthases.

Table 19. Comparison between catalyzed by different sulfoxide synthases sulfoxide and Se-ether formation at the saturating conditions. A reaction mixture containing 100 mM phosphate buffer pH 8.0, 100 mM NaCl, 2 mM ascorbate, 2 mM TCEP, 20 µM $FeSO_4$, 1 mM L-histidine or TMH, 1 mM Cys/SeCys or γGluCys/γGluSeCys and ~5 µM of sulfoxide synthase added last to a final volume of 250 µL. The reaction mixtures were incubated at 26 °C. At 2, 5, 11, 17 and 25 min 40 µL aliquots of the reactions were quenched by the addition of 20 µL 1 M phosphoric acid and analyzed by HPLC using the standard method.

Sulfoxide synthase	$k_{obs,\ sulfoxide}$, s^{-1}	$k_{obs,\ Se\text{-}ether}$, s^{-1}	$k_{obs,\ sulfoxide}$ / $k_{obs,\ Se\text{-}ether}$
TMH			
$EgtB_2$	0.2	0.0012	170
$EgtB_1$	0.75	0.012	60
$EgtB_{Chae.thermophilum}$	0.06	0.002	28
$OvoA_{E.tasmaniensis}$	0.03	0.00007	470
$OvoA_{C.reinhardii}$	0.04	0.00006	570
$EgtB_{cur}$	0.2	ND	-
L-histidine			
$OvoA_{E.tasmaniensis}$	1.3	ND	-
$OvoA_{C.reinhardii}$		ND	-

All tested sulfoxide synthases catalyze formation of hercynylselenocysteine, rather than selenoxide formation, suggests that oxygen might not be involved in the catalytic cycle. A reduction potential for selenocysteine is lower than that of cysteine due to the greater electron donating capacity of selenium versus sulfur. Thus, we proposed that the Fe(III)-coordinated selenol might be largely present as a Fe(II)-coordinated selenyl radical (Scheme 29).[77] Selenyl radical might then to attack the imidazole ring resulting in C-Se bond. In order to test this mechanism, the reaction in absence of ascorbate and presence of either Fe(II) or Fe(III) was probed (Figure 46). In the presence of ascorbate all iron is present in ferrous state and significantly more active that in the absence of ascorbate, suggesting that in the resting state iron is present in a state of ferrous iron. Therefore, the mechanism represented at the Scheme 29 does not take place and the reaction most likely requires oxygen.

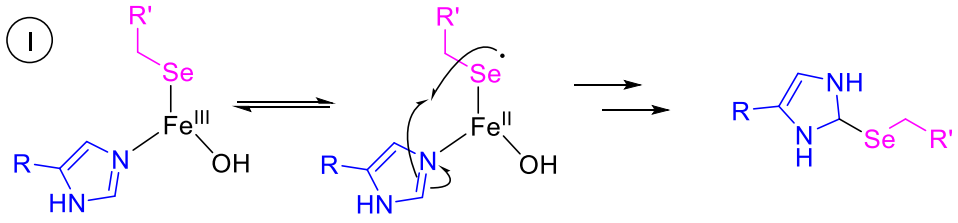

Scheme 29. The proposed mechanism of C-Se bond formation. Fe(III)-coordinated SeCys has radical character on selenium, suggesting that SeCys-coordinated complex does not require oxygen to proceed with the selenyl radical formation, which then triggers the C-Se bond formation.

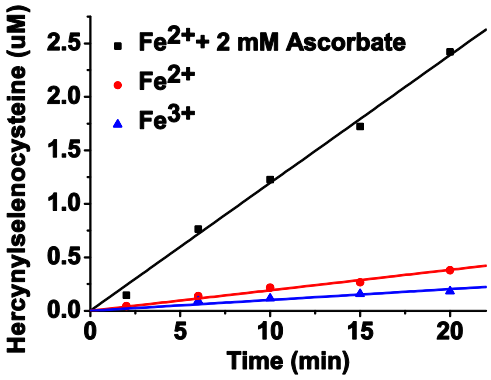

Figure 46. The formation of hercynylselenocysteine is dependent on the presence of ascorbate, suggesting that the reaction is Fe(II)-dependent. Standard conditions for this assay were as follows: a reaction mixture containing 100 mM phosphate buffer pH 8.0, 100 mM NaCl, 0/2 mM ascorbate, 2 mM TCEP, 12 µM $FeSO_4$ / $Fe_2(SO_4)_3$, 500 µM TMH, 500 µM selenocysteine and 1.7 µM $EgtB_2$ mutant were added together to final volume of 250 µL. The reactions were then analyzed by HPLC.

Taking into account that oxygen is incorporated in the catalytic cycle of hercynylselenocysteine production catalyzed by $EgtB_2$, we addressed the question why selenoether formation is significantly slower than the sulfoxide formation. We compared the active site of EgtB with cysteine dioxygenase (CDO), both enzymes contain 3-His facial triad and share similar first sphere ligands.[76] Taking into account that SeCys binding is similar to the native substrate Cys, the barrier preventing turnover could lie after the substrate binding or before irreversible oxygen consumption. One possibility could be that the $EgtB_2$:TMH:SeCys complex simply cannot efficiently activate O_2. In the case of cysteine dioxygenase, selenocysteine has been shown to not be converted to the product. Therefore, computational studies were applied to address the question of why selenocysteine could not be oxidized by CDO.[91] Even though CDO and EgtB are unrelated enzymes, the geometry and a ligand set of iron coordination in the active site are very similar between both enzymes. Furthermore, both enzymes are able to catalyze the dioxygenation of cysteine. Spectroscopic data of CDO indicated that selenocysteine well binds into the active site.[91] A QM/MM calculation found that the oxygen affinity of CDO is reduced when SeCys is bound instead of Cys. Considering similarities in the geometry of CDO and EgtB, this observation may explain why SeCys consumption is slow, due to decreased oxygen binding. Nevertheless, the $EgtB_2$-catalyzed reaction still leads to the product formation, suggests that the oxygen activation barrier is surmountable.

Since the product of the reaction was found to be the selenoether instead of selenoxide, suggests another mechanism (Scheme 30). One possibility could be that, after assembly of the Michaelis-Menten complex, off-pathway reduction of oxygen takes place to give superoxide as in case observed in cytochrome P450cam (Scheme 30, mechanism II-a), when a proximal ligand was substituted to selenocysteine.[13] However, the formation of selenoether by the $EgtB_{2\_Y93F}$ mutant was found to be more than 600 fold slower and with $EgtB_{2\_Y94F}$ ~80 fold slower, which is consistent with the sulfoxide formation catalyzed by the mutants. The iron(III)-superoxo species is likely in a protonated state during the reaction with selenocysteine. Thus, selenoether formation does not proceed

through mechanism II-a (Scheme 30). Considering that the iron(III)-superoxo species is protonated, further formation of hydrogen peroxide might take place (Scheme 30, mechanism II-b). The peroxide ligand might leave the active site prior to selenoxidation taking place, followed by subsequent selenoether release.

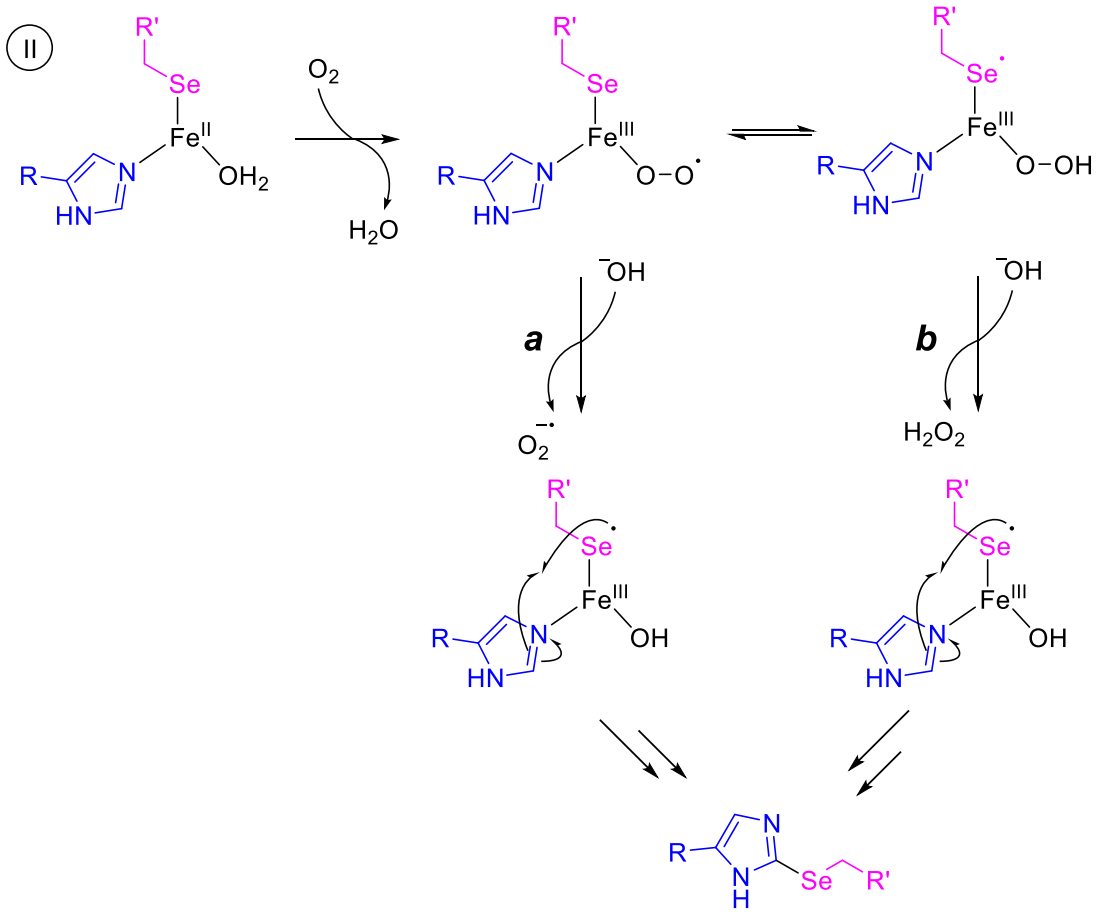

Scheme 30. Proposed mechanism for selenoether formation catalyzed by $EgtB_2$. After the assembly of the Michaelis-Menten complex, superoxide (a) or hydrogen peroxide (b) (after protonation of the Fe(III)-superoxo species) may be released from the active site resulting in a Fe(III)-coordinated selenyl radical, which further attacks the imidazole ring of TMH.

Taking into account that peroxide might leave the active site prior to selenoxidation, the next step of deprotonation on the imidazole find of TMH would become slower due to the different deprotonation rate between sulfoxide and selenoether. To probe whether the rate-limiting step upon substitution of sulfur with selenium changes, the rate of the kinetic substrate isotope effect was measured for $EgtB_2$ and $EgtB_{2\_Y93F}$ with Cys and $EgtB_2$ with SeCys in the presence of either TMH or D-TMH (Figure 47). As for $EgtB_1$, $EgtB_2$-catalyzed sulfoxide formation does not exhibit a KIE on the deprotonation step. However, the selenoether formation has a KIE of 3.1 ± 0.1. Taking into account that the selenoxide product was not observed, C-Se bond might be formed prior oxidation.

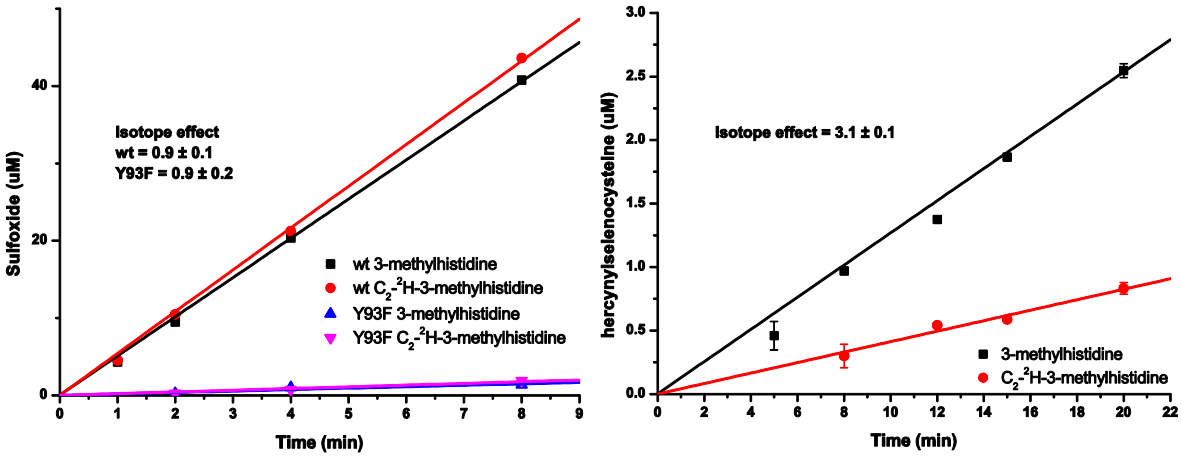

Figure 47. Left: The isotope effect on the sulfoxide formation catalyzed by $EgtB_2$ or $ErgB_{2\_Y93F}$ mutant. **Right:** The isotope effect on the hercynylselenocysteine formation catalyzed by $EgtB_2$. Standard conditions for this assay were as follows: reaction mixture containing 100 mM phosphate buffer pH 8.0, 100 mM NaCl, 2 mM ascorbate, 2 mM TCEP, 4/40 µM $FeSO_4$, 500 µM N^{α},N^{α},N^{α}-trimethyl-L-histidine/C2-^{2}H-N^{α},N^{α},N^{α}-trimethyl-L-histidine, 500 µM L-cysteine or L-selenocysteine and 1.7 µM $EgtB_2$ or 10 µM $EgtB_{2\_Y93F}$ mutant were added together to a final volume of 250 µL. The reaction mixtures were incubated at 26°C. Aliquots of the reactions were quenched by the addition of 20 µL 1 M phosphoric acid and analyzed by HPLC using the standard method.

According to the mechanism II-b (Scheme 30, p. 84), hydrogen peroxide should leave the active site before or after the deprotonation step. In order to understand whether the first irreversible step is before or after the proton abstraction step, kinetic measurements of the KIE were performed at low and high SeCys concentrations to identify whether the KIE affected only k_{cat}, k_{cat}/K_M or both. Full Michaelis-Menten kinetics could not be precisely measured due to the instability of the substrate SeCys and the slow reaction of selenoether formation (0.0012 s^{-1}). To simplify the reaction of hercynylselenocysteine formation, we considered the equation 1, which takes into account selenocysteine binding (k_1); k_2 combines all steps between the substrate binding up to the rate-limiting step, and proton abstraction from the imidazole ring is characterized by k_3.

$$EH + Se \underset{k_{-1}}{\overset{k_1}{\rightleftharpoons}} EHSe \xrightarrow{k_2} EI \xrightarrow{k_3} E + P \quad (1),$$

Following the Michaelis-Menten equation in the equation 1:

$$v = \frac{[E]_0[S]k_{cat}}{[S] + K_M} \quad (2),$$

$$K_M = \frac{[EH][Se]}{[EHSe][EI]} = \frac{k_{-1}k_3}{k_1(k_2 + k_3)} \quad (3),$$

$$k_{cat} = \frac{k_2 k_3}{k_2 + k_3} \quad (4),$$

If we assume that all steps before the rate-limiting step are reversible, and that the first irreversible step has the rate constant of k_3, then at the high substrate concentration:

$$v_{s\to\infty} = \frac{[E]_0[S]k_{cat}}{[S]} = [E]_0 k_{cat} \quad (5),$$

KIE will only influence k_{cat} (4) but not the K_M. However, if the concentration of the substrate is low ([S] < K_M), then:

$$v_{s\to 0} = \frac{[E]_0[S]k_{cat}}{K_M} = \frac{[E]_0[S]k_2k_3k_1(k_2+k_3)}{(k_2+k_3)k_{-1}k_3} = \frac{[E]_0[S]k_2k_1}{k_{-1}} = \frac{[E]_0[S]k_2}{K_S} \quad (6),$$

In equation 6 at the low substrate concentrations, the velocity does not depend on k_3. The kinetic data measured at 1 mM or 40 µM of SeCys show a KIE on k_{cat} and no KIE on k_{cat}/K_M (Figure 48). These data suggest that the deprotonation of C2 of imidazole of TMH is the first irreversible, and also rate-limiting step.[104]

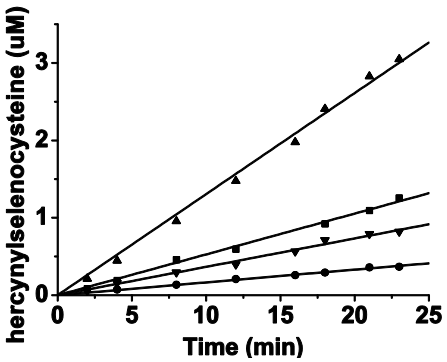

Figure 48. Isotope effect on the hercynylselenocysteine formation catalyzed by $EgtB_2$ at high and low concentration of selenocysteine. Rates at 40 µM selenocysteine with TMH (■) = 0.00044 s^{-1} and D-TMH (●) = 0.00014 s^{-1}; at 1 mM selenocysteine with TMH (▲) = 0.0011 s^{-1} and D-TMH (▼) = 0.0003 s^{-1}. Standard conditions for this assay were as follows: reaction mixture containing 100 mM phosphate buffer pH 8.0, 100 mM NaCl, 2 mM ascorbate, 2 mM TCEP, 8 µM $FeSO_4$, 500 µM N^{α},N^{α},N^{α}-trimethyl-L-histidine/C2-^{2}H-N^{α},N^{α},N^{α}-trimethyl-L-histidine, 40/1000 µM L-selenocysteine and 2 µM $EgtB_2$ added together to a final volume of 250 µl. The reaction mixtures were incubated at 26°C. At 1, 2, 4 and 8 min 40 µL aliquots of the reactions were quenched by the addition of 20 µL 1 M phosphoric acid and analyzed by HPLC using the standard method.

The deuteration of TMH at C2 makes proton abstraction the rate-limiting step in hercynylselenocysteine formation with KIE of 3.1. We therefore investigated whether the enzyme could be trapped in the intermediate form. A simpler system, where selenocysteine is a competitive inhibitor (7), can help us understand the influence of deuterated TMH on the inhibitory kinetics.

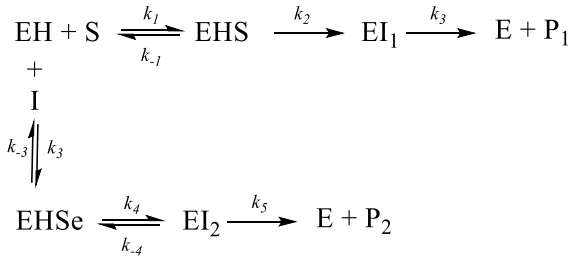

$$v = \frac{[E]_0[S]k_{cat}}{[S] + K_M\left(1 + \frac{[I]}{K_i}\right)}, \tag{7}$$

where K_i is the inhibitor constant. If $k_4 >> k_5$, the enzyme can undergo the reaction till the rate-limiting step to form EI_2. Considering that there is a strong KIE for deuterated TMH on k_5, the enzyme might be stabilized in the EI_2 form when deuterated TMH is used. This assumption will lead to the inhibition constant equals, K_i:

$$K_i = \frac{[EH][Se]}{[EHSe][EI_2]} = \frac{k_{-3}k_5}{k_3(k_4 + k_5)} \tag{8},$$

Then K_i becomes a function of k_5, which has a KIE. A decrease on K_i would be observed in case of deuterated TMH. If SeCys binds to the active site but further reaction is slowed down due to the oxygen binding to the iron-selenium complex, or any other step in the catalysis is reversible, then $k_4 << k_5$ and the inhibition constant would be equal to

$$K_i = \frac{k_{-3}}{k_3} = K_{Se} \tag{9},$$

This would result in a KIE on k_5 not influencing K_i and therefore the substrate (SeCys) release is faster than oxygen binding to the complex or all steps before deprotonation are reversible.

Inhibition kinetics were performed by using either TMH or D-TMH at saturation conditions as a second substrate. K_i was calculated for different substrates used: $K_{i,THM}$ = (36 ± 9) µM; $K_{i,D\text{-}THM}$ = (47 ± 7) µM (Figure 49). These data suggest that K_i remains the same, thus $k_4 << k_5$ (9) and the reaction proceed in the reversible manner according to the competitive inhibitory mechanism for selenocysteine. Furthermore, it suggests that the unbinding of selenocysteine is faster than the oxygen binding.

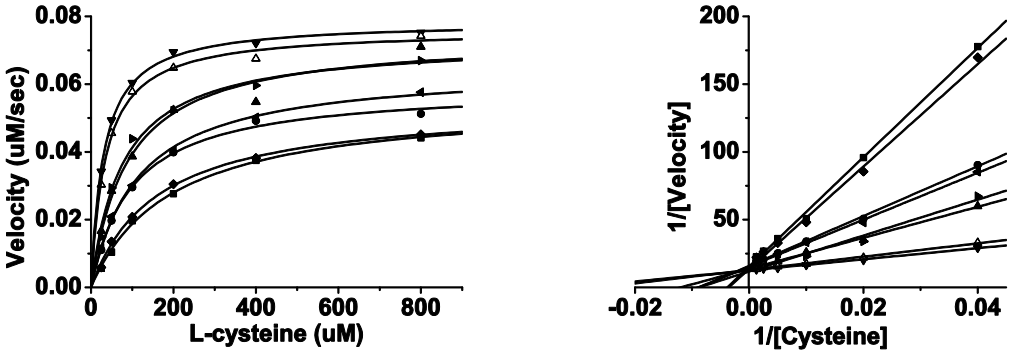

Figure 49. Selenocysteine is a competitive inhibitor to cysteine in $EgtB_2$ catalyzed sulfoxide formation. Non-deuterated and deuterated TMH was used at saturation conditions as a second substrate. Hyperbola (left) and Lineweaver–Burk (right) representations show no change in K_i for the reaction depending on the C2 deuteration of TMH. Standard conditions for this assay were as follows: reaction mixture containing 100 mM phosphate buffer pH 8.0, 100 mM NaCl, 2 mM ascorbate, 2 mM TCEP, 2 µM $FeSO_4$, 1 mM $N^{\alpha},N^{\alpha},N^{\alpha}$-trimethyl-L-histidine/C2-^{2}H-$N^{\alpha},N^{\alpha},N^{\alpha}$-trimethyl-L-histidine, (12.5 – 800) µM L-cysteine, 0.2 mM selenocysteine with TMH (■)/D-TMH (◆); 0.1 mM selenocysteine with TMH (●)/D-TMH (◄); 0.05 mM selenocysteine with TMH (▲)/D-TMH (►); 0 mM selenocysteine with TMH (▼)/D-TMH (Δ) and 0.5 µM $EgtB_2$ added together to a final volume of 250 µL. The reaction mixtures were incubated at 26°C. At 1, 2, 4 and 8 mins 40 µL aliquots of the reactions were quenched by the addition of 20 µL 1 M phosphoric acid and analyzed by HPLC using the standard method.

4.2. Proposed mechanism of hercynylselenocysteine formation

One of the mechanisms was proposed based on the kinetic data, which points towards mechanism II-b (Scheme 30, p. 84). However, if hydrogen peroxide leaves the active site it introduces an irreversible step before the aforementioned C2 deprotonation. Therefore, the mechanism required revision.

Another mechanism can be proposed, where selenoxide is formed and then reduced to selenoether. It has been shown that selenoxide reduction to selenoether is relatively facile. For example, L-methionine selenoxide is reduced to seleno-L-methionine by ascorbic acid, methimazole,[105] or endogenous thiols, such as glutathione.[106] Furthermore, the formation of selenoxide in the cell by cellular oxidants by oxidizing enzymes is well regulated. Selenoxides get reduced back to selenides with stoichiometric oxidation of reduced glutathione.[107]

Considering that the reaction mixture for $EgtB_2$-catalyzed selenoether formation contains ascorbic acid, TCEP and excess of SeCys, suggests that if selenoxide is formed, it might be immediately reduced by one of the reactants. To probe whether selenoxides can be quickly reduced in vitro at pH 8, David Lim synthesized dimethylselenoxide (DMSeO). It was shown that DMSeO is fully reduced to dimethylselenide within 10 minutes in the presence of either TCEP, ascorbate, Cys or SeCys (unpublished data). These data suggest that in the $EgtB_2$-catalyzed reaction, selenoxide might be formed and is reduced after it is released from the active site. Since the rate of the selenoether is 0.0012 s^{-1}, it was evident that no significant consumption of TCEP, ascorbate or SeCys was observed.

Furthermore, the KIE on deprotonation step of the reaction can be explained by comparing deprotonation rate of dimethylsulfoxide (DMSO) and DMSeO. David Lim has shown that deprotonation of DMSO is 4 fold faster than for DMSeO, suggestion that the deprotonation step in the catalytic cycle becomes rate-limiting when S is substituted by Se and that before the deprotonation, and oxidation has to take place (unpublished data).

Therefore, another mechanism for selenoether formation is described in the Scheme 31, whereby C-Se bond formation follows the original mechanism of sulfoxidation and results in the selenoxide formation. Binding of oxygen is harder for the selenolate-bound iron species (A). Therefore, oxygen cannot be efficiently activated, resulting in a 170-fold rate difference between the S and Se reactions, respectively. However, after oxygen is bound to the active site, the iron(III)-superoxo species is then protonated by the Y93 residue resulting in intermediate (C). Considering the KIE and deprotonation rate of the selenoxides, the next step in the mechanism is selenoxidation (D). Further deprotonation might be catalyzed by the iron(II)-O^- species (E), resulting in selenoxide formation. After the selenoxide leaves the active site of the enzyme, it reduces to the selenoether in the reaction mixture by TCEP, ascorbate or remaining selenocysteine.

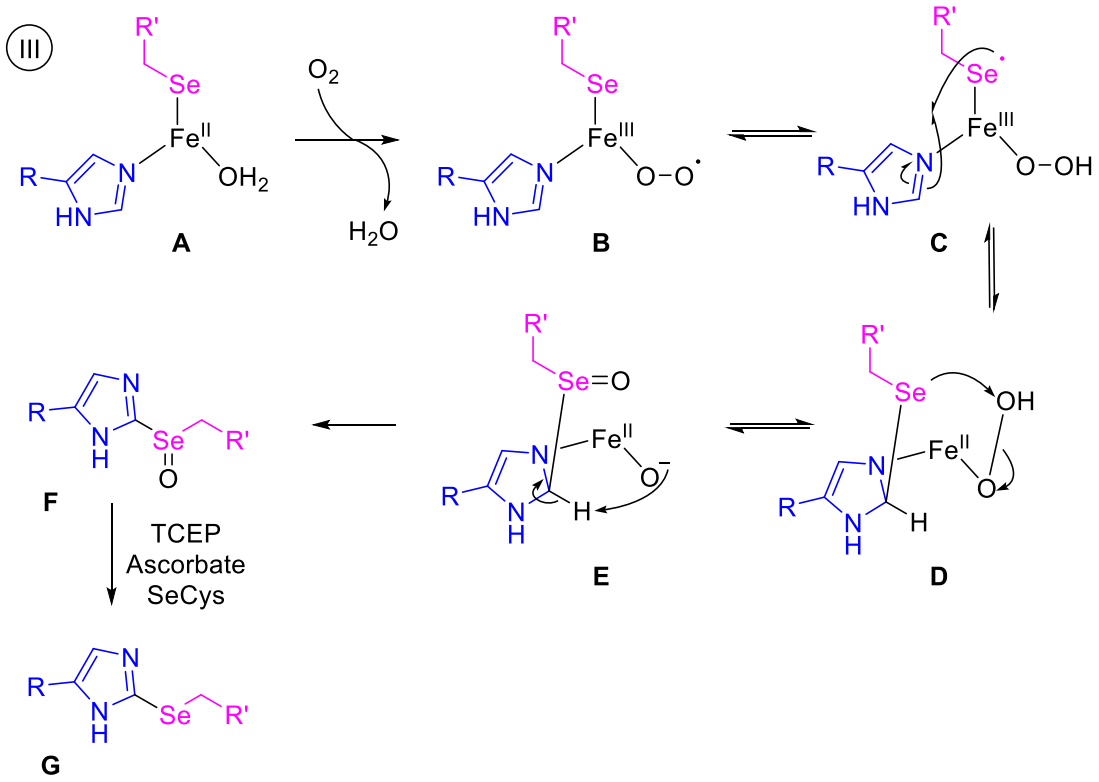

Scheme 31. The proposed mechanism of hercynylselenocysteine formation catalyzed by $EgtB_2$. After selenium binds to TMH:$EgtB_2$ complex (A), oxygen binding becomes rate-determining (B). However, after oxygen is bound, Y93 protonates the iron(III)-superoxo species resulting in (C) and stabilizes selenyl radical. Then, selenyl radical attacks the imidazole ring of TMH, resulting in C-Se bond and sp^3 carbon formation (D). Selenoether intermediate (D) is then oxidized to selenoxide (E). The iron(II)-oxo species may then deprotonate the C2 carbon of the imidazole, regenerating aromaticity. Once the selenoxide is released from the active site, it is immediately reduced by TCEP, ascorbate and remaining SeCys.

4.3. Conclusions

In this chapter we have shown that selenocysteine is an excellent mechanistic probe for determination of the $EgtB_2$ binding order. The inhibitory kinetic data showed that $EgtB_2$ has a sequential binding order, where TMH binds first, followed by Cys binding to the $EgtB_2$:TMH complex.

Replacement of cysteine with selenocysteine in the $EgtB_2$-catalyzed reaction led to the formation of hercynylselenocysteine, which was confirmed by HRMS. However, current mechanistic understanding suggests that selenoxide might still be the product of the reaction. After the selenoxide is released from the active site, it might be reduced to the selenoether. The reaction mixture contains an excess of SeCys, TCEP and ascorbate, which might quickly reduce the selenoxide, as was shown by David Lim for dimethylselenoxide. Therefore, the mechanism proposed by Pluskal *et al.*, which suggests that selenoneine biosynthesis involves hercynylselenocysteine, may require revision.[102] We suggest that the ergothioneine pathway can synthesize selenoneine, where first the selenoxide is formed by the sulfoxide synthase, is then reduced by the intracellular reductants. Then, the β-lyase EgtE catalyzes the selenoneine formation (Scheme 32). C-Se bond formation is relatively slower than for C-S bond formation due to weaker oxygen binding to the iron-coordinated selenolate. Therefore, there might be a different biosynthetic pathway of selenoneine.

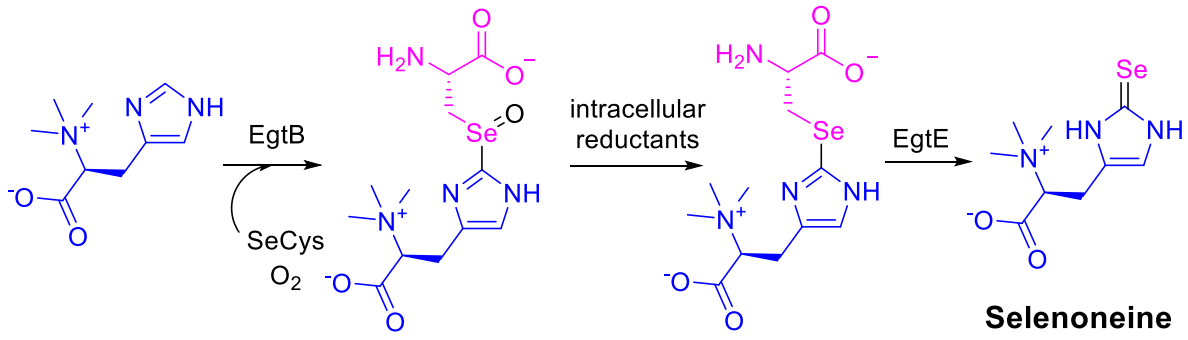

Scheme 32. The ergothioneine pathway can synthesize selenoneine. The sulfoxide synthase EgtB catalyzes the formation of the selenoxide, which is further reduced to the selenoether, followed by the elimination of pyruvate and ammonia by β-lyase EgtE.

4.4. Experimental

Selenocysteine. Selenocystine was reduced under anaerobic conditions with 2 equivalents of TCEP in H_2O.

Purification of hercynylselenocysteine. Hercynylselenocysteine was collected from ion-exchange HPLC (peak X, Figure 50). The collected peak was lyophilized and purified by DOWEX using NH_4OH. The isolated compound was lyophilized twice and dissolved in water and analyzed.

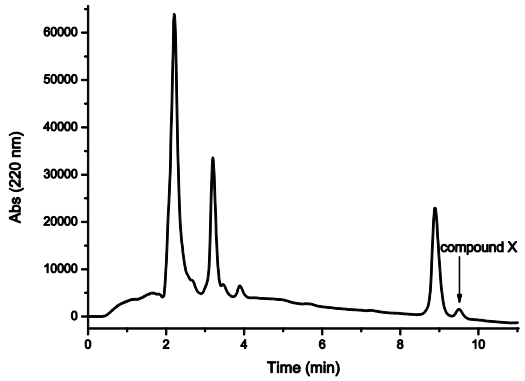

Figure 50. HPLC trace of $EgtB_2$ reaction with selenocysteine. Hercynylselenocysteine (compound X) was collected, purified and analyzed by HRMS (elution time 9.5 min).

4.5. Appendix

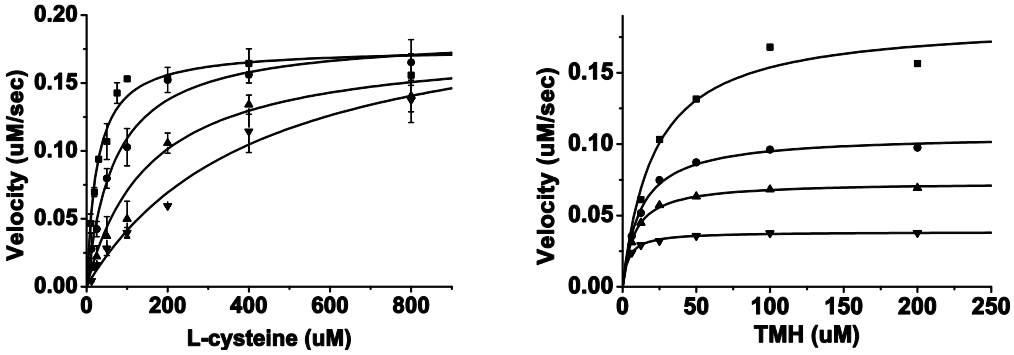

Figure 51. K_i and K_{ii} were determined by non-linear fit of Michaelis–Menten plots for $EgtB_2$ inhibition by selenocysteine. Standard conditions for this assay were as follows: reaction mixture containing 100 mM HEPES buffer pH 8.0, 100 mM NaCl, 2 mM ascorbate, 2 mM TCEP, 4 µM FeSO4, Nα,Nα,Nα-trimethyl-L-histidine, L-cysteine, 0 mM (■), 0.05 mM (●), 0.1 mM (▲), 0.2 mM (▼) L-selenocysteine and 1.3 µM $EgtB_2$ added in final volume of 250 µl. The reaction mixtures were incubated at 26°C. At 1, 2, 4 and 8 min 40 µl aliquots of the reactions were quenched by addition of 20 µl 1 M phosphoric acid and analyzed by HPLC using the standard method.

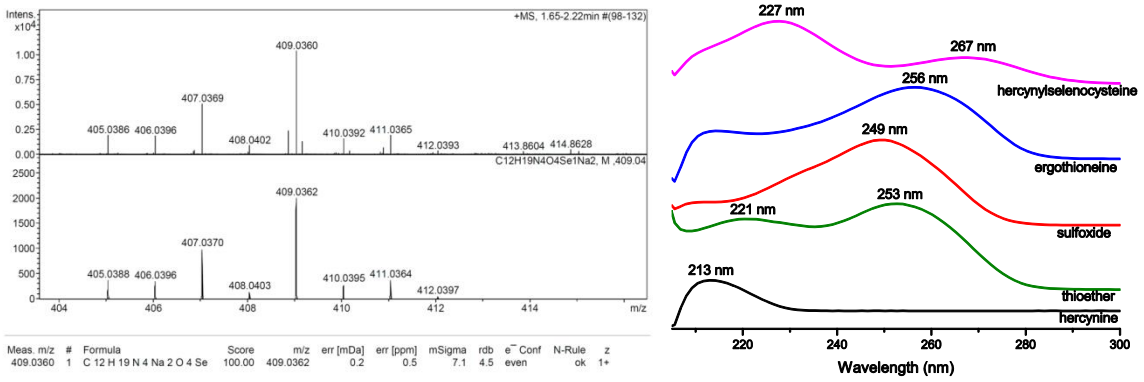

Figure 52. Left: HRMS of isolated and purified hercynylselenocysteine. Top – measured HRMS, bottom – calculated HRMS pattern. **Right.** UV-vis spectra of different sulfur- and seleno-containing compounds.

5. Distinguishing the mechanism of sulfoxide synthase by addition of hydrogen-bond

5.1. The effect of hydrogen bonding on the reactivity of sulfur

In the proposed catalytic mechanism of $EgtB_1$ (Scheme 33), after the assembly of the Michaelis-Menten complex, an iron(III)-superoxo species (**2**) is formed. The protonation of oxygen by Y377 leads to the stabilization of the thiyl radical (**3**), which then is able to attack C-2 of the imidazole ring of N^{α},N^{α},N^{α}-trimethyl-L-histidine (TMH) resulting in (**4**).Further deprotonation (**5**) leads to re-aromatization and product release (**6**). Over the course of the reaction, the sulfur atom of γGluCys is oxidized in two steps; one which leads to C-S bond formation (thiolate → thioether) and the other which leads to sulfoxidation (thioether → sulfoxide). In our proposed mechanism, we suggested that C-S bond is formed prior to the sulfoxidation. The crystal structure of the related ergothioneine biosynthetic amidohydrolase, EgtC from *Mycobacterium smegmatis* co-crystalized with the sulfoxide product of $EgtB_1$, revealed the *S*-configuration of the sulfoxide.[66] If the sulfoxidation would take place prior to C-S bond formation, then the *R*-configuration would be observed in the product.[108]

According to the proposed mechanism, the first mechanistic step involves the formation of a thiyl radical on the sulfur. It is not clear at which step of the reaction the formation of the thiyl radical takes place. We propose that the thiyl radical might be formed *via* the activation of sulfur through a proton-coupled electron-transfer (PCET) mechanism. Therefore, slowing this process (by increasing the redox potential) might aid towards the understanding of the process of thiolate oxidation to thiyl. Hydrogen bonding has been shown to remove electron density from the Me-S system. Therefore, engineering a system with an additional hydrogen-bond to the sulfur might change the covalence of the metal-ligand bond. If the addition of the hydrogen-bond influences the rate of proton transfer, this result would suggest that both proton and electron transfer are closely coupled.

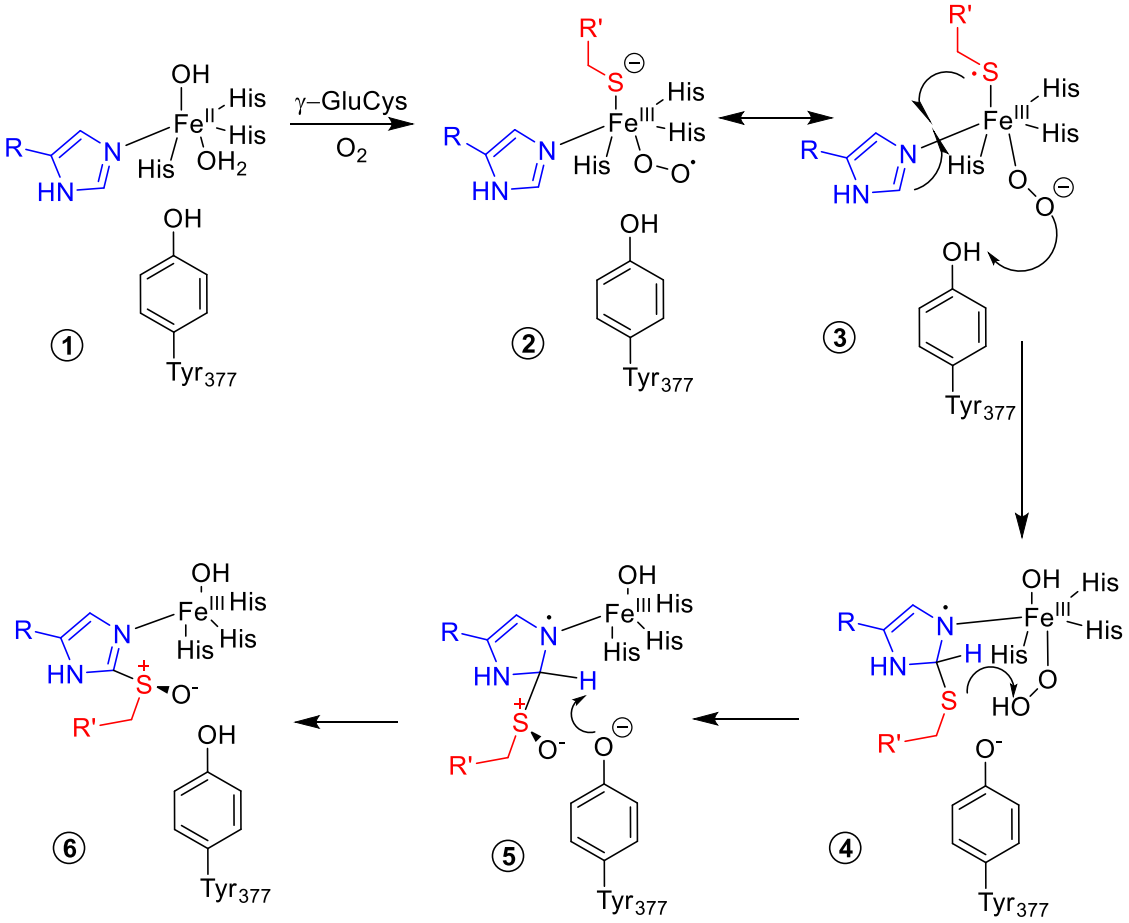

Scheme 33. Thiyl radical is a crucial intermediate in the reaction pathway of the sulfoxide synthase EgtB.

Simple valence bond theory assumes that a hydrogen atom can form only one chemical bond. However, when hydrogen is formally di-valent, the additional bond is called a "hydrogen bond". There is a large variety in the types of hydrogen bonding, including hydrogen bonds which connects atoms of higher or lower electronegativity than hydrogen, low barrier hydrogen bonds and short-strong hydrogen bonds.[109] Hydrogen bonding is crucial in determining molecular conformation and aggregation of proteins, and is involved in the function of many chemical and biological processes.[109] In the active site of an enzyme, hydrogen bonding plays an important role in substrate binding and tuning of the reactivity of catalytically important residues or substrates, particularly in thiolates or selenolates.[110,111,13]

Hydrogen bonding has been thought to affect the nucleophilicity of the metal-coordinated thiolate.[112,111] The addition of a proton to the thiolate ($R\text{-}S^- \rightarrow R\text{-}S\text{-}H$) decreases the nucleophilicity of sulfur by more than a 1000-fold.[113] More sophisticated examples have been described in the literature, where hydrogen bonding has been shown to influence nucleophilicity of the thiolate, change the redox potential or modulate the covalency together with a change of the redox potential. However, the design on a specific hydrogen bond within the active site of the protein is extremely difficult.

In the literature, the approach for the addition of a new hydrogen bond is well known. Based on the following three examples, this concept was then applied to $EgtB_1$. The first example is based on the effect of hydrogen bonding on the nucleophilicity of sulfur bond to a metal. The importance of hydrogen bonding has been studied for a Zn-S system, since the evaluation of hydrogen bonding on reaction rates is relevant to zinc thiol-activating proteins (Scheme 34).[114] These mononuclear zinc enzymes catalyze carbon–sulfur bond formation. It has been proposed that a zinc-ligated thiol is well poised for nucleophilic attack on the electrophilic substrate.[115] Examples of such Zn-containing alkyl transfer proteins are: Ada (involved in methylation sensing), MetE (methionine biosynthesis) and NisC (lantibiotic synthesis).[116] The active site zinc of these proteins is ligated by two to four cysteine residues and histidine or carboxylates.

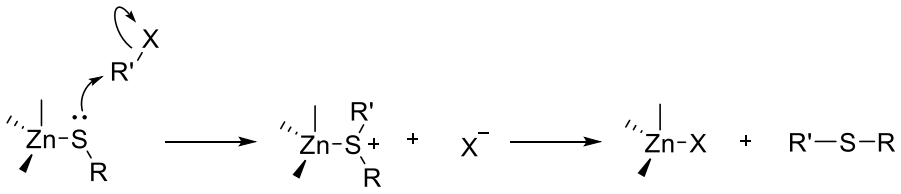

Scheme 34. Mechanism for Zn-promoted alkyl transfer.

To provide a quantitative kinetic assessment of the role of hydrogen bonding in altering the reactivity of a metal thiolate, Chiou *et al.* prepared and characterized mononuclear zinc-thiolate complexes in order to investigate the role of the additional hydrogen bond to sulfur on the nucleophilicity of the corresponding thiolate (Figure 53).[115] The rates were measured by [^{1}H] NMR for the reactions between the zinc thiolate derivatives (1–3) with iodomethane or α-bromo-toluene, generating the corresponding aryl thioether and zinc halides. The results obtained by Chiou *et al.* suggest that the nucleophilicity of zinc thiolate (2) was more than an order of magnitude diminished relative to zinc thiolate (1) due to the additional intramolecular amide N-H-S hydrogen bond (Figure 53). To probe the role of the hydrogen bond in (2), alkylation of the deuterated N-D complex was measured. The measured kinetic isotope effect (KIE) was inverse with a value of 0.33 at 60°C. The inverse KIE might be due to zero point energies differences that favor the hydrogen bonding interaction between the thiolate and amide hydrogen. N-H and N-D vibrational energy differences might increase the nucleophilicity of the thiolate by moving from H to D. These data highlight both the sensitivity of the reaction to hydrogen bonding and provide evidence for a weaker N-D-S stabilization.

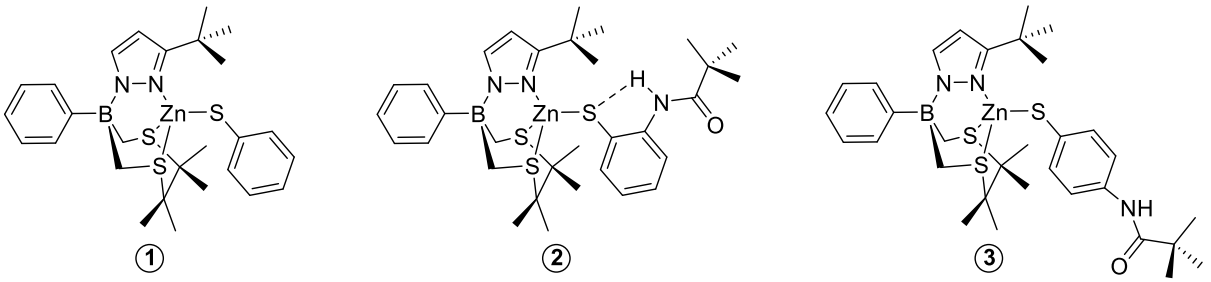

Figure 53. The zinc thiolate complexes used for hydrogen bonding interactions studies by Chiou *et al.*[115]

A complimentary study examined the effect of hydrogen bonding on the redox potential of iron-coordinated sulfur.[111] To probe how hydrogen bonding affects the redox potential changes in Fe-S proteins Yang *et al.* prepared and studied a series of gaseous cubane-type analogue complexes of the active site of [4Fe-4S] proteins: $[Fe_4S_4(SEt)_3(SC_nH_{2n+1})]^{2-}$ and $[Fe_4S_4(SEt)_3(SC_nH_{2n}OH)]^{2-}$ where n = 4, 6, 11 (Figure 54). In the second cubane complex a hydroxyl group was introduced at the end of the side chain. The $-SC_nH_{2n}OH-$ coordinated complexes were expected to form a strong intramolecular hydrogen bond between the hydroxyl group and the cubane sulfur, while the $-SC_nH_{2n+1}$-coordinated complexes were used as non-hydrogen bonding references. Comparison of these complexes with and without the additional hydroxyl group showed that, without perturbation of other environmental effects, one hydrogen bond (OH···S with a distance of 3.3 Å) to the terminal ligand S raises the oxidation potential by ~130 mV.[111]

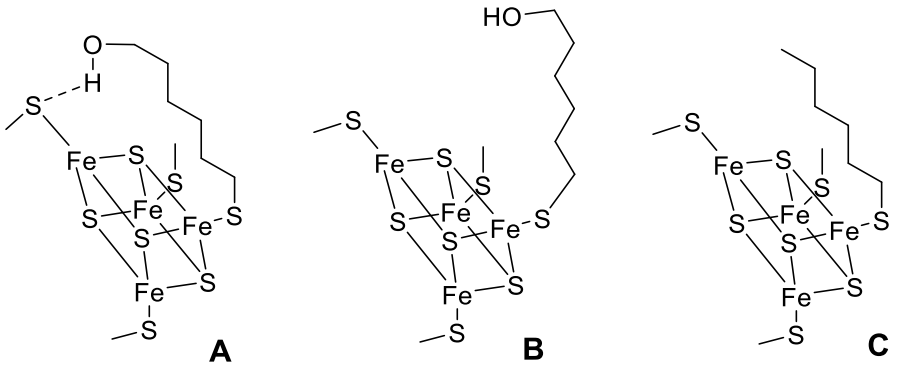

Figure 54. Structures of (A) the H-bonding conformation of $[Fe_4S_4(SCH_3)_3(SC_6H_{12}OH)]^{2-}$, (b) the non-H-bonding conformation of $[Fe_4S_4(SCH_3)_3(SC_6H_{12}OH)]^{2-}$, and (c) $[Fe_4S_4(SCH_3)_3(SC_6H_{13})]^{2-}$. Conformational structures of these complexes were isolated by MC simulations, followed by MM and DFT optimizations.

In the third example of hydrogen bonding influencing Fe-S bond was studied in P450-like complexes. Dey *et al.* showed that the covalency of a metal-ligand bond is reduced by the addition of a hydrogen bond to the sulfur atom (Figure 55).[112] Ligand K-edge X-ray absorption spectroscopy (XAS) and DFT calculations suggested that hydrogen bonding weakened the S-M bond, and that the effect was larger for the reduced, rather than the oxidized, state of the iron, resulting in an increase in the redox potential.[112]

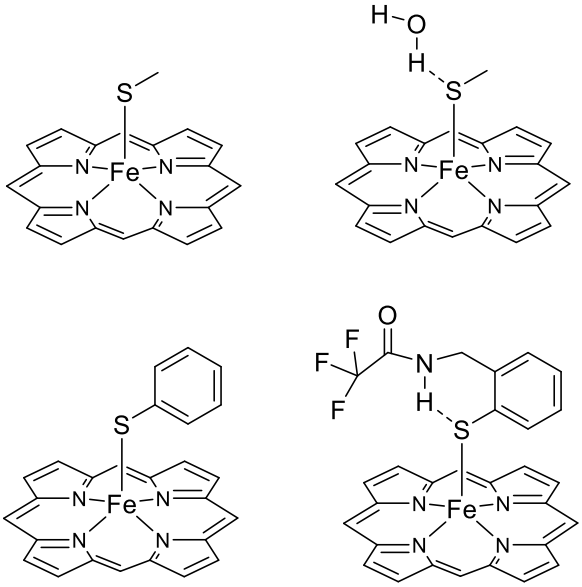

Figure 55. DFT calculations were applied to the upper complexes and lower complexes were synthesized and S K-edge XAS was used as a direct probe of changes in bonding as well as of changes in the chemical nature of the ligand.

Hydrogen bonding is a well-tested tool to modulate the reactivity of metal-coordinated sulfur atoms, thus it has the potential to probe the mechanistic proposal for EgtB. Because EgtB is a non-haem, iron-dependent enzyme containing a sulfur ligand, the reactivity of the sulfur was probed by addition of a hydrogen bond to the sulfur to determine whether a hydrogen bonding interaction might be involved in the electron-transfer pathway. Moreover, tuning the activity of EgtB may provide insight into the mechanism of sulfoxidation by the enzyme. Earlier mechanistic investigations of EgtB proposed that sulfur oxidation precedes C-S bond formation. Species (1) might be partially oxidized and be represented in two resonance structure where the inner sphere electron transfer takes place. Further proton transfer (PT) from Y377 residue results in intermediate (4). The fact that the PT can be coupled with the oxidation of the thiolate suggests the proton-coupled electron-transfer (PCET) from (1) to (4) occurs. An alternative pathway includes a formal H-atom transfer (HAT) from (1) resulting in a tyrosyl radical (3), which is followed by a reverse electron transfer (ET) from the thiolate to yield (4).

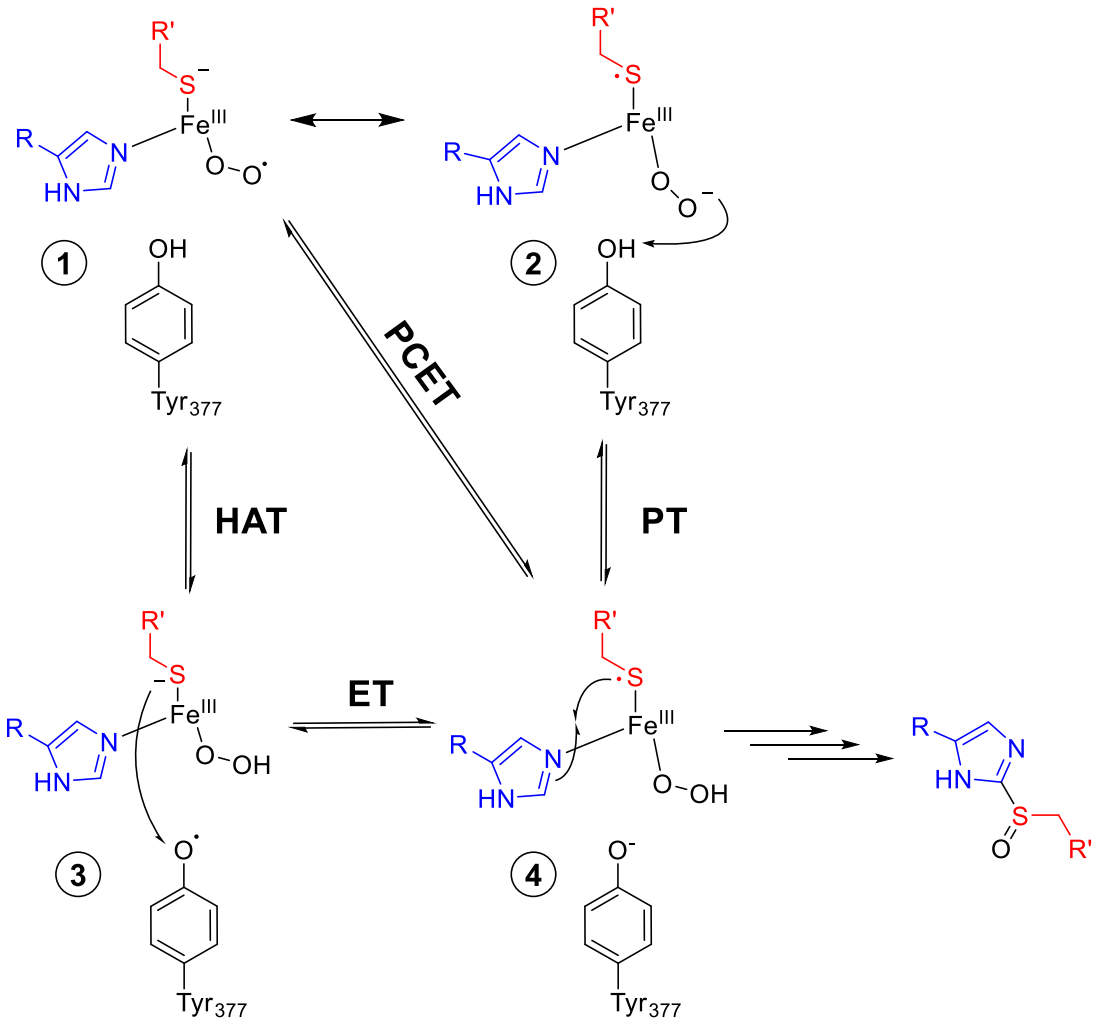

Scheme 35. Proposed mechanisms of the thiyl radical formation in the active site of $EgtB_1$. Formation of intermediate 4 can involve PT from 2 to 4 or PCET (HAT) from 1 to 3, followed by ET or PCET from 1 to 4.

5.2. Identification of the potential hydrogen bonding donor

In order to create a new hydrogen bond to the sulfur, the crystal structure of $EgtB_1$ was examined for potential residues for mutagenesis. In the crystal structure of $EgtB_1$, an alanine residue in position 82 in the active site is in close proximity to the sulfur-bound to the iron center (Figure 56, left). Mutation of this residue to serine might allow for the formation of an additional hydrogen bond to the sulfur of the γGluCys substrate. This sulfur atom is coordinated by iron and it has been shown that, when iron is in the ferric state, there is a ligand-to-metal charge transfer (LCTM) from sulfur to iron which takes place (Chapter 2). In the proposed mechanism, the thiyl radical is formed which then nucleophilically attacks the imidazole ring of N^{α},N^{α},N^{α}-trimethyl-L-histidine (TMH) resulting in C-S bond formation.

The model of $EgtB_{1\_A82S}$ predicted *in silico* (Figure 56, right) predicts the conformation of S82 which allows the formation of a hydrogen bond between the hydroxyl group of S82 and the metal-

coordinated sulfur of γGluCys (distance = 2.78 Å, angles: 135.9 and 97.6°). Moreover, homologues of EgtB containing a serine residue instead of alanine were found in the NCBI database. The model of $EgtB_{1\_A82C}$ predicts a hydrogen bond with the sulfur of the substrate (distance = 2.33 Å, angles: 144.5 and 100.4°). The addition of the hydrogen bond to the thiolate potentially changes the rate-limiting step of the reaction and the strength of the metal-ligand bond.[112] Therefore, two mutants $EgtB_{1\_A82S}$ and $EgtB_{1\_A82C}$ mutants were generated by site-directed mutagenesis, produced, and purified according to the standard protocol (see Experimental).

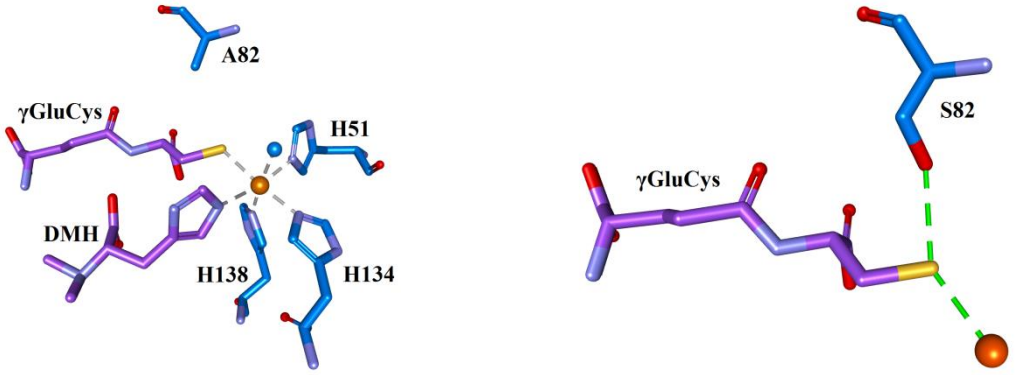

Figure 56. Active site of $EgtB_1$ (left) and a model of $EgtB_{1\_A82S}$ mutant (right) based on EgtB1 structure, generated using Accelrys Discovery Studio Client 2.5. The model of the mutant suggests the formation of a hydrogen bond between S82 and sulfur of γGluCys.

5.3. Kinetic analysis of the A82 mutants

First, mutants with either serine or cysteine residues in position 82 were compared to the wild-type enzyme. To test the effect of these mutations on the steady-state kinetics, standard Michaelis-Menten kinetic analyses were performed to quantify the sulfoxide activity of the newly generated mutants (Figure 57). In Table 20, the kinetic data of the wild-type enzyme is compared to the kinetic data derived from the mutants. For $EgtB_{1\_A82S}$ (Figure 57, left), the K_M of γGluCys remained the same, while k_{cat} and catalytic efficiency dropped by ~5 fold. ^{1}H NMR studies also show no change in the product distribution of $EgtB_{1\_A82S}$ in comparison to the wild-type enzyme (Figure 58, Figure 59). In the case of $EgtB_{1\_A82C}$, a larger difference in catalytic parameters was observed in comparison with the wild-type enzyme. In the standard Michaelis-Menten kinetics (Figure 57, right), the calculated parameters suggest a drastic drop by almost two orders of magnitude in k_{cat} for the $EgtB_{1\_A82C}$ mutant compared to that of the wild-type, as well as a 500-fold decrease in the catalytic efficiency (Table 20).

The predicted hydrogen bonding to the thiolate might lower sulfoxide synthase activity. This newly formed hydrogen bond would also weaken the S-Fe bond. The effect would be larger for the reduced than the oxidized state (due to the decreased electron donation from the thiolate to the reduced metal ion) resulting in an increase in the redox potential.[91] For $EgtB_{1\_A82S}$ mutant, the decrease in the

activity was observed only in k_{cat}, but not in the K_M of γGluCys, suggesting that the mutation does not interfere with substrate binding and points toward the formation of the new hydrogen bond.

For the $EgtB_{1\_A82C}$ mutant, the reason for an extreme drop in the catalytic efficiency remains unclear, since it is hard to predict where the proton remains, whether on C82 or the sulfur of γGluCys, because both thiolates have similar pK_a's. Thus, the thiolate of γGluCys might be protonated and, due to the equilibrium with the protonated thiolate on C82, the 500-fold drop in the catalytic efficiency might be explained (Scheme 36). Another reason for the drop in the activity for the $EgtB_{1\_A82C}$ mutant can be caused by interactions with the nearby located arginine residue, which is involved in γGluCys binding (Figure 60). Due to unclear positioning of the proton, the change in the K_M for γGluCys and possibility due to the fact that the cysteine residue having another conformation, and makes the $EgtB_{1\_A82C}$ mutant a less defined model in comparison to $EgtB_{1\_A82S}$. Therefore, $EgtB_{1\_A82S}$ was chosen as a model for future analysis of hydrogen bond formation with the thiolate in the active site of $EgtB_1$. One way to test the theory that the hydroxyl group of S82 is hydrogen bonded to the sulfur is by measuring the ligand-to-metal charge transfer (LMCT), which will be further discussed in the following section.

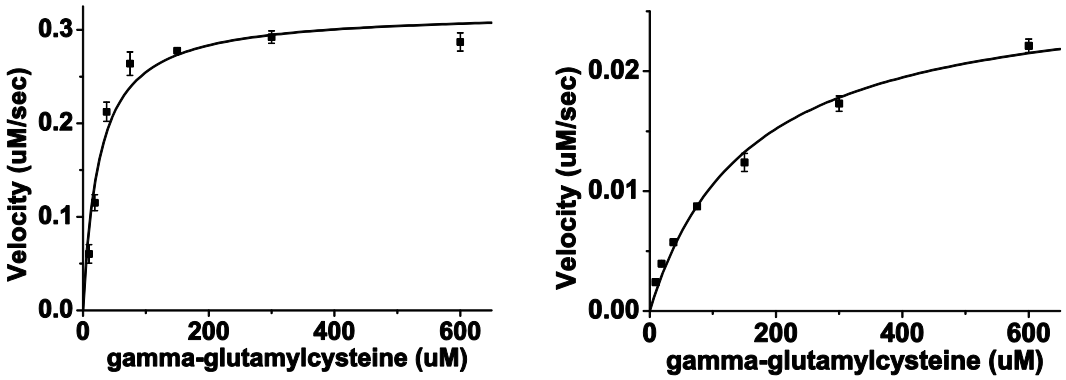

Figure 57. Michaelis-Menten kinetics of the sulfoxide synthase activity for two mutants: $EgtB_{1\_A82S}$ (left) and $EgtB_{1\_A82C}$ (right). A reaction mixture contained 100 mM phosphate buffer pH 8.0, 100 mM NaCl, 2 mM ascorbate, 2 mM TCEP, 8/12 µM $FeSO_4$, 1 mM N^{α},N^{α},N^{α}-trimethyl-L-histidine, (9 – 600) µM γGluCys and 2 µM $EgtB_{1\_A82S}$ (left) or 2 µM $EgtB_{1\_A82C}$ (right) mutant added last to a final volume of 250 µL. The reaction mixtures were incubated at 26 °C. At 1, 2, 4 and 8 mins, 40 µL aliquots of the reactions were quenched by the addition of 20 µL 1 M phosphoric acid and analyzed by HPLC using the standard method.

Table 20. Catalytic parameters of sulfoxide synthase activity for the EgtB variants at saturated conditions of TMH and varied concentrations of γGluCys.

Protein	k_{cat}, s^{-1}	K_M, 10^{-6} M	k_{cat}/K_M, s^{-1} M^{-1}
$EgtB_1$	0.75 ± 0.02	27 ± 1	28000 ± 1000
$EgtB_{1\_A82S}$	0.16 ± 0.01	26 ± 6	6100 ± 1700
$EgtB_{1\_A82C}$	0.0086 ± 0.0005	150 ± 25	55 ± 10

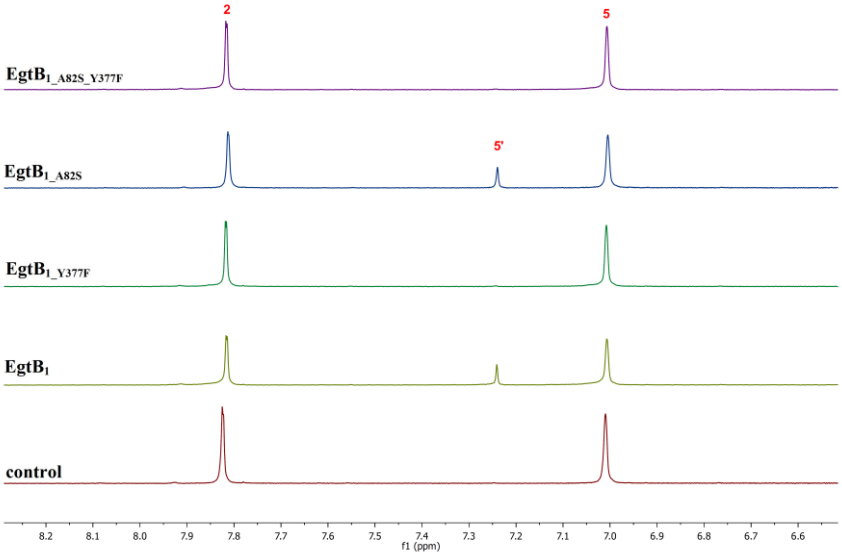

Figure 58. ^{1}H NMR spectra of the aromatic region of the $EgtB_1$ variants catalyzed reactions in excess of N^{α},N^{α},N^{α}-trimethyl-L-histidine. A reaction mixture contained 100 mM phosphate buffer pH 8.0, 100 mM NaCl, 2 mM ascorbate, 2 mM TCEP, 8 µM $FeSO_4$, 1 mM N^{α},N^{α},N^{α}-trimethyl-L-histidine, 300 µM γ-glutamylcysteine and 1 µM $EgtB_1$ variants in final volume of 2 mL were incubated overnight at room temperature.

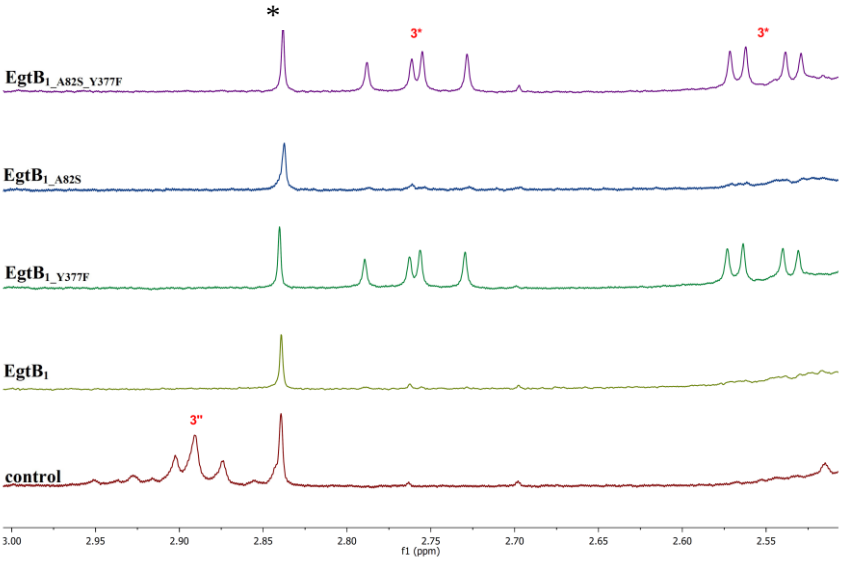

Figure 59. ^{1}H NMR spectra of the β-protons of the sulfinic acid of the $EgtB_1$ variants catalyzed reactions in excess of N^{α},N^{α},N^{α}-trimethyl-L-histidine. A reaction mixture containing 100 mM phosphate buffer pH 8.0, 100 mM NaCl, 2 mM ascorbate, 2 mM TCEP, 8 µM $FeSO_4$, 1 mM N^{α},N^{α},N^{α}-trimethyl-L-histidine, 300 µM γ-glutamylcysteine and 1 µM $EgtB_1$ variants in final volume of 2 mL were incubated overnight at room temperature. (A signal coming from the impurities of TMH is marked with an *)

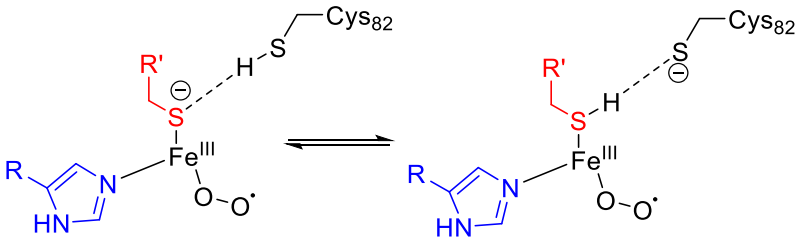

Scheme 36. Position of the proton remains unclear in $EgtB_{1\_A82C}$ mutant due to the similar pK_a's of the thiolates.

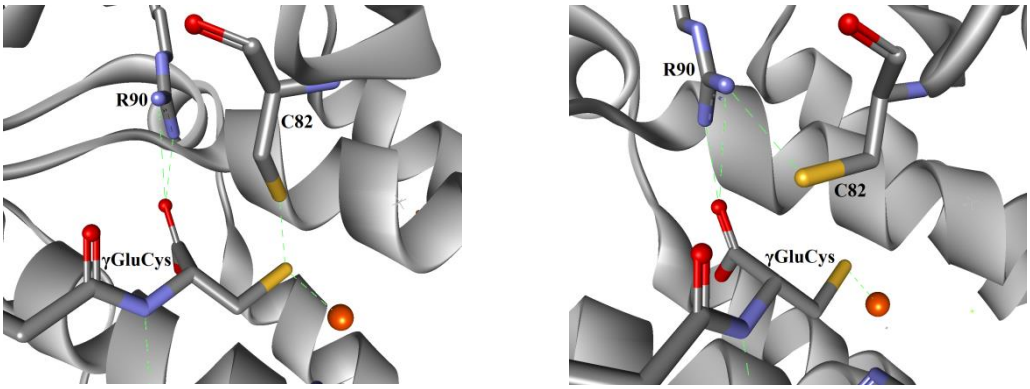

Figure 60. Two different conformations of C82 calculated in the model structure. On the left side, C82 forms a hydrogen bond with thiolate of γGluCys. The conformation of the right site represents a salt bridge between C82 and R90, which is a crucial residue in the substrate binding.

5.4. Ligand-to-metal charge transfer

Molecular electronic transitions take place when electrons in a molecule are excited to a higher energy level. One of these electronic transitions, which take place in the active site of EgtB, is a ligand-to-metal charge transfer (LMCT). LMCT is the transition of an electron from a ligand-centered orbital to a metal-centered orbital. This type of transfer is predominant if complexes that have ligands with high-energy lone pairs (for example S or Se) in combination with unoccupied low-energy orbitals on the metal center. The absorptions that arise from this process are LMCT's. A schematic description of this transition is shown in Figure 61 involving a low-spin d^5 metal center with an octahedral ligand environment. LMCT transitions result in intense absorbance bands in contrast to weak d-d transition that are parity-forbidden.

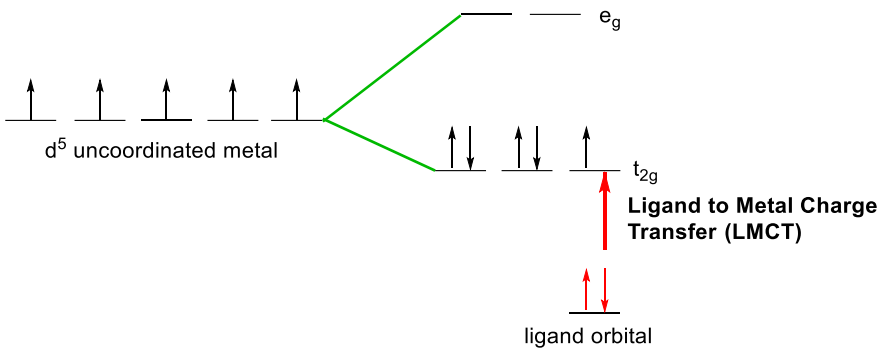

Figure 61. Ligand-to-metal charge transfer (LMCT) of an octahedral low-spin d^5 complex.

Analytical techniques are used to identify LMCT such as UV-vis and magnetic circular dichroism (MCD).[58, 77, 80] For example, superoxide reductases (SORs) are metalloenzymes that contain a non-haem, cysteinate-ligated iron center, which makes this system suitable for analyzing LMCT transitions.[117] The absorption spectrum of Fe^{III}-SOR exhibits a dominant feature at 660 nm that is attributed to an S-to-Fe^{III} LMCT transition.[80] In the MCD spectrum, related features are observed at 660 and 526 nm (15150 and 18980 cm^{-1}). Those observed characteristics were assigned as S-to-Fe^{III} charge transfer transitions originating from the S(Cys) p-based molecular orbitals possessing Fe-S π-bonding and σ-bonding character, respectively. Applying Raman spectroscopy to the system, Clay *et al.* demonstrated that excitation into the intense (Cys)S(p_π)-to-Fe(d_π) CT transition centered at 660 nm results in a strong enhancement of modes at 33.56 and 30.96 μm (298 and 323 cm^{-1}) that are assigned to extensively mixed cysteine S-C_β-C_α bending and Fe-S(Cys) stretching modes, respectively.[118] Similar studies were applied by Shearer *et al.* to a synthesized model compound which mimics the active site of SOR. This study showed that a hydroperoxo intermediate of Fe^{III} has an LMCT band at 452 nm (ε = 2780 M^{-1} cm^{-1}), which is consistent with kinetic studies involving superoxide oxidation of the SOR iron site.[58]

An alternative study was performed on another non-haem iron-dependent enzyme – cysteine dioxygenase (CDO)[77]. Absorption and MCD spectra were measured for cysteine bound to Fe^{III} containing CDO. Spectroscopic signatures of S-Fe^{III} LMCT were similar to those presented by Fe^{III}-superoxide reductase; a maximum of absorbance at 637 nm and temperature-dependent MCD features at 655 and 538 nm (15250 and 18570 cm^{-1}).

The active sites of both SOR and CDO are similar to that of $EgtB_1$ (Figure 62), thus the absorption spectrum was measured first for the wild-type enzyme in order to compare the sulfoxide synthase to other known non-haem iron-dependent enzymes. In the case of sulfoxide synthase $EgtB_1$, the sulfur of γGluCys bound to Fe^{III} exhibits a LMCT absorption band (Figure 63). The extinction coefficient for the S-Fe^{III} LMCT band for wild-type $EgtB_1$ was ~450 M^{-1} cm^{-1} with the maximum absorbance at 565 nm. A comparison between S-Fe^{III} LMCT absorption bands of different non-haem iron-dependent enzymes are shown in Table 21. The minor difference between the maximum of S-Fe^{III}

LMCT absorption bands of described systems is caused by the different coordination, origin and angles of the ligands.[77]

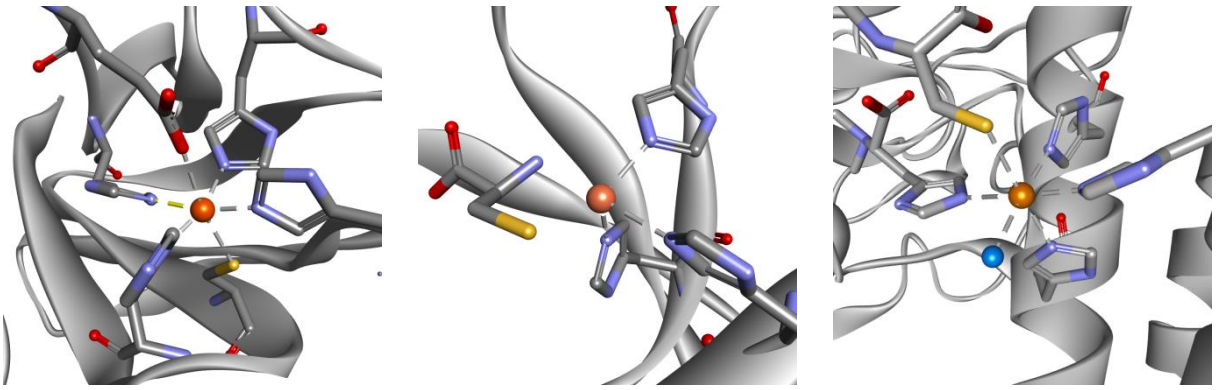

Figure 62. Iron coordination in the active sites of SOR (4BGL, 1.9 Å), CDO (4Z82, 1.7 Å) and $EgtB_1$ (4X8D, 1.98 Å). Sulfur atom is represented in yellow.

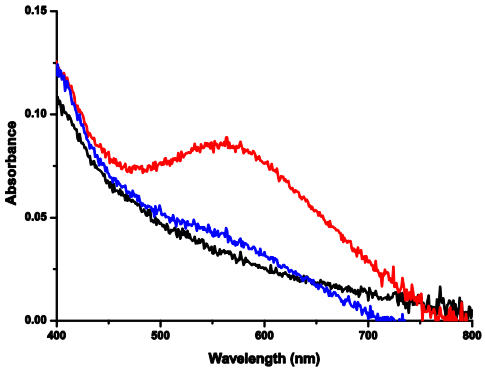

Figure 63. Absorbance of $EgtB_1$ (black) leads to an LMCT band in the presence of γGluCys (red). Reduction of Fe^{III} to Fe^{II} by sodium ascorbate leads to a loss of the LMCT band (blue).

Additionally, the absorbance was monitored for $EgtB_{1\_A82S}$ with Fe^{III} but no detectable LMCT was observed. Taking into account that the k_{cat} decreased for the mutant, the newly formed hydrogen bond might slightly change the charge distribution on the thiolate, thus reducing the extinction coefficient and blue shift would be consistent with formation of a hydrogen bond. Therefore, in order to understand why this mutation led to the drop in k_{cat}, UV-vis spectroscopy experiments were performed with the Co^{II}-charged enzyme. Co^{II} was selected because its complexes show more intense absorption bands in their UV-vis spectra, which are sensitive to the metal coordination geometry and to the nature of the ligands.

In order to measure the UV-vis spectra with Co^{II}, iron was exchanged with cobalt (see Experimental) in the active site of $EgtB_1$ and $EgtB_{1\_A82S}$. An intense absorption band at 416 nm (ε_{416} = 3170 $M^{-1}cm^{-1}$) was observed and was assigned to the sulfur to cobalt LMCT in $EgtB_1$ (Figure 64).

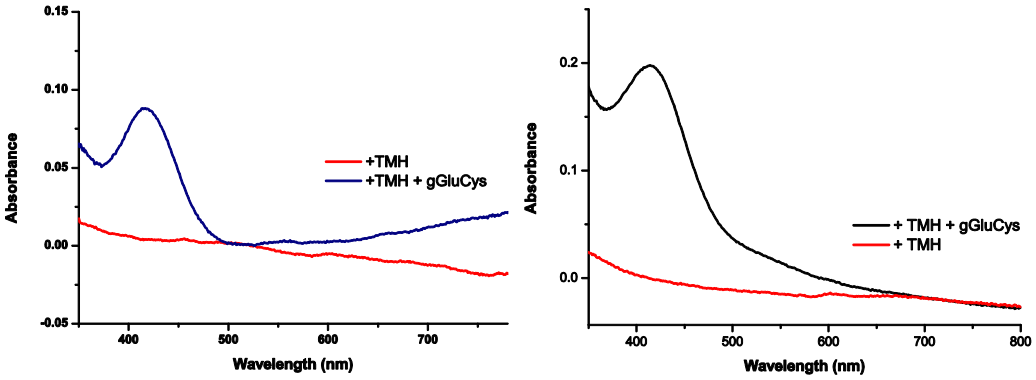

Figure 64. Abstracted absorbance of 35 (left) and 71 µM (right) of $EgtB_1$ sulfur-to-cobalt LMCT band with maximum at 416 nm. LMCT band is observed only when γGluCys is present.

Cobalt- and iron-centered $EgtB_1$ have different absorption maxima of 565 nm (Fe^{III}) and 416 nm (Co^{II}). The complex with cobalt has a higher extinction coefficient for the LMCT band, which allowed the measurement of the H-bonding mutant with an expected lower extinction coefficient. For both the $EgtB_1$ and $EgtB_{1\_A82S}$ mutant, the absorbance band was difficult to determine due to the instability of the protein sample at room temperature. At 10 °C, and with the slow addition of each compound and further incubation, a sulfur-to-cobalt LMCT band was observed at 408 nm with an extinction coefficient of 428 M^{-1} cm^{-1} (Figure 65). The introduction of S82 as a potential hydrogen-donor in close proximity to the sulfur ligand caused a significant decrease of the intensity of the LMCT absorption band by 7-fold in comparison to the wild-type. Moreover, the maximum absorbance of LMCT has a blue shift of ~8 nm which corresponds to an energy difference of ~1 kcal/mol (Figure 66), supporting the idea of the formation of the new hydrogen bond.

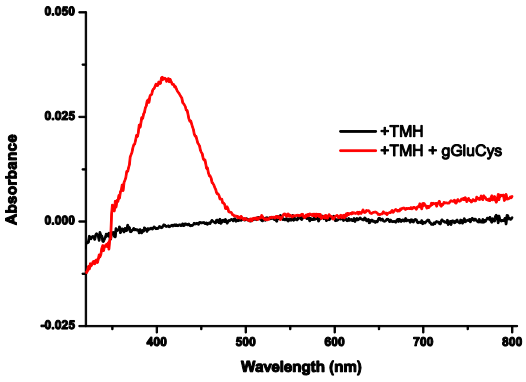

Figure 65. Abstracted absorbance of 80 µM $EgtB_{1\_A82S}$ sulfur-to-cobalt LMCT band which was observed only in the presence of γGluCys with maximum at 408 nm.

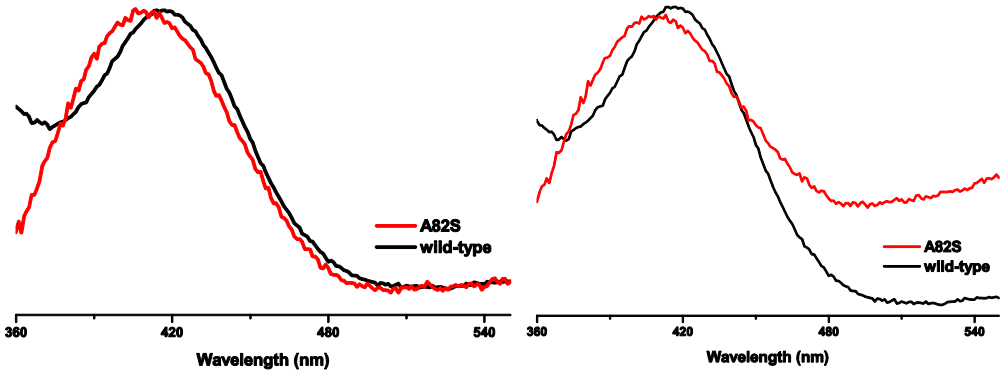

Figure 66. Superimposition of the normalized sulfur-to-cobalt LMCT bands for $EgtB_1$ wild-type and the A82S mutant shows a shift in the maximum absorbance for ~8 nm

Table 21. Characteristics of LMCT bands of thiolate to different metal centers of non-haem iron-dependent enzymes.

Protein	Metal	Max absorbance, nm	Extinction coefficient, $M^{-1}\,cm^{-1}$
Superoxide reductase[80]	Fe^{III}	660	2500
Cysteine dioxygenase[77]	Fe^{III}	637	800
$EgtB_1$[2]	Fe^{III}	565	450 ± 10
$EgtB_1$	Co^{II}	416	3170 ± 80
$EgtB_{1\_A82S}$	Co^{II}	408	430 ± 20
β-Carbonic anhydrase[119]	Co^{II}	340	3500

5.5. Kinetic solvent isotope effect

Hydrogen bonding might slow down the oxidation of the sulfur of γGluCys. This step may either precede protonation of the iron(III)-superoxo species or occur simultaneously. In order to distinguish between these pathways, the kinetic solvent isotope effect (KSIE) of the sulfoxide synthase activity was measured. As in case of the zinc thiolate complexes, an inverse KSIE was expected due to weaker deuterium bonding in comparison to hydrogen bond.[115] Thus, a more stabilized thiyl radical formation was expected. The KSIE was measured at saturating conditions at pH 6 and pH 8 and compared with the wild-type enzyme. For both mutants, a normal KSIE was observed (Figure 67). This result is not surprising since more than one proton is involved in the catalytic mechanism of $EgtB_1$. If the protonation of the iron(III)-superoxo species is coupled to sulfur oxidation, the KSIE of the protonation might increase in the mutant due to the additional hydrogen bond with sulfur. Then, if several isotope effects compete, it is hard to observe the inverse isotope effect due to higher normal isotope effect at the different steps of the reaction.

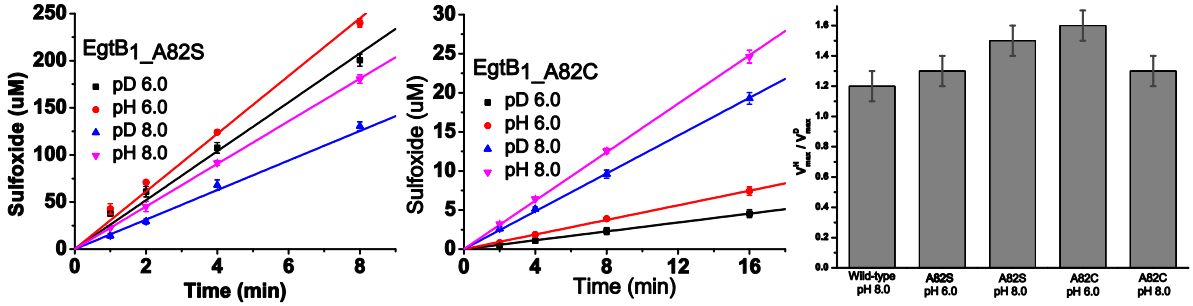

Figure 67. Kinetic solvent isotope effect on $EgtB_1$ and A82 variants. A reaction mixture containing 100 mM phosphate buffer pH 8.0, 100 mM NaCl, 2 mM ascorbate, 2 mM TCEP, 12 µM $FeSO_4$, 1 mM N^{α},N^{α},N^{α}-trimethyl-L-histidine, 1 mM γGluCys and 0.2/2/3.1 µM $EgtB_1$ wt/A82S/A82C mutant added last to a total volume of 250 µL. The reaction mixtures were incubated at 26 °C. At 1, 2, 4 and 8 mins, 40 µL aliquots of the reactions were quenched by addition of 20 µL 1 M phosphoric acid and analyzed by HPLC using the standard method. KSIE's were calculated by the ratio between the rates in H_2O and D_2O.

5.6. Disentangling multiple proton KSIE's using the proton inventory technique

In order to disentangle a multiple protons KSIE, an alternative approach was used. Protonation of the iron-superoxo species becomes rate-limiting for $EgtB_{1\_Y377F}$ with KSIE of 1.9. This mutation is not interfering directly with the serine residue; however this system can allow distinguishing the contribution of the hydrogen bond between S82 and thiolate of γGluCys. Therefore, the double mutant $EgtB_{1\_A82S\_Y377F}$ was designed. In general, KSIE's are hard to interpret due to a large number of hydrogen bonds. Nevertheless by comparing two systems, $EgtB_{1\_Y377F}$ and $EgtB_{1\_A82S\_Y377F}$, the KSIE of one proton or more protons might be distinguished. The double mutant has the same product distribution as the $EgtB_{1\_Y377F}$ and mostly catalyzes sulfinic acid formation (1:99) (Figure 59). The formation of the sulfoxide is twice as slow for the double mutant when compared to the $EgtB_{1\_Y377F}$ mutant. Overall, the KSIE on sulfoxide formation for the double mutant decreased in comparison to the $EgtB_{1\_Y377F}$ mutant from 1.9 to 1.7 suggesting that, of the multiple protons involved, there is an inverse isotope effect at least of one of them (Figure 68). Therefore, a different set up was applied to determine the number of exchangeable protons that were involved in the catalysis - a "proton inventory" technique.[120]

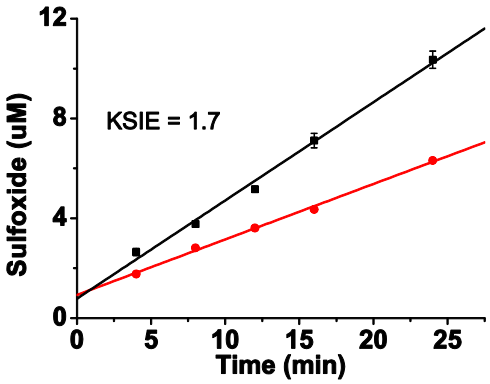

Figure 68. KSIE of sulfoxide formation catalyzed by $EgtB_{1\_A82S\_Y377F}$. A reaction mixture contained 100 mM phosphate buffer pH 8.0, 100 mM NaCl, 2 mM ascorbate, 2 mM TCEP, 4 µM $FeSO_4$, 1 mM N^{α},N^{α},N^{α}-trimethyl-L-histidine, 6.2 µM $EgtB_{1\_A82S\_Y377F,}$ and 1 mM γGluCys is added last to make a total volume of 250 µL. The reaction mixtures were incubated at 26 °C. At 4, 8, 12, 16, and 24 mins, 40 µL aliquots of the reactions were quenched by addition of 20 µL 1 M phosphoric acid and analyzed by HPLC using the standard method.

The proton inventory technique is a more thorough description of a simple KSIE. This experiment can describe the number of exchangeable protons in the structure of an enzyme or substrate that are actively involved in the catalytic mechanism, generating a kinetic or equilibrium isotope effect.[120] The resulting model can yield a list of kinetic isotope effects for each active protonic site involved.

The experimental part of the proton inventory technique involves the following: the velocity is measured in a series of isotopic water solvents. The gradient of H_2O/D_2O ratio is applied from 100 % H_2O to nearly pure deuterium oxide. As a result, there is a dependence of velocity from the atom fraction of deuterium present in the solvent (n). The final function and the shape of the curve describe the number of active protonic sites. If the curve derived from the data is linear, the interpretation of this data set is simple: the effect of KSIE arises from one protonic site in the transition state. A bowl-shaped or a dome-shaped curve indicates the contribution of more than one site. In this case, a polynomial function fit points toward a multi-proton contribution. By applying the polynomial fit, one can estimate the number of sites and then obtain a ϕ value (inverse of KSIE) by fitting the velocities measured at different H_2O/D_2O ration from atom fraction of deuterium into the appropriate Gross-Butler equation (Eq. 5.1). Gross and Butler described the equation relating rates or rate constants to deuterium content in solution, and is as follows:

$$v_n / v_0 = \frac{\prod_{i}^{TS}(1-n+n\phi_i^T)}{\prod_{j}^{RS}(1-n+n\phi_j^R)} \quad \text{(Eq. 5.1)}$$

where v_n and v_0 are the velocity in a binary solvent and in water, respectively, n = atom fraction of deuterium, RS = reactant state, TS = transition state, ϕ^R = RS fractionation factor and ϕ^T = TS

fractionation factor. The fractionation factors are obtained from inverted equilibrium isotope effects, k_D/k_H, for exchange between a bulk water site and a particular structural site of the RS or the TS.

The rates of reaction of $EgtB_{1\_Y377F}$ and $EgtB_{1\_A82S\_Y377F}$ were determined in eight mixtures of buffered H_2O and D_2O with substrates present at concentrations at least 10-fold the K_M value. The mean values of V_{max} were fit with Origin 8.5. For the fitting of the final data of V_{max} from n, two versions of the Gross-Butler equation were used:

a one-proton model: $k_n = k_0(1-n+n\phi)$ (Eq. 5.2)

and a two-proton model: $k_n = k_0(1-n+n\phi_1)(1-n+n\phi_2)$ (Eq. 5.3)

First, the proton inventory experiment was performed for the single mutant $EgtB_{1\_Y377F}$ (Figure 69). Data were fit into equations based on the Gross-Butler equation; for a one-proton (Eq. 5.2) and two-proton models (Eq. 5.3). Figure 69 on the left side shows a fit to a model for one hydrogenic side as the origin of the solvent isotope effect (ϕ = 0.53), the figure on the right side – for two proton catalysis (ϕ_1 = 0.53; ϕ_2 = 1.01). On both cases, the fit was good (R^2 = 0.994 and 0.992 respectively), but the value of the second isotopic fractionation factor ϕ_2 obtained from a two-proton model was so close to unity that the two-proton description becomes equivalent to the one-proton description. A similar analytical algorithm was applied by Garoutte *et al* for the hydrolytic reaction catalyzed by bovine trypsin.[121]

Even though the proton inventory itself carries no direct evidence on the structural location of the single center that generates the isotope effect, our knowledge of $EgtB_1$ and following mutants allows us to propose that the proton is being delivered directly from a neighboring acid, not by a distant acid through a Grotthuss mechanism.[122] The following one-proton model for the $EgtB_{1\_Y377F}$ mutant supports the proposition of the transfer of hydrogen from hydronium to the iron(III)-superoxo species, which occurs in the rate-determining step for this mutant (Scheme 37, upper mechanism). The labeled hydrogen has substantial amplitude in the reaction-coordinate motion and the isotope effect of 2 is expected (ϕ = 0.5). Thus, in the single mutant, there is a one-proton transfer occurring in the rate-determining step.

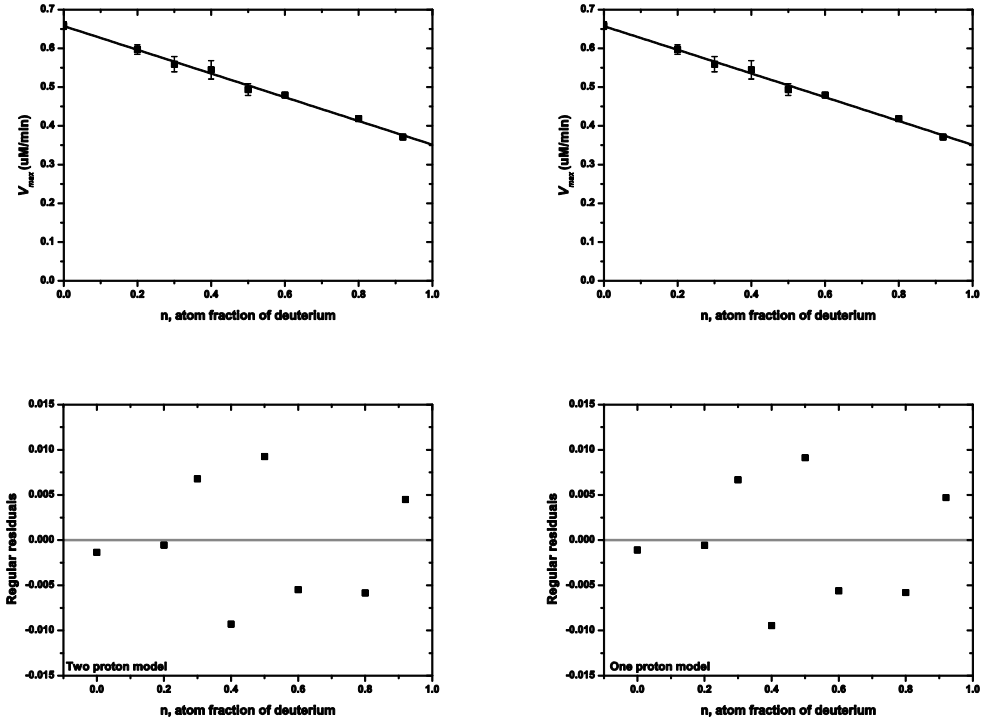

Figure 69. Proton inventory of $EgtB_{1\_Y377F}$ were fitted into 1 (ϕ = 0.53, left) and 2 (ϕ_1 = 0.53; ϕ_2 = 1.01, right) proton models. Both models reveal a single proton transfer system (regular residuals bellow each graph look the same). A reaction mixture containing 100 mM phosphate buffer pH 8.0, 100 mM NaCl, 2 mM ascorbate, 2 mM TCEP, 4 µM $FeSO_4$, 1 mM N^{α},N^{α},N^{α}-trimethyl-L-histidine, 6.6 µM $EgtB_{1\_Y377F}$ and 1 mM γGluCys were added last to a final volume of 250 µL. The reaction mixtures were incubated at 26 °C. At 4, 8, 12, 16, and 24 mins, 40 µL aliquots of the reactions were quenched by the addition of 20 µL 1 M phosphoric acid and analyzed by HPLC using the standard method.

Another proton inventory experiment was performed using the double mutant $EgtB_{1\_A82S\_Y377F}$ (Figure 70). Data were also fit in equations based on the Gross-Butler equation; for a one-proton and two-proton models. Both models have a good fit, but in this case, the fractionation factors differ in both models: for the one-proton model ϕ = 0.55, and for the two-proton model ϕ_1 = 0.4; ϕ_2 = 1.3. Therefore, in order to identify the best fit, regular residuals for both models were compared (see below each graph on the Figure 70). Residual is the difference between the observed value of the dependent variable and the predicted value. Visually calculated residuals for both plots suggested that the fit for the two-proton model has a better fit rather than one-proton model.

These data suggest that $EgtB_{1\_A82S\_Y377F}$ follows a two-proton catalysis, where two protons contribute to the solvent isotope effect. In this case, one proton has a normal isotope effect and the other an inverse isotope effect. These data are in agreement with the proposition that the serine residue is hydrogen-bonded to the thiolate, and a correlation can be drawn with the relative charge density of the sulfur, as well as the redox potential.[112] Therefore, by exchanging a proton on serine to deuterium leads to a stronger O-D bond, and thus a weaker S-D interaction which explains the inverse isotope effect of the second proton in the double mutant (Scheme 37).[123] Other possible reasons for inverse

isotope effects are likely an equilibrium between Fe-OH and Fe-OH_2 and thiolate protonation ($R\text{-}S^-$ and R-SH).

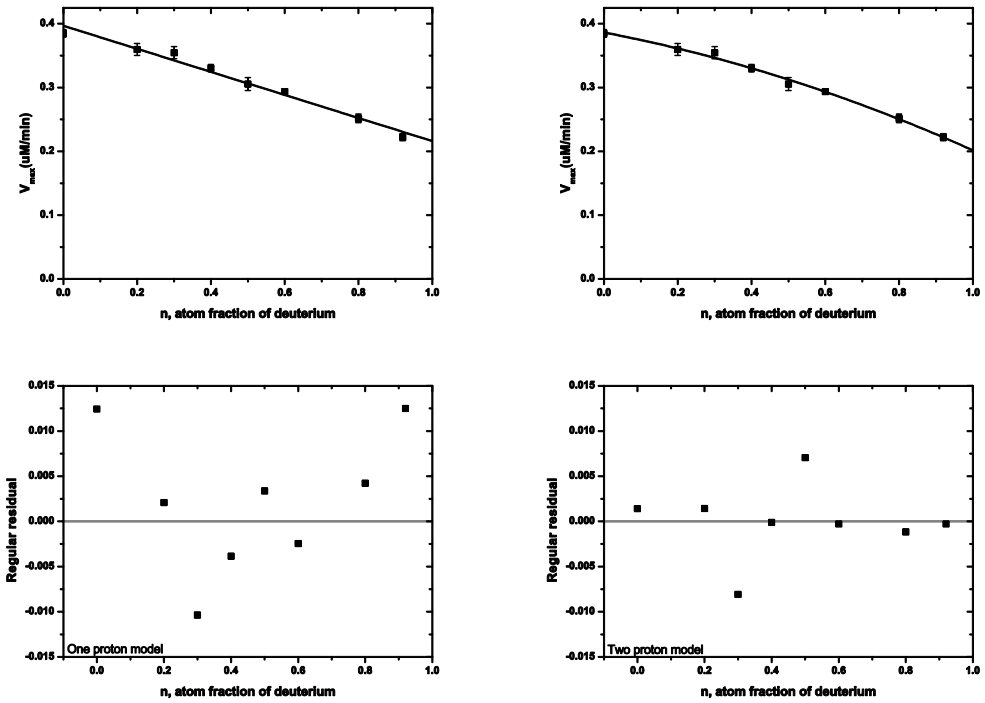

Figure 70. Proton inventory of $EgtB_{1\_A82S\_Y377F}$ were fitted into 1 (ϕ = 0.55, left) and 2 (ϕ_1 = 0.4; ϕ_2 = 1.3, right) proton models. Model for a two-proton transfer fits better than for a single proton transfer (regular residuals below each graph). A reaction mixture containing 100 mM phosphate buffer pH 8.0, 100 mM NaCl, 2 mM ascorbate, 2 mM TCEP, 4 µM $FeSO_4$, 1 mM N^{α},N^{α},N^{α}-trimethyl-L-histidine, 6.2 µM $EgtB_{1\_A82S\_Y377F,}$ and 1 mM γGluCys is added last to make a total volume of 250 µL. The reaction mixtures were incubated at 26 °C. At 4, 8, 12, 16, and 24 mins, 40 µL aliquots of the reactions were quenched by addition of 20 µL 1 M phosphoric acid and analyzed by HPLC using the standard method.

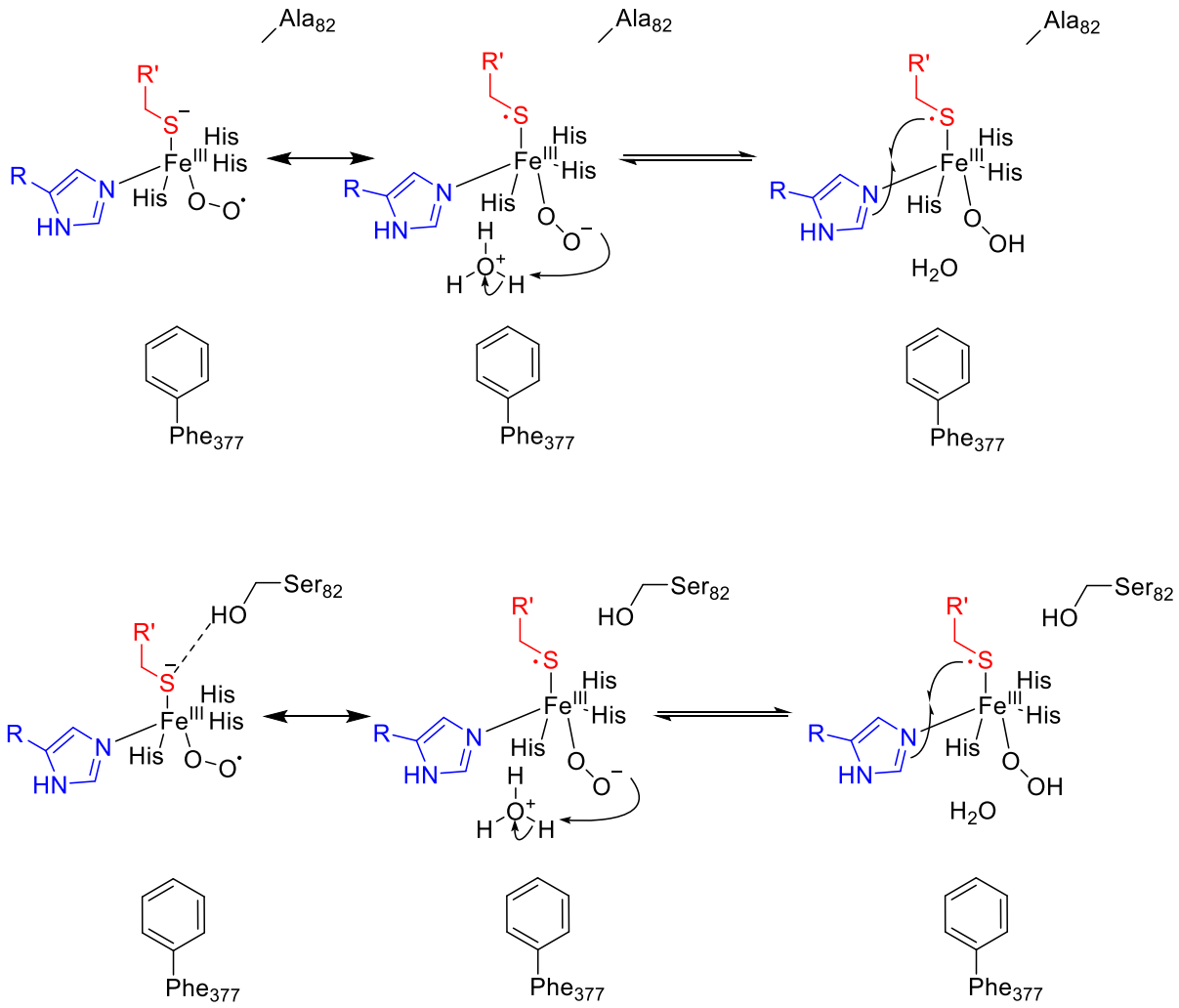

Scheme 37. Proposed mechanism of the rate-determining steps described by proton inventory technique. In the Y377F mutant, the iron-superoxo species is protonated by hydronium causing a normal isotope effect. In the double mutant, A82S_Y377F serine residue is hydrogen-bonded to the thiolate ensue an additional inverse isotope effect in the system.

5.7. Dioxygenase activity of $EgtB_{1\_A82S\_Y377F}$ mutant

In Chapter 3, we have shown that the variant enzyme $EgtB_{1\_Y377F}$ catalyzes dioxygenation of γGluCys with an efficiency similar to that of the sulfoxide synthase activity of $EgtB_1$ wild-type. After the effect of hydrogen bonding was analyzed for the sulfoxide synthase activity of the sulfoxide synthase $EgtB_1$, the effect on the dioxygenase activity was examined. ^{1}H NMR revealed that $EgtB_{1\_Y377F}$ and $EgtB_{1\_A82S\_Y377F}$ mutants catalyze formation of two products: γ-glutamylcysteine sulfinic acid (> 99%) and sulfoxide (< 1%) (Figure 58, Figure 59). The rate of γGluCys was monitored for the $EgtB_{1\_A82S\_Y377F}$ mutant and data showed that this mutant consumes γGluCys with a rate of 0.14 s^{-1}, which is 8 fold slower than $EgtB_{1\_Y377F}$ (Figure 71, left). Consumption of γGluCys at high concentrations of $EgtB_{1\_A82S\_Y377F}$ showed that oxygen binding was not affected by the mutation

(Figure 71, middle). The KSIE on γGluCys was measured at two concentrations of $EgtB_{1\_A82S\_Y377F}$ mutant with KSIE of 0.8 ± 0.1 (Figure 71, right).

The addition of a hydrogen bond to the variant enzyme $EgtB_{1\_Y377F}$ by generating $EgtB_{1\_A82S\_Y377F}$ mutant had a similar effect on dioxygenation reaction as for the sulfoxide synthase activity change between $EgtB_1$ and $EgtB_{1\_A82S}$, eight- and five-fold drop in the activity, respectively. Similarity in the activity change suggests that the formation of hydrogen bond might not only change the redox potential, but also change the oxygen binding affinity. However, the reaction with high $EgtB_{1\_A82S\_Y377F}$ concentrations revealed that oxygen binding was not affected, due to the observation that the consumption of γGluCys slowed down only after oxygen in the reaction mixture was limited. This result suggests that the oxygen binding affinity was not affected by the mutation. Thus, the addition of the hydrogen bond to the system only had an effect on the redox potential of the thiolate. Due to weaker O-D-S stabilization, an inverse KSIE is expected. The KSIE of the reaction was measured with $EgtB_{1\_A82S\_Y377F}$ is 0.85 ± 0.1, which was comparable to the KSIE of 0.9 ± 0.1 for $EgtB_{1\_Y377F}$. Hence, these results are similar within the standard deviation; it is hard to predict if a weaker O-D-S stabilization has a strong effect on the KSIE of dioxygenase activity and if the KSIE represents single or multiple protons involved in the catalysis.

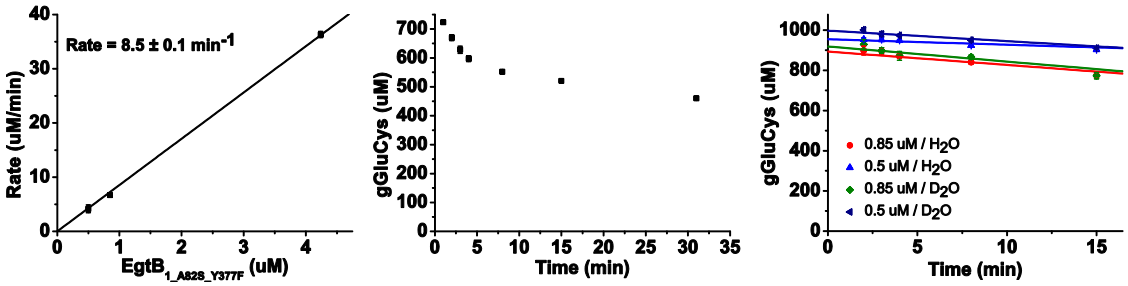

Figure 71. Consumption of γGluCys by $EgtB_{1\_A82S\_Y377F}$ mutant. **Left:** the rate of γGluCys consumption was determined at three different concentration of $EgtB_{1\_A82S\_Y377F}$ mutant. **Middle:** consumption of γGluCys at high enzyme concentration shows that oxygen binding is not rate-limiting. **Right:** kinetic solvent isotope effect on $EgtB_{1\_A82S\_Y377F}$ mutant reveals a KSIE of 0.9 ± 0.1. A reaction mixture containing 100 mM phosphate buffer pH 8.0, 100 mM NaCl, 2 mM ascorbate, 2 mM TCEP, 6 μM $FeSO_4$, 1 mM N^{α},N^{α},N^{α}-trimethyl-L-histidine, 1 mM γGluCys and 0.5/0.85/4.25 μM $EgtB_{1\_A82S\_Y377F}$ mutant added last in total volume of 250 μL. The reaction mixtures were incubated at 26 °C. At 1, 2, 4, 8, 15 and 31 mins, 40 uL aliquots of the reactions were quenched by addition of 40 uL acetonitrile. 10 μL of 20 mM 4-bromomethyl-7-methoxycoumarin (BMC) in DMSO were added and allowed to react for 30 minutes at room temperature in the dark. A 60 μL aliquot of the reaction mixture was diluted two-fold by the addition of 60 μL of 0.1% trifluoroacetic and analyzed by HPLC. KSIE's were calculated by the ratio between the rates in H_2O and D_2O.

5.8. Switching sulfur to selenium

$EgtB_1$ can catalyze the reaction with the analogue of γGluCys – γ-glutamylselenocysteine (γGluSeCys) (Scheme 38). Substitution of S with Se has been probed by Blaesi *et al.* CDO is unable to oxidize selenocysteine due to a low-energy quintet-spin intermediate on the cysteine reaction pathway,

which is absent for a low-energy O_2 adduct for selenocysteine-bound CDO.[91] Due to selenium's superior electron donating ability, the reaction of $EgtB_1$ with γGluSeCys is slower than for γGluCys. The addition of a hydrogen bond to selenium in this case might delocalize electron donation of selenium and thus make electron density on the iron-superoxo species more similar that with sulfur. In order to test this theory, the reactivity with γGluSeCys was probed for $EgtB_1$ and compared with $EgtB_{1\_A82S}$ and $EgtB_{1\_A82C}$.

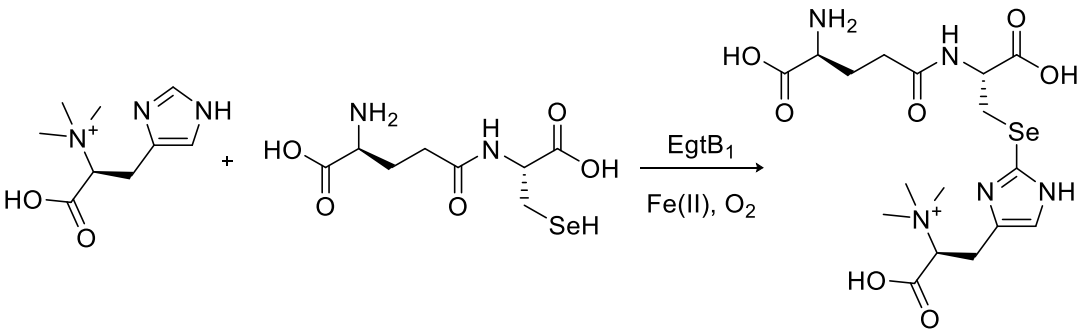

Scheme 38. Reaction catalyzed by $EgtB_1$ with TMH and γGluSeCys leading to the formation of selenoether

Kinetic experiments at the saturating conditions of both substrates show that $EgtB_{1\_A82S}$ did not lose activity, when compared to the wild-type enzyme with γGluSeCys, whereas the A82S mutant was 5-fold slower than the wild-type enzyme for sulfoxide synthase activity with γGluCys (Figure 72). $EgtB_{1\_A82C}$ showed a significant drop in activity, but this result is consistent with previous findings (Section 5.2.). Since the system with γGluSeCys is not well studied, it requires future investigation. This discovery would help us to generate an efficient enzyme for selenoneine biosynthesis by discovering an $EgtB_1$ analogue which accepts cysteine as a substrate and mutating corresponding alanine residue to serine.

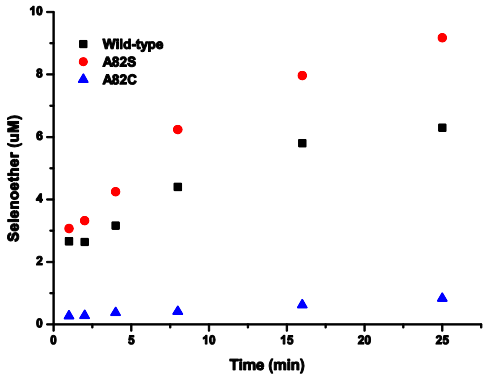

Figure 72. Selenoether formation by $EgtB_1$ variants show that the A82S mutant is more active than the wild-type enzyme. A reaction mixture containing 100 mM phosphate buffer pH 8.0, 100 mM NaCl, 2 mM ascorbate, 2 mM TCEP, 24 µM $FeSO_4$, 1 mM N^{α},N^{α}-trimethyl-L-histidine, 1 mM γ-glutamylselenocysteine, and 6 µM $EgtB_1$ wt/A82S/A82C mutant was added last to make a total volume of 250 µL. The reaction mixtures were

incubated at 26 °C. At 1, 2, 4, 8, 16 and 25 mins, 40 µL aliquots of the reactions were quenched by addition of 20 µL 1 M phosphoric acid and analyzed by HPLC using the standard method.

5.9. Conclusions

Protein design based on the crystal structure of $EgtB_1$ allowed the remodeling of the active site and the tuning of the reactivity of the sulfoxide synthase by introducing an additional hydrogen bond to the thiolate coordinated to the iron center of the enzyme. It was found that the resulting hydrogen bond between the thiolate of the substrate and S82 in the active site disturbs the formation of the proposed thiyl radical (Scheme 39, (4)). This intermediate is required in the catalytic mechanism to further proceed to the attack of this thiyl radical on the imidazole ring of the second substrate. The A82S mutant had a 5-fold drop in k_{cat} in comparison to the wild-type enzyme.

UV-Vis absorption experiments showed a weakening of the Fe-S bond when an additional hydrogen bond was introduced, leading to stabilization of the negative charge on the sulfur ligand and a blue shift of the LMCT band, corresponding to an energy difference of ~1 kcal/mol.

Furthermore, the proton inventory technique was used for the single mutant $EgtB_{1\_Y377F}$ which demonstrated that this enzyme has a KSIE of 1.9. The proton inventory also suggested that a one-proton model best fits this system, whereas for $EgtB_{1\_A82S\_Y377F}$ mutant with KSIE of 1.7, a two-proton model was better, suggesting that two protons are involved in the catalysis; one with a normal isotope effect and another with an inverse isotope effect.

Moreover, by engineering an extra hydrogen bond donor in the active site of EgtB, we can now suggest that the reaction mechanism for sulfoxide synthesis points towards a PCET, as opposed to separate ET and PT's (Scheme 39).

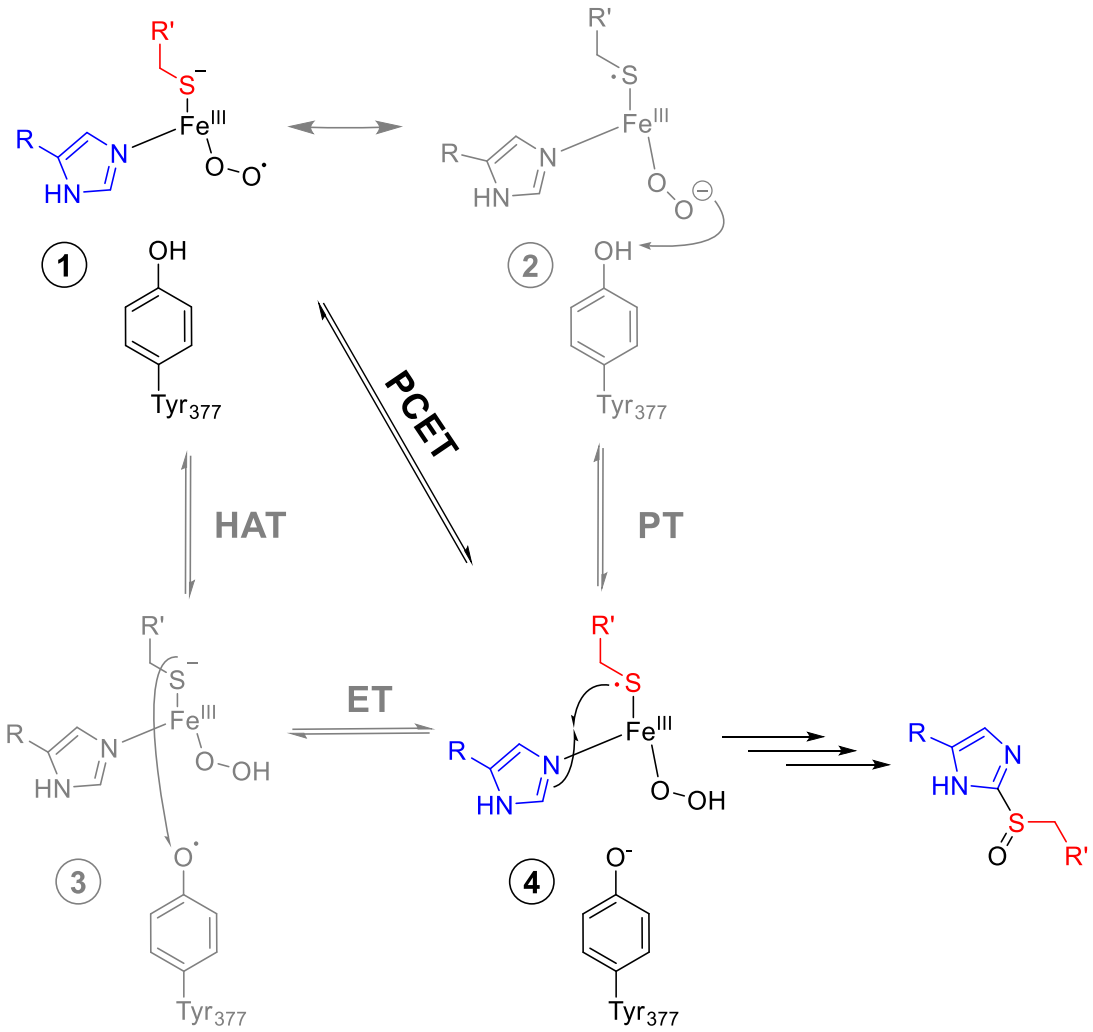

Scheme 39. Proposed catalytic step of EgtB most likely involves a PTET from 1 to 4.

5.10. Experimental

Model prediction. Model of $EgtB_{1\_A82S}$ was predicted using Accelrys Discovery Studio Client 2.5. The A82 was mutated to serine *in silico* and the local structure was optimized by the program.

Construction of EgtB variant. $EgtB_1$ mutants were constructed by site-directed mutagenesis using the following primers. The resulting fragments were cloned into pET28 vectors. All EgtB variants were produced and purified following published protocols.[2]

Primer	Sequence 5' – 3'
A82S_for	ACAGCTGTACGATTCATTTGTCCACCCGCG
A82S_rev	CGCGGGTGGACAAATGAATCGTACAGCTGT
A82C_for	ACAGCTGTACGATTGCTTTGTCCACCCGCG
A82C_rev	CGCGGGTGGACAAAGCAATCGTACAGCTGT

Recombinant protein production. $EgtB_1$, $EgtB_{1\_A82S}$, $EgtB_{1\_A82C}$, $EgtB_{1\_A82S\_Y377F}$ and $EgtB_{1\_Y377F}$ were produced and purified as described in the chapter 2.

Table 22. Calculated and observed molecular weights of proteins.

Protein	m/z, calc., Da	m/z, obs., Da	Delta, Da
$EgtB_{1\_A82S}$	51359	51534 51566	175 (gluconoylation of His Tag)[93] 207 (gluconoylation, oxidation)
$EgtB_{1\_A82C}$	51375	51580	205 (gluconoylation, oxidation)
$EgtB_{1\_A82S\_Y377F}$	51343	51518 51549	175 (gluconoylation of His Tag) 206 (gluconoylation, oxidation)

Metal-free protein samples. In order to exchange the metal center of the enzyme, $EgtB_1$ and $EgtB_{1\_A82S}$ mutant were incubated with excess of EDTA on ice for 30 minutes after purification and then dialyzed against 50 mM Tris pH 8.0, 50 mM NaCl buffer twice. Metal-free proteins were concentrated and these samples were used for the UV-vis measurements. 100 µL of the protein sample was transferred to the quartz cuvette and incubated at 10 °C. Slowly, 1.5 eq. of cobalt chloride, 1.5 eq. TMH and 1.5 eq. of γGluCys were added into the cuvette one after the other.

LCTM. Absorption spectra were recorded on a Cary 300bio spectrophotometer. Spectra of $EgtB_1$ in 50 mM Tris buffer pH 8.0, 50 mM NaCl were measured in presence or absence of 2 eq. of γGluCys, 2 eq. TMH. For cobalt-charged enzymes, samples were first dialyzed against EDTA to remove iron and then twice against 50 mM Tris buffer pH 8.0, 50 mM NaCl. Then, samples were incubated with 1.5 eq of cobalt chloride solution at 10 °C in the quartz cuvette. Scans were performed at 10 °C from 200 - 800 nm. A metal-charged protein (Fe^{III} or Co^{II}) sample was used as a blank.

Michaelis-Menten analysis/Enzyme assay. Enzyme activities were assayed in 100 mM sodium phosphate buffer pH 8.0 containing 100 mM NaCl, 2 mM TCEP, 2 mM ascorbate, 4 eq. $FeSO_4$, TMH, and enzyme. Reactions were started by addition of γGluCys and incubated at 26 °C. Aliquots of the reactions were quenched by addition of 20 µL 1 M phosphoric acid and analyzed by cation exchange HPLC using 20 mM phosphoric acid at pH 2 as the mobile phase. Compounds were eluted in a NaCl gradient. All HPLC chromatograms were recorded at 265 nm. The data were fitted to the function $v = V_{max}[s]/(K_M + [s])$. Michaelis-Menten plots are shown below. k_{cat} and k_{cat}/K_M were determined in the presence of the second substrate at a concentration at least 3-fold higher than K_M of the second substrate. The data corresponds to averages from three independent enzyme reactions.

Kinetic solvent isotope effect. To measure the KSIE's, standard reaction mixture containing 100 mM phosphate buffer pH 8.0, 100 mM NaCl, 2 mM TCEP, 4 eq µM $FeSO_4$, 2 mM ascorbate, 1 mM N^{α},N^{α},N^{α}-trimethyl-L-histidine has been adjusted to pH 8.0 or 7.56 (final pD = 8.0).[124] The premixtures were lyophilized and then dissolved in H_2O or D_2O. Further rates of the reaction were

measured as described above. At saturation concentrations of both substrates, the maximal velocity was calculated in H_2O or D_2O, and the kinetic solvent isotope effect was calculated using the formula: KSIE = v_{H2O} / v_{D2O}.

Proton inventory. Reaction mixture containing 100 mM phosphate buffer pH 8.0, 100 mM NaCl, 2 mM TCEP, 4 eq µM $FeSO_4$, 2 mM ascorbate, 1 mM N^{α},N^{α},N^{α}-trimethyl-L-histidine was adjusted to pH 8.0 or 7.56 (final pD = 8.0). Premixture were lyophilized and then dissolved in H_2O or D_2O. In the reaction mixture different % content of H_2O or D_2O was present (0 – 92%). Rates were measured at standard conditions in D_2O gradient and fitted in Origin 8.5.

6. References

1. Seebeck, F. P., In vitro reconstitution of Mycobacterial ergothioneine biosynthesis. *J. Am. Chem. Soc.* **2010,** *132* (19), 6632-3.
2. Goncharenko, K. V.; Vit, A.; Blankenfeldt, W.; Seebeck, F. P., Structure of the sulfoxide synthase EgtB from the ergothioneine biosynthetic pathway. *Angew. Chem. Int. Ed.* **2015,** *54* (9), 2821-4.
3. Goncharenko, K. V.; Seebeck, F. P., Conversion of a non-heme iron-dependent sulfoxide synthase into a thiol dioxygenase by a single point mutation. *Chem Commun.* **2016,** *52* (9), 1945-8.
4. Pau, M. Y.; Lipscomb, J. D.; Solomon, E. I., Substrate activation for O2 reactions by oxidized metal centers in biology. *Proc Natl Acad Sci U S A* **2007,** *104* (47), 18355-62.
5. Hayaishi, O.; Katagiri, M.; Rothberg, S., Mechanism of the Pyrocatechase Reaction. *J. Am. Chem. Soc.* **1955,** *77* (20), 5450-5451.
6. Wang, B.; Usharani, D.; Li, C.; Shaik, S., Theory uncovers an unusual mechanism of DNA repair of a lesioned adenine by AlkB enzymes. *J. Am. Chem. Soc.* **2014,** *136* (39), 13895-901.
7. White, M. D.; Flashman, E., Catalytic strategies of the non-heme iron dependent oxygenases and their roles in plant biology. *Curr. Opin. Chem. Biol.* **2016,** *31*, 126-35.
8. Saban, E.; Flagg, S. C.; Knapp, M. J., Uncoupled O2-activation in the human HIF-asparaginyl hydroxylase, FIH, does not produce reactive oxygen species. *J. Inorg. Biochem.* **2011,** *105* (5), 630-6.
9. Loenarz, C.; Schofield, C. J., Expanding chemical biology of 2-oxoglutarate oxygenases. *Nat. Chem. Biol.* **2008,** *4* (3), 152-6.
10. Logrono, W.; Guambo, A.; Perez, M.; Kadier, A.; Recalde, C., A Terrestrial Single Chamber Microbial Fuel Cell-based Biosensor for Biochemical Oxygen Demand of Synthetic Rice Washed Wastewater. *Sensors (Basel)* **2016,** *16* (1).
11. (a) Ray, K.; Pfaff, F. F.; Wang, B.; Nam, W., Status of reactive non-heme metal-oxygen intermediates in chemical and enzymatic reactions. *J. Am. Chem. Soc.* **2014,** *136* (40), 13942-58; (b) Kovaleva, E. G.; Lipscomb, J. D., Versatility of biological non-heme Fe(II) centers in oxygen activation reactions. *Nat. Chem. Biol.* **2008,** *4* (3), 186-93.
12. Denisov, I. G.; Makris, T. M.; Sligar, S. G.; Schlichting, I., Structure and chemistry of cytochrome P450. *Chem. Rev.* **2005,** *105* (6), 2253-77.
13. Vandemeulebroucke, A.; Aldag, C.; Stiebritz, M. T.; Reiher, M.; Hilvert, D., Kinetic consequences of introducing a proximal selenocysteine ligand into cytochrome P450cam. *Biochemistry* **2015,** *54* (44), 6692-703.
14. Denisov, I. G.; Grinkova, Y. V.; McLean, M. A.; Sligar, S. G., The one-electron autoxidation of human cytochrome P450 3A4. *J. Biol. Chem.* **2007,** *282* (37), 26865-73.
15. Leitgeb, S.; Nidetzky, B., Structural and functional comparison of 2-His-1-carboxylate and 3-His metallocentres in non-haem iron(II)-dependent enzymes. *Biochem. Soc. Trans.* **2008,** *36* (Pt 6), 1180-6.
16. (a) Amrein, B.; Schmid, M.; Collet, G.; Cuniasse, P.; Gilardoni, F.; Seebeck, F. P.; Ward, T. R., Identification of two-histidines one-carboxylate binding motifs in proteins amenable to facial coordination to metals. *Metallomics* **2012,** *4* (4), 379-88; (b) Andreini, C.; Bertini, I.; Cavallaro, G.; Najmanovich, R. J.; Thornton, J. M., Structural analysis of metal sites in proteins: non-heme iron sites as a case study. *J. Mol. Biol.* **2009,** *388* (2), 356-80.
17. Koehntop, K. D.; Emerson, J. P.; Que, L., Jr., The 2-His-1-carboxylate facial triad: a versatile platform for dioxygen activation by mononuclear non-heme iron(II) enzymes. *J. Biol. Inorg. Chem.* **2005,** *10* (2), 87-93.
18. Muller, I.; Kahnert, A.; Pape, T.; Sheldrick, G. M.; Meyer-Klaucke, W.; Dierks, T.; Kertesz, M.; Uson, I., Crystal structure of the alkylsulfatase AtsK: insights into the catalytic mechanism of the Fe(II) alpha-ketoglutarate-dependent dioxygenase superfamily. *Biochemistry* **2004,** *43* (11), 3075-88.
19. Zhou, J. K., W.L.; Bachmann, B.O.; Gunsior, M.; Townsend, C.A.; Solomon, E.I. , Spectroscopic Studies of Substrate Interactions with Clavaminate Synthase 2, a Multifunctional α-KG-Dependent Non-Heme Iron Enzyme: Correlation with Mechanisms and Reactivities. *J. Am. Chem. Soc.* **2001,** *123* (30), 7388-7398.

20. O'Brien, J. R.; Schuller, D. J.; Yang, V. S.; Dillard, B. D.; Lanzilotta, W. N., Substrate-induced conformational changes in Escherichia coli taurine/alpha-ketoglutarate dioxygenase and insight into the oligomeric structure. *Biochemistry* **2003,** *42* (19), 5547-54.
21. Yan, W.; Song, H.; Song, F.; Guo, Y.; Wu, C. H.; Sae Her, A.; Pu, Y.; Wang, S.; Naowarojna, N.; Weitz, A.; Hendrich, M. P.; Costello, C. E.; Zhang, L.; Liu, P.; Zhang, Y. J., Endoperoxide formation by an alpha-ketoglutarate-dependent mononuclear non-haem iron enzyme. *Nature* **2015,** *527* (7579), 539-43.
22. Leitgeb, S.; Straganz, G. D.; Nidetzky, B., Biochemical characterization and mutational analysis of the mononuclear non-haem Fe2+ site in Dke1, a cupin-type dioxygenase from Acinetobacter johnsonii. *Biochem. J* **2009,** *418* (2), 403-11.
23. Blasiak, L. C.; Vaillancourt, F. H.; Walsh, C. T.; Drennan, C. L., Crystal structure of the non-haem iron halogenase SyrB2 in syringomycin biosynthesis. *Nature* **2006,** *440* (7082), 368-71.
24. Buongiorno, D.; Straganz, G. D., Structure and function of atypically coordinated enzymatic mononuclear non-heme-Fe(II) centers. *Coord. Chem. Rev.* **2013,** *257* (2), 541-563.
25. Wong, S. D.; Srnec, M.; Matthews, M. L.; Liu, L. V.; Kwak, Y.; Park, K.; Bell, C. B., 3rd; Alp, E. E.; Zhao, J.; Yoda, Y.; Kitao, S.; Seto, M.; Krebs, C.; Bollinger, J. M., Jr.; Solomon, E. I., Elucidation of the Fe(IV)=O intermediate in the catalytic cycle of the halogenase SyrB2. *Nature* **2013,** *499* (7458), 320-3.
26. Neidig, M. L.; Brown, C. D.; Light, K. M.; Fujimori, D. G.; Nolan, E. M.; Price, J. C.; Barr, E. W.; Bollinger, J. M., Jr.; Krebs, C.; Walsh, C. T.; Solomon, E. I., CD and MCD of CytC3 and taurine dioxygenase: role of the facial triad in alpha-KG-dependent oxygenases. *J. Am. Chem. Soc.* **2007,** *129* (46), 14224-31.
27. Erlandsen, H.; Kim, J. Y.; Patch, M. G.; Han, A.; Volner, A.; Abu-Omar, M. M.; Stevens, R. C., Structural Comparison of Bacterial and Human Iron-dependent Phenylalanine Hydroxylases: Similar Fold, Different Stability and Reaction Rates. *J. Mol. Biol.* **2002,** *320* (3), 645-661.
28. Hausinger, R. P., FeII/alpha-ketoglutarate-dependent hydroxylases and related enzymes. *Crit. Rev. Biochem. Mol. Biol.* **2004,** *39* (1), 21-68.
29. Srnec, M.; Wong, S. D.; Matthews, M. L.; Krebs, C.; Bollinger, J. M., Jr.; Solomon, E. I., Electronic Structure of the Ferryl Intermediate in the alpha-Ketoglutarate Dependent Non-Heme Iron Halogenase SyrB2: Contributions to H Atom Abstraction Reactivity. *J. Am. Chem. Soc.* **2016,** *138* (15), 5110-22.
30. Price, J. C.; Barr, E. W.; Tirupati, B.; Bollinger, J. M., Jr.; Krebs, C., The first direct characterization of a high-valent iron intermediate in the reaction of an alpha-ketoglutarate-dependent dioxygenase: a high-spin FeIV complex in taurine/alpha-ketoglutarate dioxygenase (TauD) from Escherichia coli. *Biochemistry* **2003,** *42* (24), 7497-508.
31. Mai, B. K.; Kim, Y., Is It Fe(III)-Oxyl Radical That Abstracts Hydrogen in the C-H Activation of TauD? A Theoretical Study Based on the DFT Potential Energy Surfaces. *Inorg. Chem.* **2016,** *55* (8), 3844-52.
32. Puri, M.; Biswas, A. N.; Fan, R.; Guo, Y.; Que, L., Jr., Modeling Non-Heme Iron Halogenases: High-Spin Oxoiron(IV)-Halide Complexes That Halogenate C-H Bonds. *J. Am. Chem. Soc.* **2016,** *138* (8), 2484-7.
33. Schofield, C. J.; Baldwin, J. E.; Byford, M. F.; Clifton, I.; Hajdu, J.; Hensgens, C.; Roach, P., Proteins of the penicillin biosynthesis pathway. *Curr. Opin. Struct. Biol.* **1997,** *7* (6), 857-864.
34. Lundberg, M.; Siegbahn, P. E.; Morokuma, K., The mechanism for isopenicillin N synthase from density-functional modeling highlights the similarities with other enzymes in the 2-His-1-carboxylate family. *Biochemistry* **2008,** *47* (3), 1031-42.
35. Ge, W.; Clifton, I. J.; Howard-Jones, A. R.; Stok, J. E.; Adlington, R. M.; Baldwin, J. E.; Rutledge, P. J., Structural studies on the reaction of isopenicillin N synthase with a sterically demanding depsipeptide substrate analogue. *ChemBioChem* **2009,** *10* (12), 2025-31.
36. Clifton, I. J.; Ge, W.; Adlington, R. M.; Baldwin, J. E.; Rutledge, P. J., The crystal structure of an isopenicillin N synthase complex with an ethereal substrate analogue reveals water in the oxygen binding site. *FEBS Lett.* **2013,** *587* (16), 2705-9.
37. Baldwin, J. E. A., R. M.; Moroney, S. E.; Field, L. D.; Ting, H-H, Stepwise ring closure in penicillin biosynthesis. Intitial β-lactam formation *J. Chem. Soc., Chem. Commun* **1984,** (15), 984-986

38. Tamanaha, E.; Zhang, B.; Guo, Y.; Chang, W. C.; Barr, E. W.; Xing, G.; St Clair, J.; Ye, S.; Neese, F.; Bollinger, J. M., Jr.; Krebs, C., Spectroscopic Evidence for the Two C-H-Cleaving Intermediates of Aspergillus nidulans Isopenicillin N Synthase. *J. Am. Chem. Soc.* **2016,** *138* (28), 8862-74.
39. Chiang, C. W.; Kleespies, S. T.; Stout, H. D.; Meier, K. K.; Li, P. Y.; Bominaar, E. L.; Que, L., Jr.; Munck, E.; Lee, W. Z., Characterization of a paramagnetic mononuclear nonheme iron-superoxo complex. *J. Am. Chem. Soc.* **2014,** *136* (31), 10846-9.
40. Dominy, J. E., Jr.; Simmons, C. R.; Hirschberger, L. L.; Hwang, J.; Coloso, R. M.; Stipanuk, M. H., Discovery and characterization of a second mammalian thiol dioxygenase, cysteamine dioxygenase. *J. Biol. Chem.* **2007,** *282* (35), 25189-98.
41. Bruland, N.; Wubbeler, J. H.; Steinbuchel, A., 3-mercaptopropionate dioxygenase, a cysteine dioxygenase homologue, catalyzes the initial step of 3-mercaptopropionate catabolism in the 3,3-thiodipropionic acid-degrading bacterium variovorax paradoxus. *J. Biol. Chem.* **2009,** *284* (1), 660-72.
42. Franovic, A.; Holterman, C. E.; Payette, J.; Lee, S., Human cancers converge at the HIF-2alpha oncogenic axis. *Proc Natl Acad Sci U S A* **2009,** *106* (50), 21306-11.
43. Stipanuk, M. H.; Ueki, I., Dealing with methionine/homocysteine sulfur: cysteine metabolism to taurine and inorganic sulfur. *J Inherit Metab Dis* **2011,** *34* (1), 17-32.
44. Pean, A. R.; Parsons, R. B.; Waring, R. H.; Williams, A. C.; Ramsden, D. B., Toxicity of sulphur-containing compounds to neuronal cell lines. *J. Neurol. Sci.* **1995,** *129*, 107-108.
45. Galvan, I.; Ghanem, G.; Moller, A. P., Has removal of excess cysteine led to the evolution of pheomelanin? Pheomelanogenesis as an excretory mechanism for cysteine. *Bioessays* **2012,** *34* (7), 565-8.
46. McCoy, J. G.; Bailey, L. J.; Bitto, E.; Bingman, C. A.; Aceti, D. J.; Fox, B. G.; Phillips, G. N., Jr., Structure and mechanism of mouse cysteine dioxygenase. *Proc Natl Acad Sci U S A* **2006,** *103* (9), 3084-9.
47. Ito, N.; Phillips, S. E.; Stevens, C.; Ogel, Z. B.; McPherson, M. J.; Keen, J. N.; Yadav, K. D.; Knowles, P. F., Novel thioether bond revealed by a 1.7 A crystal structure of galactose oxidase. *Nature* **1991,** *350* (6313), 87-90.
48. Siakkou, E.; Rutledge, M. T.; Wilbanks, S. M.; Jameson, G. N., Correlating crosslink formation with enzymatic activity in cysteine dioxygenase. *Biochim. Biophys. Acta* **2011,** *1814* (12), 2003-9.
49. Li, W.; Blaesi, E. J.; Pecore, M. D.; Crowell, J. K.; Pierce, B. S., Second-sphere interactions between the C93-Y157 cross-link and the substrate-bound Fe site influence the O(2) coupling efficiency in mouse cysteine dioxygenase. *Biochemistry* **2013,** *52* (51), 9104-19.
50. Dominy, J. E., Jr.; Hwang, J.; Guo, S.; Hirschberger, L. L.; Zhang, S.; Stipanuk, M. H., Synthesis of amino acid cofactor in cysteine dioxygenase is regulated by substrate and represents a novel post-translational regulation of activity. *J. Biol. Chem.* **2008,** *283* (18), 12188-201.
51. Tchesnokov, E. P.; Faponle, A. S.; Davies, C. G.; Quesne, M. G.; Turner, R.; Fellner, M.; Souness, R. J.; Wilbanks, S. M.; de Visser, S. P.; Jameson, G. N., An iron-oxygen intermediate formed during the catalytic cycle of cysteine dioxygenase. *Chem Commun (Camb)* **2016,** *52* (57), 8814-7.
52. Joseph, C. A.; Maroney, M. J., Cysteine dioxygenase: structure and mechanism. *Chem. Commun.* **2007,** (32), 3338.
53. Kruk, J.; Aboul-Enein, H. Y., Reactive oxygen and nitrogen species in carcinogenesis: Implications of oxidative stress on the progression and development of several cancer types. *Mini Rev Med Chem* **2017**.
54. Sheng, Y.; Abreu, I. A.; Cabelli, D. E.; Maroney, M. J.; Miller, A. F.; Teixeira, M.; Valentine, J. S., Superoxide dismutases and superoxide reductases. *Chem. Rev.* **2014,** *114* (7), 3854-918.
55. Pinto, A. F.; Romao, C. V.; Pinto, L. C.; Huber, H.; Saraiva, L. M.; Todorovic, S.; Cabelli, D.; Teixeira, M., Superoxide reduction by a superoxide reductase lacking the highly conserved lysine residue. *J. Biol. Inorg. Chem.* **2015,** *20* (1), 155-64.
56. Silaghi-Dumitrescu, R.; Silaghi-Dumitrescu, I.; Coulter, E. D.; Kurtz, D. M., Computational Study of the Non-Heme Iron Active Site in Superoxide Reductase and Its Reaction with Superoxide. *Inorg. Chem.* **2003,** *42* (2), 446-456.
57. Emerson, J. P.; Coulter, E. D.; Cabelli, D. E.; Phillips, R. S.; Kurtz, D. M., Kinetics and Mechanism of Superoxide Reduction by Two-Iron Superoxide Reductase fromDesulfovibriovulgaris. *Biochemistry* **2002,** *41* (13), 4348-4357.

58. Shearer, J.; Scarrow, R. C.; Kovacs, J. A., Synthetic Models for the Cysteinate-Ligated Non-Heme Iron Enzyme Superoxide Reductase: Observation and Structural Characterization by XAS of an FeIII−OOH Intermediate. *J. Am. Chem. Soc.* **2002,** *124* (39), 11709-11717.
59. Seebeck, F. P., Thiohistidine biosynthesis. *Chimia (Aarau)* **2013,** *67* (5), 333-6.
60. Newton, G. L.; Buchmeier, N.; Fahey, R. C., Biosynthesis and functions of mycothiol, the unique protective thiol of Actinobacteria. *Microbiol. Mol. Biol. Rev.* **2008,** *72* (3), 471-94.
61. Halliwell, B.; Cheah, I. K.; Drum, C. L., Ergothioneine, an adaptive antioxidant for the protection of injured tissues? A hypothesis. *Biochem. Biophys. Res. Commun.* **2016,** *470* (2), 245-50.
62. (a) Pfeiffer, C.; Bach, M.; Bauer, T.; Campos da Ponte, J.; Schomig, E.; Grundemann, D., Knockout of the ergothioneine transporter ETT in zebrafish results in increased 8-oxoguanine levels. *Free Radic Biol Med* **2015,** *83*, 178-85; (b) Grundemann, D.; Harlfinger, S.; Golz, S.; Geerts, A.; Lazar, A.; Berkels, R.; Jung, N.; Rubbert, A.; Schomig, E., Discovery of the ergothioneine transporter. *Proc Natl Acad Sci U S A* **2005,** *102* (14), 5256-61.
63. Sao Emani, C.; Williams, M. J.; Wiid, I. J.; Hiten, N. F.; Viljoen, A. J.; Pietersen, R. D.; van Helden, P. D.; Baker, B., Ergothioneine is a secreted antioxidant in Mycobacterium smegmatis. *Antimicrob. Agents Chemother.* **2013,** *57* (7), 3202-7.
64. Hartman, P. E., Ergothioneine as antioxidant. *Methods Enzymol.* **1990,** *186*, 310-318.
65. Vit, A.; Misson, L.; Blankenfeldt, W.; Seebeck, F. P., Ergothioneine biosynthetic methyltransferase EgtD reveals the structural basis of aromatic amino acid betaine biosynthesis. *ChemBioChem* **2015,** *16* (1), 119-25.
66. Vit, A.; Mashabela, G. T.; Blankenfeldt, W.; Seebeck, F. P., Structure of the Ergothioneine-Biosynthesis Amidohydrolase EgtC. *ChemBioChem* **2015,** *16* (10), 1490-6.
67. (a) Hu, W.; Song, H.; Sae Her, A.; Bak, D. W.; Naowarojna, N.; Elliott, S. J.; Qin, L.; Chen, X.; Liu, P., Bioinformatic and biochemical characterizations of C-S bond formation and cleavage enzymes in the fungus Neurospora crassa ergothioneine biosynthetic pathway. *Org. Lett.* **2014,** *16* (20), 5382-5; (b) Melville, D. B. H., W. H.; Lubschez, R. , Tissue ergothioneine. *J. Biol. Chem.* **1954,** *206*, 221.
68. Turner, E. K., R.;, Hopkins P. B.; Shapiro B. M., Ovothiol: a novel thiohistidine compound from sea urchin eggs that confers NAD(P)H-O2 oxidoreductase activity on ovoperoxidase. *J Biol Chem. 1986 Oct 5;261(28):13056-63.* **1986,** *261* (28), 13056-13063.
69. Turner, E.; Hager, L.; Shapiro, B., Ovothiol replaces glutathione peroxidase as a hydrogen peroxide scavenger in sea urchin eggs. *Science* **1988,** *242* (4880), 939-941.
70. Braunshausen, A.; Seebeck, F. P., Identification and characterization of the first ovothiol biosynthetic enzyme. *J. Am. Chem. Soc.* **2011,** *133* (6), 1757-9.
71. Becker, S.; Terlau, H., Toxins from cone snails: properties, applications and biotechnological production. *Appl. Microbiol. Biotechnol.* **2008,** *79* (1), 1-9.
72. Krauth-Siegel, R. L.; Leroux, A. E., Low-molecular-mass antioxidants in parasites. *Antioxid. Redox Signal.* **2012,** *17* (4), 583-607.
73. Bushnell, E. A.; Fortowsky, G. B.; Gauld, J. W., Model iron-oxo species and the oxidation of imidazole: insights into the mechanism of OvoA and EgtB? *Inorg. Chem.* **2012,** *51* (24), 13351-6.
74. (a) Mashabela, G. T.; Seebeck, F. P., Substrate specificity of an oxygen dependent sulfoxide synthase in ovothiol biosynthesis. *Chem Commun (Camb)* **2013,** *49* (70), 7714-6; (b) Song, H.; Leninger, M.; Lee, N.; Liu, P., Regioselectivity of the oxidative C-S bond formation in ergothioneine and ovothiol biosyntheses. *Org. Lett.* **2013,** *15* (18), 4854-7.
75. Wei, W. J.; Siegbahn, P. E.; Liao, R. Z., Theoretical Study of the Mechanism of the Nonheme Iron Enzyme EgtB. *Inorg. Chem.* **2017,** *56* (6), 3589-3599.
76. Peck, S. C.; van der Donk, W. A., Go it alone: four-electron oxidations by mononuclear non-heme iron enzymes. *J. Biol. Inorg. Chem.* **2016**.
77. Gardner, J. D.; Pierce, B. S.; Fox, B. G.; Brunold, T. C., Spectroscopic and computational characterization of substrate-bound mouse cysteine dioxygenase: nature of the ferrous and ferric cysteine adducts and mechanistic implications. *Biochemistry* **2010,** *49* (29), 6033-41.
78. Tchesnokov, E. P.; Wilbanks, S. M.; Jameson, G. N., A strongly bound high-spin iron(II) coordinates cysteine and homocysteine in cysteine dioxygenase. *Biochemistry* **2012,** *51* (1), 257-64.
79. Tuderman, L.; Myllyla, R.; Kivirikko, K. I., Mechanism of the Prolyl Hydroxylase Reaction. 1. Role of Co-substrates. *Eur. J. Biochem.* **1977,** *80* (2), 341-348.

80. Clay, M. D.; Jenney, F. E.; Hagedoorn, P. L.; George, G. N.; Adams, M. W. W.; Johnson, M. K., Spectroscopic Studies of Pyrococcus furiosus Superoxide Reductase: Implications for Active-Site Structures and the Catalytic Mechanism. *J. Am. Chem. Soc.* **2002,** *124* (5), 788-805.
81. (a) Le Coq, J.; Ghosh, P., Conservation of the C-type lectin fold for massive sequence variation in a Treponema diversity-generating retroelement. *Proc Natl Acad Sci U S A* **2011,** *108* (35), 14649-53; (b) McMahon, S. A.; Miller, J. L.; Lawton, J. A.; Kerkow, D. E.; Hodes, A.; Marti-Renom, M. A.; Doulatov, S.; Narayanan, E.; Sali, A.; Miller, J. F.; Ghosh, P., The C-type lectin fold as an evolutionary solution for massive sequence variation. *Nat. Struct. Mol. Biol.* **2005,** *12* (10), 886-92.
82. (a) Dierks, T.; Dickmanns, A.; Preusser-Kunze, A.; Schmidt, B.; Mariappan, M.; von Figura, K.; Ficner, R.; Rudolph, M. G., Molecular basis for multiple sulfatase deficiency and mechanism for formylglycine generation of the human formylglycine-generating enzyme. *Cell* **2005,** *121* (4), 541-52; (b) Knop, M.; Dang, T. Q.; Jeschke, G.; Seebeck, F. P., Copper is a Cofactor of the Formylglycine-Generating Enzyme. *ChemBioChem* **2017,** *18* (2), 161-165.
83. Song, H.; Her, A. S.; Raso, F.; Zhen, Z.; Huo, Y.; Liu, P., Cysteine oxidation reactions catalyzed by a mononuclear non-heme iron enzyme (OvoA) in ovothiol biosynthesis. *Org. Lett.* **2014,** *16* (8), 2122-5.
84. Kelly, S. M.; Jess, T. J.; Price, N. C., How to study proteins by circular dichroism. *Biochim. Biophys. Acta* **2005,** *1751* (2), 119-39.
85. (a) Nagata, K.; Ohtsuka, J.; Takahashi, M.; Asano, A.; Iino, H.; Ebihara, A.; Tanokura, M., Crystal structure of TTHA0303 (TT2238), a four-helix bundle protein with an exposed histidine triad from Thermus thermophilus HB8 at 2.0 A. *Proteins* **2008,** *70* (3), 1103-7; (b) Rajan, S. S.; Yang, X.; Shuvalova, L.; Collart, F.; Anderson, W. F., YfiT from Bacillus subtilis is a probable metal-dependent hydrolase with an unusual four-helix bundle topology. *Biochemistry* **2004,** *43* (49), 15472-9; (c) Cooper, D. R.; Grelewska, K.; Kim, C. Y.; Joachimiak, A.; Derewenda, Z. S., The structure of DinB from Geobacillus stearothermophilus: a representative of a unique four-helix-bundle superfamily. *Acta Crystallogr Sect F Struct Biol Cryst Commun* **2010,** *66* (Pt 3), 219-24.
86. (a) Newton, G. L.; Leung, S. S.; Wakabayashi, J. I.; Rawat, M.; Fahey, R. C., The DinB superfamily includes novel mycothiol, bacillithiol, and glutathione S-transferases. *Biochemistry* **2011,** *50* (49), 10751-60; (b) Feng, J.; Che, Y.; Milse, J.; Yin, Y. J.; Liu, L.; Ruckert, C.; Shen, X. H.; Qi, S. W.; Kalinowski, J.; Liu, S. J., The gene ncgl2918 encodes a novel maleylpyruvate isomerase that needs mycothiol as cofactor and links mycothiol biosynthesis and gentisate assimilation in Corynebacterium glutamicum. *J. Biol. Chem.* **2006,** *281* (16), 10778-85.
87. Chen, L.; Lyubimov, A. Y.; Brammer, L.; Vrielink, A.; Sampson, N. S., The binding and release of oxygen and hydrogen peroxide are directed by a hydrophobic tunnel in cholesterol oxidase. *Biochemistry* **2008,** *47* (19), 5368-77.
88. Gottlieb, H. E.; Kotlyar, V.; Nudelman, A., NMR Chemical Shifts of Common Laboratory Solvents as Trace Impurities. *The Journal of Organic Chemistry* **1997,** *62* (21), 7512-7515.
89. Siakkou, E.; Wilbanks, S. M.; Jameson, G. N., Simplified cysteine dioxygenase activity assay allows simultaneous quantitation of both substrate and product. *Anal. Biochem.* **2010,** *405* (1), 127-31.
90. Li, W.; Pierce, B. S., Steady-state substrate specificity and O(2)-coupling efficiency of mouse cysteine dioxygenase. *Arch. Biochem. Biophys.* **2015,** *565*, 49-56.
91. Blaesi, E. J.; Gardner, J. D.; Fox, B. G.; Brunold, T. C., Spectroscopic and computational characterization of the NO adduct of substrate-bound Fe(II) cysteine dioxygenase: insights into the mechanism of O2 activation. *Biochemistry* **2013,** *52* (35), 6040-51.
92. Driggers, C. M.; Cooley, R. B.; Sankaran, B.; Hirschberger, L. L.; Stipanuk, M. H.; Karplus, P. A., Cysteine dioxygenase structures from pH4 to 9: consistent cys-persulfenate formation at intermediate pH and a Cys-bound enzyme at higher pH. *J. Mol. Biol.* **2013,** *425* (17), 3121-36.
93. Geoghegan, K. F.; Dixon, H. B.; Rosner, P. J.; Hoth, L. R.; Lanzetti, A. J.; Borzilleri, K. A.; Marr, E. S.; Pezzullo, L. H.; Martin, L. B.; LeMotte, P. K.; McColl, A. S.; Kamath, A. V.; Stroh, J. G., Spontaneous alpha-N-6-phosphogluconoylation of a "His tag" in Escherichia coli: the cause of extra mass of 258 or 178 Da in fusion proteins. *Anal. Biochem.* **1999,** *267* (1), 169-84.
94. Krezel, A.; Bal, W., *J. Inorg. Biochem.* **2004,** *98*, 161 - 166.
95. Paul, B. D.; Snyder, S. H., The unusual amino acid L-ergothioneine is a physiologic cytoprotectant. *Cell Death Differ.* **2010,** *17* (7), 1134-40.

96. Kimani, M. M.; Wang, H. C.; Brumaghim, J. L., Investigating the copper coordination, electrochemistry, and Cu(II) reduction kinetics of biologically relevant selone and thione compounds. *Dalton Trans* **2012,** *41* (17), 5248-59.
97. Servillo, L.; D'Onofrio, N.; Casale, R.; Cautela, D.; Giovane, A.; Castaldo, D.; Balestrieri, M. L., Ergothioneine products derived by superoxide oxidation in endothelial cells exposed to high-glucose. *Free Radic Biol Med* **2017,** *108*, 8-18.
98. Yamashita, Y.; Yamashita, M., Identification of a novel selenium-containing compound, selenoneine, as the predominant chemical form of organic selenium in the blood of bluefin tuna. *J. Biol. Chem.* **2010,** *285* (24), 18134-8.
99. Yamashita, Y.; Yamashita, M.; Iida, H., Selenium content in seafood in Japan. *Nutrients* **2013,** *5* (2), 388-95.
100. (a) Yamashita, M.; Yamashita, Y.; Suzuki, T.; Kani, Y.; Mizusawa, N.; Imamura, S.; Takemoto, K.; Hara, T.; Hossain, M. A.; Yabu, T.; Touhata, K., Selenoneine, a novel selenium-containing compound, mediates detoxification mechanisms against methylmercury accumulation and toxicity in zebrafish embryo. *Mar Biotechnol (NY)* **2013,** *15* (5), 559-70; (b) Yamashita, Y.; Yabu, T.; Yamashita, M., Discovery of the strong antioxidant selenoneine in tuna and selenium redox metabolism. *World J Biol Chem* **2010,** *1* (5), 144-50.
101. Klein, M.; Ouerdane, L.; Bueno, M.; Pannier, F., Identification in human urine and blood of a novel selenium metabolite, Se-methylselenoneine, a potential biomarker of metabolization in mammals of the naturally occurring selenoneine, by HPLC coupled to electrospray hybrid linear ion trap-orbital ion trap MS. *Metallomics* **2011,** *3* (5), 513-20.
102. Pluskal, T.; Ueno, M.; Yanagida, M., Genetic and metabolomic dissection of the ergothioneine and selenoneine biosynthetic pathway in the fission yeast, S. pombe, and construction of an overproduction system. *PLoS One* **2014,** *9* (5), e97774.
103. (a) Wessjohann, L. A.; Schneider, A.; Abbas, M.; Brandt, W., Selenium in chemistry and biochemistry in comparison to sulfur. *Biol. Chem.* **2007,** *388* (10), 997-1006; (b) Johansson, L.; Gafvelin, G.; Arner, E. S., Selenocysteine in proteins-properties and biotechnological use. *Biochim. Biophys. Acta* **2005,** *1726* (1), 1-13.
104. Northrop, D. B., Minimal kinetic mechanism and general equation for deuterium isotope effects on enzymic reactions: uncertainty of detecting a rate-limiting step. *Biochemistry* **1981,** *20* (14), 4056-4061.
105. Krause, R. J.; Elfarra, A. A., Reduction of L-methionine selenoxide to seleno-L-methionine by endogenous thiols, ascorbic acid, or methimazole. *Biochem. Pharmacol.* **2009,** *77* (1), 134-40.
106. Assmann, A.; Briviba, K.; Sies, H., Reduction of methionine selenoxide to selenomethionine by glutathione. *Arch. Biochem. Biophys.* **1998,** *349* (1), 201-3.
107. De Silva, V.; Woznichak, M. M.; Burns, K. L.; Grant, K. B.; May, S. W., Selenium redox cycling in the protective effects of organoselenides against oxidant-induced DNA damage. *J. Am. Chem. Soc.* **2004,** *126* (8), 2409-13.
108. Wei, W. J.; Siegbahn, P. E.; Liao, R. Z., Theoretical Study of the Mechanism of the Nonheme Iron Enzyme EgtB. *Inorg. Chem.* **2017**.
109. (a) Kollman, P. A.; Allen, L. C., Theory of the hydrogen bond. *Chem. Rev.* **1972,** *72* (3), 283-303; (b) Frey, P. A., Review: Strong hydrogen bonding in molecules and enzymatic complexes. *Magn. Reson. Chem.* **2001,** *39* (S1), S190-S198.
110. Mathe, C.; Weill, C. O.; Mattioli, T. A.; Berthomieu, C.; Houee-Levin, C.; Tremey, E.; Niviere, V., Assessing the role of the active-site cysteine ligand in the superoxide reductase from Desulfoarculus baarsii. *J. Biol. Chem.* **2007,** *282* (30), 22207-16.
111. Yang, X.; Niu, S.; Ichiye, T.; Wang, L. S., Direct measurement of the hydrogen-bonding effect on the intrinsic redox potentials of [4Fe-4S] cubane complexes. *J. Am. Chem. Soc.* **2004,** *126* (48), 15790-4.
112. Dey, A.; Okamura, T. A.; Ueyama, N.; Hedman, B.; Hodgson, K. O.; Solomon, E. I., Sulfur K-edge XAS and DFT calculations on P450 model complexes: effects of hydrogen bonding on electronic structure and redox potentials. *J. Am. Chem. Soc.* **2005,** *127* (34), 12046-53.
113. Wall, S. B.; Oh, J. Y.; Diers, A. R.; Landar, A., Oxidative modification of proteins: an emerging mechanism of cell signaling. *Front Physiol* **2012,** *3*, 369.
114. Penner-Hahn, J., Zinc-promoted alkyl transfer: a new role for zinc. *Curr. Opin. Chem. Biol.* **2007,** *11* (2), 166-71.

115. Chiou, S. J.; Riordan, C. G.; Rheingold, A. L., Synthetic modeling of zinc thiolates: quantitative assessment of hydrogen bonding in modulating sulfur alkylation rates. *Proc Natl Acad Sci U S A* **2003,** *100* (7), 3695-700.
116. (a) Takinowaki, H.; Matsuda, Y.; Yoshida, T.; Kobayashi, Y.; Ohkubo, T., The solution structure of the methylated form of the N-terminal 16-kDa domain of Escherichia coli Ada protein. *Protein Sci.* **2006,** *15* (3), 487-97; (b) Fu, T. M.; Almqvist, J.; Liang, Y. H.; Li, L.; Huang, Y.; Su, X. D., Crystal structures of cobalamin-independent methionine synthase (MetE) from Streptococcus mutans: a dynamic zinc-inversion model. *J. Mol. Biol.* **2011,** *412* (4), 688-97; (c) Okeley, N. M.; Paul, M.; Stasser, J. P.; Blackburn, N.; van der Donk, W. A., SpaC and NisC, the cyclases involved in subtilin and nisin biosynthesis, are zinc proteins. *Biochemistry* **2003,** *42* (46), 13613-24.
117. Yeh, A. P.; Hu, Y.; Jenney, F. E.; Adams, M. W. W.; Rees, D. C., Structures of the Superoxide Reductase fromPyrococcus furiosusin the Oxidized and Reduced States. *Biochemistry* **2000,** *39* (10), 2499-2508.
118. Clay, M. D.; Jenney, F. E.; Noh, H. J.; Hagedoorn, P. L.; Adams, M. W. W.; Johnson, M. K., Resonance Raman Characterization of the Mononuclear Iron Active-Site Vibrations and Putative Electron Transport Pathways inPyrococcus furiosusSuperoxide Reductase. *Biochemistry* **2002,** *41* (31), 9833-9841.
119. Hoffmann, K. M.; Samardzic, D.; Heever, K.; Rowlett, R. S., Co(II)-substituted Haemophilus influenzae beta-carbonic anhydrase: spectral evidence for allosteric regulation by pH and bicarbonate ion. *Arch. Biochem. Biophys.* **2011,** *511* (1-2), 80-7.
120. Venkatasubban, K. S.; Schowen, R. L., The proton inventory technique. *CRC Crit Rev Biochem* **1984,** *17* (1), 1-44.
121. Garoutte, M. P.; Bibbs, J. A.; Schowen, R. L., Solvent Isotope Effects and the Question of Quantum Tunneling in Hydrolytic Enzyme Action. *J. Nucl. Sci. Technol.* **2006,** *43* (4), 455-460.
122. Miyake, T.; Rolandi, M., Grotthuss mechanisms: from proton transport in proton wires to bioprotonic devices. *J Phys Condens Matter* **2016,** *28* (2), 023001.
123. Harada, Y.; Tokushima, T.; Horikawa, Y.; Takahashi, O.; Niwa, H.; Kobayashi, M.; Oshima, M.; Senba, Y.; Ohashi, H.; Wikfeldt, K. T.; Nilsson, A.; Pettersson, L. G.; Shin, S., Selective probing of the OH or OD stretch vibration in liquid water using resonant inelastic soft-x-ray scattering. *Phys. Rev. Lett.* **2013,** *111* (19), 193001.
124. Krezel, A.; Bal, W., A formula for correlating pKa values determined in D2O and H2O. *J. Inorg. Biochem.* **2004,** *98* (1), 161-6.

Acknowledgements

I would like to thank Prof. Florian P. Seebeck for giving me the chance to join his lab at the very beginning and let me work on this exciting project. Also I would like to thank him for teaching me how to generate ideas and solve difficult problems in a creative way. Looking back, the project was challenging, but now I see that it went toward the right direction.

I would like to thank Prof. Thomas R. Ward for his time in co-examining and reading my thesis.

I would like to thank Prof. Dennis Gillingham for chairing the PhD defense session and sharing great atmosphere on the third floor.

I would further like to thank Dr. Yves Auberson for his kindness, support and great time with SCS.

During my time in this lab I have met the best colleagues I could dream of: Gao, Leti, Matthias, Roxi, Gabriel, Pascal, Ali, Sébastien, Lukas, Thanh, Alma, Sebi, Liao, Marcel, Reto, Anja, Alice, Davey, Dima and Florian. Thank you guys for all your support, knowledge and fun! Furthermore, I am grateful to meet many cool and nice people in the chemistry department from all research groups, especially from the 3rd floor, and to share countless BBQs and beers!

The written version of this thesis would not exist without help and constructive comments provided by Davey, Kiril, Matthias, Anja and Martin, I am very thankful for your help.

I would like to thank all my flatmates from the "House of Love" – Rox, Kiwi, David, Julchen, Maurus and Rafa for the best and craziest time of living and traveling with you guys! I am grateful to meet amazing people in Basel, all of them helped me to push my limits and never give up. All great times we shared together will forever stay in my heart. I would specially like to say thanks to my dear friend Sascha for all his support and great time we spent together; to Arcadie for his constructive comments, calmness and funny jokes; to David for keeping up happy mood and scientific excitement; to Eleni for her great Greek warm friendship; to Aurelia for fun dancing and great dinners; to Domenika for her kind heart; to Kiwi for his positivity; to Julian for his craziness; and to Mia for always being close even she is far. Also, I would like to thank my Russian friends Yulia, Irog, Brus, Slavik, Max, Akursulov and Lyuba who are like my family even though I don't see them as often as I wished.

Thanks to my father Igor, I have learned how to set goals in life and push myself towards reaching them. The biggest thanks goes to my mother Elena, who is my best friend and supports me every day and every second of my life. Without her belief in me, I would not be able to finish my PhD. Also, I would like to thank my great-grandmother Olga for teaching me how to be generous and strong no matter what. Even she is not with us anymore, without her I wouldn't be the person I have become.

Curriculum vitae

Kristina Goncharenko

E-mail kris.goncharenko@gmail.com
Mobile +41774581031
Date of Birth: 15.10.1990

EDUCATION

08/2012 – 04/2017	Ph.D. student in Biochemistry in the group of Prof. Dr. F. P. Seebeck University of Basel, Basel (Switzerland)
09/2007 – 07/2012	MSc in Chemistry; Grade: 5/5 with Hons. Lomonosov Moscow State University, Moscow (Russia)

PUBLICATIONS

- Goncharenko K. V., Seebeck F. P. *Chem Commun*, **2016**, 52(9): 1945

- Goncharenko K. V., Vit A., Blankenfeldt W. and Seebeck F. P. *Angew. Chem. Int. Ed.* **2015**, 54(9): 2821

- Tishkov V. I., Goncharenko K. V., Alekseeva A. A., Kleymenov S. Yu. and Savin S. S. *Biochemistry (Moscow)*, **2015**, 80(13): 1690

- Goncharenko K. V., Savin S. S. and Tishkov V. I. *Moscow University Chemistry Bulletin*, **2010**, 65(3): 131

AWARDS AND SCHOLARSHIPS

- Swiss Government Excellence Scholarship (2013-2016)

- Best poster award at the 33rd REGIO Symposium, Mittelwihr, France, 9-11, September 2013

- "2015 Chemistry Travel Award" by SCNAT, SCS and SSFEC

- Best poster presentation award (Runners' up Prize) at SCS Fall Meeting 2015, Lausanne, Switzerland, 4 September 2015